CRANFIELD UNIVERSITY

Erminio Samuele Zanenga

Design and Engineering Methods for Open-rotor Nacelle Shaping

School of Engineering

Ph. D. Thesis

SCHOOL OF ENGINEERING
DEPARTMENT OF POWER AND PROPULSION

Full Time Ph. D.

Academic Year 2009-2010

Erminio Samuele Zanenga

Design and Engineering Methods for Open-rotor Nacelle Shaping

Supervisor: Prof. R. Singh
Industrial Advisors: E. Kitchen – A. Smith

April 2010

© Cranfield University, 2010. All rights reserved. No part of this publication may be reproduced without the written permission of the copyright owner

Dedicated to the persons I love,

on Earth and in Heaven.

Acknowledgements

This thesis is the final step of my research activities at Cranfield University. I am really grateful to my beloved parents, my entire family, and my true friends: living and working abroad was a challenging experience I faced serenely due to their loving presence in my daily life.

I am also grateful to Rolls-Royce plc for sponsoring my research within the Cranfield University Technology Centre (UTC) in Performance Engineering. In particular, I wish to thank Mark Taylor and Christopher Sheaf, for the impulse provided in defining this work, whilst I am indebted to Edward Kitchen, Angus Smith, and Richard Thorne, for their valuable support during the whole research programme. I must sincerely say thanks to Stewart Kirby and Victoria Yeomans for their help in assessing the patentability of some of the inventions created during my research, in particular the diffusive nacelle concept, and to Richard Tunstall, Stephen Brown and Arthur Rowe as well for their professional feedback during the UTC technical reviews.

I would like to express my gratitude to my colleagues and to the entire team of the Department of Power and Propulsion, principally to my supervisor, Prof. Riti Singh, for his precious teachings and guidance, and to Prof. Pericles Pilidis, Dr Vassilios Pachidis and Dr Joao Amaral Teixeira for providing me with their kind assistance whenever I needed it. I'm also grateful to Samantha Broe, Maria Negus, Gillian Hargreaves and Rachel Smith, for their tireless availability.

Last but not less important, a special acknowledgement to the wonderful girl

who never left me despite my long absence: many thanks, with all my heart.

Contents

List of Figures

List of Tables

Summary

Due to the growing transport needs in emerging economies and recent success of the low-cost airlines, the demand for short/medium-haul aeroplanes is increasing. Within the next twenty years, the existing single-aisle aircraft are likely to be replaced by new models mounting new propulsion systems. One promising configuration being considered is the open-rotor, which is a revision of the propfan. However, further progress has to be done in order to transform propfan engines, whose technology dates back to the 1980s, into viable and feasible open-rotor concepts.

Among the aspects yet to be investigated in sufficient depth is the definition of a methodology for the open-rotor nacelle design. The aim of the present research is to help enhance the knowledge in this area. Even if there are a number of important fields of investigation for open-rotor designs, this work is limited to the analysis of the pusher architecture with no exhaust impingement through rotors.

The research is initially performed combining both a graphical and a computational approach, investigating the mathematical and physical aspects involved in the definition of appropriate nacelle profiles, boundary conditions for the CFD analysis and simplified rotor modelling. The first simulations are mainly focused on a typical propfan nacelle, which is taken as a reference model: the computations provide useful results for evaluating its aerodynamic features.

Since the aerodynamic characteristics of a nacelle profile are influenced by its geometry, in particular by its curvature distribution, an effort is done to shape

the cowl without the use of commercial software, from which the mathematical aspects related to its geometry are inevitably unknown. The rigorous mathematical definition of the shape is very important also for allowing its optimisation in future works. A design method, which grants the designer to automatically obtain smooth profiles in an intuitive and efficient way, is therefore developed and applied to an innovative nacelle shape, conceived for improving the aerodynamic performance of the reference model cowling.

After a specific overview on the additional studies related to this project, guidelines for future works are provided in conclusion. The numerical results presented in this thesis should be validated by an experimental examination, which is not part of this doctoral study.

The main contribution of the present research to the scientific knowledge consists in the individuation of procedures for implementing and assessing new design techniques adoptable for pusher open-rotor nacelle shaping, such as the method based on the innovative interpolation technique defined within this dissertation: the methodology is developed to generate smooth profiles automatically, which are adaptable by changing intuitive parameters. With fast and reliable simulations for investigating the airflow over the nacelle without the need of 3D-blade modelling, this work demonstrates how to effectively predict the mutual aerodynamic interaction between the nacelle and the rotors. A reference model is analysed so that future engines can be compared with it, thus evaluating their potential enhancements: the basic characteristics and the benefits of a new diffusive nacelle, invented during the research activities, show how this concept represents an improvement of the existing pusher propfan technology.

Nomenclature

All the nomenclature used within this thesis will be presented in the following sections. The nomenclature is divided into three sections: Symbols, Acronyms and abbreviations, Glossary. The first section contains a list of all symbols used in the equations; the second section reports all the acronyms and abbreviations, while in the last section all the glossary terms are included, with proper descriptions and definitions.

Symbols

Notation	Description
A_{an}	Rotor annular area $[m^2]$.
A_c	Compressor area $[m^2]$.
A_{ex}	Nozzle exit area $[m^2]$.
A_{pt}	Power turbine outlet area $[m^2]$.
BPR	Bypass ratio.
C_b	Blade chord $[m]$.
Cp	Pressure coefficient.
Cp_{cr}	Critical pressure coefficient.

Notation	**Description**
D_c	Compressor face diameter $[m]$.
D_{fb}	Nacelle forebody drag $[N]$.
D_{fc}	Nacelle fore-cowl drag $[N]$.
D_{hl}	Highlight diameter $[m]$.
D_{hub}	Rotor hub diameter $[m]$.
D_{lip}	Lip diameter $[m]$.
D_{max}	Maximum nacelle diameter $[m]$.
D_{pre}	Pre-entry drag $[N]$.
D_{th}	Throat diameter $[m]$.
D_{tip}	Rotor diameter $[m]$.
ΔP	The rotor pressure jump $[N/m^2]$.
ENT	Engine net thrust $[N]$.
EP	Equivalent power $[W]$.
ε	Inlet recovery factor.
ϵ	Absolute error $[1/m]$.
η_{prop}	Propulsive efficiency.
η_{rot}	Rotor efficiency.
F_{ax}	Axial load $[N/m]$.
FN	Uninstalled thrust $[N]$.
FPW	Fan power $[W]$.
γ	Specific heat ratio.
J	Rotor advance ratio.

Notation	**Description**
κ	Profile curvature $[1/m]$.
L_{c-hub}	Compressor to hub horizontal length $[m]$.
L_{hl}	Highlight distance from compressor $[m]$.
L_{hl-cr}	Highlight to crest horizontal distance $[m]$.
L_{lip}	Lip horizontal distance $[m]$.
L_{th}	Throat horizontal distance $[m]$.
M_0	Flight Mach number.
$\dot{m}_0$	Total airflow processed by the engine $[kg/s]$.
$\dot{m}_c$	The 'cold' mass flow $[kg/s]$.
M_{cr}	Critical Mach number.
$\dot{m}_f$	Fuel flow $[kg/s]$.
$\dot{m}_h$	The 'hot' mass flow $[kg/s]$.
n	Rotational speed $[1/s]$.
$N.A.$	Data not available.
$\mathbb{N}$	Set of natural numbers.
OPR	Overall pressure ratio.
P	Static pressure $[N/m^2]$.
PQA	Power coefficient.
P_{t-0}	Total pressure at infinity $[N/m^2]$.
P_{t-rot}	Total pressure behind rotor zone $[N/m^2]$.
r	Local radius $[m]$.

Notation	**Description**
R_{cb}	Reaction force at the centrebody $[N]$.
R_{hub}	Hub radius $[m]$.
R_{in}	Reaction force at the intake $[N]$.
R_{tip}	Rotor radius $[m]$.
ρ	Density $[kg/m^3]$.
$\mathbb{R}$	Set of real numbers.
SFC	Specific fuel consumption $[kg/(N \cdot s)]$.
TET	Turbine entry temperature $[K]$.
TQA	Thrust coefficient.
V	Flow velocity $[m/s]$.
V_0	Flight speed.
V_{ax}	Axial velocity $[m/s]$.
V_{ex}	Nozzle exit velocity $[m/s]$.
V_j	Jet velocity $[m/s]$.
V_{rad}	Radial velocity $[m/s]$.
WCI	Corrected inlet flow $[kg/s]$.
$\dot{W}$	Power of the jet $[W]$.
X_p	Horizontal position of velocity probe $[m]$.
z	Altitude $[m]$.

Acronyms and abbreviations

ACEE

Aircraft Energy Efficiency.

AIAA

American Institute of Aeronautics and Astronautics.

AOA

Angle Of Attack.

APET

Advanced Prop-fan Engine Technology.

APU

Auxiliary Power Unit.

ATP

Advanced Turboprop Project.

CAD

Computer Aided Design.

CAGD

Computer Aided Geometric Design.

CFD

Computational Fluid Dynamics.

DEMONS

Design and Engineering Methods for Open-rotor Nacelle Shaping.

ESDU

Engineering Sciences Data Unit.

FAR

Federal Aviation Regulation.

GUI

Graphical User Interface.

HPC

High Performance Computing.

IGES

Initial Graphics Exchange Specification.

LAP

Large-scale Advanced Propfan.

LDV

Laser Doppler Velocimetry.

MHB

Maximum Half Breadth.

NASA

National Aeronautics and Space Administration.

NURBS

Non-Uniform Rational B-Spline.

OPEC

Organization of the Petroleum Exporting Countries.

PIV

Particle Image Velocimetry.

PTA

Propfan Test Assessment.

REMO

REference MOdel.

SLS

Sea Level Static.

SPL

Sound Pressure Level.

SRV

Swirl Recovery Vanes.

TRL

Technology Readiness Level.

UDF

Un-Ducted Fan.

VBA

Visual Basic for Application.

Glossary

Porcupine curvature analysis

A "Porcupine Analysis" is a method for graphically analysing the smoothness of a curve, and to verify continuity discrepancies between curves or surfaces. It consists of a graph formed by a set of spikes, each one starting from a point on curve and representing an inverse magnification of the radius of curvature at that point: the longer the spike, the greater the curvature (i.e. the smaller the radius of curvature).

Spline

In computer graphics, a "spline" is a smooth curve that interpolates a series of points in space. Before its use in Computer Aided Geometric Design (CAGD), the term was associated to a flat, pliable strip of wood or metal: this instrument was bent into a desired shape for drawing curves.

1. INTRODUCTION

The open rotor technology always played an important role in the history of aviation. The first powered aircraft, the *Wright Flyer I* (1903), was propelled by a couple of spinning wooden blades, forming two pusher propellers. Since then, propellers dominated almost half a century of human flight. With the introduction of the jet engine in the 1950s, which allowed the civil aircraft to travel faster over large distances, the propeller-driven aircraft lost part of its predominance and its limits became evident. During a subsonic cruise at high flight speeds, in the range $0.6 < \text{Mach} < 0.9$, critical losses associated with supersonic phenomena appear around the propeller blades, especially at the tips where the velocity of the rotor increases. On the contrary, even at high cruise speeds, the airflow entering a jet engine is decelerated through an intake before it reaches the fan, avoiding it to become supersonic over a large portion of the fan blades. In the last three decades, both the propeller technology and the jet engine have been constantly improved. The former was revolutionised by the turboprop, whose civil versions recently[1] fly up to Mach ~ 0.7, the latter by the turbofan, which obtained a great success: with the introduction of the bypass duct, this kind of engine offered improvements not only in terms of better SFC, but also of lower noise production.

Despite of these enhancements, the actual technology is now considered old, due to the changes expected to occur in the next two decades: short and medium haul

[1] The Piaggio P-180 Avanti II is the world's fastest turboprop business aircraft (source: `http://www.piaggioaero.com`, January 2009). The fastest turboprop aircraft ever built and still in use is the military bomber Tupolev Tu-95 Bear, with its maximum speed of Mach 0.82 at an altitude of 7620 meters (source: `http://www.aviation.ru/Tu/95/Tu-95.html`, January 2009).

aircraft operating in the civil aviation market are experiencing a long in-service life and are likely to be replaced. This substitution can reasonably happen provided a new competitive aero-engine is available. In fact, only if the new propulsion systems are substantially better than the existing options would there be a business case for the successor aircraft.

To solve this problem, various engine manufacturers worldwide are trying to propose what they judge to be the best solution for the future short-medium haul 'cleaner' propulsion [128]. From an engineering perspective, this means to gain for the next generation of aero-engine a substantial reduction of fuel consumption and combustion emissions. Among the models proposed for the future, there are the geared turbofan and the open-rotor. The former, meant to be operative in a short term, is basically a refined turbofan; the latter, envisaged to be operative in a medium-long term (two decades), is a reassessment of the propfan. The concept of propfan is almost thirty years old and has been put aside at the beginning of the 1990s, when the fuel price was too low to justify its massive usage. An example of this propulsive system and its possible installations is presented in Fig. 1.1.

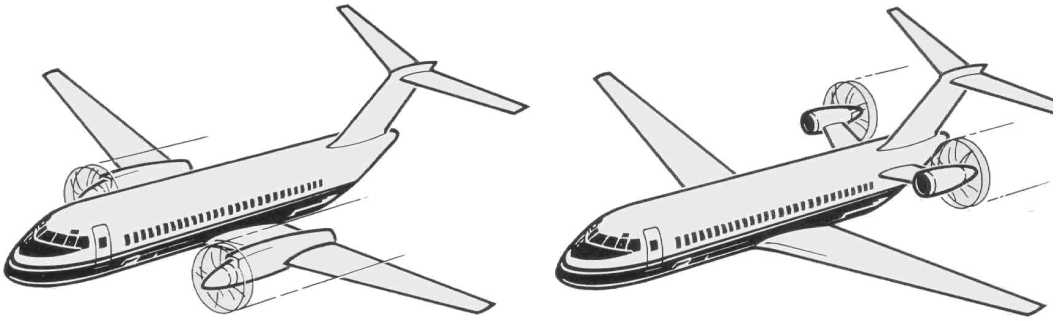

Fig. 1.1. Tractor and pusher propfan concepts (source: ref. [71]).

The present work aims to further develop the propfan technology, contributing to its transformation into the open-rotor of the future. Prior to proceed any further, it is worthy to notice that the expression 'open rotor' refers to a family of mechanical devices employed to propel different means of transport. It is possible to define the open rotor as an unshrouded, rotating, bladed device used to gener-

ate thrust for the propulsion of a vehicle, independently of its application (such as an aircraft, a ship or a submarine). Hence, even if the expression 'open rotor' might be intended as a general definition, in this work the made-up word *open-rotor* is used to indicate the next generation of propfan, being it pusher or tractor, single-rotating or contra-rotating[2]. The next sessions delineate the path followed to define the aim and objectives of this research. Consequently, the structure of the work will be presented at the end of this chapter.

1.1. Context of the project

The current project is targeting, as already mentioned, the next generation of propfan: the so called open-rotor. However, there is no chance of improving an existing technology without knowing it first. A preliminary step towards a better understanding of the propfan is to analyse the context in which it was conceived. After a revision of the energetic issues affecting the aviation industry of the past and present time, a historical review of the propfan technology is reported.

1.1.1. The energy problem

The cost of energy has always been a key driver for the economy of every nation. During the years, the price for energy tends to rise, lifting the expenses of life in general and the cost of aviation as well. When the cost of energy tends to increase too rapidly due to particular economical and political reasons, airlines experience many economical difficulties, thus demanding from the manufacturers more efficient aircraft and engines, in order to keep the operational and maintenance costs as low as possible. For instance, during the 1970s the fuel price suddenly increased

[2]When the propellers or open rotors rotate in opposite directions while are mounted coaxially the denomination to use should be 'contra-rotation', meaning a rotor in front of (or on top of) the other on the same axis; 'counter-rotation' should be used instead when there are two individual shafts driving two propellers or open rotors on different axis and in opposite rotational directions. Although the author is aware of this difference, in the past the two expressions have been used incorrectly so often in books, manuals, reports and on websites, that nowadays they are commonly accepted as synonyms.

due to the oil embargo imposed by the Organization of the Petroleum Exporting Countries (OPEC). Since the United States was dependant on foreign oil supplies, the American Government started several research projects on reduction in fuel consumption. These efforts faded away at the end of the 1980s, because the fuel prices did not grow as much as expected. After 25 years, another oil crisis took place in the international scenario, and it has currently affected the aviation market: Fig. 1.2 clearly shows how the rise of fuel cost in the last few years is even more rapid than the previous one. Since the mid 1980s, the price of a barrel[3] of crude oil

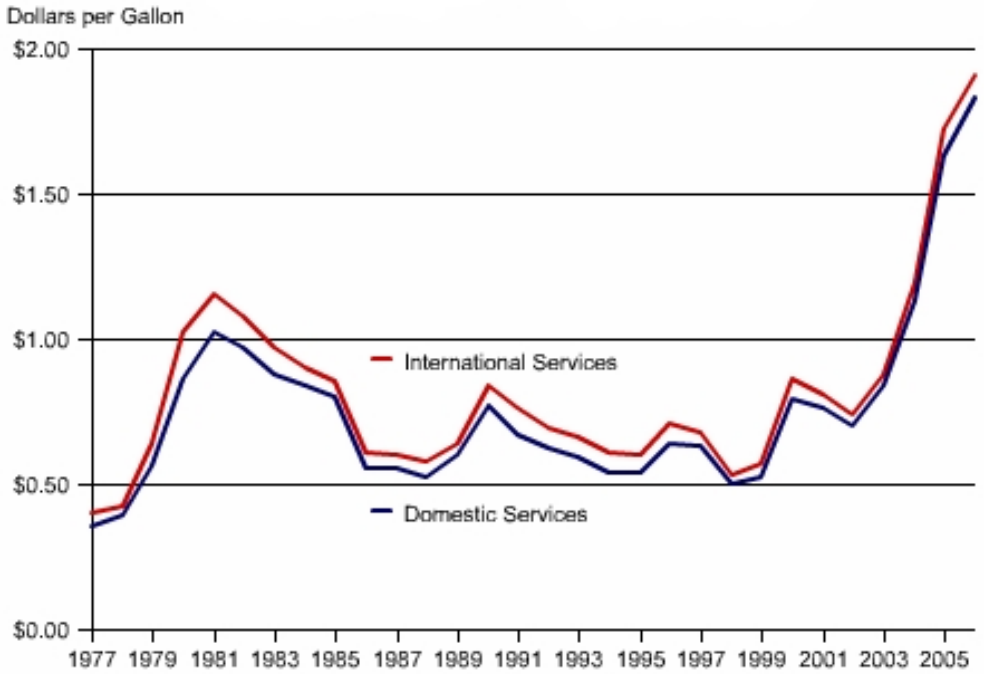

Fig. 1.2. Airline fuel cost and consumption (source: data available at Bureau of Transportation Statistics on 21^{st} of May, 2008).

had been generally under \$25/barrel, maintaining this level until September 2003. Although experiencing various peaks and falls, the mean tendency of oil price has been to grow almost constantly until recent times. For instance, throughout the beginning of 2008[4], oil hit several new record highs, and a price per barrel maximum of \$133.13 was reached on May 21st, 2008. An increasing demand from

[3] An oil barrel is 42 US gallons (158.9873 litres).

[4] The beginning of this year was the most recent period of time in which the author conducted this energy cost analysis.

Fig. 1.3. Jet fuel and crude oil price (source: `http://www.iata.org`).

expanding economies, mainly in China and India, contemporaneously in contrast with the oil supply curtailed by the OPEC, have been the most important factors contributing to the modern rise in oil prices. Furthermore, the price increases of this period can be also attributed to a confluence of factors, including reports from the U.S. Department of Energy and others showing a decline in petroleum reserves[5], social worries over peak oil[6], Middle East tension, and economic speculations. Regulations and environmental efforts have also increased the shortage and price of oil, affecting the jet fuel cost as reported in figures[7] 1.3 and 1.4.

Given the difficulties in forecasting the oil price trend due to the numerous uncertainties, airlines do spend their efforts seeking a better fuel economy. Airways already adopt special operational and planning techniques[8] on the international scenario. In terms of operational conditions, the strategy is usually composed by several actions, such as:

- onboard weight reduction

[5]"Record oil price sets the scene for $200 next year", AME, July 6, 2006 - `http://www.ameinfo.com/90848.html`, May 2008.

[6]EnergyBulletin.net, Peak Oil News Clearinghouse.

[7]Source: `http://www.iata.org/whatwedo/economics/fuel_monitor/price_development.htm`, May 2008.

[8]As suggested by the Q&A on the Fuel-Related Challenges Facing U.S. Airlines by Vice President and Chief Economist of Air Transport Association John Heimlich, June 2006.

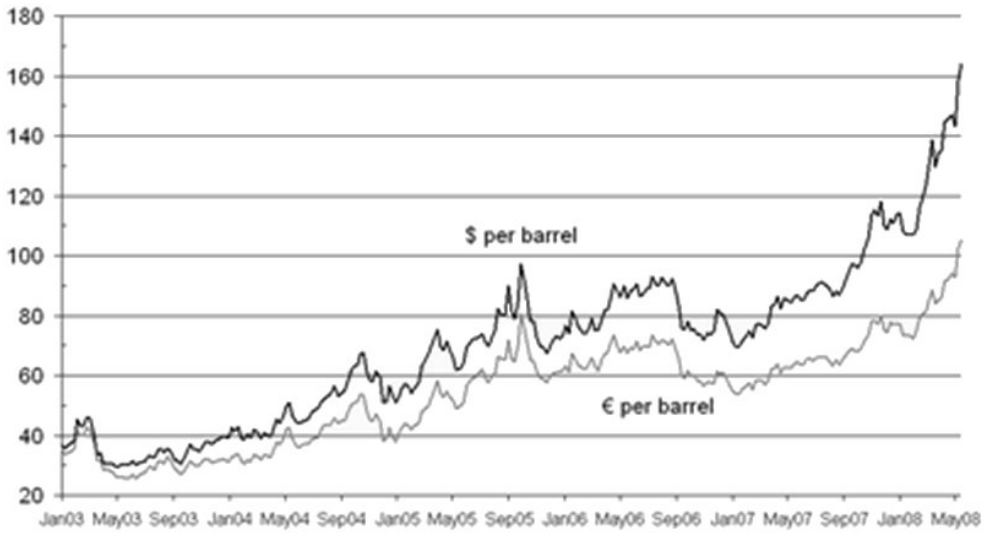

Fig. 1.4. Jet fuel price - currency comparison (source: `http://www.iata.org`).

- more accurate measurement and redistribution of the belly cargo
- selective engine shutdown during ground delays
- employment of single-engine taxi during normal operations
- usage of extra fuel on certain flights to avoid refuelling at more expensive locations
- cruising longer at higher altitudes and employing shorter, steeper approaches.

In terms of planning for fuel usage, the main strategy of airlines includes:

- reorganisation of hubs and schedules to reduce congestion
- usage of airport power rather than onboard Auxiliary Power Unit (APU) when at the gates
- optimisation of flight planning for minimum fuel-burn routes and altitudes
- installation of winglets on in-service aircraft to reduce their in-flight drag
- fleet modernisation with more fuel-efficient aeroplanes.

This last point intrinsically relies not only upon the innovative aircraft designs, but also upon the performance of future engines. In terms of engineering parameters, the fuel efficiency of an engine is assessed with the specific fuel consumption SFC: it quantifies the amount of fuel needed to provide a given power for a given period; it is defined as

$$SFC = \frac{\dot{m}_f}{ENT} \tag{1.1}$$

where $\dot{m}_f$ is the fuel flow and ENT is the net thrust of the engine. A sample

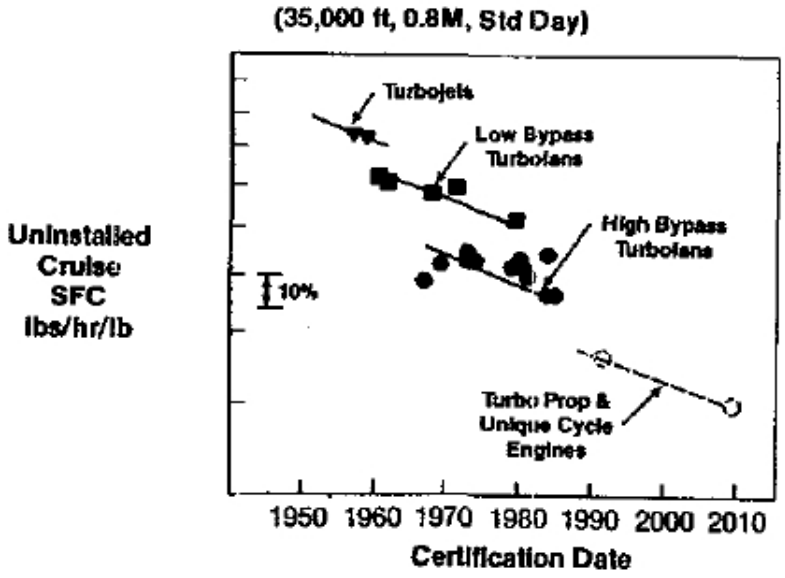

Fig. 1.5. SFC trend in subsonic engines (source: ref. [144]).

historical trend of SFC improvements is plotted in Fig. 1.5: as the engine technology progressed, reductions of SFC were achieved. These technological advances were possible thanks to components with enhanced efficiencies, able to operate at higher pressure ratios and temperatures, as demanded by the conditions of new thermodynamic cycles.

It is evident from Fig. 1.5 how the advent of turbofans led to further SFC reductions: the main feature of these engines was the introduction of a bypass duct for separating the airflow entering the core of the engine from the airflow used to generate thrust directly from a fan installed before the compressor. For

this reason, from an engineering point of view, turbofans are typically characterised by the bypass ratio BPR, which is defined as

$$BPR = \dot{m}_c/\dot{m}_h \tag{1.2}$$

where $\dot{m}_c$ is the 'cold' mass flow of air bypassed and $\dot{m}_h$ the 'hot' mass flow of air passing through the engine core. With the introduction of higher BPR values, turbofans finally disposed of the same thrust of turbojets by augmenting the ingested airflow $\dot{m}_0 = \dot{m}_c + \dot{m}_h$ and reducing the jet efflux velocity V_j, resulting in a lower expenditure of kinetic energy and hence of fuel. It is out of the purpose of this work to revisit all the performance parameters of an aero-engine; however, without losing in generality, the previous consideration can be easily understood from the following relation

$$ENT = \dot{m}_0 \cdot (V_j - V_0) \tag{1.3}$$

which defines the net thrust in the approximated case of inlet and unchoked propelling nozzle having equal mass flows, and also from

$$\eta_{prop} = \frac{V_0}{\frac{1}{2} \cdot (V_0 + V_j)} \tag{1.4}$$

which defines the propulsive efficiency[9] of the engine in the same approximated case. The first turbofan engines[10] had low bypass ratios ($0.3 < BPR < 2$) but, compared to the turbojets, had improved propulsive efficiency and lower noise levels. The technology evolved into more efficient and quieter engines called 'high bypass turbofans' ($BPR \sim 4$, up to 8). Nevertheless, none of these engines reached the low fuel specific fuel consumption of a turboprop. However, the turboprop had a

[9] According to ref. [157], the propulsive efficiency is defined as "[...] the useful propulsive power produced by the engine divided by the rate of kinetic energy addition to the air".

[10] For instance the Rolls-Royce Conway or the JT3D of Prett&Whitney.

practical inconvenient for medium-haul flights employment: its maximum operative speeds (Mach ~ 0.65), were sensibly lower than those of turbofans (Mach ~ 0.8). In the early 1970s, the National Aeronautics and Space Administration (NASA) in the United States looked at a new engine able to save fuel and guarantee cruise speed around Mach ~ 0.75. This propulsive concept was conceived as a consequent evolution of the turboprop and was named[11] *propfan*.

1.1.2. Historical background: from turboprops to propfans

The historical reason of the propfan origination has been the oil embargo of 1973, imposed by the OPEC to the United States and its allies in Western Europe: as already mentioned in 1.1.1, the consequent increase in oil price affected particularly the airline industry, which therefore needed a new kind of engine with improved SFC.

The Aircraft Energy Efficiency (ACEE) program, a NASA-industry effort, examined the problem in general[12]: the basic goal was to learn how to use fuel energy more efficiently for propulsion and lift generation. The program worked not only for improving engines and finding more efficient ways of propelling aeroplanes through the atmosphere, but also for reducing aircraft drag and decreasing the weight of airframe materials. The cross-disciplinary plan combined six subsonic technologies, whose equivalent programs were respectively:

- Engine Component Improvement
- Energy Efficient Engine
- Advanced Turboprop Program
- Energy Efficient Transport
- Composite Primary Aircraft Structures

[11] The idea to evolve turboprops in order to let them have the same operative employment of the turbofans led to the name 'prop-fans', by eliminating the suffix 'turbo' from both the words.
[12] The following information is derived from ref. [115].

- Laminar Flow Control

The first three programs focused on aero-engine development. In particular, the 'Engine Component Improvement' project involved the enhancement of existing engine components by using improved aerodynamics and materials, applying clearance control techniques, and increasing the bypass ratio. Elements included fan blade improvements, turbine aerodynamics, blade cooling seals, and active clearance control. While this program projected a fuel saving of 5 percent, the 'Energy Efficient Engine' project, completed in 1983, demonstrated or identified design and technology advances[13] that could reduce turbofan engine fuel consumption by an estimated 15 to 20 percent. Technology derived from the program was applied to the CF6-80C, PW-2037, and PW-4000 engines. Despite these achievements, since 1978 NASA determined that the greatest possible gains in fuel economy could be obtained in the form of an advanced turboprop engine. Against the criticism from many in the aeronautical community, who believed that a propeller based propulsion system would be a technological step backward, NASA set up the Advanced Turboprop Project (ATP) at the Lewis Research Center[14]. This program aimed at greater efficiency for future turboprop-powered aircraft cruising at or near jet transport speeds ($0.65 < \text{Mach} < 0.85$). The advanced turboprop technology was an important option for medium-range transports, promising fuel savings of 25 percent or more, as compared to equally advanced turbofan engines. The goal of engineers at NASA is resumed by figure[15] 1.6. The theoretical and practical endeavours for the successful development of this technology consisted in the assessment of its technical issues, considering also the government aims related to safety, efficiency at high speeds, and environmental protection. The path towards innovation

[13] Compressor, fan, and turbine-gas-path improvements; improved blading and clearance control; structural advances.

[14] The complete presentation of the ATP program is reported in ref. [71].

[15] The term 'ELECTRA', which appears in the figure, refers to the American turboprop airliner Lockheed L-188 Electra, the first turboprop airliner built in the United States. Offering performance slightly inferior to that of a full turbojet aircraft but at lower operating cost, it first flew in 1957.

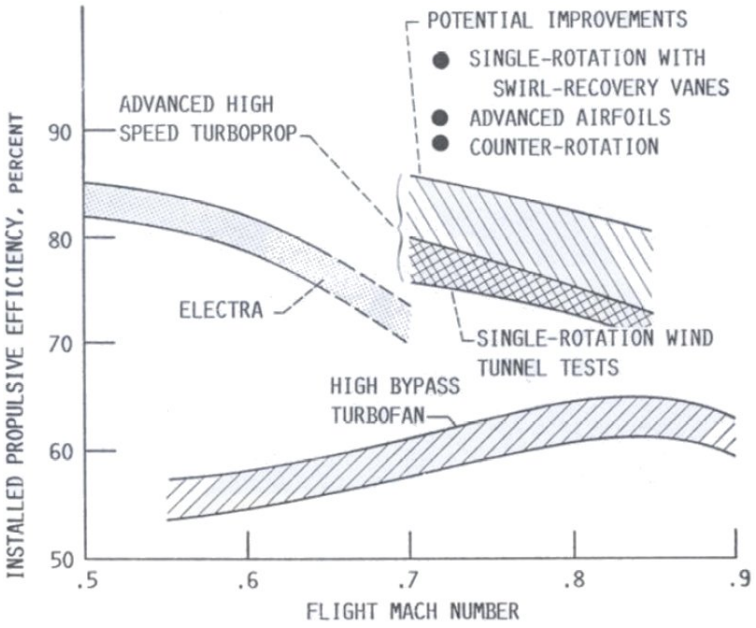

Fig. 1.6. Installed propulsive efficiency trends for advanced turboprops compared with equivalent technology turbofans (source: ref. [78]).

presented ulterior challenges: funding was very limited due to political opposition, while additional studies had to be performed to support the value of the advanced turboprop concept, which was later simply renamed propfan. Areas of technical concern included propeller efficiency at cruise speed, propeller and aircraft interior noise, installation aerodynamics and maintenance costs. Nevertheless the ATP project resulted the most profitable of the ACEE efforts: thin, swept-tip, multi-bladed, high-speed single-rotation, as well as contra-rotation, geared and ungeared versions of turboprop propulsion systems were successfully tested. The Advanced Turboprop Project had four technical stages:

1. *Concept development*, from 1976 to 1978
2. *Enabling technology*, from 1978 to 1980
3. *Large-scale integration*, from 1981 to 1987
4. *Flight research*, in 1987.

The 'enabling technology' phase focused on building subscale propeller models to test and establish the feasibility of the propfan concept, providing a comprehensive

database to assist industry in choosing a configuration, including whether single or contra-rotation best suited the application. It was already evident how the wing and nacelle had to be properly integrated in order to avoid drag penalties, aircraft stability and control problems, thus assuring an effective installation. The 'large-scale integration' phase concentrated on obtaining definitive data on noise at cruise conditions, fuselage noise attenuation, efficient wing mounting, and large-scale blade design. In 1985 the first Large-scale Advanced Propfan (LAP) assembly was tested (SR-7L): performance data were recorded and the high-speed acoustic measurements were completed. The data agreed favourably with predictions and with earlier data. After static testing was completed under the LAP project, NASA used the SR-7L propfan for further evaluation in the Propfan Test Assessment (PTA) project[16].

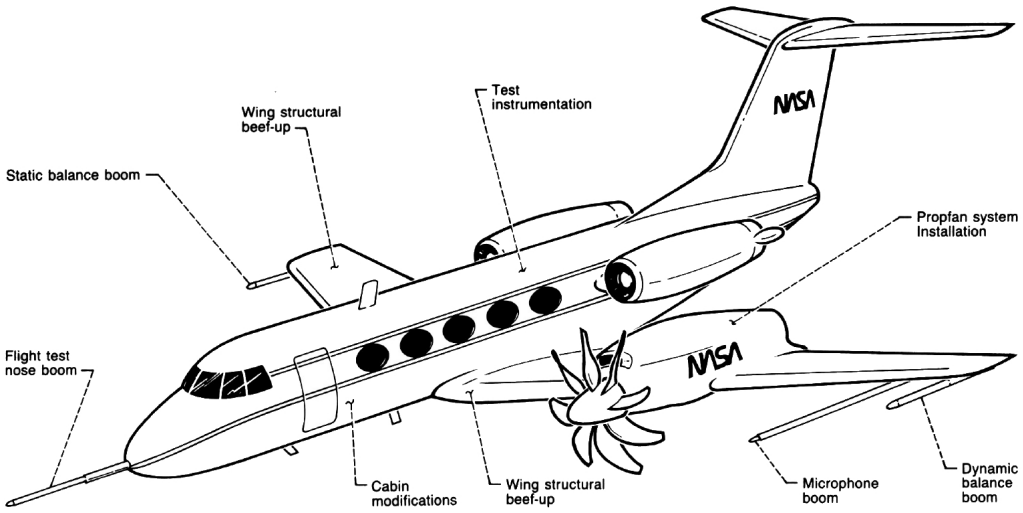

Fig. 1.7. The PTA aircraft (source: ref. [71]).

The objectives of this project were:

- verification of blading structural integrity
- evaluation of the acoustic characteristics of a large-scale propfan at cruise conditions

[16]The PTA aircraft was a modified Gulfstream II, as shown in Fig. 1.7. See ref. [20] and ref. [120] for further ground and flight testing documentation.

- compatibility test of the engine, fan, and nacelle
- measurement of propulsion system performance
- acquisition of data on propulsion system temperatures and stresses.

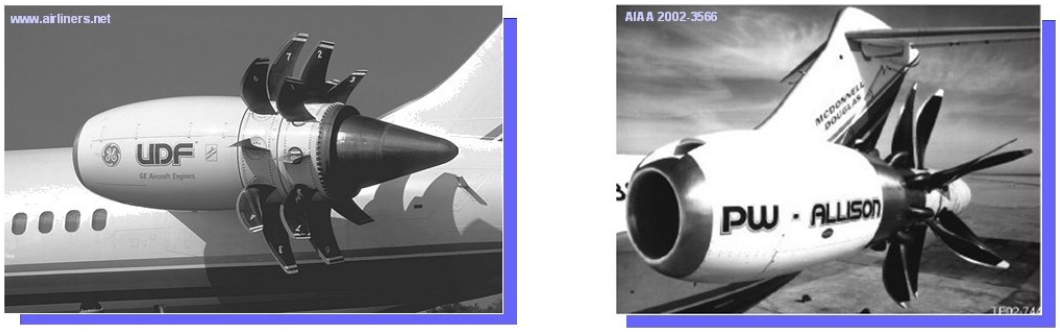

Fig. 1.8. The GE-36 and 578-DX engines mounted on a MD-80 for flight test (source: `http://www.airliners.net` and ref.[81]).

Since the propfan blade stresses and propulsion system temperatures, pressures, and vibrations were within specified limits, and specific fuel consumption was better than expected, these results successfully cleared the propulsion system for flight tests. While NASA with the PTA program was pursuing propfan research in the direction of a single-rotation tractor system, two of its industrial partners, General Electric and Pratt & Whitney, kept on developing a saleable pusher propfan: the GE-36 Un-Ducted Fan (UDF) and the 578-DX respectively (Fig. 1.8). Even if both engines had a pusher architecture, they were based on a completely different configuration. Prett & Whitney [30] (also abbreviated with P&W), in cooperation with Allison [28] and Hamilton Standard, opted for a geared blading system [27] (as shown in Fig. 1.9), General Electric (also abbreviated with GE) for a gearless blading system [144]. Since 1983, GE started a cooperation with Lewis Research Center to develop an engine based on a contra-rotation blade concept: the UDF, shown in Fig. 1.10. This engine was based on a gearless, dual-rotation pusher propulsion system, which had two contra-rotating external fans, each with eight sweptback blades driven directly by a contra-rotating internal turbine. This

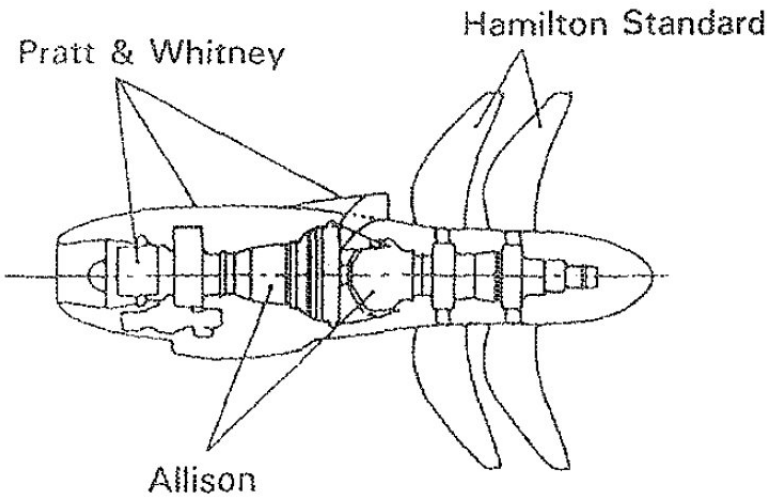

Fig. 1.9. The P&W-Allison 578-DX engine: lateral view (source: ref. [46]).

gearless design allowed for weight reduction by eliminating the gearbox and its oil cooling system.

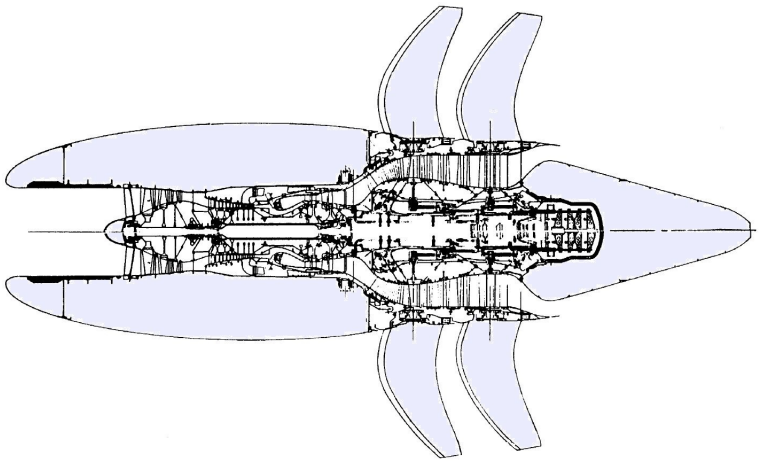

Fig. 1.10. The GE-36 UDF engine: lateral view (source: ref. [11]).

Full scale engines of all these programs were developed and installed on several aeroplanes to collect operative data and to demonstrate the performance of the advanced propfan technology. In 1987, three series of flight tests verified the readiness of ATP technology for commercial engine systems development:

- NASA/GE/Boeing tests of the UDF engine on a B-727 aircraft
- NASA/Lockheed PTA of a single-rotation advanced turboprop on a Gulfstream II aircraft

- GE/McDonnell Douglas flight tests of the UDF on an MD-80 aircraft
- P&W-Allison/McDonnell Douglas flight tests of the 578-DX on an MD-80 aircraft.

The results of these tests showed that propfan engines could accomplish 30-40% lower specific fuel consumption than the current technology turbofan engines. Even though NASA successfully demonstrated the feasibility of the technology, the American agency itself reduced its efforts in 1988. In the late 1980s, when fuel prices were at their lowest level of that decade, the economic benefit of the propfan was not significant anymore. As a consequence, the PTA project ended in June 1989, while airlines decided not to adopt the technology in the 1990s. Despite the significant Russian and European interest in propfan technology, NASA continued to conduct only limited research until 1995. Without a ready market, GE, P&W and other international companies cancelled their efforts in 1990: airlines would not select the pusher propfan, which was not easily adaptable to most existing commercial airframes. For instance, in the case of pusher propfan, which required rear fuselage mounts, aircraft manufacturers would have to redesign an entire new airframe to accommodate such an engine, but the promised fuel savings were not enough to offset the higher initial costs of an all new aircraft with advanced avionics, structures, and aerodynamics along with high-speed turboprops.

Within the European context, other engine manufacturers showed an interest in the realisation of the propfan technology. For instance, Rolls-Royce promoted the study of a contra-rotating geared pusher propfan: the RB-509. Rated[17] at $13,000\,hp$ $(9,685\,kW)$, this engine was considered [80] in the preliminary design of the A-85 advanced propfan airliner, but was never produced nor flight tested. An image of the Cranfield 150 passenger short-range A-85 aircraft rear mounting two RB-509 is given in Fig. 1.11. Rolls-Royce also contributed to the assessment of turboprop enhancements [75] and patented [36] a "propfan aircraft propulsion

[17]Source: `http://www.skomer.u-net.com/projects/turbines.htm`, May 2008.

Fig. 1.11. Cranfield A-85 aircraft mounting two RB-509 (source: ref. [58]).

engine". In the Eastern Europe, the propfan concept was conceived [89] since the 1980s as an evolution of existing turboprop engines, and grew until the first years of 2000. The Ivchenko Progress company successfully developed the Progress D-27, a propfan engine for commercial and military transport aircraft. The D-27, illustrated in figure[18] 1.12, presents a tractor architecture, with a reduction gearbox linking the power turbine to the contra-rotating high-speed blades. Four D-27 powered the Antonov An-70, a medium-distance large aircraft which had to replace the obsolete An-12 military transporter. Work on the An-70 began in the early 1990s and the maiden flight of the first prototype took place on 16 December 1994 in Kiev, Ukraine. Although the plane was fully tested and internationally certified prior the 2006, its serial production did not begin especially because of high production costs and concerns about excessive cabin noise. Currently[19], there is no mass-produced aircraft using the Progress D-27.

It is evident how social and economical reasons caused the 'propfan bust' more than any technical issues. While an energy crisis spurred the concept along, influencing the American Congress to fund the ATP project, the main uncertainty came not from the attempt to discover if the technology did really work, but rather from

[18]Source: `http://www.aeronautics.ru/img/img006/d27_engine_001.jpg`, May 2008.
[19]Last checked in March, 2010.

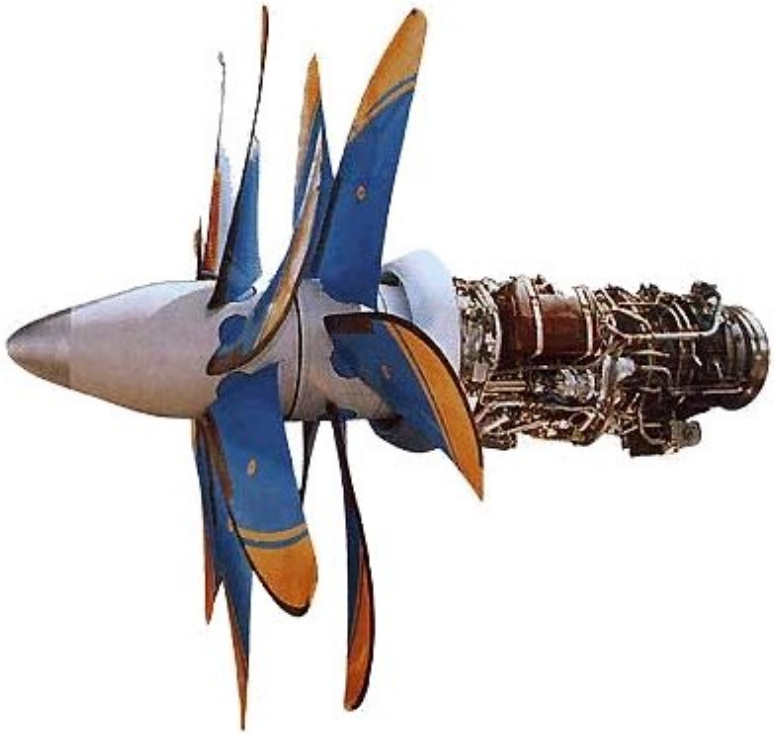

Fig. 1.12. Progress D-27 propfan (source: `http://www.aeronautics.ru`).

the failure in mitigating the concern among government, industry and the public to accept this technology.

1.1.3. The next generation: from propfans to open-rotors

As already said at the beginning of this introductory chapter, the 100-150 seat aircraft operating at Mach numbers up to 0.7 and 0.8 are acknowledged as the first application of the open-rotor, including the large feederliners or regional airliners with 100-120 seats. The market of the single-aisle aircraft seems very appealing (Fig. 1.13). For instance, accordingly to the "Global Market Forecast 2004-2023" of Airbus, by 2023 "[...] the world's major airlines will need 13,800 single-aisle passenger aircraft to accommodate traffic growth and renew their fleets" (Fig. 1.14); "[...] the demand for mainline single-aisle aircraft will be largely focused in North America and Europe, although deliveries to the Asia Pacific region with its growing low cost presence will total 2,650 deliveries, or 19% of total worldwide

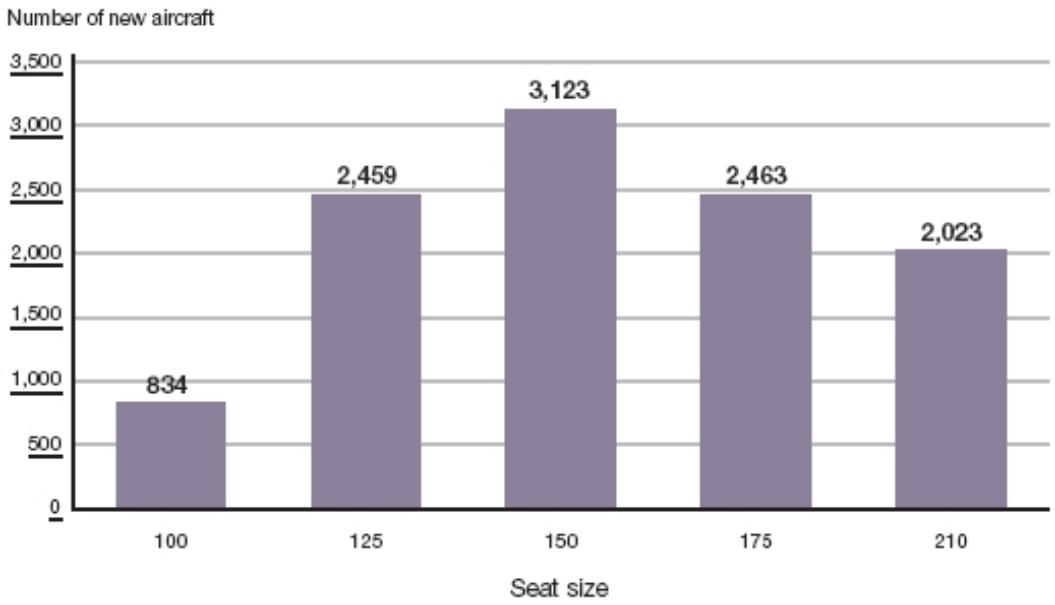

Fig. 1.13. Single-aisles demand (source: "Global Market Forecast 2004-2023" of Airbus).

single-aisle deliveries. Latin America, the Middle East and Africa will between them take a significant 12% of deliveries". Aircraft manufacturers are waiting[20] for the new engine technology, considering that the single-aisle aircraft will be mainly flown on short[21] flights, as shown in Fig. 1.15. In order to satisfy airframe manufacturers and airlines needs, the aerospace industry must invest further on advanced technologies, mainly devoted to fuel consumption and CO_2 pollution reduction. Recent progress in aero-acoustic modelling and design allow the 'old' propfan configurations to be reconsidered, motivating the application of innovative open-rotors on the short and medium haul aircraft.

1.2. Technical rationale for open-rotors

The technological characteristics of the propfan have been attractive for the aeronautic market of the 1980s, but for modern aviation they still represent the tech-

[20] As Airbus chief operating officer customers John Leahy said in "Flight International 20-26 June 2006, p. 13": it is not credible "[...] that a quantum leap in single-aisle aircraft efficiency will be possible until the arrival of new engine technology in middle of the next decade". Regarding the A320 replacement, Leahy declared that "[...] the business case for a new-generation single-aisle aircraft would not be viable unless it offered at least 10% improvement in fuel burn".

[21] Less than 600 nautical miles, corresponding to a Paris-Rome distance.

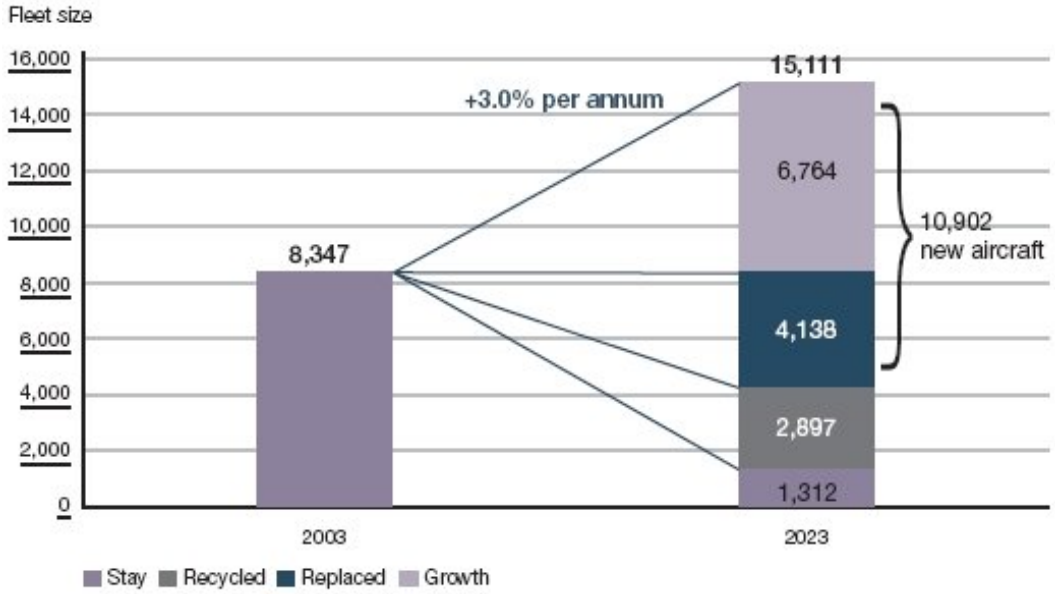

Fig. 1.14. Forecast future single-aisle fleet (source: "Global Market Forecast 2004-2023" of Airbus).

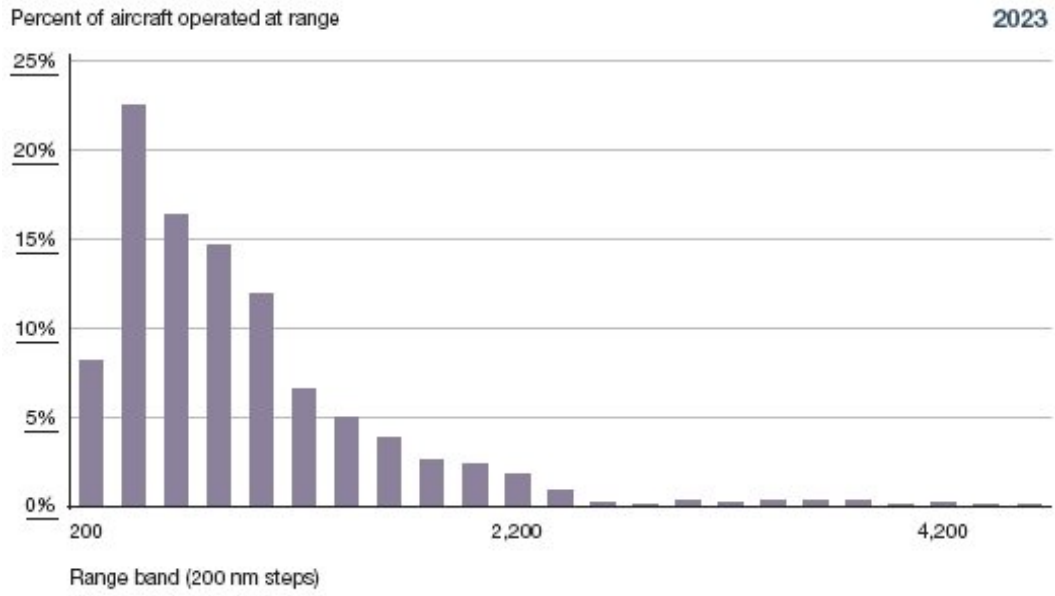

Fig. 1.15. Range distribution of future single-aisle aircraft (source: "Global Market Forecast 2004-2023" of Airbus).

nical baseline of the open-rotor. The primary goal of the new propulsion system is to provide high propulsive efficiency and low fuel consumption employing an open rotor able to operate at the cruise speeds of most commercial airliners, varying in the range $0.7 < \text{Mach} < 0.85$.

1.2.1. The need for *SFC* improvements

As suggested in section 1.1, especially through Fig. 1.5 and 1.6, an aircraft is theoretically more fuel efficient when driven by a conventional propeller or turboprop engine rather than a turbojet or turbofan. However, even if performing higher specific fuel consumption than a conventional propeller engine, the turbojet and the turbofan allow higher cruise speeds[22] ensuring shorter flight times. This is an important advantage, although the SFC parameter is of paramount importance not only from an engineering point of view, but also for all the consequences implied by its improvement: less operative costs and less pollutant emissions. The former is a crucial aspect for airlines, the latter grants the potential to satisfy airworthiness requirements, which are expected to become more stringent due to political reasons. The conventional propeller designs exhibit excellent efficiencies at speeds below Mach 0.65, whilst exceeding this limit usually results in supersonic relative speeds at the blade tips, even if the flight speed is still subsonic. As a consequence shock waves start to form on the propeller, causing a significant drag rise due to air compressibility effects and compromising the propeller efficiency, which becomes very low. When these phenomena occur, the blades undergo severe structural stresses, increasing the hazard of a total structural failure of the propeller. In order to achieve SFC improvements, the first challenge is the design of high-speed blades able to overtake these technical constraints with a new kind of propeller.

[22] Typically Mach ~ 0.8 for commercial airliners.

1.2.2. Propfan blading and rotor configurations

Although further studies in high-speed blading are currently taking place within the scientific community[23], the basic improvements in propeller design were already achieved in the 1980s, as reported in ref. [7] and [12]. The principles of high-speed blading are graphically resumed by figures 1.16 and 1.17.

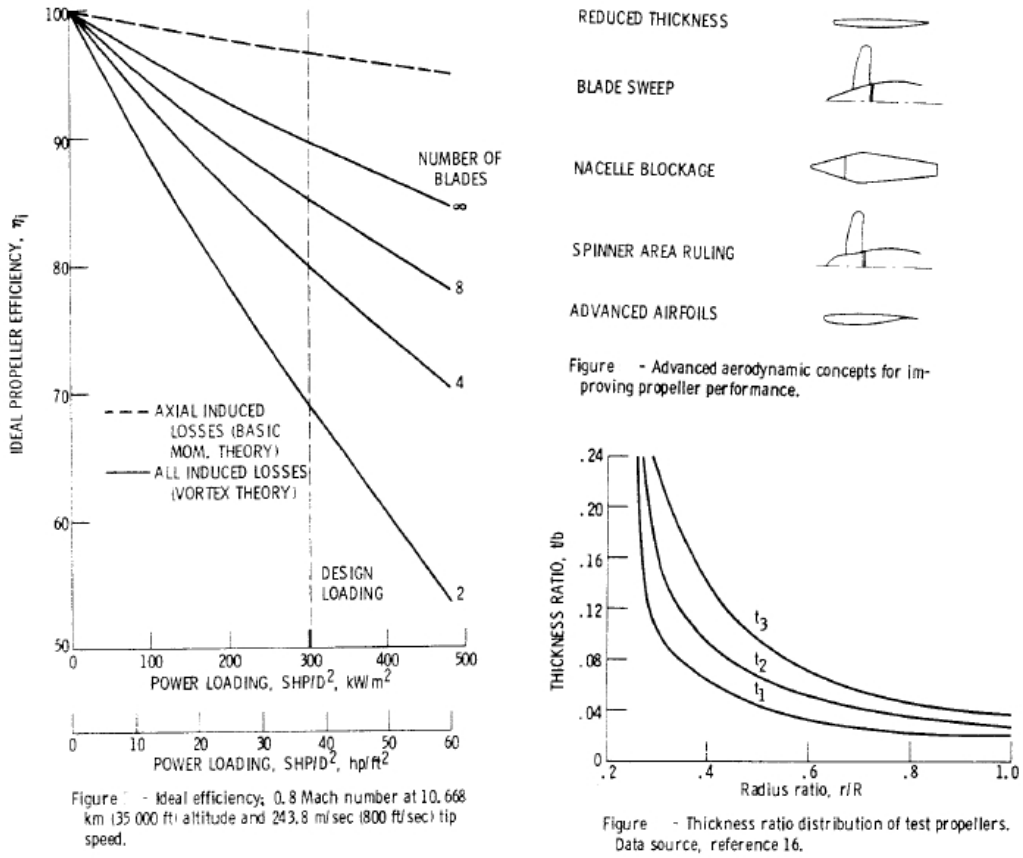

Fig. 1.16. The high-speed blade concept: chart group 1 (source: ref. [109]).

The study of these blades started with the cooperation of Daniel Mikkelson[24], from NASA Lewis, and Carl Rohrbach from the US propeller manufacturer Hamilton Standard: the aim was to discover how propellers could be redesigned to fly faster, higher and more efficiently. The collaboration of Mikkelson and Rohrbach led to a joint work between NASA and Hamilton Standard[25]. The two engineers concluded

[23] For example ref. [145], [146], and [166].

[24] Ref. [82] and [109] are examples of his important work.

[25] Initially the project involved only Hamilton Standard (for instance see ref. [35]). However the engine manufacturers (General Electric, Allison and Pratt & Whitney) and the airframe

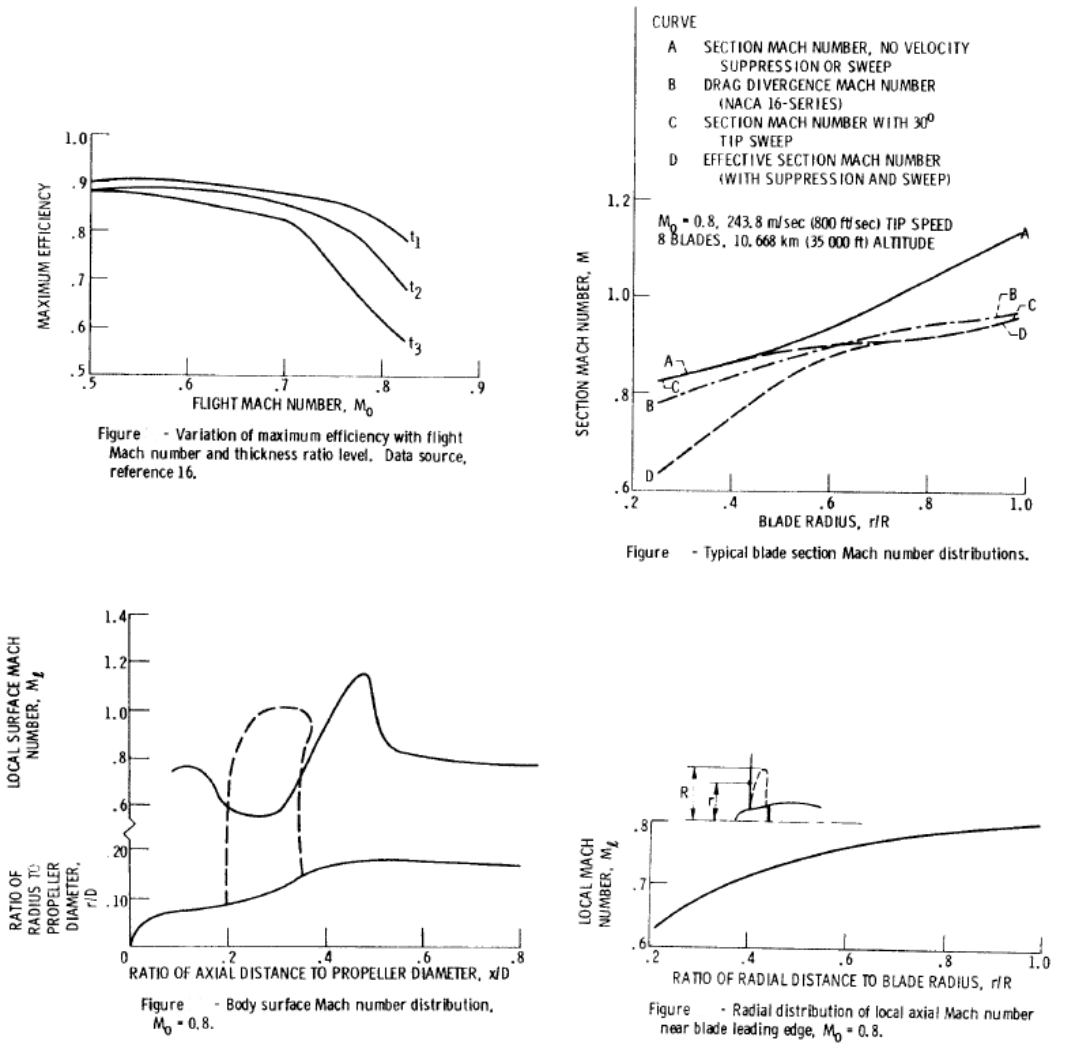

Figure - Variation of maximum efficiency with flight Mach number and thickness ratio level. Data source, reference 16.

Figure - Typical blade section Mach number distributions.

Figure - Body surface Mach number distribution, M_0 = 0.8.

Figure - Radial distribution of local axial Mach number near blade leading edge, M_0 = 0.8.

Fig. 1.17. The high-speed blade concept: chart group 2 (source: ref. [109]).

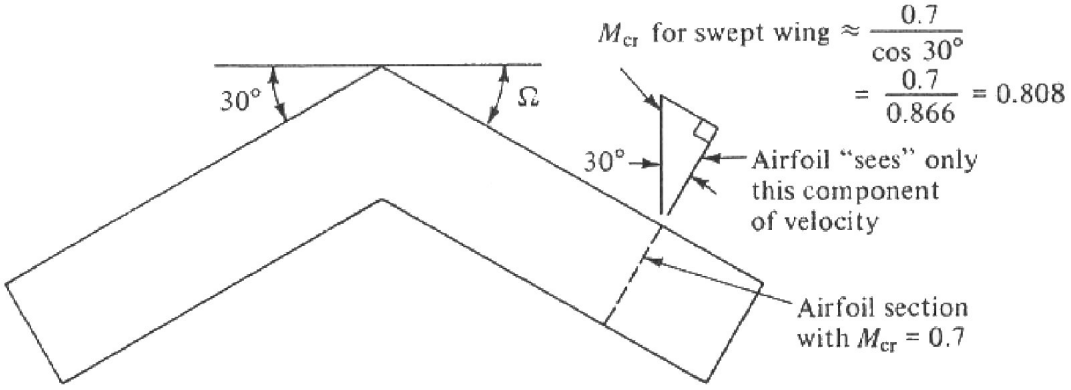

Fig. 1.18. The swept blade concept (source: ref. [25]).

that sweeping the blades, as illustrated in Fig. 1.18, could reduce noise and increase efficiency of any open rotor installation[26].

The concept can be easily resumed as follows. Fitted on an aircraft cruising at Mach 0.65 and over, and spinning at 1300 to 1700 rpm, a propeller experiences local flow velocities near or above Mach 1. To minimise these effects, the shape of a high-speed blade should have the same features of a thin and swept supersonic aircraft wing. By sweeping the blades backwards at an angle between 20 to 45 degrees, it is possible to obtain an effective decrease of the critical Mach number beyond which the drag of the aerofoil increases severely. Compared to a conventional propeller blade, a propfan blade is very thin[27] in order to produce less drag thanks to its reduced frontal area[28]. With these characteristics, the Mach number at which the aerofoil drag rise occurs is thus increased, therefore allowing a propfan powered aircraft to fly at higher cruise Mach numbers. The research efforts of the 1980s covered not only the blade design and its application on single-rotating propfan (Fig. 1.19), but also the performance[29] of contra-rotating propfan blading (Fig. 1.20). Few years later, in 1990, Rolls-Royce patented an open rotor blading [117], which combined blade sweep and aerofoil profile to reduce the noise levels of open rotor devices rotating at supersonic tip speeds.

As shown in the previous pictures, a propfan uses a great number of blades (8 or more) with a longer chord compared to a conventional propeller. The aerodynamic loading on each blade is increased, permitting a decrease of propeller diameter for a given amount of thrust. As a direct consequence, any engine adopting this kind of blading is easier to install on aircraft due to ground and fuselage clearance

industry (Lockheed, McDonnel-Douglas and Boeing) took part in the development of the propfan.

[26] An exhaustive literature survey on this topic can be fount in the accurate bibliography of ref. [71].

[27] This is not true for the root region of the blade, which has to be thick enough to guarantee an appropriate structural strength to the device. To avoid shock wave formation at the root, the spinner (or the hub) is usually area-ruled, as suggested in ref. [82].

[28] See also the work of ref. [123].

[29] As shown in ref. [78] and [79].

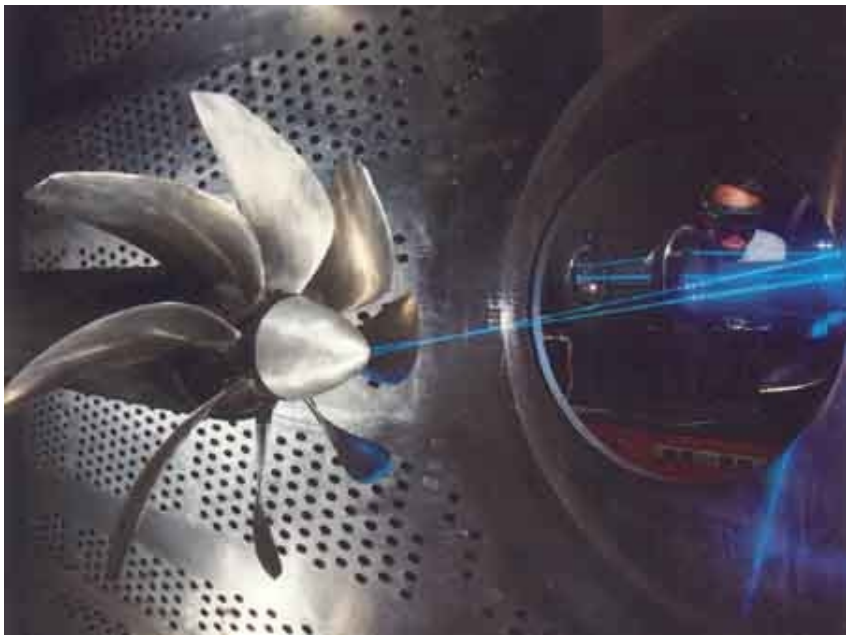

Fig. 1.19. Single-rotating propfan tested at NASA Lewis Wind Tunnel (source: ref. [71]).

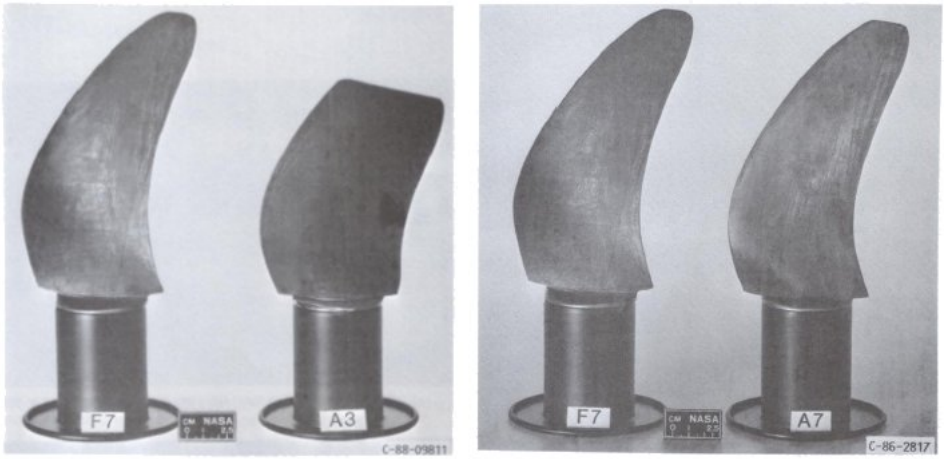

(a) F7/A3 PROPELLER CONFIGURATION BLADES.

(b) F7/A7 PROPELLER CONFIGURATION BLADES.

Fig. 1.20. Contra-rotating blades tested at NASA Lewis Wind Tunnel (source: ref. [78]).

reasons. However, these blades are highly loaded at high speed conditions and must withstand great structural demands, along with foreign object impact damage. Therefore, high-speed blading is made of a special manufacture. For instance, the GE-36 blades consisted of a central titanium spar surrounded by a molded composite/fibreglass aerofoil shell, being it hollow and filled with a low density foam or honeycomb material in order to save weight [11]. Figure 1.21 shows a cutaway view of the UDF blades. Rolls-Royce patented [29] its own 'hollow aerofoil blade' in 1987. This special blading, shown in Fig. 1.22, is potentially applicable to propfan engines and is composed by KEVLAR fibres.

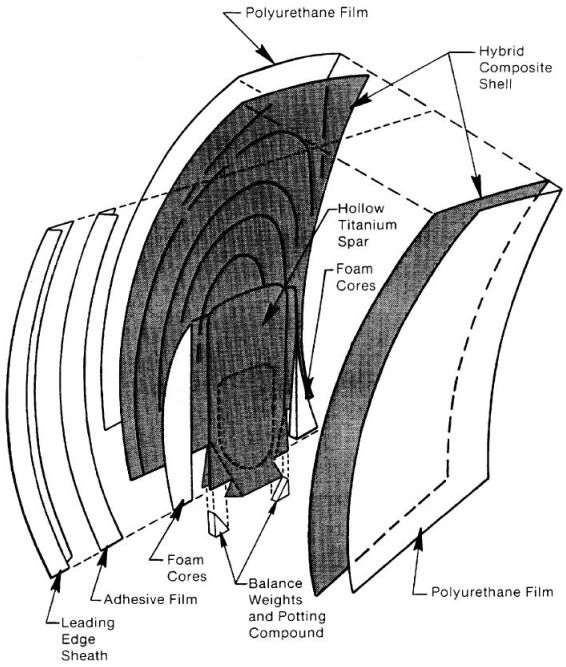

Fig. 1.21. The UDF blade construction (source: ref. [11]).

The new blading technology was developed taking also into account different configurations of open rotor. The basic configuration features a single rotor. This is the simplest and cheapest design: the propeller is spinning axially, consequently the resulting kinetic energy of the airflow is not only translational (useful for thrust) but also rotational (not useful for thrust). This rotational component is called propeller swirl and is a form of energy loss, so that the efficiency of single-rotating propfan is approximately 80% at design conditions.

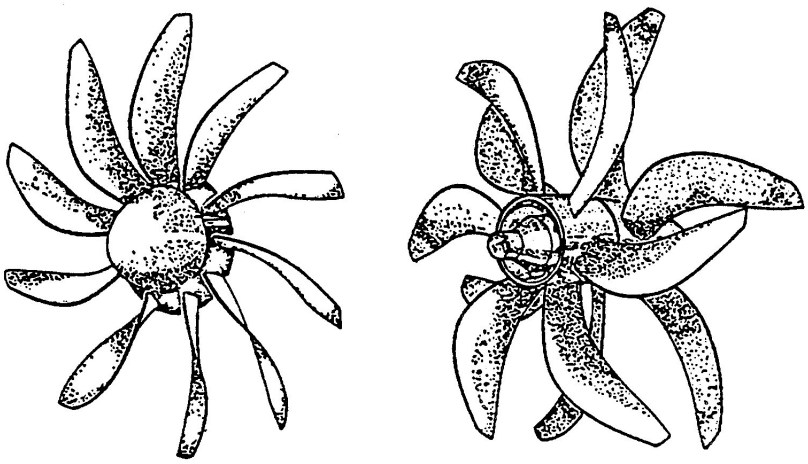

Fig. 1.22. The patented Rolls-Royce open rotor blading (source: ref. [25]).

In order to partially recover this energy, the single-rotation configuration could be modified with the addiction of Swirl Recovery Vanes (SRV), featuring a set of stationary aerofoils (vanes) mounted behind the single rotation propfan blades. This design, shown in Fig. 1.23, partly recovers the rotational swirl and it is less complex than the contra-rotating configuration, but it is also less efficient.

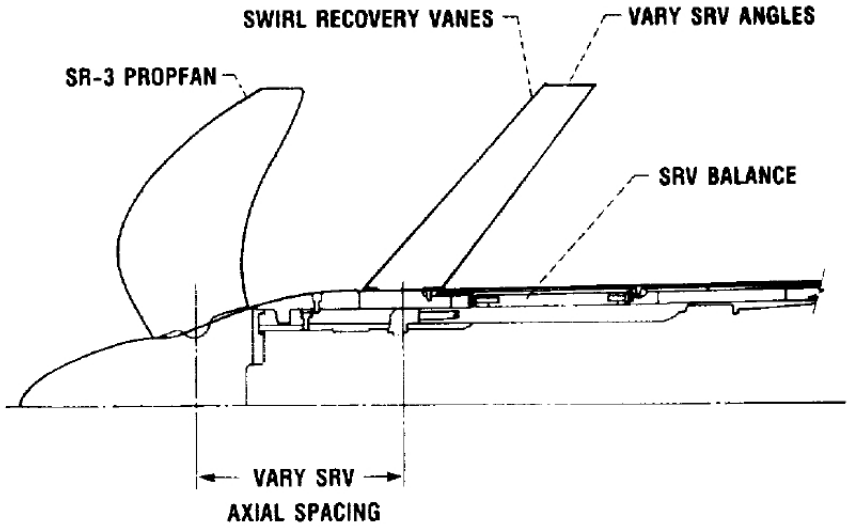

Fig. 1.23. NASA Lewis swirl recovery vane experiment (source: ref. [161]).

In fact, a better recovery of the energy losses experienced by single-rotation propellers is furnished by the contra-rotating[30] configuration: two propellers, mounted

[30]The first intensive studies on contra-rotating open rotors belong to the Second World War period: for instance, see ref. [37].

on the same shaft axis, spin in opposite directions, so that the rear propeller redirects the rotational swirl of the airflow into the translational direction, therefore increasing thrust and propulsive efficiency; according to both ref. [71] and Fig. 1.6, the augmentation of net efficiency is about 8-10% over a wide range of flight speed ($0.65 < \text{Mach} < 0.85$). Furthermore, the diameter of propeller rows can be reduced because a contra-rotating propfan can allow twice as much power as a single-rotation propfan of same diameter. Hence, ground and fuselage clearance are reduced, while each rotor hub will receive less power (as a consequence its design is less complex). In addition to that, the cancellation of torque and gyroscopic effects in the contra-rotating configuration potentially allows any gearbox to be lighter in comparison to that of a single-rotation device. Continuous improvements of the contra-rotating technology were achieved in the past, as shown in ref. [83]. However, contra-rotation adds new issues, such as the unsteady aerodynamic interactions between blade rows, which make noise reduction more difficult. Figure 1.22 shows single-rotating and contra-rotating open rotors. All these configurations have been designed to be applied on various engine architectures, which are better described in the next paragraph.

A last but nonetheless important consideration should be done on the implementation of the ice protection system, which is of special concern during the development of new blades[31]. The ice protection system mostly used on normal propellers is the electrical resistance heater. It can be bonded on or moulded inside the leading edge of the propeller blades. The power density of the heater generally varies in chordwise and spanwise directions to optimise heat distribution with the lowest power consumption[32].

Several experiments were carried out by NASA with the purpose to collect data regarding ice accretion prediction and impingement limits. Figure 1.24 illustrates a comparison between flight test data and the ice accretion predicted by LEWICE,

[31] The new open-rotor has to meet the requirements of the JAR/FAR Part 25, Appendix C.
[32] If the engines are protected from ice ingestion, usually spinners are not deiced nor anti-iced.

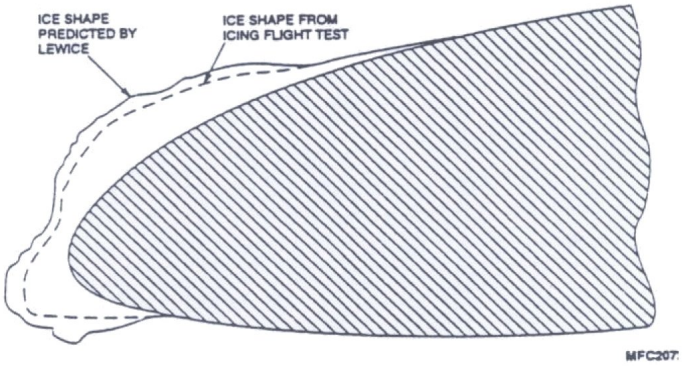

Fig. 1.24. Ice accretion: a comparison between LEWICE predictions and flight test data (source: ref. [138]).

a computer program developed at NASA Lewis.

1.2.3. General review on propfan architectures

The architecture of an engine is defined by the way this is installed on the aircraft to provide thrust. The installations basically can be of two types: tractor or pusher. In theory, both the typologies allow the engine to be mounted on the wing or fixed to a pylon on the rear fuselage or tail. However, the propfan installations studied in the past did not consider any pusher architecture on wing, as shown in Fig. 1.25. The wing-mounted solution allows a lighter rear fuselage structure. Positioning the engines close to the centre of gravity of the aircraft ensures a better balance and stability during flight, but introduces cabin noise penalties. There are also integration problems, due to the strong aerodynamic interaction between the wing, the nacelle and the rotor as well. Moreover, the large propfan diameters[33] strictly influence the wing design and the aircraft layout: ground clearance has to be guaranteed avoiding the use of large undercarriage legs. As regards the aft-mounted propfan, a weight penalty arises because of its adverse effects on centre of gravity, though the wing is left more uncluttered. However, any rear installation potentially solves blade containment issues and reduces cabin noise[34], even if additional cabin noise treatment in the rear fuselage is required. In order to provide an acceptable

[33]Large if compared to the diameter of a turbofan delivering the same thrust.
[34]This is particularly true for the pusher architecture.

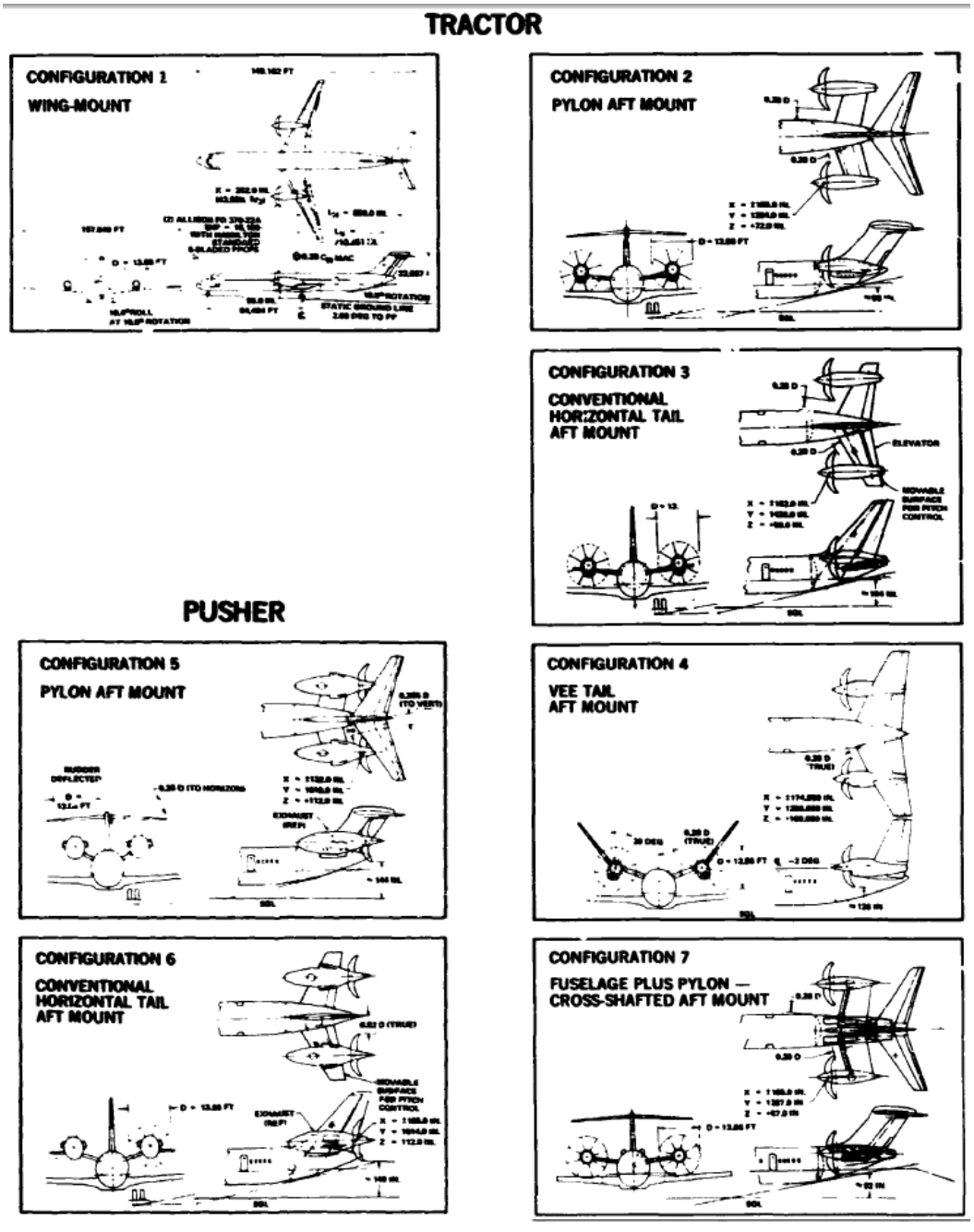

Fig. 1.25. Propfan architectures and installation on aircraft (source: ref. [68]).

clearance at takeoff and to avoid adverse effects of the wing wake, the aft-mounted propfan must be installed high on the fuselage or over the tail beams (Fig. 1.25). Considering the propfan engines which were flight tested in the past, the tractor architecture was always associated with a wing-mounted installation, while the pusher architecture with a rear-mounted installation[35].

1.2.4. Power transmission systems

As anticipated in paragraph 1.1.2, there are two main ways to transmit energy from the gas generator to the open rotor: the power turbine can be connected to the open rotor directly, or through a shaft connected to a gearbox.

When the gas generator is 'linked' to the propeller by means of a gearbox, the advantage consists in the possibility to drive the power turbine and the propeller at optimal speeds, because propellers operate efficiently at low rotational speeds, while the compressor and turbine stages operate efficiently at high rotational speeds. This configuration can work on both tractor and pusher architectures. The reduction gearbox is not a new concept in aviation. However, a propfan gearbox must be stronger and have a longer service life with low maintenance if compared to that of a turboprop: the power required by propfan engines[36] is higher than the power of conventional turboprop powered aircraft. An improved geared design has been implemented in the demonstrator 578-DX of Pratt & Whitney - Allison; the gearbox, rated at 13,000 horsepower, was designed using a 'planetary' gear configuration. A preliminary design of an improved gearbox is shown in Fig. 1.26. Also Rolls-Royce patented a gearbox-driven pusher propfan, as shown in Fig. 1.27.

As mentioned before, another power transmission system is the gearless power-turbine: this configuration can be adopted only on a pusher architecture. The gearless power-turbine was designed for the first time by General Electric and used on the UDF engine. With this system, the propeller experiences a loss of efficiency,

[35]Further considerations on propfan-aircraft integration are presented in ref. [65].
[36]Between 12,000 and 20,000 shaft horsepower.

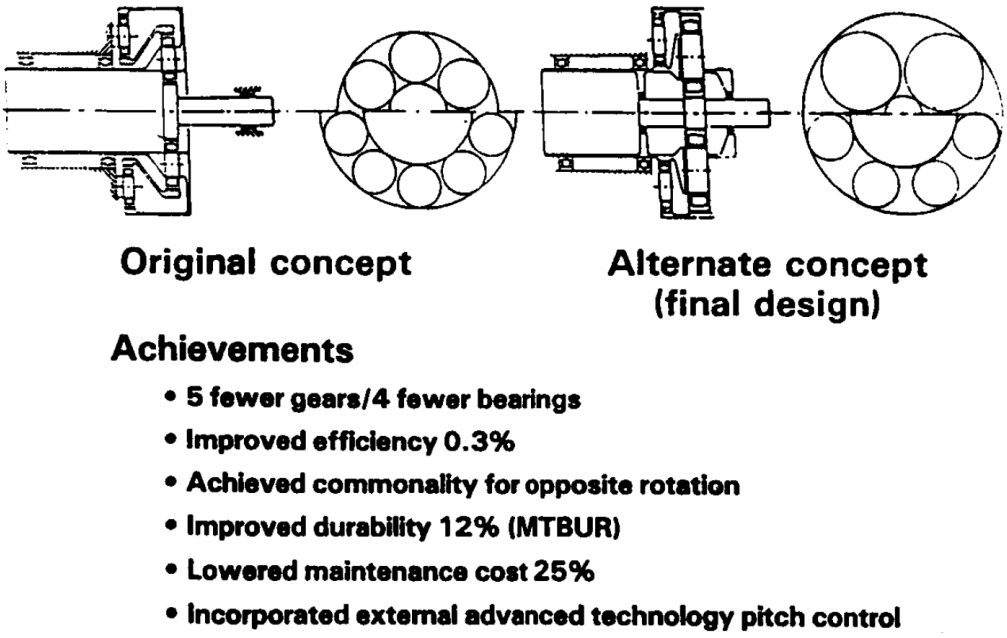

Fig. 1.26. Preliminary design of an improved gearbox (source: ref. [125]).

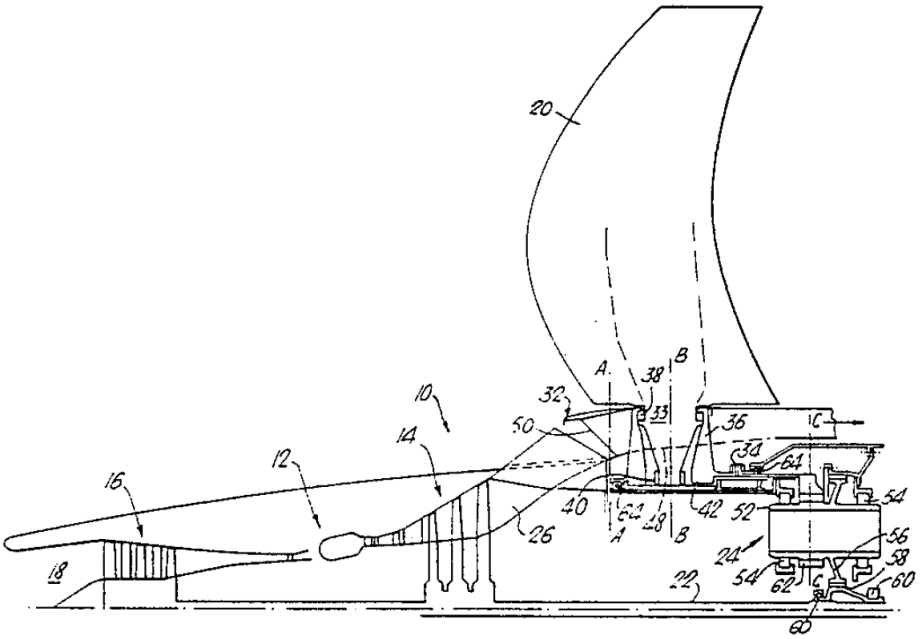

Fig. 1.27. The Rolls-Royce "Propfan aircraft propulsion engine" (source: ref. [36]).

because it is forced to operate not at optimum rotational speeds. The gearless power-turbine also implies a design complication regarding the power-turbine/rotor sealing. However, this solution presents the great advantage of eliminating the gearbox weight and complexity, reducing maintenance time and costs[37]. The GE power-turbine is shown in Fig. 1.28: the blade rows spin in opposite directions as the exhaust gas expands through them. The two rotors of the power-turbine produce roughly the same torque being mechanically independent.

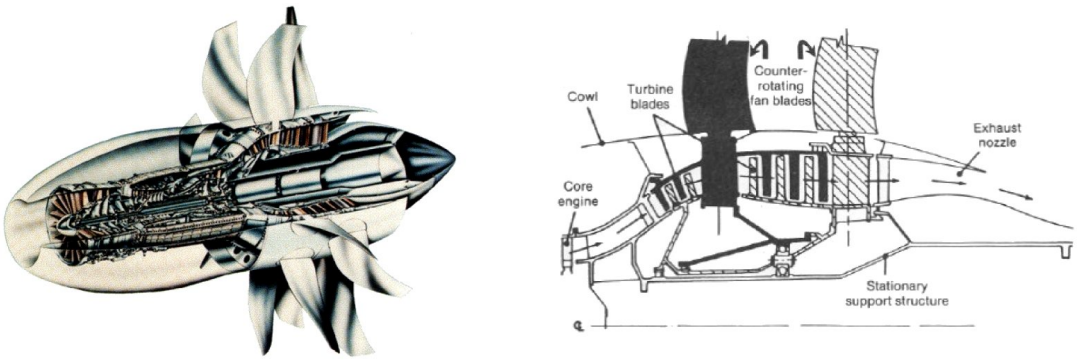

Fig. 1.28. The gearless UDF power turbine (source: ref. [74]).

Although huge differences exist between these configurations, on both systems it is possible to integrate an appropriate pitch mechanism, useful not only to optimise the in-flight performance of the engine, but also to generate reverse thrust on ground and during landings. The variation of the propeller pitch, well illustrated in Fig. 1.29, is necessary to maintain the optimum Angle Of Attack (AOA) between rotor blades and airflow, not only in flight but also at takeoff and landing. For instance, it is easier to start the engines with a blade pitch angle of zero, because the propeller presents minimum drag, thus minimising the engine effort to turn the propeller. Moreover landing distances can be shortened varying the pitch to obtain reverse thrust: wind tunnel tests [70] showed that a contra-rotating propfan can achieve a reverse thrust equal to 60% of takeoff thrust, whilst the reverse thrust of a conventional turbofan can only be 40-50% of takeoff thrust. Through the variable pitch mechanism (an example of which is given in Fig. 1.30) and a synchronizing

[37] Actually a turboprop requires a steady and intensive maintenance.

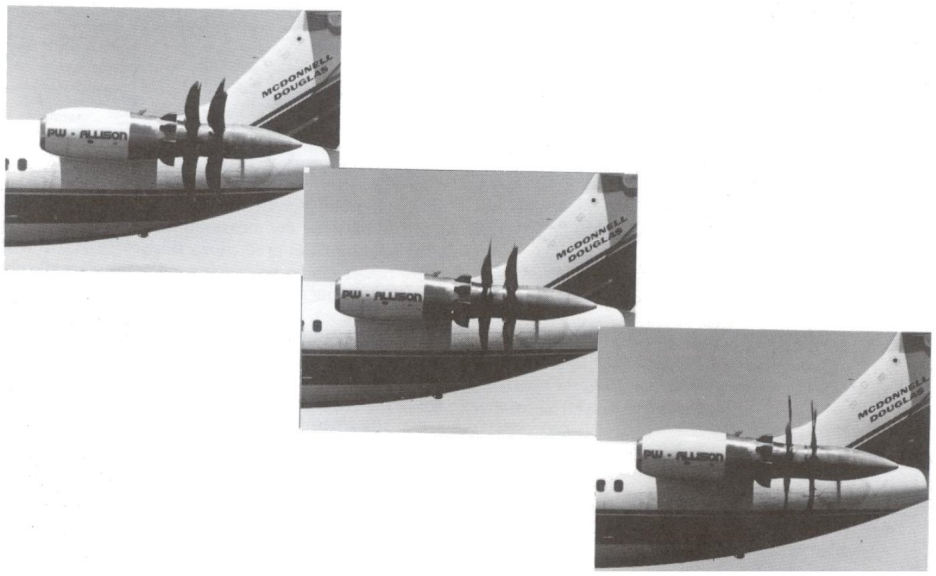

Fig. 1.29. Pitch mechanism in action on the P&W 578-DX (source: ref. [52]).

system it is also possible to reduce noise emissions by eliminating the beating or pulsing of noise. Furthermore the blade pitch variation can be employed to control thrust in flight. When the power-turbine speed is kept constant by a fuel flow governor, thrust is controlled by the pilot, who manually varies the propeller pitch through an apposite servo system. A graphical resume of the design studies of single-rotating and contra-rotating gearboxes and pitch-change mechanisms is given in Fig. 1.31. These designs were produced during the Advanced Prop-fan Engine Technology (APET) program, which was extended in 1984 in order to include them.

1.2.5. Propfan: unsolved problems

The open-rotor is conceived as an innovative aero-engine developed on the basis of the previous propfan technology, as mentioned in paragraph 1.1.3, which highlighted its economical aspects and benefits. In the present paragraph, the expected evolution of the propfan into open-rotor is described considering technical issues only[38]. The development of the open-rotor logically starts from the knowledge ac-

[38]In fact there is a further issue: the psychological refuse of passengers in front of an aircraft propelled by open-rotor engines. Potentially, it might seem to them an unsafe engine or a

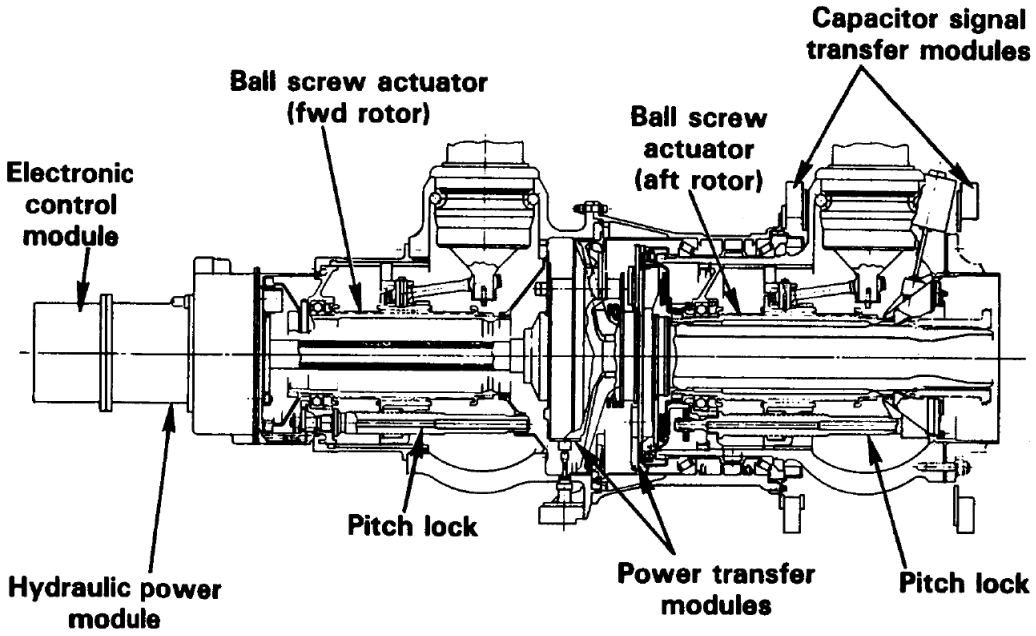

Fig. 1.30. Rotary hydraulic pitch control concept (source: ref. [125]).

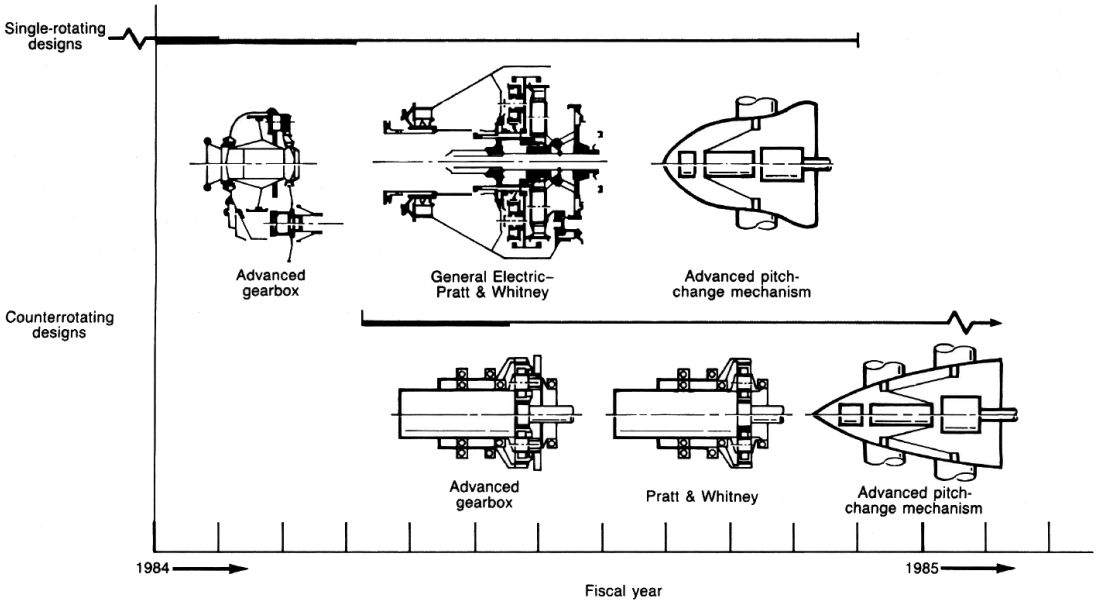

Fig. 1.31. Gearbox and pitch designs in APET studies (source: ref. [71]).

quired during the advanced turboprop development, and must proceed answering to the unsolved problems which affected these engines. The main issues associated with propfans can be divided into two categories:

- problems related to the open rotor
  - acoustics
  - flutter
- difficulties in improving the nacelle design
  - cowl shaping
  - intake design.

As regards the first category, the major concern is the noise produced by the high-speed blades: the new technology must meet the standards of acceptable community noise near airports, as dictated by the Federal Aviation Regulation (FAR). A collection of introductory material on open rotor aerodynamics and acoustics can be found in ref. [7]. The challenge is to reduce the cabin noise level generated by a propfan[39], making it become at least similar to that of a conventional turbofan. The ducted fan and the bypass flow allow the turbofan to produce noise levels relatively lower than those emitted by a propfan. In fact, the tip speed of the unshrouded blades of the propfan can easily reach supersonic conditions, thus producing a great amount of noise, especially when the aircraft is cruising at high subsonic speeds. The propfan also creates strong wakes and vortices, which increase noise levels not only at cruise, but also during takeoff and landings, when the AOA of the engine varies sensibly. There is experimental evidence [162] suggesting that the noise radiation characteristics of a propfan at angle of attack do significantly differ from those of a propfan at zero AOA.

The noise generated by the engine in a region close to the open rotor is called 'near-field noise'. Near-field noise influences passenger comfort directly. Several

technological step backward.

[39]See the important work of ref. [63] on the propfan noise level assessment.

studies on the near-field noise produced by a wing mounted propfan[40] showed that the Sound Pressure Level (SPL) decreases inboard of the propfan and increases outboard when the angle of attack increases. Thus the SPL decreases close to the cabin during takeoff and climb: this fact is advantageous, since it tends to improve the comfort of passengers. However, at takeoff the noise level below the propfan increases while the noise level above the propfan decreases: this feature has an unwanted impact on the noise levels near airports. Moreover, because of the aerodynamic interactions occurring between multiple rows of blades, the contra-rotating propfan produces higher near-field noise levels than the single-rotating propfan, especially at positive angle of attack. The 'interaction noise' is exactly produced by the interaction of the strong wakes, created by a leading edge vortex, with the aft row of blades. A passive way to attenuate near-field noises is to isolate the sidewalls of the fuselage through special construction and assembling techniques[41].

As regards the noise levels which propagate over long distances, they are classified as 'far-field noise'. Due to the high angle of attack, propfan engines generate high far-field noise levels during takeoff and climb. The atmosphere attenuates very high levels of noise in the high-frequency range[42], even if the role it plays in low-frequencies noise attenuation is not significant: one solution for far-field noise reduction could be to increase the cruise altitude of any aircraft propelled by propfan engines, but this would penalise their rotor efficiency.

Among the problems in open-rotor design there are not only the acoustic issues, but also the aeroelastic response and mistuning of the high-speed blading. The aeroelastic response of a blade refers to its tendency to vibrate when loaded by the aerodynamic forces (lift and drag) acting on it. Each blade has to be designed to operate efficiently and to exhibit a stable aeroelastic response, otherwise an extreme

[40] In particular ref. [56] and [114].
[41] For example see ref. [88].
[42] For instance the high-frequency noise levels of turbofans are easily decreased by the atmosphere.

unstable and undamped vibration may occur inducing large structural stress in the blade, which can lead to its total failure. This phenomenon is called 'blade flutter' and is a dangerous and undesirable characteristic of aeroelastic response. Therefore a propfan must experience blade flutter at a Mach number significantly greater than the Mach number at which it is designed to operate. However, blade flutter can also occur at low speeds if the propeller is working at high angle of attack. This condition is known as 'stall flutter': it happens if the flow separates from the surface of the blade, causing a total loss of lift on the blade and hence a loss of thrust. The aeroelastic response of a propfan blade is influenced primarily by blade thickness and sweep angle. Since the blades are thin and highly swept[43], they can deform and bend easily when loaded by aerodynamic and centrifugal forces. Moreover, adjacent blades influence the airflow field and consequently their aerodynamic loading: these phenomena are known as 'cascade effects'. In particular, for a propfan blade at the stall flutter condition, each blade moves between attached flow and separated flow depending on its location in the plane of rotation of the rotor. The oscillation induced by this situation may provoke severe vibratory stresses, resulting in fatigue failure of the propfan blade: thus it is another important design condition [123].

The ability of a blade to induce vibrations in another one, thereby increasing the likelihood of flutter, can be limited by 'blade mistuning': every single blade of the open rotor is designed to have slightly different resonant frequencies and mode shapes. It has been demonstrated [107] that, for a wide range of off-axis flow angles, blade pitch angles and rotational speeds, the intentional mistuning has a beneficial effect on the aeroelastic response of propfan blades, even if mistuning procedures highly depend on the characteristics of the particular system. However, mistuning procedures can actually increase blade stresses if not implemented properly [86]. The scientific community (especially NASA along with industry) not only spent a lot of efforts toward calculating the aeroelastic response of propfan thanks to

[43]For instance see Fig. 1.19 to 1.22.

numerical and experimental techniques, but also continued the investigation on this topic even when the ATP program ended[44], because it still represents a challenge in open-rotor optimisation.

A completely different but still important challenge in propfan improvement regards the second category of unsolved problems affecting this kind of engine: the achievement of new methods for open-rotor nacelle design. As shall be highlighted by the literature survey of chapter 2, which is fully dedicated to the investigations on this important topic, the documents available in the public domain do not widely cover the analysis of propfan nacelle shaping. This lack of information represents an obstacle to the open-rotor development, preventing a comprehensive understanding of the aerodynamic interaction between the rotors and the nacelle. Therefore, without this information, it is difficult to predict how the nacelle itself can be eventually shaped taking advantage from this interaction, and consequently improving the performance of the rotor.

One of the reasons that might justify this lack in propfan nacelle analysis is hidden behind its design context described in section 1.1: in the 1980s, the main goal was to prove the feasibility of the concept and, even roughly, demonstrate the real benefits of the new technology, basically consisting in a specific fuel consumption improvement. Adopting this strategy, the main problem to solve was the high-speed propeller design[45], and, as a direct consequence, the noise control and reduction, and then again the attenuation of vibrations and other structural problems.

1.3. Aim and structure of the Ph.D. work

Though reasonably considered a secondary aspect in the past, today the definition of a nacelle design method tailored for open-rotors becomes a key issue for the

[44] See for instance ref. [106].
[45] A large amount of material on this topic is available in literature, for instance see ref. [12].

development of the new propfan generation. The aim of the present research is to help enhance the knowledge in this area, developing new methodologies for nacelle design applied to these novel engines. It follows that the title of the project[46] is Design and Engineering Methods for Open-rotor Nacelle Shaping (DEMONS). The objectives leading to the attainment of the project target are listed below:

1. Choice of the project strategy
2. Definition of the research process
3. Specification of a preliminary design methodology
4. Realisation of the nacelle design method/s.

The first two goals consist in the accomplishment of organisational tasks, which are necessary at this stage: the project basically starts as a new research, thus it needs to be defined also in its strategical aspects. The third and fourth objectives include both theoretical and practical contents, dealing with engineering techniques that might be computational or experimental.

Obviously, the prospective results of the present research consist in the discovery of useful guidelines for designing an open-rotor nacelle. This work is consequently structured taking into account this purpose and all the goals mentioned above. After this introductory chapter, the second chapter contains the literature survey on the existing nacelle design methodologies. The third chapter defines the project strategy, and consequently the research process, by analysing the literature review of chapter 2 and taking into account the academic requirements. The fourth and the fifth chapters investigate the physical and mathematical aspects involved in the definition of the methodologies for appropriately shaping an open-rotor nacelle. These methods then represent the basis for the study reported in the sixth chapter, which illustrates how to apply them for developing an innovative nacelle shape. A specific overview on the additional studies related to this project is then provided

[46]See also appendix C.

in the seventh chapter. The main results are commented in the final chapter, which concludes providing suggestions for future works. All the supplementary material, which is integrating some of the chapter parts wherever needed, is collected in a set of appendixes at the end of this thesis, before the bibliographical references.

2. LITERATURE SURVEY ON PROPFAN NACELLE DESIGN

The first chapter can be considered as an introductory literature overview, which contextualises the propfan technology and indicates several references related to its history. The present survey instead focuses only on those papers, reports and books that somehow treated the nacelle design problem for propfans. Moreover, the assessment of the existing nacelle design methodologies through this literature review represents an important mean of synthesis, useful for the definition of the project strategy discussed in chapter 3.

Among the available publications, the first important source of information is the NASA report of reference [71], which has been cited yet in chapter 1 many times: it offers a wide presentation of the propfan development as an evolution of the turboprop engines. Although it does not describe in depth all the several technical and historical characteristics of the propfan, it is an useful starting point for a literature survey, since it provides a very accurate bibliography related to the whole advanced turboprop program, with particular attention to acoustics, performance, theory and design. However, the specific topic of the nacelle design is not covered in details. While the historical development and the theoretical principles of the aerodynamics of propellers are summarised in ref. [156], the basics of open rotor installations are introduced in ref. [150] and [158]. Some theoretical and experimental fundamentals on propeller-body interference are also

available in ref. [8] and [10]. Ref. [18] regulates the entire station designation of open rotor engines, while ref. [9] and [14] give the guidelines for both thrust and drag determination[1].

Apart from these notes, which are of general nature, the specific material on propfan nacelle design available in the public domain is very poor: as regards this argument, it is necessary to consider studies made on turboprop nacelles, such as the Computational Fluid Dynamics (CFD) analysis of ref. [66] and [142]. Although these documents treat the problem of nacelle design deeply, the quantity of papers or reports on the topic is small. This highlights the need for further investigating this research field, even if accurate studies were probably executed in the past by engine manufacturers but were never published, since they are actually unavailable in the open literature. The following sections will describe the existing relevant publications on this matter, dividing the material into two parts addressed to the tractor and pusher propfan respectively. This distinction is necessary due to the design and aerodynamic differences of the two architectures. Indeed the discussion upon the various issues connected to propfan nacelle shaping can not be separated from the notions already introduced in paragraphs 1.2.3 and 1.2.4: the architecture of the engine, and consequentially its power transmission system, inevitably affect the design of both cowl and intake.

2.1. Tractor architecture

The literature on the nacelle design for tractor propfans regards mainly the inlet design and the influence of the rotor wake on the aerodynamic performance of the nacelle.

[1] An interesting investigation on inflight determination of net installed propulsive efficiency is given by ref. [43].

2.1.1. Inlet design

Tractor-propfan inlets are usually curved ducts of different type: S-ducts (scoop or chin), bifurcated and annular ducts are the most common examples. These different intake configurations are collected in the graphical representation of Fig. 2.1. A simple and clear introduction to this kind of inlet design is given in ref. [87].

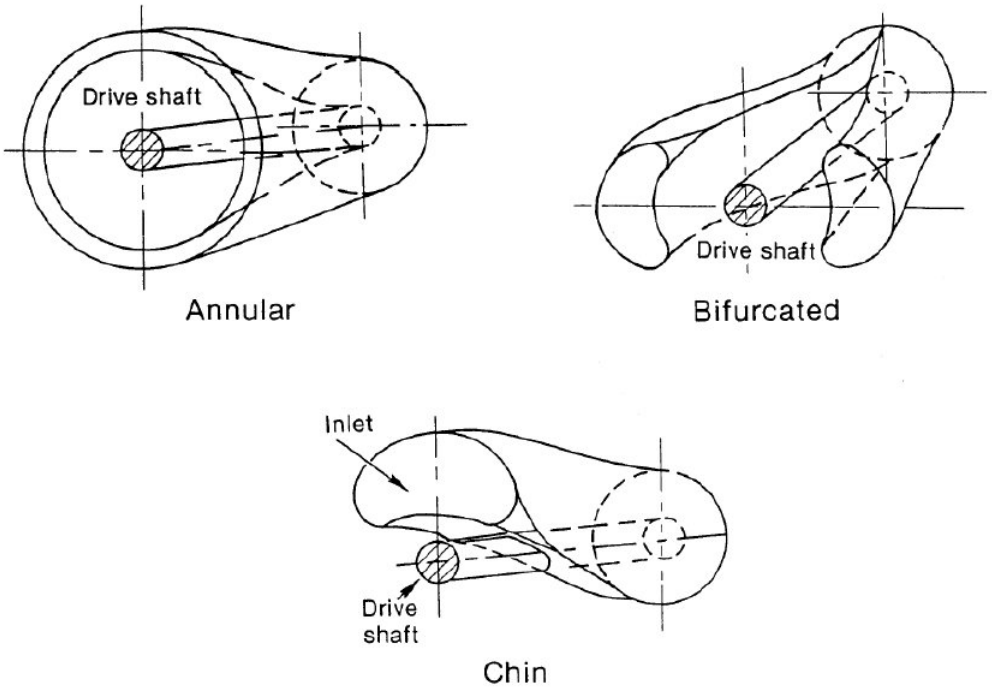

Fig. 2.1. Intakes for tractor propfan (source: ref. [126]).

This book also introduces some important notions regarding the fairings of finite length and the installation of the jet engines. The aerodynamics of these intake typologies is further described in ref. [67]. An interesting introduction to drag phenomena due to internal-flow systems is given in ref. [76], which is an optimal guide for drag analysis in general. These lectures offer a wide understanding of the matter without focusing on the propfan concept.

Unfortunately, the Engineering Sciences Data Unit (ESDU) documents do not provide significant informations on the topic: there is material on pipe bends, but this assumes fully developed flow and it aims more at industrial applications. On the contrary, the papers cited in the following brief subparagraphs give a technical

overview on the design methods for tractor propfan inlets.

2.1.1.1. Specific works on S-duct inlets

Ref. [95] and [96] (which is revised by the previous one) give an assessment of the work done for single-rotation tractor propfan intake design up to 1987. Various design trade-offs are discussed, though focusing mainly on single-scoop intake with boundary layer diverter. An analytical design of S-duct diffusers for turboprop installations with an offset gearbox, followed by experimental verification, is presented in ref. [105], while ref. [84] treats the analytical and experimental analysis of a complex tridimensional inlet for turboprop applications. Suction tests of single-scoop intake with option of thirty-degrees turning wedge have been studied in ref. [72] to simulate propeller-induced swirl. Total pressure recovery and distortion were measured not only in the previous reference, but also in ref. [104], testing various intake lip and throat profiles of a single-scoop intake with a propeller spinner (but no propeller): the wind tunnel tests ran with airflow up to Mach 0.35 and incidence of ten degrees. Further investigation on S-duct inlets for turboprop offset gearbox applications is found in ref. [103]. Of course some of the works mentioned on turboprop engine are very useful for the preliminary studies of tractor propfan intakes, because their nacelle architecture is very similar though the propeller blades are completely different. More recent work (chronologically ordered: ref. [13], [116], [24], [90] and [108]) has been conducted on the S-duct, also studying the RAE M2129 model: this is a diffuser of circular cross-section which has been used as a test case for CFD studies. It has an intake lip, although some computations have been done for the duct alone without an external flow region.

2.1.1.2. S-scoop, twin-scoop and annular inlets

With the work of ref. [73], S-scoop, twin-scoop and annular intakes, placed behind a propeller, have been analysed in a wind tunnel at Mach 0.6, 0.7, 0.8; the total

pressures were measured at the throat, so evaluating the performance of the intake entry region rather than a curved duct. A comparison of theory and experiment for propfan intakes is given by ref. [99].

2.1.1.3. Intake particle separators

A particle separator is a device primarily used to prevent aero-engines from ingesting foreign objects, such as sand or similar, through the air intake. Usually this consists of an additional, if needed switchable inlet channel, which increases the air flow over a duct less curved than the compressor inlet. Due to their inertia, 'heavier than air' debris usually continue their path towards this alternative channel, where they cause no harm. While the 'clean air' deviates into the compressor inlet, the 'contaminated air' is discarded, arising some performance degradation. For this reason, particle separators might not be fixed and only switched on when required by the circumstances.

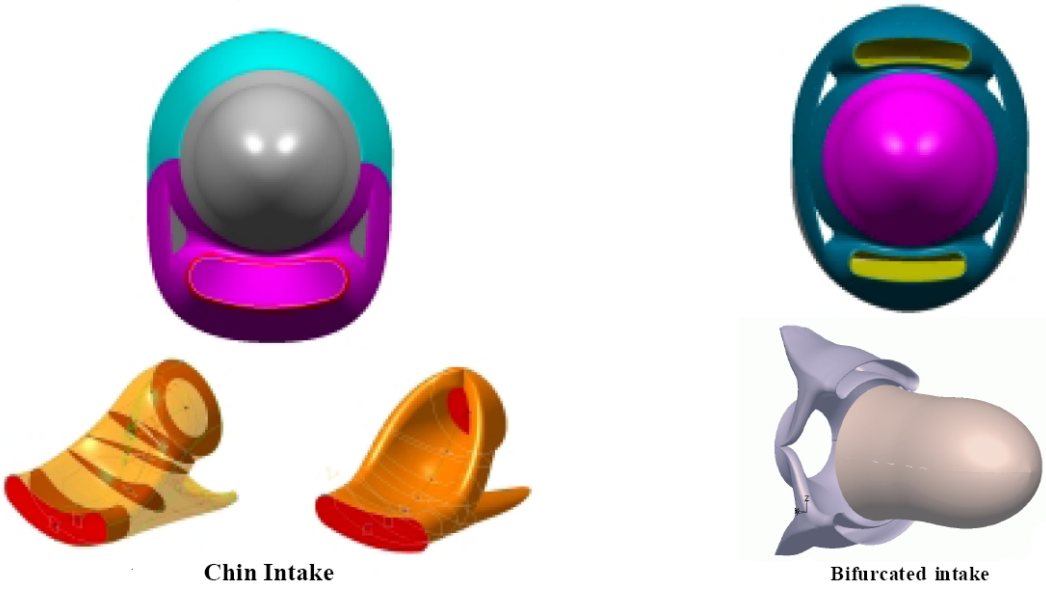

Fig. 2.2. Intake particle separators (source: ref. [97]).

The main studies conducted on intake particle separators are quite recent and partly connected with the design of innovative inlets, such as the bifurcated intake of ref. [33]. Other work done on turboprop inlets, such as in ref. [97] and [127],

is very useful to investigate this topic. Figure 2.2 clearly shows how the intakes of Fig. 2.1 can be modified introducing the particle separators.

2.1.2. Rotor wake influence

When considering engines with a tractor architecture, the assessment of the effects caused by the propeller wake is inevitable. In more detail, the rotor wake plays a strong influence on the machine performance, because it can negatively distort the incoming air which enters the core. On the other hand, the intake generates a back-pressure in the flow between the propeller blades and the inlet itself, contributing to create a situation of blade stressing. Therefore, in 1985 NASA, Lockheed, Hamilton Standard, United Technologies and Boeing made wind tunnel tests to ensure that these blade stresses were acceptable. The results, as mentioned in ref. [71], showed that "[...] the inlet should be located approximately one blade width behind the propeller in order to achieve high inlet [pressure] recovery and low blade stresses". The aerodynamic interactions between propeller and nacelle were also investigated during the PTA program as reported in ref. [23], while a study on the flow generated behind both single-rotating and contra-rotating propellers at angle of attack was done in ref. [148]. The influence of the rotor wake on the aerodynamics of the nacelle is usually regarded as an installation issue. A prediction method on the aerodynamic performance for high speed propeller-nacelle integration is presented in ref. [55]. A method for the prediction of the installation effects of tractor propfan at subsonic speeds is given by ref. [45]. Ref. [133] offers a flow prediction method for the engine installation effects on transport aircraft at transonic speeds, while the consequences on the propeller-nacelle force coefficients due to the variation in solidity and inclination are presented in ref. [64]. Other material on propulsion system installation design and aerodynamic effects is given in ref. [38] and [94].

2.2. Pusher architecture

The propfan prototypes with pusher architecture, unveiled in Fig. 1.9 and 1.10, show a nacelle with significantly different projected area compared to that of turbofan commonly installed on commercial aircraft[2], that is

$$\left(\frac{D_{hl}}{D_{\max}}\right)_{turbofan} > \left(\frac{D_{hl}}{D_{\max}}\right)_{open-rotor} \tag{2.1}$$

where D_{hl} is the highlight diameter and $D_{\max}$ is the maximum nacelle diameter. Despite this difference, which is important for the aerodynamic implications it might introduce, the material available on the design methodologies for pusher propfan nacelles is extremely poor. Few but important information is presented in the design report of the UDF engine (ref. [11]), which explains not only some structural features of the nacelle[3], but also how the UDF had a 'pitot intake'-forebody integration designed to provide "[...] low inlet spillage drag and consequently low distortion into the unducted fan at all operating conditions within the flight envelope". Moreover, there are included important guidelines[4] on the forebody shaping: "[...] The forebody is shaped such that its maximum diameter is larger than the blade hub diameter and is located approximately one blade-length upstream of the first rotor. This type of flowpath shape allows the flow to diffuse just upstream of the UDF blade rows, thereby lowering the blade inlet Mach numbers. It also provides a gentle concavity to the streamlines through the blades, thus eliminating unnecessary accelerating curvatures and high Mach number regions inside the blade rows. The flowpath through the blades is area-ruled to recognize the flow blockage due to the local blade thickness. Area ruling is accomplished by scalloping the blade platforms from a cylindrical shape to alleviate the high through-flow Mach numbers that occur in the region where the blades are the thickest. The cir-

[2] See also subsection 3.1.3.
[3] See paragraph 2.12 and chapter 12 of ref. [11].
[4] These are qualitative and not quantitative guidelines, hence they do not represent a rigorous design method.

cumferential average radius is then used in the axisymmetric flow analysis". In the same document appear also interesting considerations about the nacelle ventilation system[5].

As regards other sources, the analysis of ref. [113] describes a first computational investigation on the aft-mounting installation problem. A potential source of information can be individuated within the rotor design context, since the presence of a forebody in front of the blade rows inevitably influences the rotor performance. Although interesting papers regarding the design procedure of the contra-rotating blades were published (such as ref. [44] and [140]), the forebody shape (constituting the major part of the whole nacelle) was always assumed known in advance, that is before starting the blade design procedure. The wind tunnel and flight tests of the existing engines provided the experimental pressure distribution on the nacelle and its mounting pylon (ref. [147] and [51] respectively). Some interesting works were accomplished in order to describe the flow field around the nacelle in the proximity of the rotor and through the blades (ref. [110] and [119]). Important considerations can be inferred about the airflow velocity profile and the induction effects of the rotor over the nacelle, but the data describing the mutual influence between the forebody and the rotor are insufficient. In general, no technical guidelines concerning nacelle design methods emerge from all the documentation cited so far.

As regards ESDU reports, there is nothing specific on propfan nacelle design. However, some of the technical documents present a useful reference for pitot intake design and forebody shaping in general, especially regarding the geometric definition of the shapes forming the different parts of a nacelle and their drag estimation. General considerations about drag representation and airframe drag calculations (including nacelle integration) are given in ref. [5] and [19].

[5]Ref. [11] reports: "[...] The nacelle ventilation system is designed to duct ambient air into the nacelle cavity to provide cooling for critical components. The heat source to these components is radiation from the outer rotor structure [...]. The composite nacelle [...] behaves as an insulator; consequently, heat must be removed by the ventilation air flow circuit".

2.2.1. Pitot intake

The pitot intake is the typical inlet of turbofan engines. In principle, as shown in Fig. 1.9 and 1.10, it represents also the simplest inlet for a pusher propfan, although in this case it should be substantially different from a classic turbofan intake (examples of which are reported in [67]). In fact, the ratio of its highlight diameter D_{hl} and length L_{hl} is expected to be smaller due to the engine configuration itself:

$$\left(\frac{D_{hl}}{L_{hl}}\right)_{turbofan} > \left(\frac{D_{hl}}{L_{hl}}\right)_{open-rotor} \tag{2.2}$$

Considering one-dimensional flow, the mass flow and momentum functions of gas in ducts are collected in ref. [4]. The basic guidelines for pitot intake shaping are illustrated in ref. [15] and refer to the typical NACA 1-series geometry. As regards the drag estimation methods, ref. [16] and [17] treat respectively the surface pressure coefficient and the wave-drag coefficient distributions for axisymmetric fore-cowls of various shapes, accounting for the problems related to transonic phenomena ($M \leq 1.5$). Spillage drag is considered in ref. [6]. Although the previous references are intended as a guide for turbofan inlets, these documents can be useful in order to find clues on the aerodynamic performance assessment of new open-rotor intakes.

2.2.2. Cowl design

The cowl of a pusher propfan is basically the main part of the body placed in front of the rotor zone (i.e. the forebody). From a geometrical point of view, its profile can be preliminarily studied without considering the inlet integrated in the pusher architecture. Ref. [1] reports in details the geometrical characteristics of typical bodies used in forebody shaping. As regards drag estimation, ref. [2], [3] and [112] consider the drag of axisymmetric bodies at subsonic conditions. However, no documentation in literature presents the methodologies for shaping the external

cowl of a pusher open-rotor.

3. DIRECTION OF THE PROJECT

The technical administration of a project is essential to better plan present and future works, which potentially might contribute to further expand the achievements of the current research. Indeed this aspect is particularly important for DEMONS because the project is completely new and it is not the follow-up of a previous study. The purpose of this chapter is to determine the direction to be followed during the project. This is accomplished by choosing the project strategy and defining the research process, thus fulfilling the first two goals proposed in section 1.3.

3.1. The project strategy

As noticed in the introductory chapter, there could be a relevant number of important fields of investigation for propfan designs, but this research will be limited to the analysis of the external aerodynamic issues related to the open-rotor nacelle shaping. In order to carry out such an analysis, it is necessary to organise the actions to take for achieving the last two objectives of this project, which are the specification of a preliminary design methodology and the realisation of a nacelle design method. The strategy to accomplish this task relies on the identification of an existing engine to be used as a REference MOdel (REMO), upon which the initial studies can be focused. In fact, it is desirable that any future

design methodology allows to recreate what already exists. Hence, before defining the research process, it is opportune to determine what kind of nacelle has to be designed. After an evaluation of the existing propfan architectures, the selection of their configuration is essential for determining the reference engine mentioned above.

3.1.1. Evaluation of the open-rotor architecture

The simplest way to distinguish open-rotor engines is to classify them between pusher and tractor architectures (Fig. 3.1). The literature survey of chapter 2

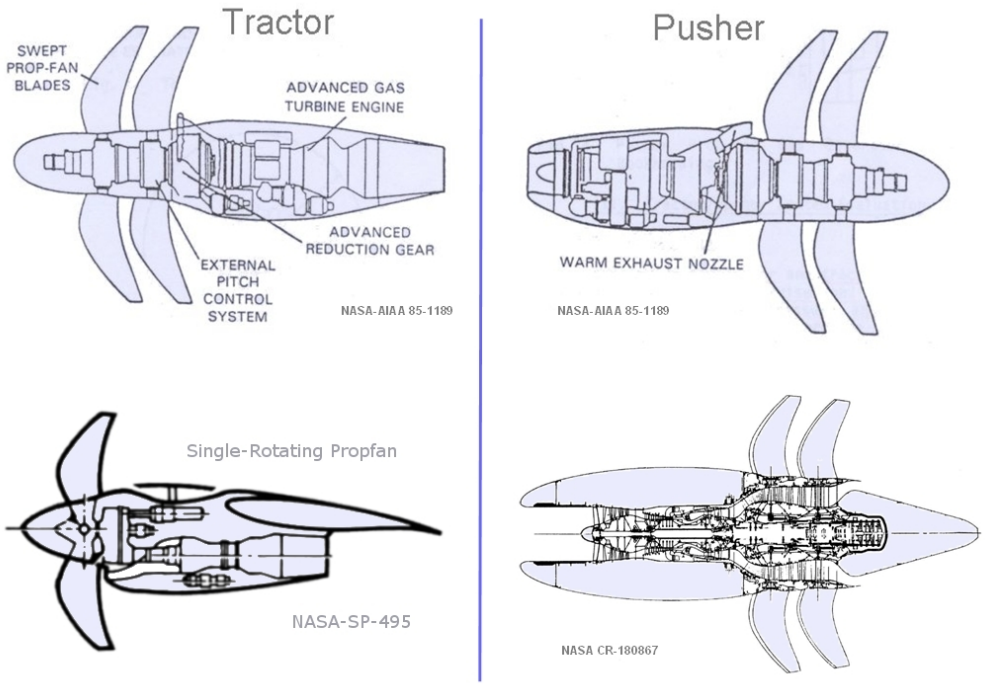

Fig. 3.1. Examples of tractor and pusher propfan architectures (source: reported near each engine in 'name-number' format).

showed how the scarce analysis available in propfan nacelle design mainly regards the tractor architecture, such as the investigations on the propeller-nacelle aerodynamic performance prediction ([55] and [64]) and the installation aerodynamics at subsonic speed [45], or the studies accomplished for the design of inlets in single-rotation tractor configuration ([91], [92], and [93]; examples of intakes are shown

in Fig. 2.1).

In the case of propfans adopting the pusher architecture, no fundamental works within the literature have been identified such as the basic definition of a theoretical, computational and/or experimental method for nacelle shaping. This is a serious shortage of information, especially considering the issues related to the aerodynamic interaction of the cowl with the rotor-root region. By adopting an appropriate nacelle shape, the achievement of a diffusion effect just in front of the hub is of paramount importance. Due to the high aerodynamic and mechanical loads acting on the open rotor stages, the root of each blade has to be kept thick enough to guarantee the structural robustness of the rotor itself. Given the relatively high cruise speed at which the new open-rotors are expected to operate (Mach 0.8), the airflow passing between the 'thick' blade roots may easily become transonic and even supersonic. This results in aerodynamic losses as well as possible mechanical excitation, phenomena which have to be avoided or at least limited by designing appropriate nacelle profiles.

As suggested by previous considerations, the tractor solution and the problems related to the rotor design of both the architectures have been examined in literature more widely, probably because the tractor propfan presented more similarities with the turboprop and seemed its natural successor. Although it is evident that also pusher propfan prototypes, which have been tested in the past, were equipped with a nacelle, from the published literature it is not possible to retrieve the design methods adopted by the engineers who pioneered this technology. Consequently, it might be inferred that the methods used were probably an adaptation of the turbofan nacelle design methods, but there is not any direct proof in the public domain supporting this theory.

Nowadays, given the possibility to install rear-mounted engines favoring cabin-noise reduction while keeping the aircraft with an uncluttered wing, both airframe and aero-engine manufacturers are showing a renewed interest in the pusher layout

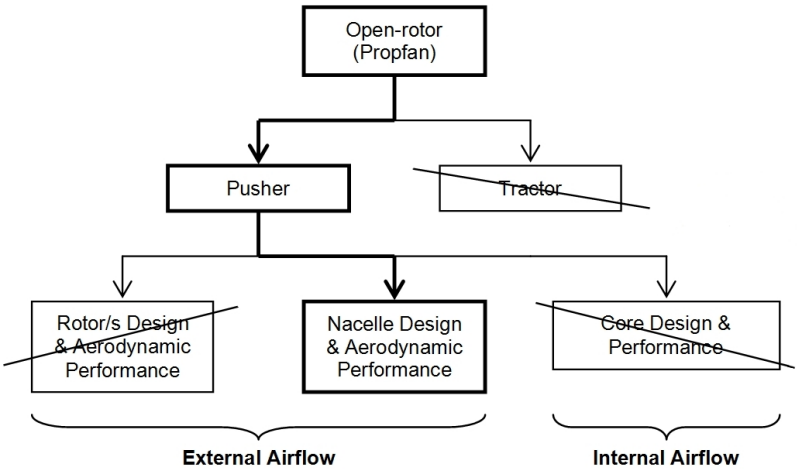

Fig. 3.2. Selection of engine architecture.

[62], which therefore will be studied in this work. Hence, as highlighted by Fig. 3.2, the aim of the present research is intentionally tailored to the basic definition of theoretical, computational and/or experimental methods providing the guidelines for pusher open-rotor nacelle shaping.

3.1.2. Selection of the open-rotor configuration

Once selected the pusher architecture, the open-rotor nacelle can be divided into three main components: forebody, rotor zone and afterbody. While for the tractor architecture the rotor can be single rotating or contra-rotating, for the pusher architecture, which is better suited to swirl-recovery, only contra-rotating blades have been usually adopted in the past. Although present, the afterbody, which is aerodynamically affected by the rotor wake and the exhaust gas interaction, does not represent the main part of the nacelle, which is constituted by the forebody. Therefore the present research is concentrated especially on the forebody design.

As remarked in Fig. 3.3, the whole forebody is composed of two main components: the intake and the external cowl. The former may be a pitot intake or an alternative intake (annular, chin or bifurcated, similarly to inlets for tractor engines); the latter can be divided into two main zones: fore-cowl and aft-cowl, the maximum-diameter point being the junction of these two profile elements. The

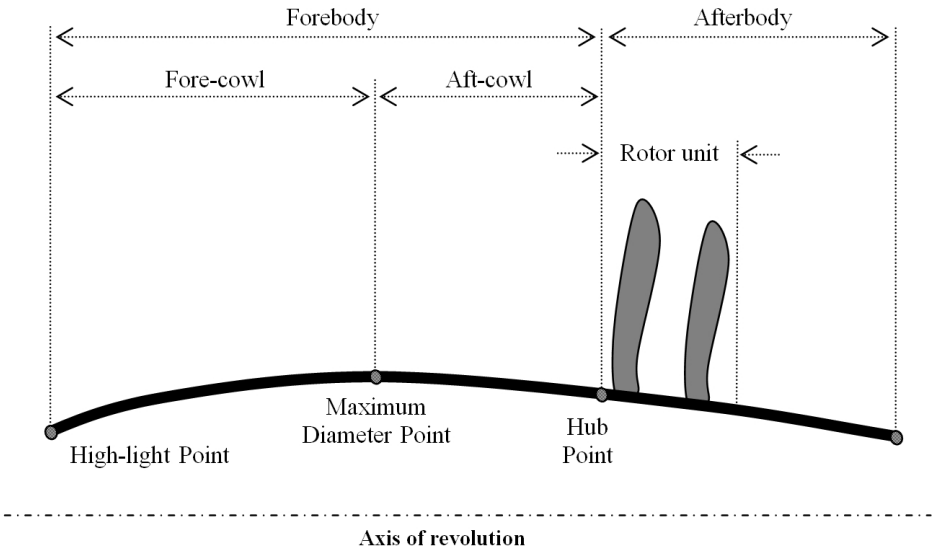

Fig. 3.3. Designation of open-rotor sections for pusher architecture without impinged exhaust system.

aerodynamic characteristics of the fore-cowl are affected by the intake configuration and, together with the aft-cowl, by the pylon interaction, as illustrated in Fig. 3.4. Concerning the inlet, Fig. 1.9 and 1.10 demonstrate how in the past the pitot intake was already adopted for pusher propfan, even if the existing configuration could be reassessed[1]. The research thus takes into account the influence of this kind of inlet on the external airflow. Besides, every nacelle is structurally connected to the airframe of the aircraft with at least one pylon: its presence inevitably influences the airflow behind it and consequently the performance of any open rotor operating within its wake. However, with the purpose to concentrate the efforts purely on the shape analysis of the external cowl, the present study can consider the isolated nacelle only[2]. As regards the aft-cowl in the isolated nacelle case, its design affects the airflow entering the rotors, especially at the root of the blades, although ignoring the presence of a pylon for the engine installation on the airframe. The quality of the external airflow (in terms of speed, boundary layer and turbulence) may have a big impact on the rotor efficiency[3], thus conditioning the

[1] As suggested in section 8.2.3.

[2] However, as reported in chapter 7, some preliminary investigations on pylon integration are available.

[3] Even for a contra-rotating propfan, these considerations are particularly valid and referred to

Fig. 3.4. The UDF engine mounted on its ground test rig (source: `http://www.cjdby.net`, June 2008).

performance of the whole engine. As shown by the pusher engines of Fig. 3.1, the configuration of the aft-cowl[4] is determined by the exhaust system, which might be impinged delivering the gas just in front of the rotor blades, or not impinged, passing through a power turbine and discharging the gas through an exhaust nozzle (consisting in the nacelle afterbody).

Targeting the interest of various manufacturers, who are currently considering a preliminary 'direct drive' layout of the pusher open-rotor without exhaust gas through the external blades [48], the present study focuses on the aerodynamic issues related to the nacelle shape with no exhaust impingement on the rotor blades, with the objective of better understanding the aerodynamic interaction of the external-cowl with the rotor-root region.

3.1.3. Choice of the reference model

Since the GE-36 engine tested by NASA [11] is the only existing propfan with pusher architecture and without exhaust impingement through the rotor, it is use-

the first row of blades.

[4] A clear schematic example is also given in ref. [18].

ful to start the investigations considering a reference model (herein called REMO) having a similar shape. A reference model is needed because it offers the opportunity to recreate an engine that already flew, whose features can provide terms of comparison on the results obtained from the present research. Moreover, based on the analysis of a reference nacelle, it is possible to study how to refine the preliminary method and how to improve the existing nacelle aerodynamics. As regards the UDF program, the following considerations arise from the literature survey:

- UDF Nacelle Aerodynamic Design: in the UDF Design Report [11], paragraph 5.1.1, it is stated that "[...] the F404 UDF inlet was designed as an isolated nacelle with minimal spillage drag down to zero inlet mass-flow-ratio and a cruise drag rise above Mach $\sim$ 0.8. Avoidance of spillage drag was a top priority consideration to provide the lowest possible flow field distortion to the unducted fan at all engine power settings. Similarly, the inlet lip was designed to operate free of external lip separation at incidence angles well beyond the expected 10° maximum flight test engine incidence angle. A generous internal lip contraction ratio was selected for low core intake total pressure distortion at all anticipated flight conditions. [...] The large projected inlet area[5] [...] of the core engine was well beyond normal turbofan high speed inlet design experience, a major reason for the unusual appearance of the UDF inlet. Airflow demand characteristics of the F404 core permitted much smaller inlet thrust and highlight radii than were selected for the demo UDF design. While reducing these dimensions is desirable for a number of reasons, it was found that large increases in forebody length would be required to effectively thin the external forebody and provide the desired high speed drag rise characteristics. The final forebody design provides sufficient length for inlet acoustic treatment requirements while maintaining a balance between high speed and low speed inlet performance characteristics.

[5] Identified as the ratio between the maximum cowl diameter and the nacelle internal diameter, measured in front of the compressor stage.

A longer inlet would have added unnecessary weight, drag, and would have made installation more difficult".

The statements above clearly suggest that the forebody of the UDF nacelle is similar but not equal to a turbofan nacelle: adopting a pitot intake implies a higher external projected area. Furthermore, some minor refinement were done for spillage reasons and to best adapt the nacelle to the F404 gas generator. Spillage is an area of concern especially for intake selection and consequently forebody shaping. It is interesting to note that previous configurations were designed mainly to avoid spillage. Alternative intake configurations to a straight pitot will be more difficult to design without spillage.

- Fan aerodynamic design procedure: in the UDF Design Report [11], paragraph 5.2.1 and paragraph 5.2.2, it is stated respectively that "[...] The aerodynamic design of the F7-A7 blades includes the nacelle forebody and the nozzle aftbody flowpaths in the axisymmetric flow calculations", and "[...] The flow calculation models the nacelle and nozzle flowpaths and the circumferential average flowpath through the blade hub region".

It is evident that the studies on the blades and the rotor design were conducted assuming the nacelle shape as given and known in advance. This is also implied in the design procedure for the UDF open rotor clearly described in ref. [140]. The same can be inferred by the studies conducted later in ref. [147].

- UDF installation problem: in the UDF Design Report [11], paragraph 5.1.3, it is stated that "[...] The F404 UDF nacelle design was completed prior to an independent design of the flight and ground test support pylon by The Boeing Company, which has claimed responsibility for aerodynamic integration of the F404/UDF with the pylon and the B727 aircraft. Boeing transonic wind tunnel (BTWT) testing of the UDF flow-through nacelle model on the B727 has been conducted to optimize engine placement, investigate drag

> trends, and measure wing and pylon wake characteristics. Installed UDF nacelle/pylon drag levels reportedly followed anticipated trends up to Mach = 0.7, beyond which drag divergence was encountered. This is thought to result from body-to-body interference as the pylon and nacelle should produce subcritical flow fields on an isolated basis. For a production engine, this problem would be addressed by nacelle area ruling, re-contouring the nacelle, or thinning/lengthening the support pylon [...]".

This paragraph underlines that there was a need for area ruling the nacelle and re-contour it, in this case due to the pylon interaction, but this work was not done, since the engine was never produced for commercial purposes but only for the test flights. Area ruling comments are very important as high drag would limit the achievable flight envelope of any flight configuration. Furthermore, information was found also regarding the backward influence of the rotor on the forebody: accordingly to the study done in ref. [119], there is a small influence of the rotor on the incoming airflow. When the experimental tests were run on a UDF scaled model, results showed that the tangential and radial velocity changes were negligible, but the axial velocity seemed to be affected, even if the effect had not a very big magnitude[6]. These comments on axial velocity imply that there is a need to account an additional increase of airspeed when calculating the forebody drag. It is unknown yet how big is the velocity change and how far forward it does occur in a full scale model. In addition, this inflow suction ahead of the rotor should reduce the adverse pressure gradient over the rear of the cowl, thus tending to prevent possible boundary layer separation.

Given the nacelle design context for pusher propfans, all these considerations, and the last one in particular, remark an existing gap in the scientific knowledge. At this point, it is worthy to notice that, although conceived as a refinement of the existing propfan technology, a new open-rotor engine is still an innovative device

[6]Page 8 and 9 of ref. [119], paragraph title: "Measured Flow Field Upstream of the Front Rotor".

whose evolving technological maturity has to be properly assessed. Considering the Technology Readiness Level (TRL) definition of NASA[7], the present research could be collocated into a TRL 3, that is the "Analytical and experimental critical function and/or characteristic proof of concept" for the new engine. In fact, the context of this work is the preliminary evaluation phase, preceding the engine technological development, intended to identify new methods for open-rotor nacelle shaping. Despite all aspects highlighted above, the 'proof of concept' of the new open-rotors has to inevitably account for the interaction effects between the external cowl of the nacelle and the rotor stages. In order to discover the characteristics of these effects while developing new design methodologies, the research was developed following the process described in the following section.

3.2. The research process

The DEMONS project can be organised with a traditional phased approach. Hence, its activities were initially arranged by identifying a sequence of three main steps to be completed:

- Phase I: project initiation and planning stage (May 2007 - January 2008).
- Phase II: project execution stage (February 2008 - December 2009).
- Phase III: project completion stage (January 2010 - May 2010).

The expression 'research process' identifies the executive plan of the project: it has to define the contents of the Phase II, clarifying their logical interconnection. This stage, representing the achievement of the second objective of DEMONS, is essential for arranging the work, thus allowing its practical development. Two are the fundamental elements that give a structure to the research process, and they consist in

[7] See ref. [100].

- determining the design parameters for the considered engine configuration
- monitoring the external airflow behaviour with respect to the variation of the chosen design parameters.

Of the two points, the first has essentially a theoretical basis, and might be accomplished graphically or analytically. The design of the nacelle shape can be initially obtained using a specific commercial Computer Aided Geometric Design (CAGD) software, such as CATIA®v5, and eventually refined with a further work dedicated to define the nacelle profiles mathematically. The second point is based on a flow-field investigation, which may consist of two elements:

- *visualisation of the airflow investing the nacelle* for different settings of the design parameters and flight conditions: e.g. shock-wave formation monitoring, flow separation and boundary layer characteristics with or without rotor interaction;
- *estimation of nacelle drag*: given the wide amount of aspects involved, this field of investigation can be considered as connected to the present research but independent from it.

By using modern engineering techniques, there are two different ways to expand these last sub-elements, by proceeding with a computational approach or an experimental approach. The computational development of the project offers a qualitative prediction in terms of airflow visualisation, and a qualitative (potentially even quantitative) prediction as regards the calculation of the integral parameters such as drag. The experimental approach, with the employment of apposite instrumentation[8], is able to give a quantitative description in both cases. What clearly emerges from these observations is that both strategies are useful for the development phase of the research programme, although hardly feasible simultaneously,

[8]For instance the Particle Image Velocimetry (PIV) or the Laser Doppler Velocimetry (LDV) as regards the visualisation task.

especially if done by the doctoral candidate alone. A rough trade-off between the two approaches is based on the determination of their pros and cons: the computational approach is only predictive, but it would involve lower management costs. This approach is very useful with the purpose to execute a preliminary aerodynamic assessment of the nacelle designed with the new procedures, and it offers the possibility to run a first sensitivity analysis on the parameters governing the nacelle shape. Anyway, the results collected need to be validated by experiments. Moreover, drag computation is still a field of research[9] and there is work in progress in order to obtain more reliable predictive codes. However, there are not guidelines in literature to reasonably coordinate the assembling of an experimental rig dedicated to this problem.

These considerations suggest that for a new project such as DEMONS, based on a research area that officially is mostly unexplored, it is better to undertake a computational approach, rather than collecting experimental data, difficult to interpret once obtained without a rigorous criterion. This is one of the reasons why at this stage the project will proceed only through a computational development. Another justification for this choice is that the modern computational capabilities (both hardware and software) have drastically increased during the last two decades. Therefore, after a period of more than twenty years (very long for the computer science) it is also interesting to completely reassess the propfan technology, which was born and developed with old CFD methods and very primitive[10] hardware. Given the limited amount of time available and the complexity of the topic, the computational approach shall be mainly concentrated on the assessment of the aerodynamic characteristics of the airflow all over the forebody, eventually including some drag computations, but neither investigating nor developing any drag prediction technique. The commercial software chosen to run the

[9] As testified by the recent CFD Drag Prediction Workshop events organised by the American Institute of Aeronautics and Astronautics (AIAA).

[10] Obsolete if compared to the operational capabilities of the modern personal computer and their ever faster processors.

CFD calculations is the Gambit-Fluent® platform.

The research process is then developed throughout three main steps:

1. Definition of a preliminary design method based on the open-rotor reference model

2. Evaluation of an innovative design methodology able to keep the benefits and overcome the limits presented by the preliminary design method defined at step 1

3. Use of the achievements obtained at step 2 for designing a new open-rotor nacelle, able to overcome the nacelle aerodynamic limits eventually emerging at step 1.

Next chapters represent an embodiment of the research process outlined within this section. More in details, Fig. 3.5 suggests the logical interconnection among the contents of chapter 4, 5 and 6.

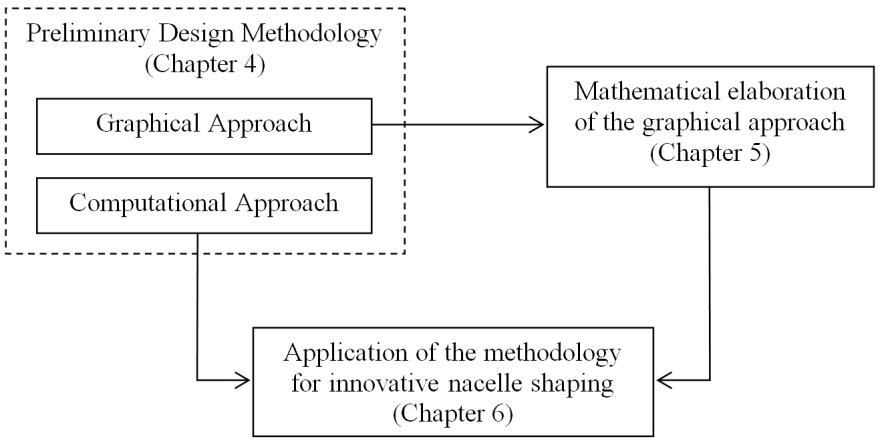

Fig. 3.5. The research process.

4. THE PRELIMINARY DESIGN METHODOLOGY

Before any new design method can be achieved, it is convenient to select and design an existing pusher propfan nacelle, so that it might become a reference model, or REMO. Given the project strategy presented in chapter 3, the reference model chosen is the GE-36, also known as UDF. The REMO can be used not only to develop new design methods, but also to provide a starting example of analysis with CFD simulations. In fact, a first interpretation of the aerodynamic characteristics of its nacelle is essential to better understand how the preliminary design method can be adapted, aiming to improve the design features of the cowl profile itself.

Therefore, in accordance with the research process defined in section 3.2, the preliminary design methodology can be composed by two complementary parts, covering the graphical and computational aspects of the methodology. For this reason, the following two sections are named *Graphical approach* and *Computational apporach* respectively. It is worthy to mention that, despite their titles, in both sections appear theoretical elements. However, these titles have a different purpose: 'graphical approach' refers to the development of the design method for obtaining the nacelle shape, 'computational approach' refers instead to the development of the techniques for properly simulating the REMO engine and the aerodynamic behaviour of its nacelle, once it is designed with said method.

4.1. Graphical approach

The studies related to the graphical design of a pusher open-rotor nacelle are collected within this section. After an overview of the approximate methods for graphically recreating an existing nacelle, an explanation of the importance of geometric continuity in curve shaping is provided. Then it follows the description of a first procedure to opportunely determine forebody profiles with pitot intakes. With this procedure it is possible to recreate a nacelle profile for the REMO engine that is matching the original UDF shape.

4.1.1. Approximative methods

The nacelle of the REMO engine is based on the GE-36 nacelle. One way to rapidly recreate a model of the UDF shape is to import a scaled image of its lateral profile into CATIA®v5. This is feasible, for instance, using **Scan2CADv7**, a shareware software able to read a scanned image and convert it into a `*.*dxf` file, which is a file format supported by CATIA®v5. The UDF cross section, already shown in the previous chapters[1], is available in the design report[2] of the GE-36: here it is illustrated in the centre of Fig. 4.1. The original image was converted from a `*.*pdf` file into a rastered image (a `*.*bmp` file), after being processed in **Gimp**[3]. Then it was imported into **Scan2CADv7**, which allows the designer to create a `*.*dxf` version of it, importable into CATIA®v5, as shown in Fig. 4.1: the white lines refer to the vectorisation resulting from the rastered image. The `*.*dxf` file has been loaded into CATIA®v5 and scaled taking the known[4] and fixed length of the rotor tip, R_{tip}, as a reference to determine the correct scaling factor.

Although the procedure described above is fast, it is far from being precise: the profile appears to be a set of segments rather than smoothed lines. However, these

[1] See Fig. 1.10 and 3.1.
[2] The only documentation available regarding its nacelle shape is reported in ref. [11].
[3] Gimp is an opensource software for image visualisation and modelling.
[4] From ref. [11].

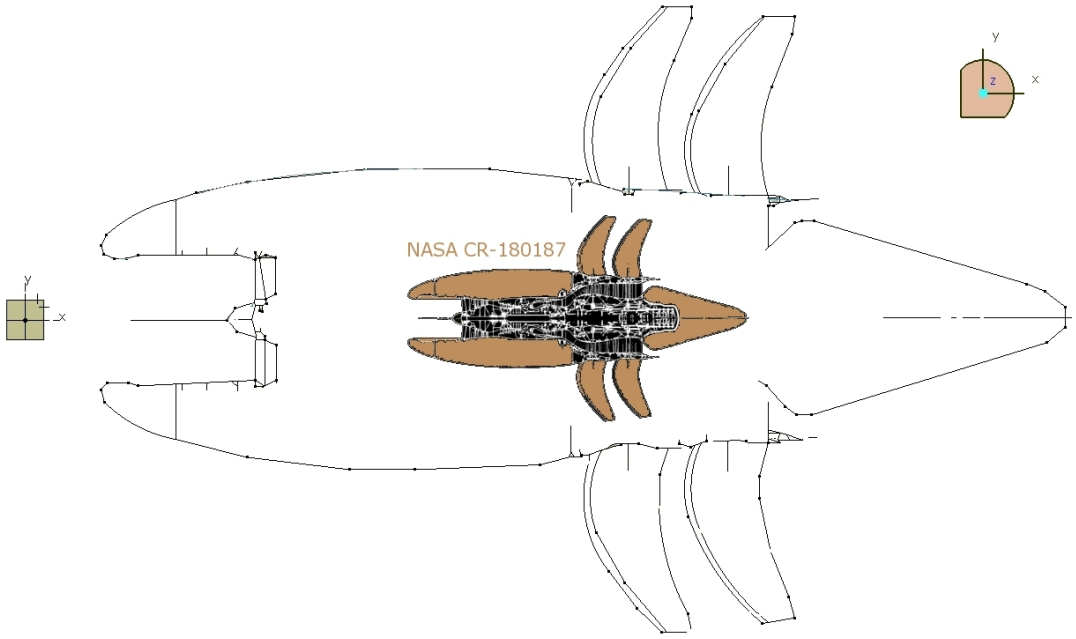

Fig. 4.1. Rastered and vectorised images of the UDF.

segments are useful anyway, since they unveil the true proportions of the whole model. Moreover, they also reproduce the rotor zone and the nozzle, thus providing direct information on these parts of the engine.

In order to achieve further information about the real profile of the UDF forebody, one possibility is to import a set of its contour points into CATIA®v5. The coordinates of these points can be captured manually from a digitalised image of the UDF shape, such as the one depicted in the centre of Fig. 4.1. The tool used for accomplishing this task is the free software **Qplot**. The correct proportion of the engine cowl is granted by setting the opportune length units on the reference axes of the **Qplot** working environment, in accordance with the original measures reported in ref. [11].

This 'points-capture' method is not providing the precise stations of the UDF forebody, although it offers the opportunity to better perceive the geometrical characteristics of its real profile (Fig. 4.2). Even if it is possible to generate an interpolation line (or spline) in CATIA®v5 for connecting all these points with a unique line, nonetheless the result would be not satisfactory for many reasons.

Fig. 4.2. Points defining the UDF forebody.

First of all, the coordinates of the points are close to the original profile, but not necessarily belonging to it. Secondly, since the points are captured manually, it is inevitable to introduce positional errors that would affect the quality of the interpolation line in terms of curvature changes: due to the misplacement of the points, its shape could locally present unrealistic convex to concave and concave to convex trends, varying casually all over the cowl length.

In any case, even supposing that the reference cowl is ideally recreated without introducing errors, still these procedures are only useful for obtaining a graphical indication of its original shape, nothing more. Unfortunately, it is not possible to infer how the profile was made from scratch. As already mentioned in the previous chapters, the design procedure of the UDF original nacelle is not known from the public domain, and neither are the exact geometric coordinates of its profile curves. For this reason, the REMO is not intended to be a perfect replica of the UDF, but an open-rotor with a similar shape, which can be achieved by graphical methods and recreated using the commercial suite CATIA®v5.

The next step then consists of defining a graphical procedure to design the REMO shape. Before doing so, however, it is worthy to mention a few considerations on the intrinsic quality of the geometry that said procedure should provide as an output. More in details, the comments made on the approximate methods pre-

sented above show how it is not easy to interpolate a given set of points maintaining an appropriate shape, nor properly rectify the segments of a vectorised model to obtain a smooth profile. This problem is related to the geometric continuity of the shape, which defines its smoothness as well.

4.1.2. Notions about geometric continuity

When performing computer aided design, the designer typically expects an intuitive technique for creating free form geometric objects. This kind of objects can be obtained by activating a process that generates the geometric object in conformity with the constraining subparts provided by the designer. Therefore the designer has to specify in advance the necessary and/or prominent subparts of the geometric object itself through which said object is constrained to pass. More in details, such subparts may be higher dimensional geometric objects, surfaces, curves/lines and/or points. For instance, a designer may define and position a plurality of points through which a desired curve must pass, as will be described in paragraph 4.1.3. Said curve is often required to be free form while keeping geometric characteristics (such as differentiability and curvature) typically referred to as 'fair' or 'smooth'.

There are existing guidelines[5] in use for CAGD when designing lines and surfaces, which describe in mathematical terms the quality of the curve (to which the adjectives 'fair' or 'smooth' usually refer) from a geometrical point of view. Said quality is commonly addressed as the 'geometric continuity' of parametric curves and surfaces, which is a widely researched topic[6] in CAGD. Parametric splines are generally used in CAGD, and consist of piecewise functions where each of the segments is a parametric function. The equations governing the way these segments join together are called continuity constraints, and they are chosen to assign a given order of 'smoothness' to the spline. The first degrees of geometric continuity

[5]For instance see ref. [31] and [32].

[6]The formal definitions, the basic notions and many useful literature links on this topic are provided in ref. [31] and [149].

can be intuitively described as follows:

- $G0$: 'connection' constraint along the curve
- $G1$: 'tangency' constraint between any joining points of the curve
- $G2$: 'curvature' constraint over the curve
- $G3$: 'rate of change of curvature' constraint between any joining parts of the curve.

Clearly, all lines can be divided into an arbitrary number of segments and the levels of continuity apply at any junction between segments. If a curve is compliant at a higher G number then it is compliant at a lower G (i.e. a $G3$ compliant curve is $G2$, $G1$ and $G0$ compliant).

These concepts represent a fundamental feature in automotive design. In fact, the importance of imparting different levels of geometric continuity at the junction between curves depends on the field of application. For instance, whilst position continuity is a sufficient condition in architectural drawing, other applications require higher order of smoothness. Such is the case for aerospace design, where tangency and curvature constraints usually apply to practical problems. In fact, due to aerodynamic reasons, when an object is shaped with smooth profiles the energy losses of the air flowing all over its body can be reduced. This is particularly true at high flight speed. In transonic regime, for example, any profile discontinuity might favour the formation of localised supersonic flow regions, called 'sonic bubbles', which contribute to drag rise and negatively influence an airflow distortion.

This negative behaviour can usually be discouraged by imposing to the aerodynamic shape a high order of geometric continuity. In fact, for all bodies moving through the air in the transonic regime, high orders of geometric continuity decrease the tendency to form sonic bubbles on the body surface, especially at locations situ-

ated far from a stagnation point. The flow slows down in proximity of a stagnation point, so that $G1$ or even $G0$ constraints might be tolerable on that zone.

Consequently, in order to provide good aerodynamic characteristics not only for the flow-path of the forebody, but also for the airflow entering the open rotor stages, the determination of a criterion granting $G3$ continuity away from stagnation points should be a necessary condition for correctly designing the nacelle of a pusher open-rotor flying fast up to Mach 0.8 cruise speeds. However, this is not a sufficient condition: other issues emerge whenever the curvature of the profile varies rapidly, regardless of its geometric continuity level. It is worthy to remember that the curvature can be intuitively defined[7] as the amount by which a line deviates from being straight[8]. High speed airflows generally tend to separate or accelerate rapidly when encountering zones of sharp curvature variations, depending on the situation. Both the events are unwanted, because they represent a source of energy losses. For this reason, even if the shape has $G3$ continuity, its curvature profile should not

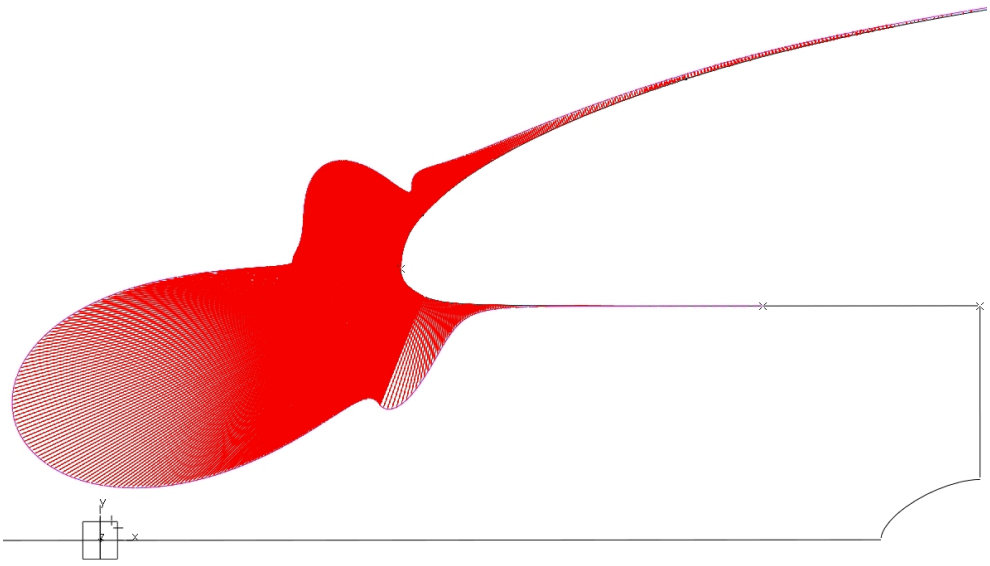

Fig. 4.3. Intake presenting bad $G3$ continuity features.

present marked oscillations which can cause flow distortions at high flight speeds.

[7] The curvature is defined in different ways depending on the context of analysis. The concept of curvature is better deepened in section 5.3.

[8] Or flat, in the case of a geometric object.

For instance, Fig. 4.3 illustrates an example of pitot intake whose lip presents $G3$ characteristics but strong curvature oscillations. After the flow impacts the stagnation point, wich is not far from the highlight if the engine is flying at zero incidence, the air follows the intake shape by rapidly accelerating away from the stagnation point itself. When doing so, every time the airflow reaches a profile part with strong changes in curvature (like those situated in the regions of oscillating curvature) it might inevitably results in localised supersonic flow.

All these notions are indispensable and must be taken into account during the definition of a design method, and also for the procedure presented in the next paragraph.

4.1.3. Graphical design procedure

The design of a new nacelle starts from knowing the basic dimensions of the engine core: D_c, L_{c-hub} and D_{hub}. Since the cycle analysis of the core performance is evaluated before the realisation of the nacelle itself, these lengths are usually available. The nacelle design process ends with an output shape formed by curves, thus another aspect to consider is the quality of the profile obtained from the design procedure in terms of geometric continuity. The goal of the design procedure presented in this paragraph is to create a $G3$ nacelle for a pusher open-rotor with pitot intake using a commercial software, such as CATIA®v5: hence it is named 'graphical design procedure'.

An efficient way adopted in this work to simplify the procedure since the beginning is to consider 2D profiles only. After all, without losing in generality, a nacelle can be considered as a body of revolution, having a well defined 2D profile at each azimuthal position (with the engine axis corresponding to the axis of revolution, around which the azimuth angle is considered to vary).

Potentially there are several ways to parameterise a nacelle profile and to design it. The procedure proposed herein is a new example, and it is based on a set of con-

struction points, control conics and connection curves. The control conics basically are circles which, together with tangency support lines, are used to impose a given value to the curvature constraints; these constraints are introduced in concomitance with the construction points. The connection curves, which are parametric and may be splines or conics, form the wireframe of the nacelle cowling. This procedure is developed considering that the forebody has to be freely configurable and modifiable using a set of parametric relations. The parameters involved within these relations must be easily changeable, in order to obtain advanced configurations and/or adapt the nacelle profile accordingly not only to engine-core geometry, but also to the aerodynamic characteristics of the airflow over the cowl. The computational investigations shall provide a mean for understanding the quality of the aerodynamic performance of the profile generated with this graphical method.

The procedure to design a 2D profile of pusher open-rotor nacelle with pitot intake and $G3$ characteristics consists of the following steps.

1. The profile is generated within a CATIA®v5 part file of extension `*.*CADpart`. There are two axis systems: an absolute axis system and a relative axis system, which is governing the orientation of the 2D nacelle in the 3D space. The engine consists of a set of open bodies:

   - **Start** - All the constitutive elements (mentioned in the following bullets) forming the engine are spatially referred to the position of a single point called 'Pivot' and its orientation in the 3D space, which is fixed with the relative axis system.

   - **Compressor_Face** - This open body is constituted by a point defining the upper limit of the compressor, and a straight line connecting this point to the Pivot.

   - **Rotor_Zone** - This open body reproduces the zone of the engine where the open rotors are expected to operate. A very important element belonging to this open body is the 'Hub' point, delimiting the separation

between the nacelle forebody and the afterbody.

- **Centre_Body** - This open body is made up with two points and a conic curve able to recreate a centre body.
- **3C_Profile** - This open body comprehends both the internal and external profile of the nacelle, which are represented by two secondary open bodies. The prefix '3C' stands for 'triple C', because each profile part is generated by the following three layers of elements: Construction points, Control conics, Connection curves.
  - **External_Profile** - As regards the external profile, the construction points are two: the 'Highlight' point and the 'Crest' point, which is the maximum radius point. The control conics are two circumferences tangent to these construction points, used to impose curvature constraints to the forebody shape. The direction of tangency at the 'Hub' point is decided by a straight line adopted to build the control circle at this point. The connection curves are two splines: the first links the 'Highlight' and 'Crest' points, the second links the 'Crest' and 'Hub' points. These two splines are automatically generated imposing *horizontal tangency* and *curvature continuity* constraints at the 'Crest' point, while their curvature at 'Highlight' and 'Hub' points is imposed to be equal to the curvature of the respective control conics.
  - **Internal_Profile** - As regards the internal profile, the construction points are two: the 'Throat' point, that is the minimum radius point within the intake, and the 'Lip' point, which is an intermediate point located between the 'Highlight' and the 'Throat' points (in turbofans, lip and throat might coincide). The control conics are two circumferences tangent to the 'Highlight' and 'Throat' points[9],

[9]This is the second circumference tangent to the 'Highlight' point, and it can differ from the

and used to impose curvature constraints to the inlet shape. The connection curves are two splines and a conic; the first spline connects the 'Highlight' and 'Lip' points, the second spline connects the 'Throat' and 'Compressor' points, whilst the conic connects the 'Lip' and 'Throat' points. The two splines are automatically generated imposing *tangency continuity* and *curvature continuity* constraints at the 'Highlight, 'Lip', 'Throat' and 'Compressor' points. Vertical tangency is imposed at the 'Highlight' point, horizontal tangency is imposed at 'Throat' and 'Compressor' points. The curvature of the two splines is imposed to be the same of the respective control circle at 'Highlight', and null to the 'Compressor' point. The tangency and curvature at the 'Lip' point are imposed by the conic connecting the 'Lip' and 'Throat' points, which might be an ellipse, a parabola or an hyperbole. This connection curve is a conic and not a spline because it guarantees that the 'Throat' point be a real minimum radius point. In fact, using a spline for this purpose when recreating almost straight intakes (e.g. similar to the GE-36 inlet) could result in a line with a different minimum radius point.

2. Given the values of terms D_c, D_{hub} and L_{c-hub} (known once fixed the characteristics of the engine-core, see Fig. 4.4), the construction points are created using eight parametric relations:

   - Diffusion:

$$D_{th} = \frac{D_c}{a} \tag{4.1}$$

   - Internal diameter contraction:

$$D_{hl} = b \cdot D_{th} \tag{4.2}$$

one defined within the external profile.

- External cowl projected area:

$$D_{max} = \frac{D_{hl}}{c} \tag{4.3}$$

- External crest distance:

$$L_{hl-cr} = d \cdot D_{max} \tag{4.4}$$

- Throat distance from compressor:

$$L_{th} = e \cdot D_c \tag{4.5}$$

- Highlight to compressor distance:

$$L_{hl} = f \cdot D_c \tag{4.6}$$

- Lip diameter:

$$D_{lip} = g \cdot D_c \tag{4.7}$$

- Lip distance from compressor:

$$L_{lip} = h \cdot D_c \tag{4.8}$$

The eight coefficients a, b, c, d, e, f, g, and h are non-dimensional values, which govern the construction points of the nacelle. These parameters can be easily changed in order to obtain advanced configurations and/or adapt the forebody profile according to various engine-core dimensions and operative contexts. Equations from 4.1 to 4.8 form a linear system, in which the geometrical meaning of all the terms[10] is clarified by Fig. 4.4.

[10]The input length units are fixed to be millimetres into CATIA®v5 by default.

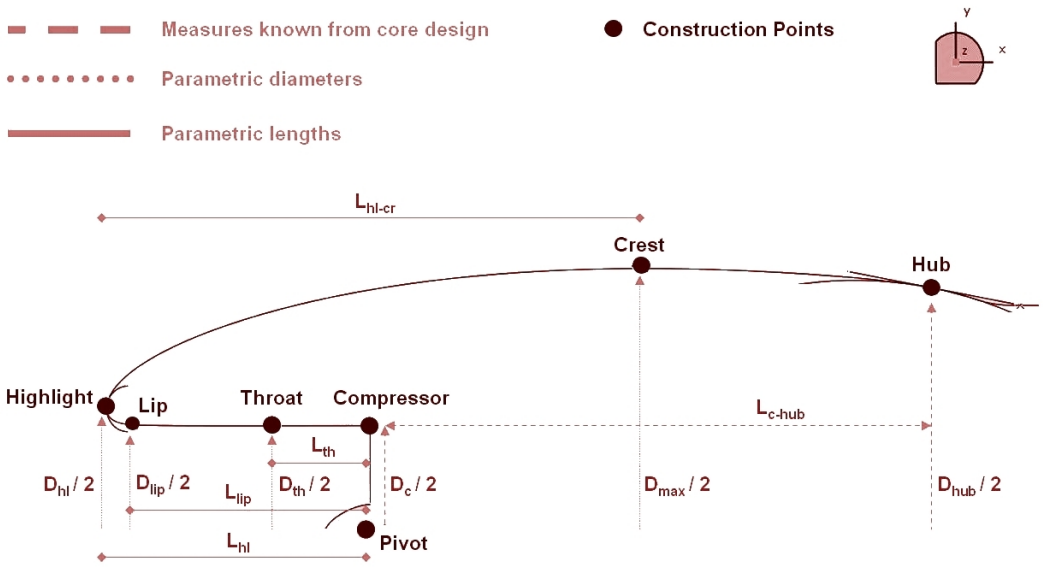

Fig. 4.4. Lengths used to define the construction points.

3. The tangency and curvature constraints of the control conics and connection curves are controlled with other non-dimensional parameters, whose values can be regulated directly by the designer in the curve settings of CATIA®v5.

The present procedure automatically offers a profile having $G2$ continuity. Another advantage of this procedure relies on the possibility to achieve an approximated $G3$ continuity, by manually adjusting the built-in parameters of the connection curves.

An example of application for the design procedure presented in this section is given by the REMO nacelle design, which is a reconstruction of the UDF forebody. The inlet design features and other useful parameters of the GE-36 nacelle, here proposed in Fig. 4.5, are given in the UDF design report. From this report emerged that the parameter L depicted in Fig. 4.5 was not defined, while the so called "Internal Lip Contraction Ratio" should be $D_{HL}/D_{TH} = 1.16$ and not $D_{HL} = 1.16$ as illustrated in the original figure of the UDF intake. The only length exactly reported is the tip diameter, corresponding to 11.67 ft, i.e. 3.557016 m, so that $R_{tip} = 3.557016/2 = 1.778508$ m. Since the hub to tip radius ratio is given ($R_{hub}/R_{tip} = 0.425$), then $R_{hub} = 755.866$ mm and, according to the notation adopted within this section, $D_{hub} = 2 \cdot 755.866 \sim 1608.426$ mm, which is the value

used in CATIA®v5 to best fit the scaled models presented in section 4.1.1. In

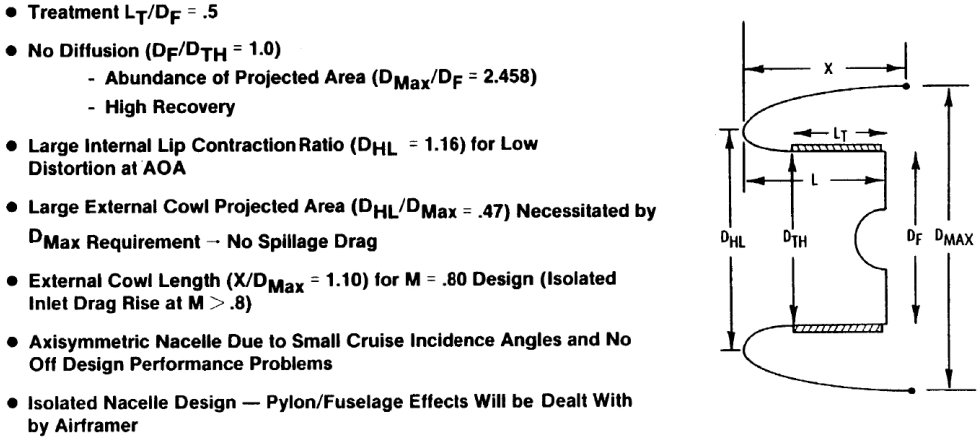

Fig. 4.5. Inlet design features of the UDF (source: ref. [11]).

Fig. 1.10 it is evident how the initial relation $L_T/D_F = 0.5$ was not maintained in the final shape, and the reason of this is described within the UDF design report [11] as follows: "[...] it was found that large increases in forebody length would be required to effectively thin the external forebody and provide the desired high speed drag rise characteristics. The final forebody design provides sufficient length for inlet acoustic treatment requirements while maintaining a balance between high speed and low speed inlet performance characteristics"; again from Fig. 1.10 it is clear how L_T is slightly superior to R_{hub}, confirming that the proposed relation $L_T/D_F = 0.5$ was not respected.

The term L_{c-hub} is set to be $L_{c-hub} = 1988.612\ mm$, so that the horizontal distance between the crest point and the hub is about one blade length[11] (in the present design it is fixed at 86% of the blade-tip radius, that in first approximation is $R_{tip} - R_{hub}$, that is a blade length). Moreover, from the original design it can be inferred that the compressor radius is about three times the difference $(R_{tip} - R_{hub})$, that is $D_c/2 \sim 0.35\ m$. By fixing the term D_c, all the elements of relations 4.5, 4.6, 4.7 and 4.8 are known once fixed the respective coefficients. By applying the

[11] Within the UDF design report of ref. [11], paragraph 5.2.1, it is stated: "[...] The forebody is shaped such that its maximum diameter is larger than the blade hub diameter and is located approximately one blade length upstream of the first rotor".

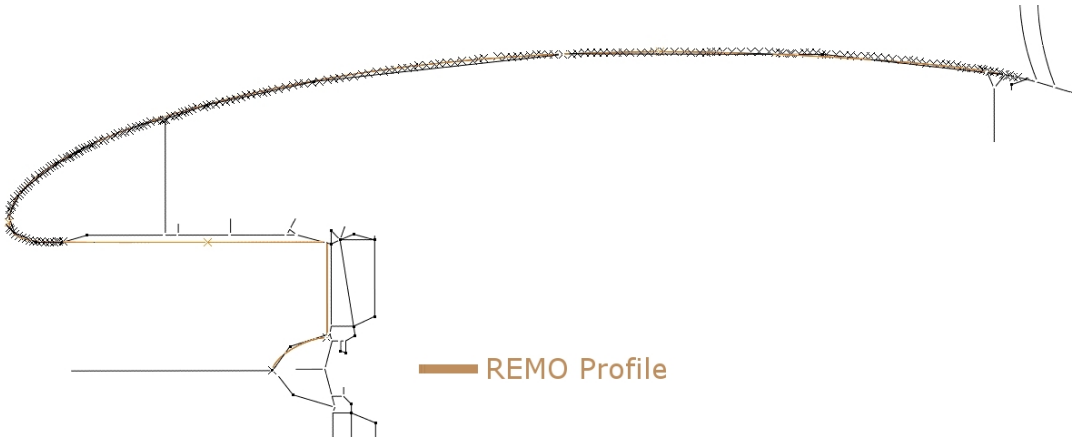

Fig. 4.6. UDF nacelle matching.

procedure presented in this section it is possible to match the original UDF shape. The values of the coefficients in equations from 4.1 to 4.8 used within the procedure to match the UDF nacelle are:

- $a = 1$
- $b = 1.16$
- $c = 0.468$
- $d = 1.1$
- $e = 0.5$
- $f = 1.33143$
- $g = 1.00857$
- $h = 1.19714$

As regards the spinner, its dimensions are obtained roughly comparing it to the radius of the compressor: the spinner length is slightly less than the half of compressor radius, while its height is about a quarter of compressor radius.

Figure 4.6 shows that the design procedure is able to match both the vectorised image and construction points of the UDF, although there is still a little margin of

error because it is impossible to know precisely the exact coordinates of its original shape: the segments and points of the GE-36 nacelle illustrated on the background are obtained from the approximative methods presented in section 4.1.1. Hence, although respecting the proportions, the REMO nacelle profile is not a faithful replica of the original UDF nacelle. With the graphical procedure presented in this section, it is also possible to generate a REMO profile with pitot intake that broadly matches the UDF shape keeping $G3$ continuity features, as shown in Fig. 4.7. The curvature obtained is completely continuous all over both the external

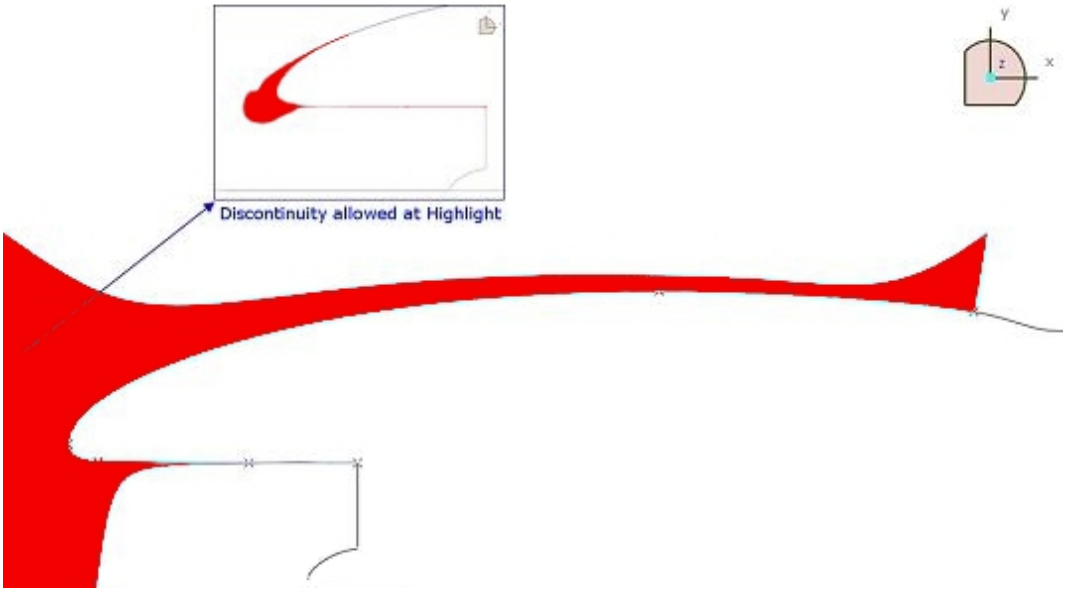

Fig. 4.7. Porcupine curvature analysis (in red) of the REMO forebody.

and internal forebody, except at the highlight where a discontinuity is admitted (Fig. 4.7). In normal flight conditions, the stagnation point is expected to be located in this vicinity. Hence the airflow impacting this area will be slow and the discontinuity in curvature between the external and internal part should not cause sonic bubble formation and propagation. This is true at cruise particularly, though the effects introduced by any curvature jump should be carefully assessed for different flight conditions, such as takeoff, climb and landing.

4.2. Computational approach

The computational evaluation of a nacelle design procedure relies on the development of numerical environments able to predict the aerodynamic characteristics of the nacelle profile when it is interacting with other parts of the engine. In the particular pusher open-rotor context, the availability of the REMO profile allows the designer to run CFD simulations using boundary conditions whose values are typical of the UDF operative scenarios, trying to achieve aerodynamic performance consistent with those of the UDF. Although this last information is available in literature [11], the few accessible experimental data on the UDF aerodynamic performance [119] are not sufficient for a complete validation of CFD simulations, but are sufficient to assess the REMO aerodynamic performance from a qualitative perspective. The flow-field investigations are developed computationally, making use of the Gambit-Fluent® software. Several aspects have to be considered and investigated to accomplish this task: the determination of the in-flight conditions of the engine, the modelling of the open rotors, and the implementation of appropriate tools for conducting a sensitivity analysis on the aerodynamics of the external airflow.

Before presenting the proposed solutions to these issues, which are described in the following paragraphs, it is opportune to highlight the importance of this matter by mentioning an example of simulation, which can be conducted as a preliminary investigation on these topics. At the very beginning of the research program, a first attempt was made to simulate a generic nacelle of an engine cruising at the same REMO conditions, but supposing that the characteristics of its thermodynamic cycle were widely unknown. This situation is not uncommon, especially while working at very low TRL phases, when the installation aerodynamicist probably just knows the compressor main characteristics. In this situation, the designer could try to simulate the engine without exhaust system, using a long axisymmetric support wall to replace the nozzle. A demonstrative two-dimensional

axisymmetric domain for this kind of CFD simulation is shown in Fig. 4.8. To keep the example as simple as possible, in this primitive analysis the rotor is not implemented in the model intentionally. It is evident from the illustration that the nozzle exhaust, which is not affecting the airflow on the forebody, is replaced by a solid of revolution[12]: the nacelle is simply closed gently with a support shape, created to accompany the airflow to the outflow boundary. The advantage of this

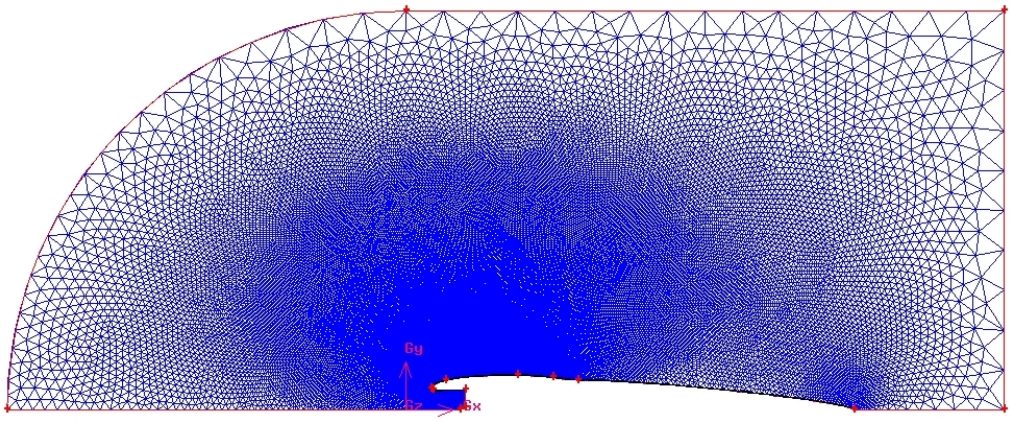

Fig. 4.8. Demonstrative simulation domain.

expedient is that a simulation can run even without knowing the performance of the whole engine at different in-flight operative points. The compressor is the only part where pressure, temperature and massflow values need to be calculated in order to introduce the right values in the appropriate boundary condition. These values, if the engine cycle is unknown, can always be determined at least approximately by hand[13]. Obviously, this is not an accurate and fast procedure, which might become tedious when different flight conditions have to be simulated several times. Another disadvantage of this method consists in introducing high turbulence levels along the support, especially when investigating flight conditions at high Mach numbers (transonic regime). This may excessively increase the time of simulation when using fine grids and more accurate viscous models, spending

[12] Although Fig. 4.8 presents a 2D domain, simulations can be done in axisymmetric conditions, considering the revolution of the 2D plane around the horizontal axis, which coincides with the bottom line of the domain.

[13] A reference compressor map is needed for accomplishing this task.

computational resources finding a solution over a wall zone which does not exist in reality. Another issue related to this fake support is that it might be difficult to run 3D simulations of the engine, in particular when it has to be analysed as installed on an aircraft model.

To overcome these problems, a model of the core-engine cycle has to be developed. The effort put in simulating the performance of the core engine is then payed back by a reduction of time in determining the physical parameters for the boundary conditions whenever they are needed at different operative conditions. Another advantage is that the exhaust system can be integrated in the model and simulated with the appropriate values, thus avoiding the problems related to the turbulent flow along the support wall. Moreover, the elimination of this fake support allows for using the model also in 3D simulations, without introducing any unreal disturbance in the flow-field, especially for the analysis of airframe-integration cases.

4.2.1. The cycle performance prediction

The definition of the boundary conditions within the CFD simulations is not a trivial task. Apart from the far-field and outflow conditions imposed by the altitude and the cruise Mach number, other boundary conditions such as the compressor face and the power turbine exit station cannot be easily determined unless a cycle model of the whole engine is available. In this work, the REMO thermodynamic

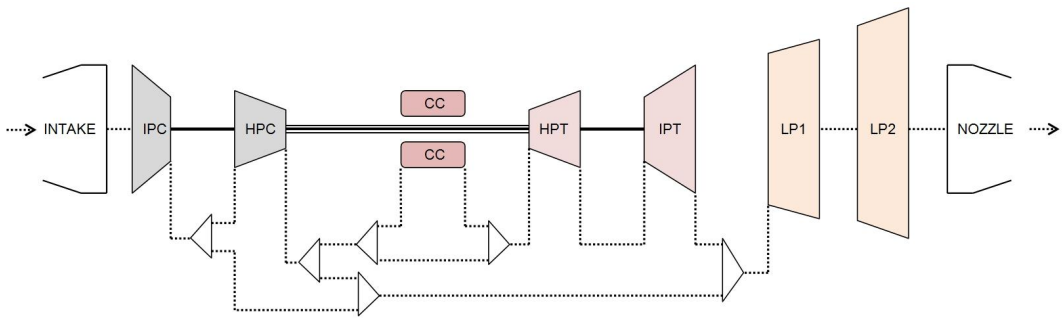

Fig. 4.9. Simplified UDF-cycle scheme.

cycle is reproduced in Turbomatch, the Cranfield University software which enables

performance calculation for an engine at design-point and off-design conditions. Being a UDF-like engine, the REMO cycle is based on the information retrievable in the open literature (ref. [11] and [124]). A simplified scheme of this cycle is depicted in Fig. 4.9, whilst the complete scheme[14] and the programming code used for the simulations are reported in appendix A. The Turbomatch model is based on the scheme of the original UDF, which was a combination of a modified F404 core engine and a power turbine unit driving the open rotors.

Table 4.1. Predictions of UDF-cycle performance (source: ref. [11] and [124]).

Design Point	SLS
FN $[lbf]$	25000 to 31111
FPW $[hp]$	14437 to 20000
TET $[°F]$	2369 to 2520
OPR	17.52

The main parameters used to define the model are presented in Table 4.1. Since several cycles and their modified versions were reported in the original UDF documentation for pre-test calculations, Table 4.1 provides ranges of values in which the cycle is expected to work. The cycle predictions are obtained starting from the design-point conditions at Sea Level Static (SLS) conditions, selecting a TET of $2472\,°F$. Considering that typical values for civil engines might be close to 0.9975, the inlet recovery factor is imposed to be $\varepsilon = 0.995$. A shaft power of 12895000 $W = 17292.48$ hp, which is a value within the range of fan power values shown in Table 4.1, is chosen for the power turbine unit in order to obtain a nozzle exit area of 0.5323 m^2, which is in good agreement with the area computed from the UDF model imported into CATIA®v5.

The main input parameters are provided in Table 4.2, while the main results

[14] See Fig. A.1.

Table 4.2. Turbomatch main input parameters at design-point (source: ref. [11] and [124]).

Parameters at SLS	Data from Literature	Input Data
$FPW\ [kW]$	10765.7 to 14914	12895
$TET\ [K]$	1571.5 to 1655.4	1628.7
$WCI\ [kg/s]$	57.153	57.153
ε	N.A.	0.995

of the design-point calculation are given in Table 4.3. The net thrust of the core at design-point is $12984N = 2919\ lbf$, which approximately corresponds to 10% of the mean value of the FN data reported in Table 4.1. The OPR matches the original value of 17.52.

Table 4.3. Turbomatch results at design-point.

Parameters at SLS	Data from Literature	Output Results
$ENT\ [N]$	N.A.	12984
OPR	17.52	17.52149
$A_{ex}\ [m^2]$	0.532*	0.5323
$V_{ex}\ [m/s]$	N.A.	229.4

* From UDF model reproduced in CATIA®v5.

An example of data at off-design conditions for the core-engine is provided in Table 4.4. The off-design conditions are computed considering variable rotor efficiencies and TET: the performance map of F7A7 blades[15] in reference [147] shows that the net efficiency of the rotor is 0.62 at take off (SLS) and 0.81 at maximum climb design point, which is close to the 0.849 target of the "Full-Scale Goal" stated in Table 5-2 of reference [11].

Not all data presented in Table 4.4 are obtained from Turbomatch directly. In fact, it is possible to evaluate PQA, ENT and TQA by knowing the equivalent

[15]The blades are shown in Fig. 1.20.

Table 4.4. Off-design conditions corresponding to the design-point of the fan.

Parameters at $M = 0.72$, $z = 35\ kft$	From Literature[§]	From Turbomatch
$A_c\ [m^2]$	0.359[*]	0.359
$A_{pt}\ [m^2]$	0.766[*]	0.766
η_{rot}	0.812	0.81
$TET\ [K]$	N.A.	1430[†]
$EP\ [W]$	N.A.	5698310.5
PQA	4.1 to 4.2	4.15
$ENT\ [N]$	22645.9[‡]	21608.762
TQA	1.27	1.2

[*] From UDF model available in [11] and reproduced in CATIA®v5.
[†] Guessed value.
[‡] Original data: net thrust of 5091 lbf.
[§] Source: ref. [11] and [124].

power EP, which is calculated by Turbomatch automatically, and keeping both the cruise speed and altitude constant: in this case $M_0 = 0.72$ and $z = 35\ kft$ respectively, so that $V_0 = 213.6\ m/s$ and $\rho = 0.379597\ kg/m^3$.

More in details, the evaluation of PQA, ENT and TQA can be done as follows. First of all, from reference [11], $D_{tip} = 11.67\ ft = 3.557\ m$ and $R_{hub}/R_{tip} = 0.425$, so that $R_{tip} = D_{tip}/2 = 1.779\ m$ and then $R_{hub} = 0.755\ m$. Therefore, $A_{an} = \pi \cdot (R_{tip}^2 - R_{hub}^2) = 3.14 \cdot 2.595 = 8.15\ m^2$; it is worthy to clarify that the in-flight steady-state deflections of the blades are neglected within this cycle performance prediction, so that the annular area A_{an} is always considered constant and equal to $8.15\ m^2$. Taking into account the advance ratio $J = 2.8$, which is known from Table 5-1 of reference [11] and is defined as

$$J = \frac{V_0}{n \cdot D_{tip}} \tag{4.9}$$

hence $n \cdot D_{tip} = V_0/J = 76.286\ m/s$ and consequently $PQA = 4.15$ from

$$PQA = \frac{EP}{\rho \cdot (n \cdot D_{tip})^3 \cdot A_{an}} \tag{4.10}$$

Considering $\eta_{rot} = 0.81$, which is known from reference [147], the total equivalent net thrust

$$ENT = \frac{EP \cdot \eta_{rot}}{V_0} \tag{4.11}$$

becomes $ENT = 21608.762\ N$, thus the thrust coefficient

$$TQA = \frac{ENT}{\rho \cdot (n \cdot D_{tip})^2 \cdot A_{an}} \tag{4.12}$$

is $TQA = 1.2$. Since the rotor efficiency can be defined as

$$\eta_{rot} = J \cdot \frac{TQA}{PQA} \tag{4.13}$$

it is possible to verify from the values obtained before that $J \cdot TQA/PQA = 0.8096$ in accordance with the input rotor efficiency, which is 0.81. The power coefficient PQA is in good agreement with the data available in literature. The values of ENT and TQA are of the same order of magnitude, though lower than the original data. Anyhow the level of accuracy is sufficient for the purposes of this work. The compressor face area A_c and the area at the outlet station of the power turbine A_{pt} are used as an input in Turbomatch to perform off-design calculations at these stations; the numerical values of A_c and A_{pt} are obtained from the UDF model reproduced in CATIA®v5.

Another example of off-design condition analysis, useful to assess the cycle model, is the following. At $z = 35\ kft$, the flight speed is $V_0 = 237.3\ m/s$ when flying at Mach 0.8 and, in accordance with the charts of reference [147], J can vary from 2.9 to 3.35 when $M_0 = 0.81$; in particular, if the advance ratio is $J = 3$, then the rotor efficiency is $\eta_{rot} \sim 0.77$. Hence, running a Turbomatch off-design simulation

at Mach 0.8 assuming $\eta_{rot} = 0.77$, the equivalent power results $EP = 7119016\ W$. Fixing $J = 3$ it follows from equation 4.9 that $n \cdot D_{tip} = 237.3/3 = 79.1\ m/s$, and consequently, from equation 4.10, $PQA = 4.65$: this power coefficient is in good agreement with the value reported in literature[16] (~ 4.6 for $M_0 = 0.81$).

The above calculations show that the Turbomatch model provides a consistent aerothermodynamic description of the REMO configuration. Using this Turbomatch model, it is possible to determine mass-flow, static/total pressures and temperatures at each engine station, and use them as input values of the boundary conditions parameters for the CFD simulations.

4.2.2. The rotor model

The simplicity of the CFD model and the computational resources needed for the simulations depend on the rotor model. Therefore, the way in which the rotor is represented plays an important role within the present study. The open rotors can be simulated by an actuator disk model for compressible flows, or by the integration of a 3D blade(s) system into the domain. A trade-off on how to simulate the open rotors can be done on the basis of the following considerations:

- The actuator disk model for compressible flows
  - *Positive features*
    - it allows 2D investigations
    - it is possible to work with very simple geometries both in 2D and 3D simulations
    - it allows to run simulations with less computational time
    - it provides a very simple way to take into account the rotor effects in case the blade shape and rotor performance should change, thus

[16] See ref. [147].

it easily keeps connected the work done by rotor aerodynamicists and nacelle aerodynamicists

  - *Negative features*
    * The flow field over the blade, especially among the contra-rotating stages, is not well represented.

- Blade modelling[17]
  - *Positive features*
    * The flow field over the blade, especially among the contra-rotating stages, is well represented
  - *Negative features*
    * it forbids 2D investigations
    * it implies to work in 3D and reproduce the geometry of the blades
    * it penalises fast computations
    * it is difficult to adapt the nacelle design techniques once the blades or the rotor characteristics[18] have been eventually modified due to optimisation processes (carried on by rotor aerodynamicists), customer needs (e.g. different thrust demand) or evolving regulations (e.g. noise reduction). Moreover, the amount of time needed to assess the aerodynamic properties of the nacelle after any rotor changes would be extremely time consuming.

Basically the former method allows 2D investigations and the use of very simple geometries both in 2D and 3D cases, thus running simulations in less computational time compared to the latter, whose main advantage is the possibility to reproduce

[17] This kind of investigation is well documented in various works, presenting and comparing both computational and experimental results, such as ref. [41], [42], [101], [102], [110], [119], [131], [137], [139], [151] and [160].
[18] Such as power, tip diameter, blade aerodynamic loading, relative position of the rotors.

the airflow effects between the blades more accurately. Given the particular purpose of the present research, that is to identify design methods for the open-rotor nacelle with pusher architecture and not to reproduce accurately the flow-field in the rotor region, the first model seems to be the more appropriate[19]. Although the real geometric shape of the blades cannot be reproduced faithfully with a 2D line or a 3D flat surface (representing the actuator disk zones in 2D and 3D domains respectively), there is evidence in literature[20] that high-speed propellers of tractor and pusher propfans can be satisfactorily modelled without reproducing the whole blades but instead using actuator disks. Reference [154], reporting the case of an existing tractor propfan flying at transonic speed and simulated in Fluent®, demonstrates how the simulation of the engine installation with an actuator disk is still satisfactory for nacelle aerodynamic performance prediction, so that 3D models with 3D blades are not compulsory. The theoretical aspects connected to the actuator-disk application for high-speed blades modelling are described in the following subparagraphs.

4.2.2.1. Axial momentum theory in compressible flow

The axial momentum theory represents the first step in the description of phenomena involving a change in physical quantities that might be approximated with a discontinuity surface. The axial momentum theory, which is a one-dimensional theory, can be expanded introducing different parameters to simulate 2D or even 3D effects on the analysed physical system, and usually in these cases the discontinuity surface is called 'actuator disk'. For instance, the propeller has been studied in the past[21] with both simple and complex axial momentum theories. However, when speaking of simplified axial momentum theory, academic texts and sources such as [8] and [130] often demonstrate or refer to the case of incompressible flows

[19] As it is also suggested in ref. [40].
[20] For instance ref. [154] and [164].
[21] For a brief but effective review on the historical and mathematical development of the propeller theory see ref. [156].

only. When studying high-speed propellers it is mandatory to consider the air as a compressible fluid. Thus it is convenient to expand the axial momentum theory accounting for the compressibility effects of the air. In such a way, the actuator disk for compressible flows can be adopted to model not only high-speed propellers, but also various phenomena: ref. [77] describes the actuator disk theory for inclined flows, cascades, flames and normal shock waves, offering a wide source of references for these cases.

For the purpose of the present study the theoretical investigation is limited to a simple axial momentum theory suitable for the simulation of high-speed open rotors. Some of the basic concepts of this topic are reported in literature[22], and the methodology adopted to derive the following equations is inspired by reference [152]. Considering the scheme of figure 4.10, the open rotor is simplified by a line

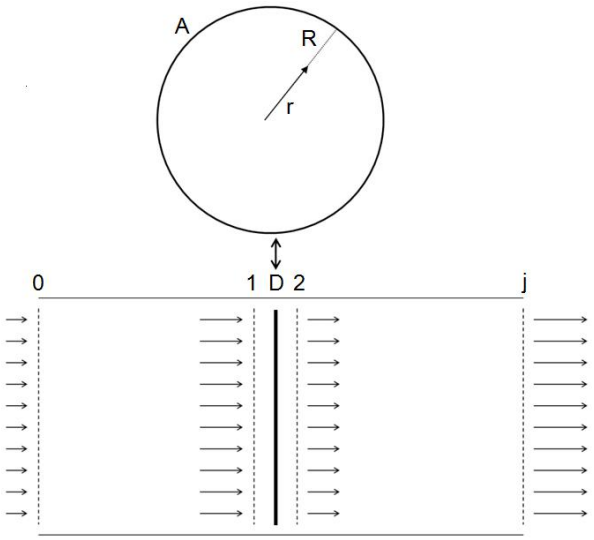

Fig. 4.10. Axial momentum theory for compressible flows: velocity profiles.

D, which represents a surface of discontinuity: the total pressure after this line is

$$P_{t-2} = P_{t-1} + \Delta P_{tot} \tag{4.14}$$

[22]The equations for one-dimensional compressible flows are collected in ref. [153], while the axial momentum theory for compressible flow has been treated in many different works, such as ref. [50], [122] and [155], and clearly used in CFD simulations (ref. [98]).

and the entropy across this boundary (stations $1, 2$) is not conserved. Calling $A = \pi \cdot R^2$ the area that would be occupied by the discontinuity surface (provided it be a circle of radius R) in a 3D domain, the generated thrust is

$$F = \Delta P \cdot A \tag{4.15}$$

and can be also defined from conditions far or near the discontinuity line $\mathbf{D}$, that in this one-dimensional analysis is equally called 'actuator disk'. Thus the thrust becomes

$$F = \dot{m} \cdot (V_j - V_0) \tag{4.16}$$

or even

$$F = \dot{m} \cdot (V_2 - V_1) + (P_2 - P_1) \cdot A \tag{4.17}$$

according to the momentum balance on the two different control volumes, respectively far (stations $0, j$) and near (stations $1, 2$) the actuator disk. The power ideally transmitted to the jet is

$$\dot{W} = \frac{\dot{m}}{2} \cdot \left(V_j^2 - V_0^2\right) \tag{4.18}$$

which, considering equation 4.16, becomes

$$\dot{W} = F \cdot \frac{(V_j + V_0)}{2} \tag{4.19}$$

and consequently thrust can be expressed as

$$F = \frac{2 \cdot \dot{W}}{(V_j + V_0)} \tag{4.20}$$

that is a function of the power. After considering air (thus $\gamma = 1.4$) as a perfect gas

$$p = \rho \cdot \Re \cdot T \tag{4.21}$$

where $\Re$ is the gas constant and T the temperature, then conservation of mass for a steady one-dimensional compressible flow through the disk region A implies

$$\dot{m}_1 = \dot{m}_2 \Rightarrow \rho_1 \cdot A \cdot V_1 = \rho_2 \cdot A \cdot V_2 \Rightarrow \rho_1 \cdot V_1 = \rho_2 \cdot V_2 \Rightarrow \rho \cdot V = \frac{\dot{m}}{A} = \text{cost} \quad (4.22)$$

while it is also true that

$$\frac{P}{\rho^\gamma} = \text{cost} \quad (4.23)$$

which is called 'pressure-density relation'. Conservation of energy implies that the total enthalpy is preserved before the disk (from station 0 to 1) and after the disk (from station 2 to j); moreover, it can be assumed that this conservation occurs isentropically. For this reason not only

$$P_1 = \frac{P_0}{\rho_0^\gamma} \cdot \rho_1^\gamma \quad (4.24)$$

and

$$P_2 = \frac{P_0}{\rho_0^\gamma} \cdot \rho_2^\gamma \quad (4.25)$$

but, assuming that the variation in total energy of the flow can be associated to a variation of axial kinetic energy only (hence $P_j = P_0$ and $\rho_j = \rho_0$), it is also possible to write the following equations. Considering a constant specific heat ratio of air $\gamma = 1.4$ and an isentropic flow so that P/ρ^γ is constant, the power of the jet $\dot{W}$ divided by the area A of the disk is

$$\frac{\dot{W}}{A} = \frac{\dot{m}}{A} \cdot \frac{\left(V_j^2 - V_0^2\right)}{2} \quad (4.26)$$

where $\dot{m}$ is the mass flow rate, and the balance of thrust evaluated far from (stations 0, j) and near (stations 1,2) the disk gives

$$\frac{2 \cdot \dot{W}}{A \cdot (V_j + V_0)} = \frac{P_0}{\rho_0^\gamma} \cdot (\rho_2^\gamma - \rho_1^\gamma) - \left(\frac{\dot{m}}{A}\right)^2 \cdot \left(\frac{1}{\rho_1} - \frac{1}{\rho_2}\right) \quad (4.27)$$

while, supposing that the total enthalpy before the disk is conserved,

$$\frac{\gamma}{\gamma-1}\cdot\frac{P_0}{\rho_0}+\frac{V_0^2}{2}=\frac{\gamma}{\gamma-1}\cdot\frac{P_0}{\rho_0^{\gamma}}\cdot\rho_1^{\gamma-1}+\frac{1}{2\cdot\rho_1^2}\cdot\left(\frac{\dot{m}}{A}\right)^2 \tag{4.28}$$

and, assuming the conservation of total enthalpy behind the disk, then:

$$\frac{\gamma}{\gamma-1}\cdot\frac{P_0}{\rho_0}+\frac{V_j^2}{2}=\frac{\gamma}{\gamma-1}\cdot\frac{P_0}{\rho_0^{\gamma}}\cdot\rho_2^{\gamma-1}+\frac{1}{2\cdot\rho_2^2}\cdot\left(\frac{\dot{m}}{A}\right)^2 \tag{4.29}$$

All the terms of these equations have been opportunely adjusted considering the relations 4.22, 4.24 and 4.25. Equation 4.26 derives directly from equation 4.18, and equation 4.27 derives from equations 4.17 and 4.20, while the last two relations 4.28 and 4.29 are the 'Bernoulli equations for compressible flows'[23]. Equations 4.26, 4.27, 4.28 and 4.29, valid for an adiabatic flow process of a thermally and calorically perfect gas, can be grouped to form a non-linear system:

$$\begin{cases} \frac{\dot{W}}{A}=\frac{\dot{m}}{A}\cdot\frac{\left(V_j^2-V_0^2\right)}{2} \\ \frac{2\cdot\dot{W}}{A\cdot(V_j+V_0)}=\frac{P_0}{\rho_0^{\gamma}}\cdot\left(\rho_2^{\gamma}-\rho_1^{\gamma}\right)-\left(\frac{\dot{m}}{A}\right)^2\cdot\left(\frac{1}{\rho_1}-\frac{1}{\rho_2}\right) \\ \frac{\gamma}{\gamma-1}\cdot\frac{P_0}{\rho_0}+\frac{V_0^2}{2}=\frac{\gamma}{\gamma-1}\cdot\frac{P_0}{\rho_0^{\gamma}}\cdot\rho_1^{\gamma-1}+\frac{1}{2\cdot\rho_1^2}\cdot\left(\frac{\dot{m}}{A}\right)^2 \\ \frac{\gamma}{\gamma-1}\cdot\frac{P_0}{\rho_0}+\frac{V_j^2}{2}=\frac{\gamma}{\gamma-1}\cdot\frac{P_0}{\rho_0^{\gamma}}\cdot\rho_2^{\gamma-1}+\frac{1}{2\cdot\rho_2^2}\cdot\left(\frac{\dot{m}}{A}\right)^2 \end{cases} \tag{4.30}$$

The problem of determining a solution for the system 4.30 is closed in the unknown terms $\dot{m}/A$, ρ_1, ρ_2 and V_j once the variables V_0, P_0, ρ_0, $\dot{W}$ and A are known; usually these variables are available from any existing preliminary performance analysis of the engine. The non-linear system 4.30 can be solved computationally[24], resulting in a set of velocity profiles whose general representation is shown in Fig. 4.10, wherein the disk is simplified by a straight line **D**, because this representation occurs in a mono-dimensional case: from the magnitude of the vectors it is evident that $V_j > V_1 > V_2 > V_0$. This means that an actuator disk introduces velocity

[23] According to the denomination used in ref. [153].
[24] For example creating a simple script in Matlab®.

drops after its discontinuity surface when compressible flows are involved in the model: $V_2 < V_1$, even if both V_2 and V_1 are greater than V_0. This is an interesting aspect, confirmed also by data available in literature [122]. Such a result, although not intuitive, is correct because the flow is compressible: in this case, according to the conservation of mass, it is the quantity $\rho \cdot V$ to be preserved across the disk, not V (see equation 4.22). In fact, for compressible flows ρ is not constant and, across the disk, the relation $V_1 = V_2$, true for incompressible flows, becomes $\rho_1 \cdot V_1 = \rho_2 \cdot V_2$ instead. The pressure jump introduced by the discontinuity surface affects the density of the flow, so that $\rho_2 > \rho_1$ and consequently $V_2 < V_1$.

At this point it is worthy to make a survey on the usage of actuator disks for the simulation of high-speed propellers, focusing on how the open rotors operating at compressible and even transonic-flow regimes can be simulated with the help of these simplified models.

4.2.2.2. Actuator disk theory and high-speed propellers

The high-speed propellers of tractor and pusher propfans have been modelled in the past with actuator disks. Different Euler and Navier-Stokes codes were developed to determine the flow-field around these engines. Most of this work, however, was not based on commercial software.

The early attempts to simulate the aerodynamic influence of a propfan on the airframe through an actuator disk did not make an explicit reference to the actuator disk itself. A method to incorporate the influence of the propeller in the Euler equations with a 'slipstream simulator' has been developed in ref. [159]. In ref. [165] and later in ref. [134] the flow prediction for propfan configurations using Euler equations was based on the axial momentum theory. The open rotor was clearly simulated through an actuator disk, which could reproduce propeller power and swirl effects as a boundary condition defined accordingly to two different methods, both depending on the 'known variables': blade force distributions on

the propeller, or total pressure/temperature and swirl characteristics.

For the transonic flow analysis of wing-fuselage configurations, in ref. [39] the slipstream of the rotor was modelled as a small perturbation to the ultimate wake of the undisturbed slipstream. In ref. [163] numerical Navier-Stokes solutions of two propfan cases (NASA/Hamilton standard SR1 and SR3) were obtained simulating high-speed propeller flows with an actuator disk modelled through an axial force term and a peripheral torque term, both function of the propeller radius.

With the method used in ref. [49] to investigate the propeller effects in airframe-integration studies, the rotor was modelled by an actuator disk having jump conditions prescribed along the disk. The quantities specified behind the actuator disk were: the jump in the stagnation enthalpy, the jump in the entropy, the jump in the circumferential velocity (or swirl) and the jump in radial velocity, all of them considered across the actuator disk. Thus the inviscid flow-field was determined by properly incorporating these quantities into the Euler equations. This method was successfully implemented into CFD codes used to study the case of a contra-rotating propfan of the pusher type. A similar case was studied in ref. [164], and comparisons between the aerodynamic characteristics of the inviscid flow on the airframe with and without the propeller disk were discussed, also considering different angles of attack. The report presented the results of flow simulations for a complex aeroplane configuration using a combination of Euler equations and actuator disk model.

Even in ref. [98] the propeller was replaced by an actuator disk in the Euler equations, with the aim to investigate the effects of a tractor propfan on the aeroplane configuration. A numerical simulation of the propeller/wing interactions for transport aircraft based on the actuator disk theory was done also more recently in ref. [111].

All the works cited previously were not developed using commercial software. The goal of the present research is to identify nacelle design methods using com-

mercial software (Gambit®, Fluent® and CATIA®v5). As regards Fluent®, the actuator disk can be reproduced by the solver with an internal boundary condition called *FAN*; the input of this boundary condition is the total pressure jump across the disk and, optionally, its swirl characteristics. In the past, the case of a tractor propfan flying at transonic speed and simulated in Fluent with a *FAN* condition[25] was studied in ref. [154]: the results demonstrated how, for nacelle aerodynamic performance predictions, the simulation of the engine installation with an actuator disk is still a valid choice, confirming that the reproduction of 3D models with 3D blades is not mandatory; without losing accuracy, the effects of the open rotor over the nacelle were obtained faster when computed with the actuator disk. For this reason in the present work the *FAN* boundary condition is adopted within the models in order to simulate the open-rotor stages.

Moreover, the employment of actuator disk models is still appropriate when predicting the wake effects of contra-rotating blades due to their swirl recovery. Even if the aerodynamic performance of the nacelle is not affected by the propeller wake in the specific case of pusher open-rotors, however the avoidance of missed swirl effects (especially in 2D simulations, where the swirl can not be specified) is important to limit the computational errors all over the domain, thus improving the quality of the whole flow-field.

4.2.2.3. The 2D rotor model for the REMO engine

With Fluent®, as already mentioned in the previous subparagraph, the actuator disks can be reproduced by the solver with an internal boundary condition called *FAN*. The two rotors can be replaced by two finite lines in 2D domains (or finite disks in 3D domains), conventionally placed in the same position of the pitch-change mechanism. The input of this boundary condition is the total-pressure jump across the disk and, optionally, its swirl characteristics (3D only). The pressure-

[25] This boundary condition has appeared in literature to be used not only for high-speed propeller investigations, but also for rotorcraft aerodynamic assessments such as in ref. [54].

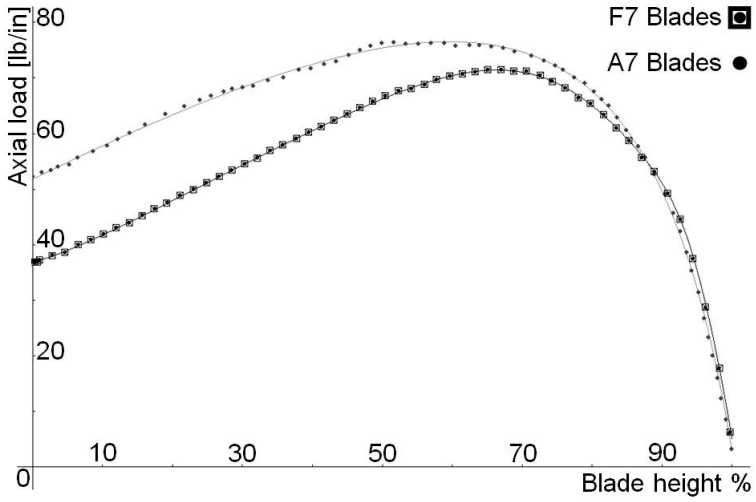

Fig. 4.11. Axial loads (spanwise direction) of F7A7 contra-rotating stages at cruise.

jump input can be inferred from the characteristics of the UDF blades available in [11]: the aerodynamic load curves of both the F7 (front) and A7 (rear) stage at cruise can be extrapolated[26] and recreated doing a regression analysis. The two equations obtained from this procedure are of the form

$$y(x) = \frac{\sum_{n=0}^{7} a_n \cdot x^n}{\sum_{m=0}^{2} b_m \cdot x^m} \tag{4.31}$$

for the F7 blades and

$$y(x) = \frac{\sum_{n=0}^{2} a_n \cdot x^n}{b_0 + b_1 \cdot x} \tag{4.32}$$

for the A7 blades: they are represented in Fig. 4.11. Hence[27], the proper spanwise pressure jump $\Delta P(r)_{Disk}$ introduced by each rotor is here approximated, knowing their axial aerodynamic load $F_{ax}(r)$, as follows:

$$\Delta P(r)_{Disk} \approx \frac{F_{ax}(r)}{2 \cdot \pi \cdot r} \cdot \eta_{rot} \tag{4.33}$$

[26] For instance using the free software **Qplot**.
[27] See also ref. [47].

This pressure jump can be imported into the *FAN* boundary condition profiles of Fluent®, after executing a proper unit conversion (from lb/in^2 to N/m^2). In general, given the flexibility of this procedure, whenever a new $\Delta P(r)_{Disk}$ is provided by a rotor-aerodynamics analysis, it would be easy to change it within the Fluent® *FAN* boundary condition.

4.2.3. Simulation techniques

The actuator disk modelling can be used with both 2D and 3D domains. However, according to what stated at the beginning of section 4.1.3, initially the domain of simulation must be a two-dimensional 'wireframe'. Said wireframe, which can be created in CATIA®v5, comprises the external borders, the engine profile, the rotors, and the exhaust nozzle. The external borders are kept far from the engine

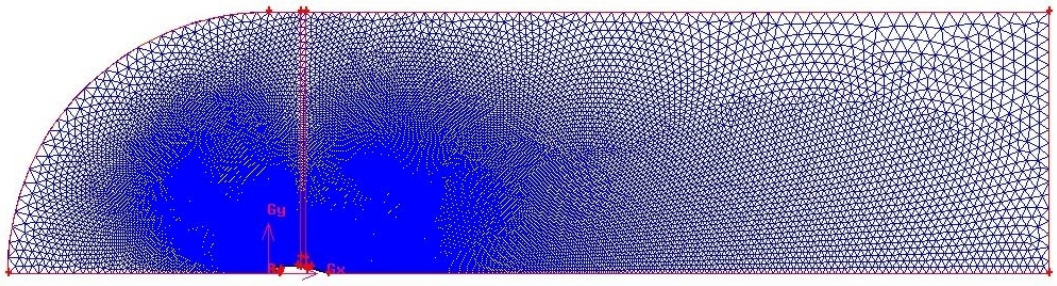

Fig. 4.12. The 2D simulation domain created in CATIA®v5 and meshed with Gambit®.

profile, with a distance of about ten times the nacelle length, except for the rear section of the domain, whose distance is tripled in order to capture the mixing effects of the rotor wake with the exhaust gas, as shown in Fig. 4.12. The engine is kept at zero angle of attack to be consistent with the two-dimensional model, while the domain is chosen to be axisymmetric about the centreline of the engine. This is useful also in Fluent®, because axisymmetric cases require less computational power than full 3D simulations. The domain is exported in a file format, such as the Initial Graphics Exchange Specification (IGES) format[28], importable into Gambit®, where it is meshed. The grid consists of an unstructured triangular mesh

[28]The file extension is `*.*igs`; see section 5.3 for further details.

(92464 cells in Fig. 4.12). The edges are generated to provide an unstructured grid which becomes fine near the model shape, but coarse near the other parts of the domain, as illustrated in Fig. 4.13.

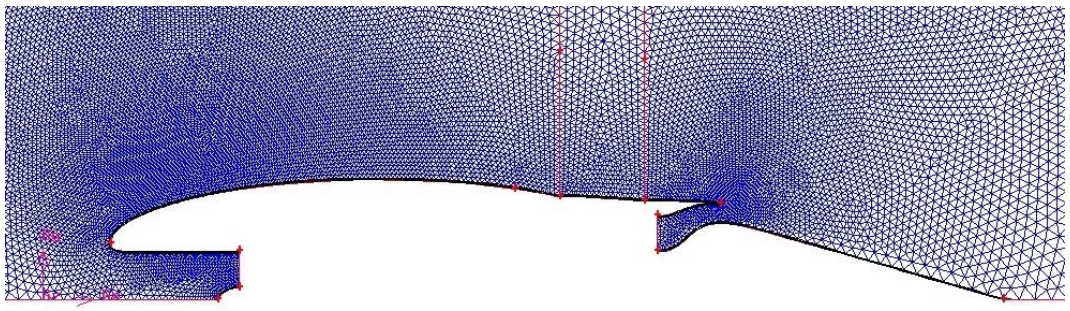

Fig. 4.13. The REMO engine and the grid.

The boundary layer cells are set on those structural parts of the engine which are considered as walls (centrebody, nacelle, hub and nozzle). The rotors, simulated by actuator disks, are modelled by straight vertical lines located in the horizontal positions where the pitch/change mechanism of the real engine is expected to be placed. Said lines are best visible in Fig. 4.15, 4.16, 4.19, and 4.22.

Since the experimental data available in literature[29] are not enough to allow a complete validation, the simulations are intentionally kept as simple as possible. The basic settings consist of an axisymmetric pressure-based solver and a Spalart-Allmaras viscous model. The working fluid is air modelled as an ideal gas, while the boundary conditions are case dependent: for each flight case the values of the physical parameters involved in the simulation have to be evaluated in advance with Turbomatch, according to the model presented in section 4.2.1. The details of the procedure to select the simulation settings is provided in appendix B.

The results of the simulations can be investigated developing a set of graphical tools, used to perform a sensitivity analysis on how the airflow varies over the nacelle when its profile and/or configuration are adjusted by the designer. A way to assess the aerodynamic performance of the nacelle is to analyse how its pres-

[29] As already noticed at the beginning of section 4.2, after the survey of chapter 2.

sure coefficient Cp varies on the forebody, especially when its shape is modified, eventually checking that Cp values are less than critical.

The pressure coefficient Cp is a non-dimensional number. In aerodynamics, Cp describes the relative pressures throughout a flow field, and it is defined as

$$Cp = \frac{P - P_0}{\frac{1}{2} \cdot \rho_0 \cdot V_0^2} \tag{4.34}$$

where P is the local static pressure, while ρ_0, P_0 and V_0 are respectively the density, pressure and velocity in the uniform free stream.

For compressible fluids such as air, the pressure coefficient can be greater than one close to a stagnation region, while negative and decreasing values of Cp correspond to an increasing velocity of the flow. The following equation[30]

$$Cp_{cr} = \frac{2}{\gamma \cdot M_{cr}^2} \cdot \left[\left(\frac{1 + \frac{\gamma-1}{2} \cdot M_{cr}^2}{1 + \frac{\gamma-1}{2}} \right)^{\frac{\gamma}{\gamma-1}} - 1 \right] \tag{4.35}$$

can be used to determine the critical pressure coefficient Cp_{cr}, which is a unique function of the critical Mach number, defined as the free-stream Mach number at which sonic flow is first encountered on the profile (aerofoil, nacelle or any flying part).

The values of critical pressure coefficients do not depend on the shape of the object, because they are computed according to equation 4.35: Cp_{cr} values at typical flight speeds are reported in Fig. 4.14.

When calculating the pressure coefficient distribution over the profile of a nacelle flying at M_0 speed, it is desirable that Cp be always less than Cp_{cr} all over the profile itself, meaning that the flow never becomes supersonic when encountering the nacelle.

Since every change in the shape corresponds to a curvature[31] change, any graph comparing Cp and curvature is very informative for the assessment of the flow qual-

[30] See ref. [26] for further details on the demonstration.
[31] The concept of curvature is particularly described in section 5.3.

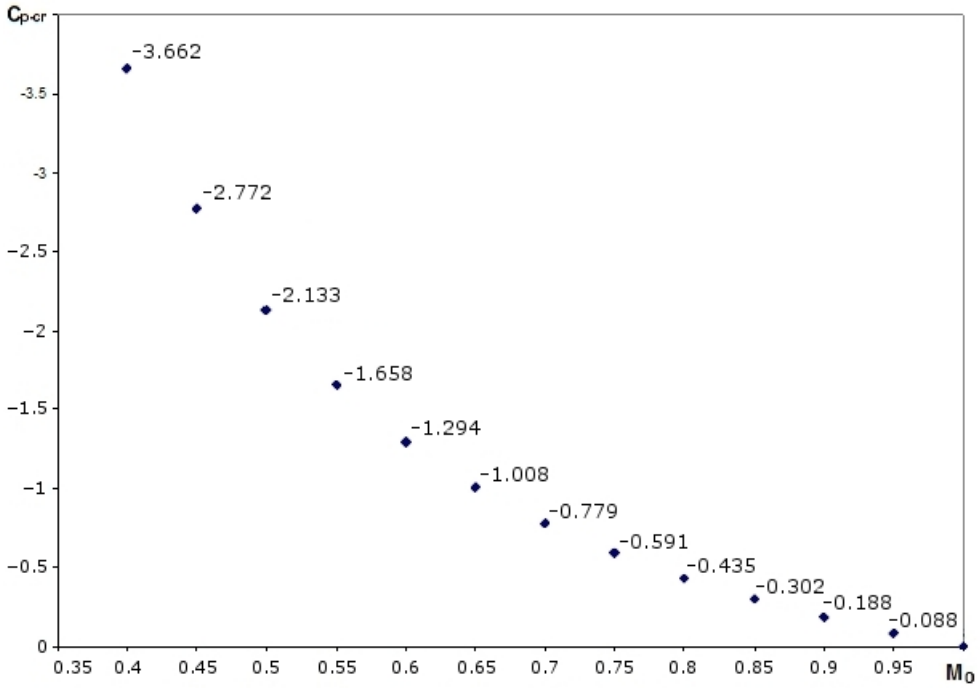

Fig. 4.14. Values of critical pressure coefficients as a function of M_0.

ity along the nacelle. The Cp values are obtained from Fluent® at several points, which depend exclusively on the grid chosen for the specific simulated case. Using an unstructured grid, it is neither easy nor convenient to know in advance where the points for Cp calculation are located. However, when exporting Cp values from Fluent®, the coordinates of these points are automatically provided by the software itself. In order to evaluate the curvature of the nacelle at these specific points, it is necessary to create a Visual Basic for Application (VBA) script which instructs CATIA®v5 on how to export its values. The resulting information can be collected in graphs like those of Fig. 4.20 and 4.23. Another useful graphical tool can be developed to compare the ratio of the local and free-stream velocity components of the airflow in front of the rotor, measured along the blade spanwise direction. The horizontal position X_p of the measurement station is determined from the information provided in reference [119]: at the radial location $r/R_{tip} = 0.52$ the vertical probe is placed axially at 67% of the local blade chord upstream of the blade leading edge (LE). Adopting this rule, the REMO simulation results can be compared with the

scale-UDF experimental data of reference [119]. These data are good for comparison purposes, nevertheless they are not used as a reference for validation, because the two models are similar but not identical. Moreover, since the X_p length is a relative distance from the LE, and it is not an absolute coordinate of the forebody, an inaccuracy is also introduced when comparing the simulation results with the experimental data. In fact, there is a difference of blade geometries: F7A7 type in the simulation, F4A4 type in the experiments. According to the information available in [119], the scale F4A4 stages are such that $D_{tip} = 62.7\ cm$ and $C_b(r/R_{tip} = 0.52) = 0.125 \cdot D_{tip} = 7.837\ cm$, hence $(X_p)_{scale-UDF} = 0.67 \cdot 7.837 = 5.25\ cm$. The scale factor between the REMO and scale-UDF models is derived from their front rotor diameter ratio $(D_{tip})_{REMO}/(D_{tip})_{scale-UDF} = 357.74/62.7 = 5.706$; its inverse value $(D_{tip})_{scale-UDF}/(D_{tip})_{REMO}$ is about 0.175, in good agreement with the original UDF scale factor of [119], which was set to 0.17. If the REMO rotors were F4A4 blades then $(X_p)_{REMO-F4A4} = 5.706 \cdot 5.25\ cm = 299.56\ mm$. Considering the information of [11], the F7A7 blades are such that $C_b(r/R_{tip} = 0.52) \sim 18\ in = 45.72\ cm$, hence $(X_p)_{REMO-F7A7} = 0.67 \cdot 45.72\ cm = 306.32\ mm$. The difference $|(X_p)_{REMO-F7A7} - (X_p)_{REMO-F4A4}|$ between the two rotor stages might introduce a horizontal length error of about 7 mm in the full size model used for the simulations. Bearing in mind the scale model, this quantity can be scaled down to $0.7\ cm/5.706 = 0.123\ cm$: this value is relatively small representing 0.2% of the scale-UDF nacelle length (64 cm from nose to front-pitch mechanism), so that the uncertainty due to the difference of blade geometry could be neglected. The graphs reporting the ratio of velocity components and the Cp-curvature analysis, like those of Fig. 4.18 and 4.20 respectively, can be used to qualitatively assess the differences of the nacelle aerodynamics when it works with or without rotors and to understand the behavior of the airflow when the forebody shape changes according to different nacelle models.

4.3. Simulations and results

The REMO nacelle was simulated under three different conditions:

1. $M_0 = 0.72$, $z = 35\ kft$ (fan design-point)
2. $M_0 = 0.7$, $z = 35\ kft$ (Cp comparison test)
3. $M_0 = 0.8$, $z = 35\ kft$ (high-speed study)

These first and the third case represent significant situations in which the engine could operate within the flight envelope. The second case is also considered for comparing the Cp profiles with the data available in literature. The three cases are analysed in the following paragraphs.

4.3.1. Fan design-point conditions

The main goal of this investigation is to assess the aerodynamic performance of the REMO nacelle comparing the axial and radial velocity components before the front rotor of the REMO and scale-UDF models. All the parameters used for the simulation, i.e. $M_0 = 0.72$, $\eta_{rot} = 0.81$ (known from reference [147]) and $\varepsilon = 0.995$, at an altitude of 35000 ft = 10668 m, are those typical of the F7A7 design point. The axial load of the F7A7 blades, at these conditions, is known from [11]. Therefore, considering what stated in paragraph 4.2.2, both rotors can be modelled in Fluent® as actuator disks. The resulting axial velocity contours are depicted in Fig. 4.15.

As expected, due to compressibility effects over the actuator disks, a velocity drop appears behind the rotor stages, in accordance with the principles illustrated in Fig. 4.10. At other locations, the computed velocities are in good agreement with Turbomatch predictions. Moreover, it is known from reference [140] that $P_{t-rot} = 1.12 \cdot P_{t-0}$ for the UDF, and so for the REMO engine. Thus $\Delta P_{tot} = P_{t-rot} - P_{t-0} = 0.12 \cdot P_{t-0}$. In this case $P_{t-0} = 33675.364\ Pa$, so $\Delta P_{tot} = 4041.044\ Pa$. As shown in Fig. 4.16, the results are in good agreement with this value.

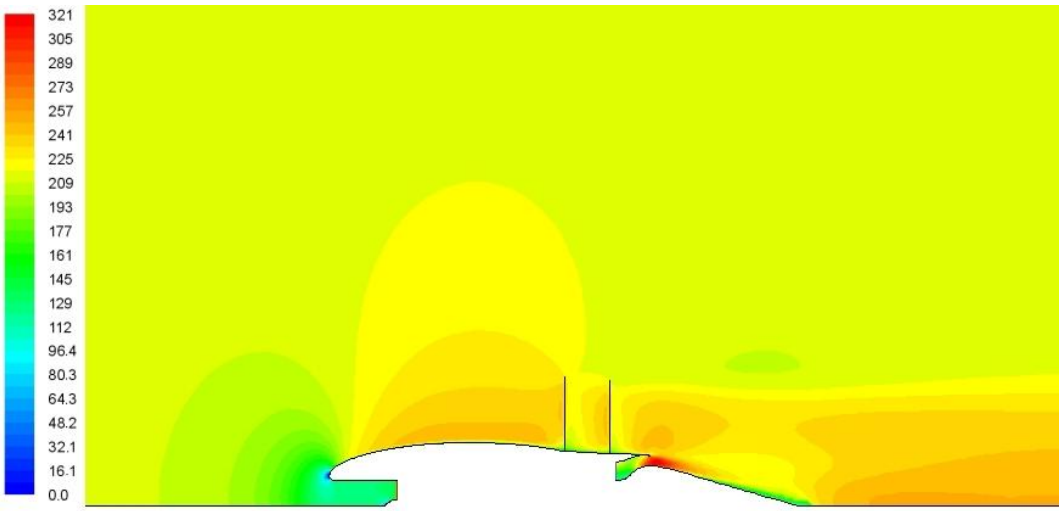

Fig. 4.15. V_{ax} $[m/s]$ contours ($M0 = 0.72$, $\eta_{rot} = 0.81$, $\varepsilon = 0.995$, $z = 35\ kft$).

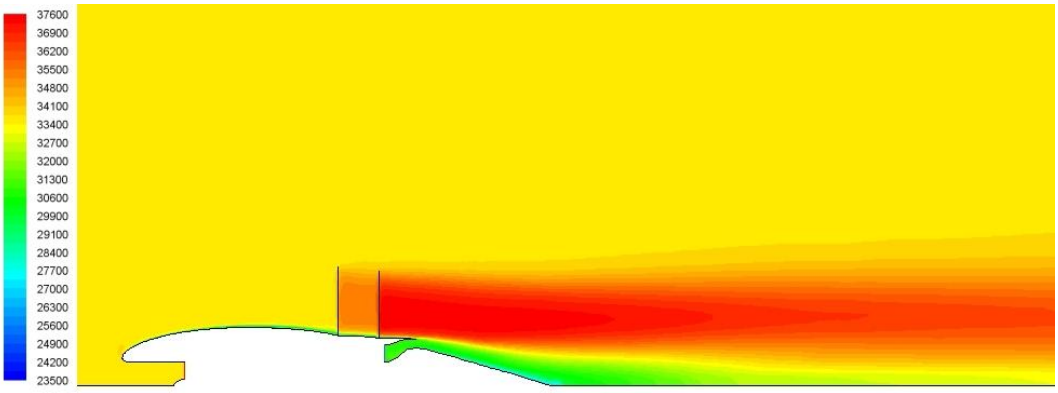

Fig. 4.16. P_t $[Pa]$ contours ($M0 = 0.72$, $\eta_{rot} = 0.81$, $\varepsilon = 0.995$, $z = 35\ kft$).

Considering the grid spacing adjacent to the walls, the Y^+ values are all contained in the range $30 < Y^+ < 300$, as reported in Fig. 4.17. This is a satisfactory range for the coarse grid of the present study. These values were checked to be adequate also for all other cases presented in this dissertation, even if the related figures are herein omitted for the sake of brevity.

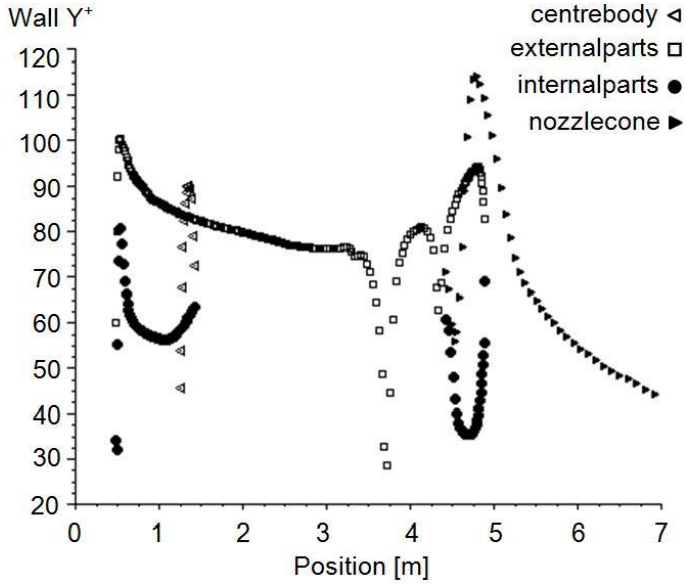

Fig. 4.17. Wall Y^+ of all nacelle parts at fan design-point conditions.

The flow-field predicted by the simulation can be compared to the circumferentially averaged velocity distributions measured in reference [119] before the front rotor: these data are reported in Fig. 4.18 together with the computational results. The graph shows the ratio between the local velocity and the free stream speed as a function of a non-dimensional blade length, where 0 coincides with the hub and 1 coincides with the blade tip in spanwise direction. The presence of the rotors mostly affects the axial component: $(V_{ax})_{no-rotor}$ values, which represent the axial velocity magnitudes calculated without the influence of the rotors, are increased by 11% near the hub and 3% at the blade tip, and are in good agreement with the experimental values. In accordance with the considerations of reference [119], the rotors have a minor influence on the radial component of the velocity, introducing a small variation of V_{rad}, whose values, however, are greater than experimental

data.

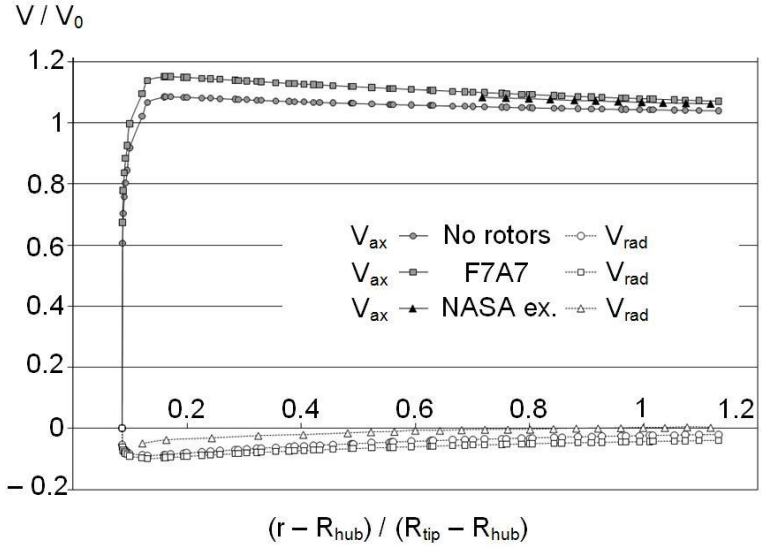

Fig. 4.18. Non-dimensional velocity distributions, measured before the rotor zone.

Anyway, such a behaviour is not due to the presence of the actuator disks: $(V_{rad})_{no-rotor}$, that is the radial velocity calculated without the influence of the rotors, is different from zero and greater than experimental data. This observation suggests that the differences between the two model shapes (which might be similar but not equal, as explained in paragraph 4.1.3) are probably introducing this sort of discrepancy: the radial velocity is very sensitive to the curvature changes of the forebody shape. After all, the scale-UDF model had a closed forebody (visible in Fig. 4.21) and its aft-cowl profile could be slightly different even from the original UDF engine. In fact, the purpose of the experiments was to focus not on the nacelle aerodynamics, but on the aerodynamic phenomena at the rotor tip regions, on the two rotor stages aerodynamic interaction and on the flow-field of the wake. Since the tangential component of velocity is negligible in the experiments (as suggested by reference [119]) and null in the simulations (due to the 2D axisymmetric model), this component is not reported here and its absence should not significantly affect the prediction of the axial and radial components. Even if this is not a rigorous validation case, the trend of spanwise variation of the velocity components is in good agreement with the experimental predictions,

meaning that the main qualitative behavior of the flow in front of the rotor is well captured. This is important to guarantee a level of confidence when estimating the effects of nacelle design changes on the velocity profile in future investigations.

4.3.2. Pressure coefficient analysis

The goal of this simulation is to compare the pressure coefficient distributions over the REMO nacelle with the scale-UDF forebody data available in reference [147]. The parameters used for the simulation are: $M_0 = 0.7$, $\eta_{rot} = 0.8$ (known from reference [147]) and $\varepsilon = 0.995$, at an altitude of $35000ft = 10668\ m$. At these conditions, the axial load of the F7A7 blades is unknown. However, since Mach 0.7 is close to Mach 0.72, the axial load can be approximated, imposing it equal to the load at $M_0 = 0.72$ given in reference [11].

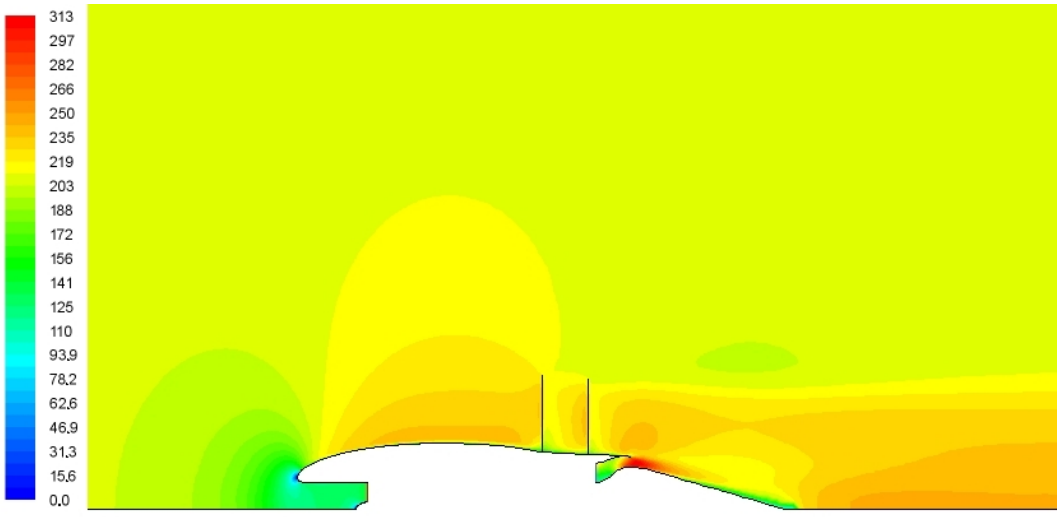

Fig. 4.19. V_{ax} $[m/s]$ contours ($M_0 = 0.7$, $\eta_{rot} = 0.8$, $\varepsilon = 0.995$, $z = 35\ kft$).

The resulting flow-field of the axial velocity V_{ax} is illustrated in Fig. 4.19. All the computed velocities are in good agreement with Turbomatch predictions[32].

The pressure coefficients are calculated over the external cowl, i.e. the part of nacelle profile between the highlight and hub points. As illustrated in Fig. 4.20, the curvature change along the external cowl is gentle enough to grant a smooth

[32]Detailed results are provided in appendix A.

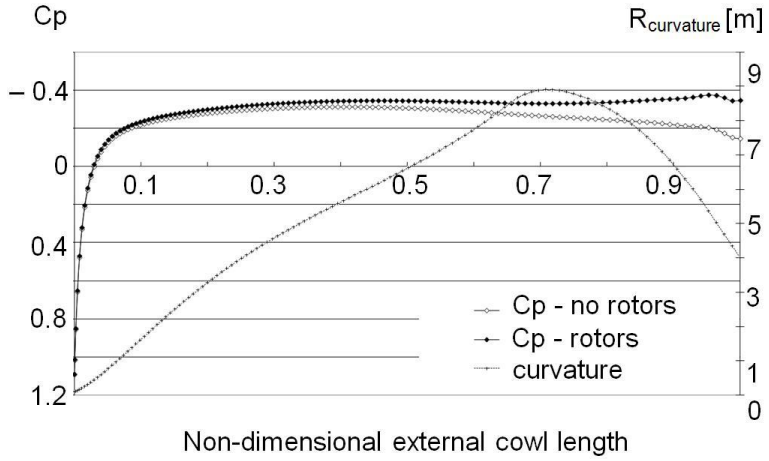

Fig. 4.20. Cp-Curvature values for the REMO external cowl at $M_0 = 0.7$ ($0 \equiv$ highlight, $1 \equiv$ rotor hub).

Cp profile, which is always below the critical value ($Cp_{cr} = -0.779$ at $M_0 = 0.7$, as indicated in Fig. 4.14). The magnitude of the values is compatible with the experimental results shown in Fig. 4.21. The difference in the Cp near the hub is probably due to the over-estimated pressure jump of the rotor. In fact, the

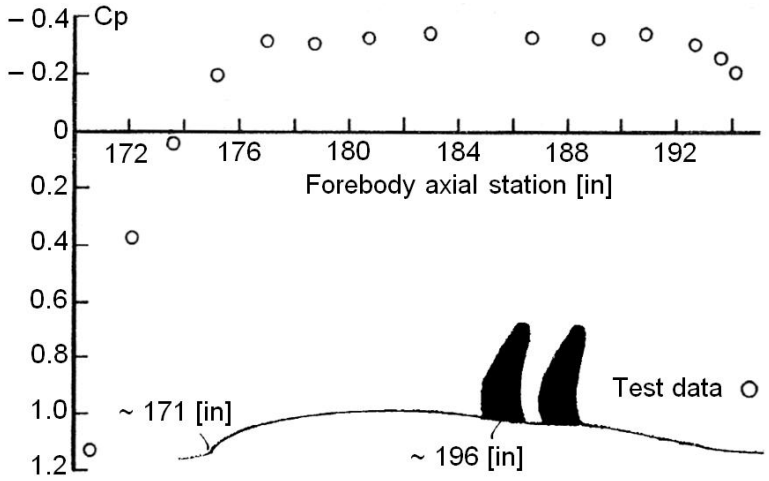

Fig. 4.21. Experimental Cp of scale-UDF [119].

axial load at $M_0 = 0.72$ is expected to be higher than the one at $M_0 = 0.7$. Evaluating the effects of the nacelle with and without rotors, it is evident how the introduction of the rotors is affecting the Cp, whose values start to become more negative after 30% of the forebody length. This is a consequence of the 'suction effects' of the rotors, which are accelerating the flow towards themselves,

and practically deleting most of the diffusion effects[33] introduced by the convex forebody shaped with maximum diameter larger than the hub diameter[34].

Hence the presence of the rotors has a non-negligible influence on the flow-field along about 70% of the forebody length, starting from the rotor hub going towards the highlight point. Eventually, the nacelle of future modified REMO versions has to be designed taking this interaction effect into account.

4.3.3. High speed study

The future open-rotor is expected to fly faster than Mach 0.72, which is the fan design-point condition for cruise of F7A7 blades. This last simulation investigates the REMO nacelle performance at a flight speed beyond Mach 0.72: Mach 0.8 represents a challenging high-speed goal. The parameters used for the simulation are: $M_0 = 0.8$ and $\varepsilon = 0.995$, at an altitude of $35000 ft = 10668\ m$. Although it is

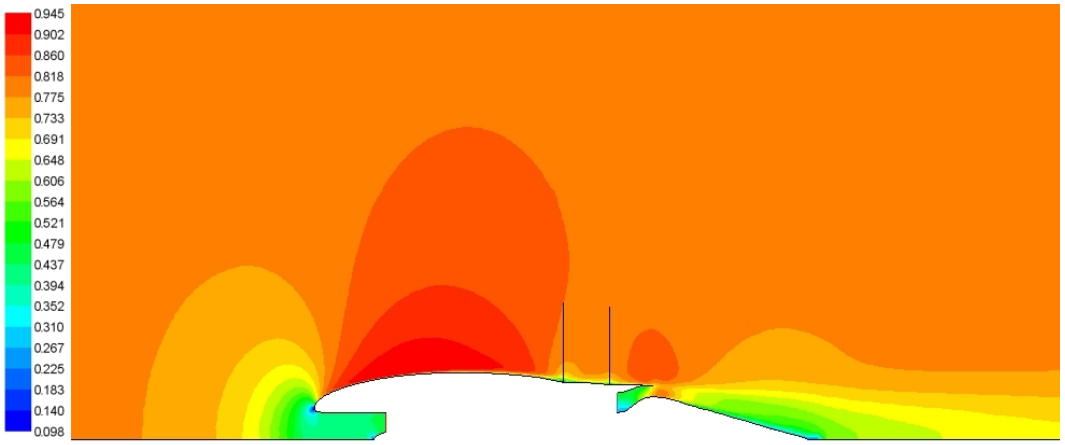

Fig. 4.22. Contours of Mach number with no ΔP through rotors ($M_0 = 0.8$, $\varepsilon = 0.995$, $z = 35\ kft$).

known from reference [147] that $\eta_{rot} = 0.77$, at these conditions the axial load of the F7A7 blades is unknown. Moreover, since Mach 0.8 is far from 0.72, the axial load cannot be imposed equal to the load at $M_0 = 0.72$ given in reference [11]. As a consequence, only the 'no-rotor' case is simulated. The resulting flow-field is here

[33] The diffusion effects occur when Cp is increasing.
[34] This configuration is also described in section 2.2.

depicted by Mach contours in Fig. 4.22. At this cruise speed, the REMO profile is still presenting good aerodynamic quality: Mach number is less than 1 all over the external cowl, while the Cp (Fig. 4.23) is higher than the Cp at $M_0 = 0.72$, but is still below its critical value ($Cp_{cr} = -0.435$ at $M_0 = 0.8$). Despite the absence of the rotors, the results suggest that the Cp distribution on the REMO profile is not drastically changed when the flight speed is increased up to the lower transonic regime.

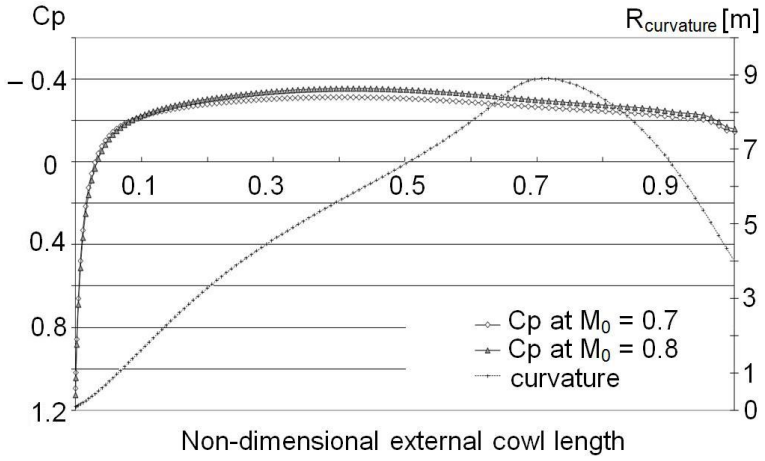

Fig. 4.23. Cp-Curvature values for the REMO external cowl without rotors ($0 \equiv$ highlight, $1 \equiv$ rotor hub).

However, Cp values are getting closer to the critical one, that is $Cp_{cr}(M_0 = 0.8) = -0.435$. Consequently, the introduction of the rotor effects, which tend to decrease Cp as already demonstrated in Fig. 4.20, could lead to the formation of sonic phenomena especially on the aft-cowl. This behaviour is connected to the fact that the REMO nacelle is similar to the UDF nacelle, which was conceived for cruising at speed inferior to Mach 0.8.

4.3.4. Overview of the simulation results

Further to what stated in paragraphs 4.3.1, 4.3.2 and 4.3.3, another important consideration can be inferred by carefully interpreting the results achieved. More in details, from the analysis of the pressure coefficients, shown in Fig. 4.20 and

4.23, the Cp does not present oscillations. This is due to the $G3$ continuity of the forebody shape.

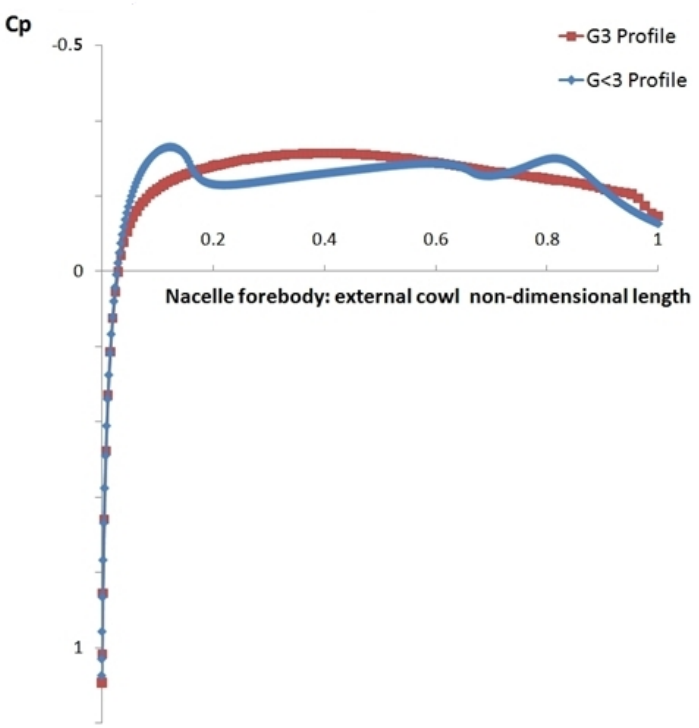

Fig. 4.24. Cp profiles of the same REMO nacelle designed with different geometric continuity levels.

As regards the reference model, the importance of designing the external profile keeping a high degree of geometric continuity ($G3$ in particular) proves to be crucial in avoiding sonic bubble formation over the forebody, as indicated by the Cp profiles captured in Fig. 4.24. Indeed the oscillations of a Cp distribution, like those appearing over the forebody with geometric continuity inferior to $G3$, are an indication of potential sonic flow formation on the nacelle. Consequently, it is worthy to develop a design method to obtain $G3$ profiles automatically preserving the characteristics described in paragraph 4.1.3. The next chapter illustrates a new technique developed to satisfy this purpose.

5. THE C3 INTERPOLATION PROCEDURE

A rigorous mathematical definition of the nacelle profile is very important not only to have full control of its geometry, but also to allow its shape optimisation in future works. An effort has to be made for shaping the nacelle without the use of commercial software for Computer Aided Design (CAD), as done in section 4.1 instead, where equations from 4.1 to 4.8 represent the parametric relations linking the coordinates of the construction points, but do not form a parametric curve which analytically defines the profile of the nacelle. Despite its rapidity and ease of use, the main limitation of the graphical approach is that the mathematical aspects related to the nacelle geometry are inevitably unknown. In this chapter an alternative solution is proposed. Given the importance played by geometric continuity[1] in the design of aerodynamic profiles, a new design procedure, which grants the designer to automatically obtain G3 profiles in an intuitive and efficient way, will be developed without using CAD commercial software.

5.1. An overview on curves for CAGD

Before going any further into the mathematical definition of a new design procedure, it is essential to assess the typology of curves[2] generated in CAGD software.

[1] Defined in paragraph 4.1.2.
[2] The history of curves for CAGD is summarised in [57].

The parametric curves typical of this discipline[3] are: Bezier curves, B-Splines, and Non-Uniform Rational B-Spline (NURBS). In particular, the modern commercial software is commonly based on NURBS curves[4], which potentially can reproduce any kind of curve. In fact, the NURBS are an extension of B-Spline curves and overcome the limits of Bezier curves, whose main limitation is, among others, the inability to faithfully reproduce conic curves (i.e. the circle).

Conventionally several methods for shaping and eventually reshaping free-form curves represented by computers have been achieved[5], which include:

1. **Curve-fitting techniques**: particularly suited to shape description, where the basic shape is obtained by experimental evaluation or mathematical calculation (such as airfoils, engine manifolds, mechanical and/or structural parts). This kind of methods creates the curve by interpolating a set of points and eventually reshape its form by moving the sample points and/or modifying the derivative constraints at these points. In order to achieve this, several interpolation methods can be used, e.g. the cubic spline curve (which is the mathematical counterpart of the physical loftsman's spline).

2. **Approximation techniques**: particularly useful for 'ab initio' design problems, which depends on both aesthetic and functional requirements. The methods grouped under this kind of techniques indirectly create and modify the forms by setting and varying the control points and knots peculiar to the B-Spline (the Bezier curve being a special case of B-spline) or the more general Non-Uniform Rational B-Spline (NURBS) curves (described for example in ref. [118]). Said techniques are most popularly used for the expression of curves and surfaces in the CAD systems of today. When some of the control points are forced to coincide with points which have to be interpolated, the

[3] An explanation of the mathematical principles for defining these curves is herein omitted but widely and clearly provided in ref. [34] and [129].
[4] The generic equations for expressing the NURBS curves are given for instance in ref. [118].
[5] As explained, for example, in ref. [129].

B-spline can also be used as a method for curve-fitting.

Both categories, however, present some disadvantages. The former, for instance, necessitates the solving of simultaneous equations prior to each reshaping. This might represent an issue if the methods belonging to this category are implemented on old computers equipped with processors having low performance. However, the computational power of modern CPUs has largely increased compared to the past and still does increase. Therefore the problem of solving simultaneous equations is not an issue when running this kind of methods on a modern or recent (indicatively 1 to 3 year old) computer.

On the other hand, the latter family of methods for designing by approximation presents the following problems when indirectly reshaping forms by altering, increasing or decreasing control points, knots, weights and other form-defining parameters:

- The reshaping phase, accomplished indirectly through the alteration or other manipulation of form-defining parameters, involves a lack of naturalness: the operator cannot directly touch the form to be reshaped. Besides, parameters and therefore reshaping methods differ with the representing techniques (e.g. uniform, non-uniform, or normalised knots).

- To achieve the desired reshaping, control points or other form-defining parameters (such as knots and weights) must be changed or moved. However, the parameters to be moved and the amount of their movement are difficult to determine because the rate of contribution of the individual control points or other parameters to the form they make up is not linear. Accordingly, these methods are difficult to use without having knowledge of the characteristics of the individual form-defining parameters.

The procedure described in paragraph 4.1.3 is a sort of graphical interpolation technique, which is not affected by the problems typical of an approximation tech-

nique: along with the control points, the designer is setting the tangency and curvature constraints and does have full command of their geometric characteristics. The CAGD software CATIA®v5 is based on NURBS curves[6], which can be used to interpolate points in space. Unfortunately, the architecture of the 'spline generator' of CATIA®v5 is unknown: it is not easy to discover how the tangency and curvature constraints are applied to the interpolation NURBS within the software, because the algorithm is obviously kept secret due to commercial reasons and intellectual property rights. Therefore, once moving away from this software, it becomes critical to handle the design procedure: the variables involved in the parameterisation of NURBS are supposed to be many, and they are far from being intuitive[7], involving not only control points but also other parameters called weights and knots, which are the main elements[8] forming a NURBS. In CATIA®v5, as in any other commercial software, the designer is helped by the Graphical User Interface (GUI), and do not interfere directly with the parameters of the NURBS. He does not define the weights, the knots vector and the control points, which are handled by the software itself automatically and 'behind the scenes'. In practice, the easiness of use and versatility granted by the GUI of the commercial software is counterbalanced by a practical limitation: it can hardly be fitted into third-party programs such as in-house optimisers, whilst the mathematics and algorithms remain basically unknown.

Hence, it is convenient at this point to further investigate the existing interpolation techniques in order to find or eventually define an appropriate method for shaping open-rotor nacelles, possibly maintaining the guidelines provided with the procedure of paragraph 4.1.3.

[6]Information retrieved on `http://en.wikipedia.org/wiki/CATIA` in June 2009.
[7]This becomes evident even when a simple NURBS modification technique is adopted, such as the one proposed in ref. [135].
[8]For the mathematical definition of these elements see ref. [118].

5.1.1. Existing interpolation techniques

The main interpolation schemes relate to splines. Apart from B-Splines, used both for interpolation and approximation, interpolation splines are polynomial curves of different types[9] (quadratic, cubic, quintic, cardinal, Catmull-Rom, Kochanec-Bartels).

Lines can be generated considering their mathematical definition in parametric form. In fact, curves may be described by expressing X, Y and Z coordinates as a function of some numerical parameter(s), for instance t. The levels of continuity of the mathematical derivatives of the coordinates with respect to the selected parameter may be defined as $C0$, $C1$, $C2$, $C3$, and so on. This denomination is intentionally similar to the classification of the geometric continuity levels described in 4.1.2, because parametric continuity implies geometric continuity, although geometric continuity does not necessarily imply parametric continuity[10]: indeed geometric continuity is a strict generalisation of parametric continuity[11].

The methods to interpolate a given set of points are based on piecewise polynomials. In practice, the curve passing through the points is obtained as a concatenation of segments. The two extremes of each segment connect two consecutive points one another. Each segment is a polynomial, thus the name 'piecewise polynomial interpolation'. Depending on the degree of the polynomial used, these interpolating functions can be called Quadratic (degree 2), Cubic (degree 3), Quartic (degree 4), Quintic (degree 5), and so on. Moreover, these piecewise polynomials can be parametric: even if, in a three-dimensional coordinate system, a curve can be expressed as a function of the orthogonal components X, Y and Z, however it is often convenient to use a parametric representation of the curve, where each coordinate value is represented as a function of a variable that is common to all coordinate components. As already mentioned before, such a variable may be de-

[9] As shown, for instance, in ref. [132].
[10] Ref. [32] provides a simple though significant example for understanding the difference between geometric and parametric continuity.
[11] As shown in ref [31].

scribed as t, with $0 \leq t \leq 1$, resulting in the following $x = f(t)$, $y = g(t)$, and $z = h(t)$ for a three dimensional system. Parametric piecewise polynomials of degree n can represent a parametric curve that is represented by polynomials of order $n+1$. As an example, parametric piecewise polynomials of third degree can represent a parametric cubic curve that is represented by fourth order polynomials: $x = f(t) = a_x \cdot t^3 + b_x \cdot t^2 + c_x \cdot t + d_x$, $y = g(t) = a_y \cdot t^3 + b_y \cdot t^2 + c_y \cdot t + d_y$, $z = h(t) = a_z \cdot t^3 + b_z \cdot t^2 + c_z \cdot t + d_z$. These equations may be easily represented in matrix notation, where the coefficient vectors can be derived to yield curves of many different properties.

Given its particular connection with geometric continuity, parametric continuity is an important property to be considered. The maximum order of parametric continuity automatically achievable when interpolating with piecewise polynomials is the degree of the polynomial minus one. In fact, the n^{th} order of the piecewise polynomial considered coincides with the degrees of freedom available for setting the interpolation conditions among its two extreme points. The condition of passing through these points requires the loss of two degrees of freedom. Therefore, a piecewise polynomial of order n interpolating two points selected by the designer has $n-2$ degrees of freedom left. Since $n = d+1$, being d the degree of the polynomial, thus the remaining degrees of freedom are $d+1-2 = d-1$, meaning that given a piecewise polynomial interpolating two points, which represent two positional constraints, the number of derivative constraint imposable, which correspond tho the level of parametric continuity, is $d-1$. For instance, for interpolating points holding $C2$ continuity the piecewise polynomials should be at least of third degree. The following methods are commonly used to create curves[12] having $C2$ continuity:

- Cubic Hermite spline: the curve is obtained by specifying the derivatives at each interpolated point.

[12] A general review of the characteristics of these curves is contained in ref. [132], but also in ref. [34].

- Cardinal spline: after imposing a set of conditions on the derivatives, the curve is obtained with the evaluation of these derivatives at each interpolated point.

- Kochanec-Bartels spline: special case of Cardinal spline.

- Catmull-Rom spline: special case of Kochanec-Bartels spline.

The most used for interpolation problems is the cubic polynomial: the conditions between the interpolated points are usually related to the tangency the curve must have at that point. Ref. [60] explains geometrically and graphically how to provide a flexible and direct control over the tangency and curvature properties of the curve, in particular when a cubic B-Spline is involved, but there is no evidence of doing so holding $G3$ continuity. Another example is provided by ref. [141], where cubic splines have been used to reproduce aerofoil profiles. However, by adopting third-degree polynomials, the maximum parametric continuity achievable is $C2$ (in fact $d = 3$ thus $d - 1 = 2$).

A further possibility is to extend these methodologies and adopt polynomials with higher degree, in order to have a more direct control of the tangency and curvature of the shape. When using high-degree polynomials, occasionally $C3$ continuity might be achieved if the parameters defining the curves are selected appropriately; quintic Hermite curves, such as the ones presented by ref. [59], could be used to make smooth piecewise defined curves as those suggested in ref. [136].

All these techniques ensure the curves be parametrically smooth of order two ($C2$ continuity), but they are not automatically generated with $C3$ continuity. This represents an obstacle if $C3$ continuity is needed instead. For instance, for aerodynamic reasons a designer could need to create a line having G3 continuity, and he could use a line having $C3$ which implies $G3$ continuity. When the degree of the polynomials is less than 4, $C3$ continuity is not achievable because there are

not enough degrees of freedom on the curve to impose the continuity of the third parametric derivative. Interpolating functions with degree higher than 5 are generally not convenient to use: the number of constraints to give for completing the degrees of freedom on the curve increases, and it is not always intuitive to assign their values. From a theoretical point of view, $C3$ continuity could be conveniently achieved with quartic and quintic polynomials. However, as mentioned before, the existing methods of this kind are not able to automatically create lines holding $C3$ continuity independently from the values of the positional and derivational conditions entered by the designer. That is, the degree of parametric continuity varies depending on how the designer selects the values of the positional and derivational conditions used to construct and modify the curve. Hence the degree of parametric continuity may vary depending on the decisions made by the designer, whenever he changes the values of the positional and derivational conditions used to construct and modify the curve. This is in contrast with the goal of the present study, which is to intuitively create nacelle profiles preserving $G3$ continuity.

5.2. Definition of a C3 interpolation technique

The achievement of a $G3$ profile can be the result of a $C3$ interpolation of the construction points forming the nacelle. In this section, a methodology for obtaining such a profile is described. The philosophy behind the graphical approach presented in paragraph 4.1.3 is here revisited. It is known that after applying tangency and curvature constraints in concomitance of the construction points, the shape of the nacelle can be modified by varying the tangency and curvature values at these locations. The main features of a new design procedure are now fixed as the following:

- Selection of 3 points to define the external cowl constraints (highlight point, mid-point, such as the crest, and rotor hub point).

- Selection of 3 points to define the internal-profile constraints of the pitot intake (highlight, throat, and compressor face points).
- Use of parametric splines to connect these points.
- Impose opportune constraints for granting C3 continuity to the profile at the location of the construction points mentioned above.

This procedure can be concretised by defining a specific interpolation technique for connecting a generic number of construction points in a two- or three-dimensional orthogonal space, holding $C3$ parametric continuity, consequently assuring $G3$ geometric continuity. However, this is not a trivial task. Once the curves forming the profile are imposed to be constrained, another problem consists in how to design the profile keeping a parametric control of its shape. Furthermore, it is particularly useful to strictly connect this parametric control to the geometric constraints of the curve, and not to additional points, knots or weights (as typically happens with Bezier, B-splines or NURBS curves), which do not lie on the profile itself, and do not have a direct and intuitive geometrical meaning for the designer.

Following the considerations made in previous section, and in particular in paragraph 5.1.1, the connection curves forming the profile are selected to be splines, created by quintic piecewise polynomials, which are functions of a given parameter. If the parameter for the spline generation is set to be t, in analogy with the physical variable of time, the curve is the equivalent of a path of motion. Therefore, one way to impose parametric continuity is to set velocity and acceleration constraints in concomitance of the construction points. The tangency and curvature characteristics of the spline are no longer used to constrain the profile, but can be derived anyway knowing the velocity and acceleration characteristics along the spline. In fact, the velocity in a given point on the curve is parallel to its tangent unit vector, while the curvature in the same point can be calculated as a function of both velocity and acceleration in that point (further details are given in section

5.3, in particular equations 5.15 and 5.19).

This simple procedure keeps the number of design variables low, whilst the designer can generate and control new profiles in a very intuitive way, without focusing his attention on how to maintain a $G3$ profile all along the body shape. More in details, the methodology consists of an interpolation scheme based on piecewise quintic polynomials (i.e. polynomials of fifth degree and sixth order) of the form

$$\overset{1\times d}{\mathrm{P_i}}(t) = \sum_{\mathrm{j}=0}^{5} \overset{1\times d}{\mathrm{C_{i,j}}} \cdot t^j \tag{5.1}$$

with $i \in \mathbb{N}^+$, $j \in \mathbb{N}$ and $t \in \mathbb{R} : t = 0, ..., 1$ (where $d = 2$ in two dimensional space or $d = 3$ in three dimensional space), which is a power basis function of fifth degree and denotes a vector of dimensions $1 \times d$ representing the position vector as a function of a given parameter t.

When t is not kept constant, with $t \in \mathbb{R}$, t can be considered as time in a physical sense. Alternatively, t can be determined as a dimensionless parameter of time from

$$t = \frac{\tau - T_s}{T_e - T_s} \tag{5.2}$$

with $T_s \leq \tau \leq T_e$, where τ is the real time in physical sense, sampled between a start time T_s and an end time T_e, being $T_e - T_s$ the period of interpolation between two interpolated points.

Whatever the way t is chosen, the polynomial 5.1 provides several position vectors, thus forming a trajectory in space. The first three derivatives of said quintic polynomials are

$$\frac{d\ \overset{1\times d}{\mathrm{P_i}}(t)}{dt} = \overset{1\times d}{\mathrm{P'_i}}(t) = \sum_{\mathrm{j}=0}^{5} j \cdot \overset{1\times d}{\mathrm{C_{i,j}}} \cdot t^{j-1} \tag{5.3}$$

$$\frac{d^2 \overset{1\times d}{\mathrm{P_i}}(t)}{dt^2} = \overset{1\times d}{\mathrm{P''_i}}(t) = \sum_{\mathrm{j}=0}^{5} j \cdot (j-1) \cdot \overset{1\times d}{\mathrm{C_{i,j}}} \cdot t^{j-2} \tag{5.4}$$

$$\frac{d^3 \overset{1\times d}{\mathrm{P_i}}(t)}{dt^3} = \overset{1\times d}{\mathrm{P'''_i}}(t) = \sum_{\mathrm{j}=0}^{5} j \cdot (j-1) \cdot (j-2) \cdot \overset{1\times d}{\mathrm{C_{i,j}}} \cdot t^{j-3} \tag{5.5}$$

with equations 5.3 and 5.4 representing the velocity and acceleration vectors respectively.

Fig. 5.1 is a graphical plot of a simplified $C3$ line, wherein the generic interpolating points are reported in space, together with the corresponding velocity and acceleration vectors (so called thinking of t as time or a dimensionless parameter of time in a physical sense).

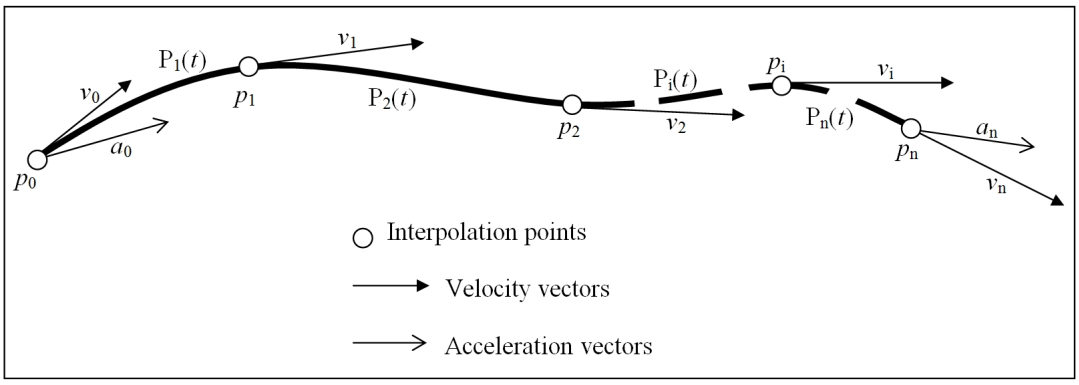

Fig. 5.1. Drawing of a simplified $C3$ line.

The interpolation line shown in Fig. 5.1 may be obtained joining together $n \geq 2$ curves of the form 5.1 (with $1 \leq i \leq n$) passing through $\mu = n + 1$ points constrained by positional and derivational relations imposed over each interpolated point. These relations are opportunely selected requiring the interpolating line comprised between the two extreme points to be $C3$ continuous.

A procedure for imposing $C3$ continuity in accordance with previous considerations is now defined and presented in the flow diagram of Fig. 5.2. This diagram represents the main structure of the method for interpolating three or more points with piecewise parametric quintic polynomial curves, resulting in a $C3$ line of the

same type reported in Fig. 5.1.

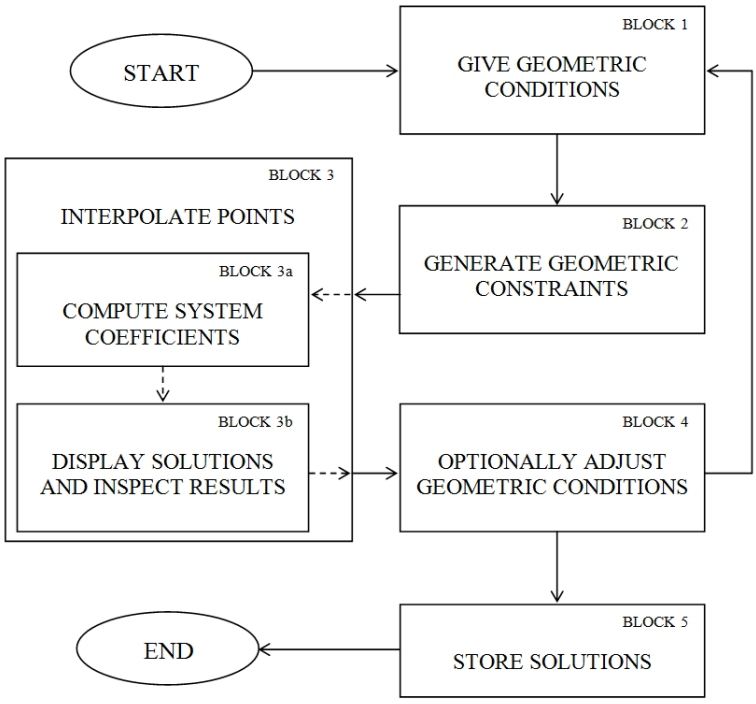

Fig. 5.2. Main structure of the $C3$ interpolation method.

The designer selects the geometric conditions (step of block 1) characterising the interpolation line, which are the positions of the interpolated points $\overset{1\times d}{p_{\mathrm{i}-1}}$, $\overset{1\times d}{p_{\mathrm{n}}}$ (with $1 \leq i \leq n$), the velocity components at each point $\overset{1\times d}{v_{\mathrm{i}-1}}$, $\overset{1\times d}{v_{\mathrm{n}}}$ (with $1 \leq i \leq n$), and the acceleration components at the extreme points $\overset{1\times d}{a_0}$, $\overset{1\times d}{a_{\mathrm{n}}}$. Whilst the extreme conditions ($\overset{1\times d}{p_0}$, $\overset{1\times d}{v_0}$, $\overset{1\times d}{a_0}$ and $\overset{1\times d}{p_{\mathrm{n}}}$, $\overset{1\times d}{v_{\mathrm{n}}}$, $\overset{1\times d}{a_{\mathrm{n}}}$) and all the points ($\overset{1\times d}{p_{\mathrm{i}-1}}$, $\overset{1\times d}{p_{\mathrm{n}}}$, with $1 \leq i \leq n$) must be selected by the designer, the intermediate velocity vectors (i.e. $\overset{1\times d}{v_{\mathrm{i}-1}}$ for $1 < i \leq n$) might be given directly by the designer or alternatively calculated automatically using a data pre-processing scheme[13]. All the geometric conditions must be given according to the scheme of Fig. 5.3.

Fig. 5.3 is the structure of block 1 reported in Fig. 5.2. The constraint equations granting $C3$ continuity are then considered according to the order reported in the scheme of Fig. 5.4.

[13]This data pre-processing scheme may be for instance that typical of monotone cubic interpolation proposed in ref. [61].

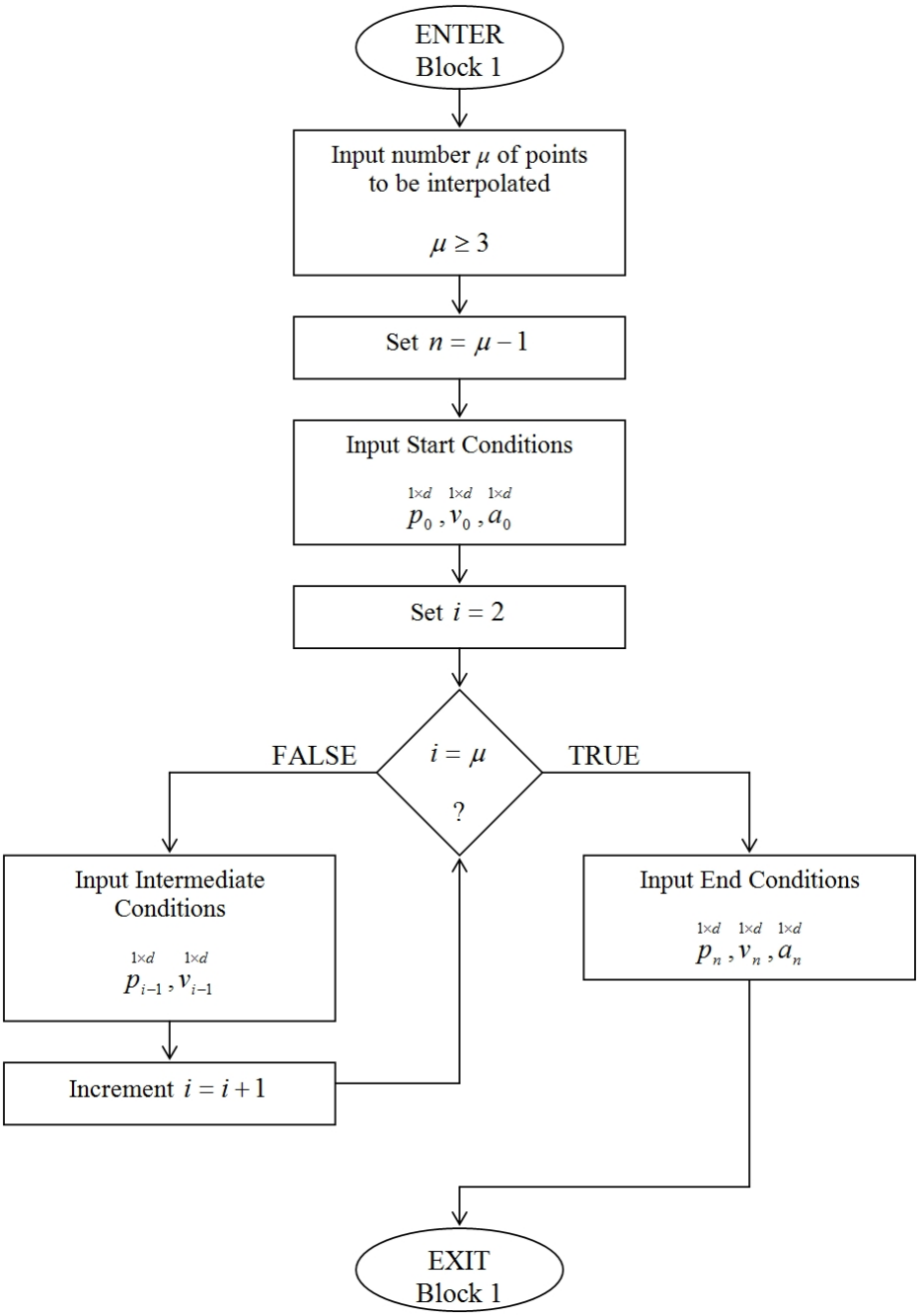

Fig. 5.3. Structure of block 1 in the $C3$ interpolation method.

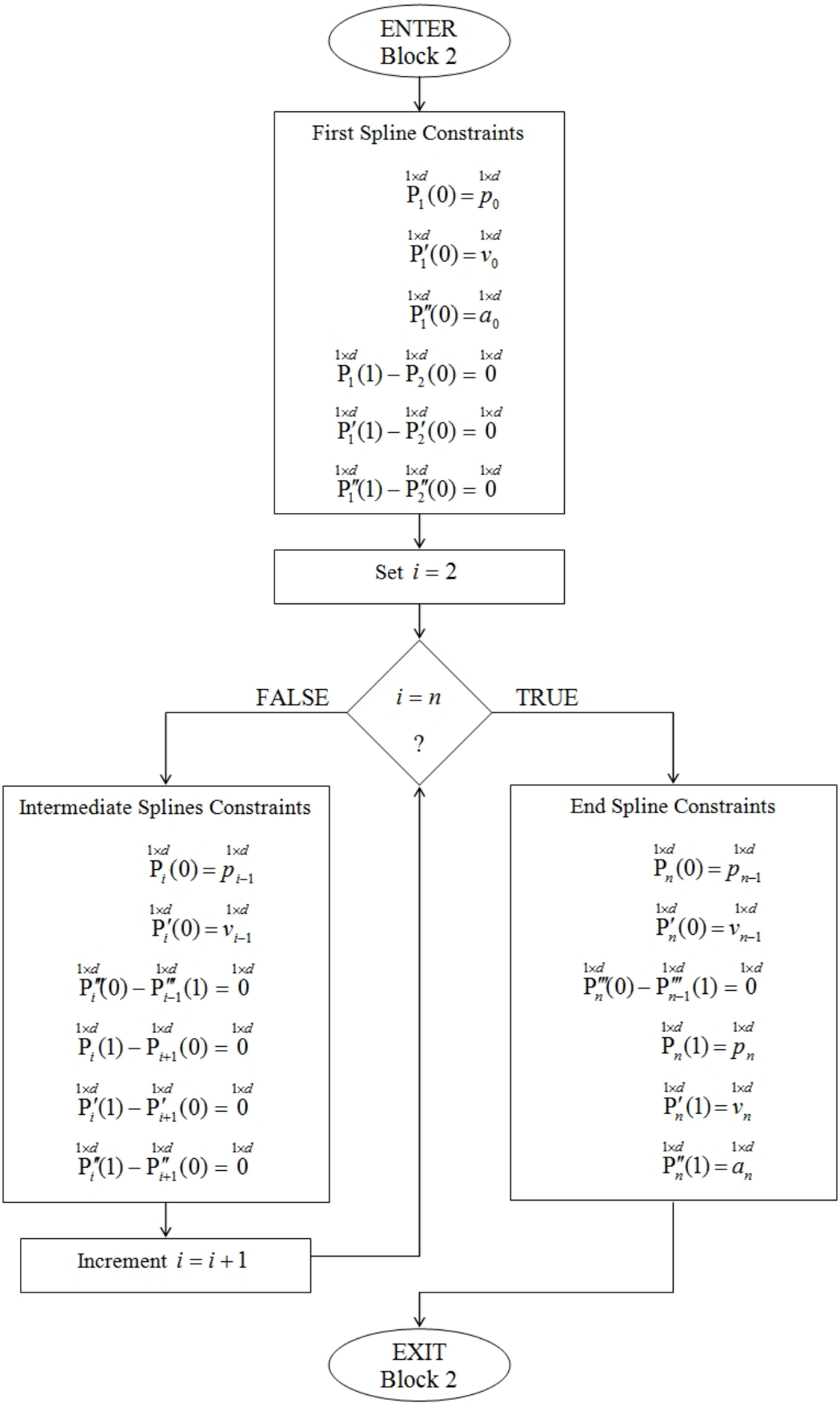

Fig. 5.4. Structure of block 2 in the $C3$ interpolation method.

Fig. 5.4 is the structure of block 2 reported in Fig. 5.2. Once said equations are written, they form a linear system of the type

$$\overset{6n\times 6n}{[A]} \cdot \overset{6n\times d}{[x]} = \overset{6n\times d}{[B]} \tag{5.6}$$

where the matrix $\overset{6n\times 6n}{[A]}$ is composed by zeroes and integers whose absolute value is of the form $\frac{j!}{(j-k)!}$ (or $\frac{j!}{2\cdot(j-k)!}$ or $\frac{j!}{6\cdot(j-k)!}$ when these simplifications are allowed within the system), with $0 \leq k \leq 3$ ($k \in \mathbb{N}$ corresponds to the derivative degree) and $0 \leq j \leq 5$.

More in details, the matrix $\overset{6n\times 6n}{[A]}$ is of the type

$$\overset{6n\times 6n}{[A]} = \begin{bmatrix} M & N_U & Z & \cdots & Z \\ N_L & N & N_U & \ddots & \vdots \\ Z & N_L & \ddots & \ddots & Z \\ \vdots & \ddots & \ddots & \ddots & N_U \\ Z & \cdots & Z & N_L & N \end{bmatrix} \tag{5.7}$$

where M, N_U, N_L, N, and Z are the matrices

$$\overset{6\times 6}{[M]} = \begin{bmatrix} 1 & 0 & 0 & 0 & 0 & 0 \\ 0 & 1 & 0 & 0 & 0 & 0 \\ 0 & 0 & 2 & 0 & 0 & 0 \\ 1 & 1 & 1 & 1 & 1 & 1 \\ 0 & 1 & 2 & 3 & 4 & 5 \\ 0 & 0 & 2 & 6 & 12 & 20 \end{bmatrix} \tag{5.8}$$

$$\overset{6\times6}{[N_U]} = \begin{bmatrix} 0 & 0 & 0 & 0 & 0 & 0 \\ 0 & 0 & 0 & 0 & 0 & 0 \\ 0 & 0 & 0 & 0 & 0 & 0 \\ -1 & 0 & 0 & 0 & 0 & 0 \\ 0 & -1 & 0 & 0 & 0 & 0 \\ 0 & 0 & -2 & 0 & 0 & 0 \end{bmatrix} \tag{5.9}$$

$$\overset{6\times6}{[N_L]} = \begin{bmatrix} 0 & 0 & 0 & 0 & 0 & 0 \\ 0 & 0 & 0 & 0 & 0 & 0 \\ 0 & 0 & 0 & 6 & 24 & 60 \\ 0 & 0 & 0 & 0 & 0 & 0 \\ 0 & 0 & 0 & 0 & 0 & 0 \\ 0 & 0 & 0 & 0 & 0 & 0 \end{bmatrix} \tag{5.10}$$

$$\overset{6\times6}{[N]} = \begin{bmatrix} 1 & 0 & 0 & 0 & 0 & 0 \\ 0 & 1 & 0 & 0 & 0 & 0 \\ 0 & 0 & 0 & -6 & 0 & 0 \\ 1 & 1 & 1 & 1 & 1 & 1 \\ 0 & 1 & 2 & 3 & 4 & 5 \\ 0 & 0 & 2 & 6 & 12 & 20 \end{bmatrix} \tag{5.11}$$

$$\overset{6\times6}{[Z]} = \begin{bmatrix} 0 & 0 & 0 & 0 & 0 & 0 \\ 0 & 0 & 0 & 0 & 0 & 0 \\ 0 & 0 & 0 & 0 & 0 & 0 \\ 0 & 0 & 0 & 0 & 0 & 0 \\ 0 & 0 & 0 & 0 & 0 & 0 \\ 0 & 0 & 0 & 0 & 0 & 0 \end{bmatrix} \tag{5.12}$$

$$\overset{6n\times d}{[x]} = \begin{bmatrix} \overset{1\times d}{C_{1,0}} \\ \overset{1\times d}{C_{1,1}} \\ \overset{1\times d}{C_{1,2}} \\ \overset{1\times d}{C_{1,3}} \\ \overset{1\times d}{C_{1,4}} \\ \overset{1\times d}{C_{1,5}} \\ \vdots \\ \overset{1\times d}{C_{n,0}} \\ \overset{1\times d}{C_{n,1}} \\ \overset{1\times d}{C_{n,2}} \\ \overset{1\times d}{C_{n,3}} \\ \overset{1\times d}{C_{n,4}} \\ \overset{1\times d}{C_{n,5}} \end{bmatrix} \qquad (5.13) \qquad \overset{6n\times d}{[B]} = \begin{bmatrix} \overset{1\times d}{p_0} \\ \overset{1\times d}{v_0} \\ \overset{1\times d}{a_0} \\ \overset{1\times d}{0} \\ \overset{1\times d}{0} \\ \overset{1\times d}{0} \\ \vdots \\ \overset{1\times d}{p_{i-1}} \\ \overset{1\times d}{v_{i-1}} \\ \overset{1\times d}{0} \\ \overset{1\times d}{0} \\ \overset{1\times d}{0} \\ \overset{1\times d}{0} \\ \vdots \\ \overset{1\times d}{p_{n-1}} \\ \overset{1\times d}{v_{n-1}} \\ \overset{1\times d}{0} \\ \overset{1\times d}{p_n} \\ \overset{1\times d}{v_n} \\ \overset{1\times d}{a_n} \end{bmatrix} \qquad (5.14)$$

The unknown matrix $\overset{6n\times d}{[x]}$ is the vector of the unknown vector coefficients $\overset{1\times d}{\mathrm{C}_{\mathrm{i,j}}}$ (equation 5.13), while the matrix $\overset{6n\times d}{[B]}$ (defined in equation 5.14) is the corresponding vector of the known terms, which includes null vectors of the form $\overset{1\times d}{0}$ and the geometric condition vectors $\overset{1\times d}{p_{\mathrm{i-1}}}$, $\overset{1\times d}{v_{\mathrm{i-1}}}$, $\overset{1\times d}{p_{\mathrm{n}}}$, $\overset{1\times d}{v_{\mathrm{n}}}$, $\overset{1\times d}{a_0}$, $\overset{1\times d}{a_{\mathrm{n}}}$ (with $1 \leq i \leq n$).

At the step indicated in block 3 of Fig. 5.2, the interpolation of points occurs into two sub-steps. The first sub-step, which refers to block 3a, is to solve the linear system 5.6 generated in block 2 of Fig. 5.2. This system can be solved in different ways (e.g. with an LU solver). The second sub-step consists in using the

coefficients $\overset{1\times d}{C}_{i,j}$, resulting from the computation made in block 3a, within the block 3b of Fig. 5.2, whose logic scheme is presented in Fig. 5.5. This is done in order to record the interpolation line formed by the n piecewise curves of the form 5.1 together with their derivatives.

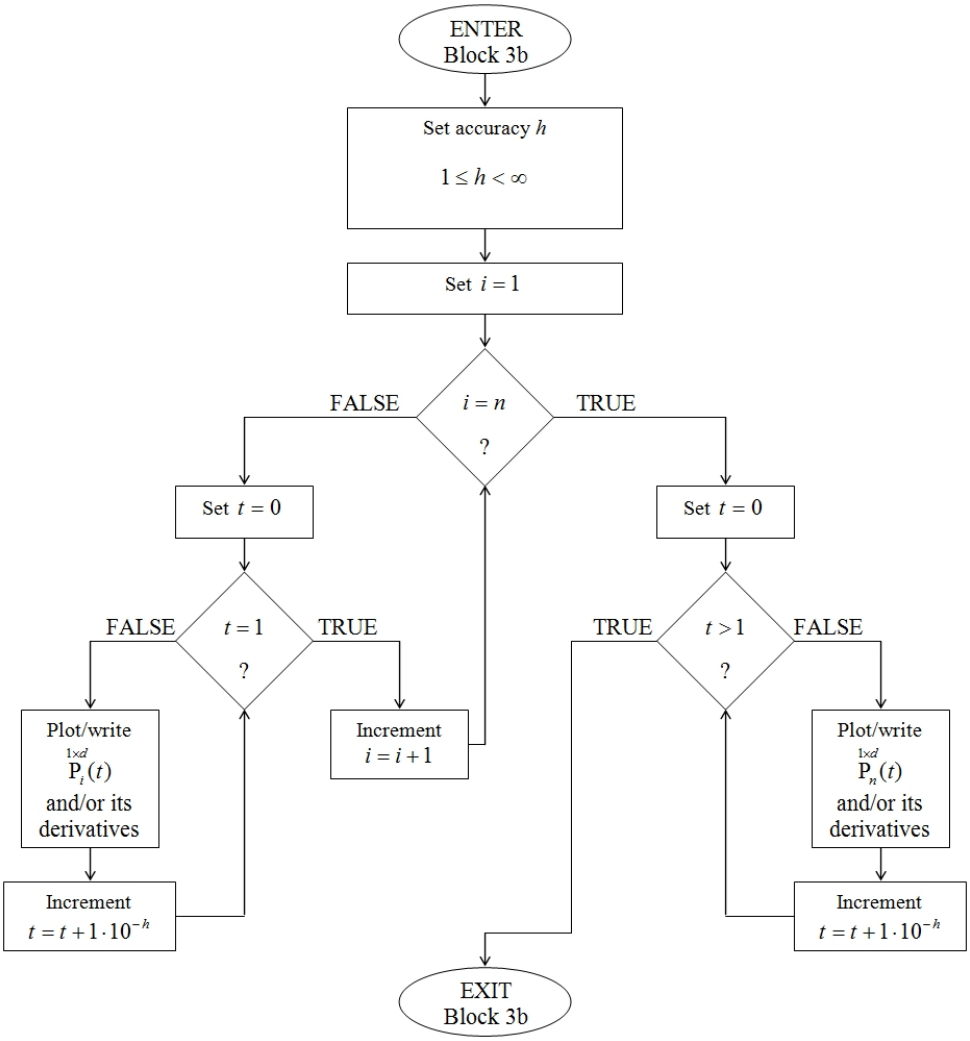

Fig. 5.5. Structure of block 3b in the $C3$ interpolation method.

Fig. 5.5 is the structure of block 3b reported in Fig. 5.2. Once the curve is recorded, the designer can then adjust the geometric conditions to modify the curve accordingly to his needs (step of block 4). This process can be repeated until the designer decides to proceed storing the curve and interpolated points in a database (step of block 5).

The whole procedure works in 2D or 3D and can be applied to design smooth lines in space, which could be used not only to generate solids of rotation but also planar sections of engine nacelles, or frames of completely asymmetric bodies.

5.3. Implementation of the method

The method discussed in section 5.2 has been developed theoretically. The main benefits of its application, however, have a practical basis. In particular, this method can be implemented into an apposite software. Computer graphics are usually achieved[14] by using some traditional programming languages, such as C++, Fortran or Pascal.

In this work a numerical computation program is used instead. Given the high mathematical and matricial representation upon which the method is based, Matlab® was chosen as the basis software to develop this design tool. In fact, Matlab® incorporates many mathematical and programming commands and libraries, whose algorithms are very optimised. This commercial program, which is spread among industrial, government and academic users around the world, also includes remarkable graphical capabilities. Moreover, since Matlab® is based on C language, it runs relatively fast: its basic element is an array that does not require dimensioning, so it takes less time to be computed[15].

The following is a list of the capabilities developed in Matlab® code for reproducing the $C3$ interpolation method presented in section 5.2.

- **Representation of the interpolation curves in a 3D space**. This is allowed automatically by the method, since it is defined accounting for the three-dimensional coordinates of the position, velocity and acceleration vectors involved within the design scheme.

[14] See ref. [22].
[15] Information retrieved on ref. [22].

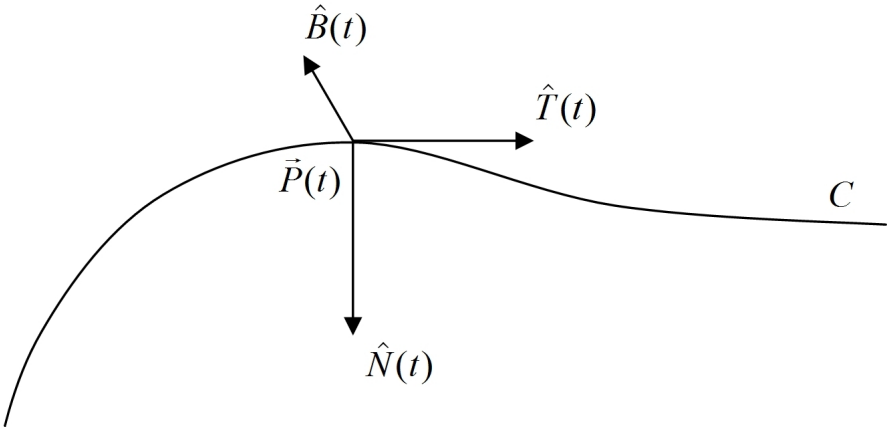

Fig. 5.6. Vectors in the Frenet-Serret frame.

- **Representation of the TNB frame**. The Frenet-Serret or TNB frame is the representation in space of the Tangent, Normal, and Binormal unit vectors of a curve, often called $\hat{T}$, $\hat{N}$, and $\hat{B}$; alternatively, since $\hat{T}$, $\hat{N}$, and $\hat{B}$ are unit vectors, they might also be called $\hat{e}_1(t)$, $\hat{e}_2(t)$, and $\hat{e}_3(t)$ respectively. These vectors are intrinsic properties of a curve, because they depend only on the figure itself and not on the particular choice of the coordinate axes[16]. Given the generic curve C of Fig. 5.6 parameterised in t, then $\hat{T}(t)$, $\hat{N}(t)$, and $\hat{B}(t)$ are defined[17] as follows

$$\hat{T}(t) = \frac{\vec{P}'(t)}{\left|\vec{P}'(t)\right|} \tag{5.15}$$

$$\hat{N}(t) = \frac{\vec{L}(t)}{\left|\vec{L}(t)\right|} \tag{5.16}$$

$$\hat{B}(t) = \hat{T}(t) \times \hat{N}(t) \tag{5.17}$$

where $\vec{P}(t)$ is the position vector as a function of the parameter t, $\vec{P}'(t)$ and

[16] Any geometric figure may have intrinsic and extrinsic properties. For instance, a triangle has three angles and three edges, regardless of the choice of coordinates, whilst the slope of a curve depends on the particular coordinates chosen, which makes it an extrinsic property of the curve.

[17] For a full demonstration of the relations see for instance ref. [121] and [132].

$\vec{P}''(t)$ are its first and second derivatives with respect to parameter t, while $\vec{L}(t)$ is the difference between $\vec{P}''(t)$ and the projection of $\vec{P}''(t)$ onto $\vec{P}'(t)$; in particular, $\vec{L}(t)$ can be expressed as:

$$\vec{L}(t) = \vec{P}''(t) - \frac{\vec{P}''(t) \bullet \vec{P}'(t)}{\left|\vec{P}'(t)\right|^2} \cdot \vec{P}'(t) \tag{5.18}$$

Knowing $\hat{N}(t)$ from eq. 5.16 and 5.18, and considering from eq. 5.17 that $\hat{N}(t) = \hat{B}(t) \times \hat{T}(t)$, the curvature $\vec{\kappa}(t)$ is then defined as

$$\vec{\kappa}(t) = \frac{\left|\vec{P}'(t) \times \vec{P}''(t)\right|}{\left|\vec{P}'(t)\right|^3} \cdot \hat{N}(t) = \frac{\vec{P}'(t) \times \vec{P}''(t)}{\left|\vec{P}'(t)\right|^3} \times \hat{T}(t) \tag{5.19}$$

Therefore, it is evident how the tangent $\vec{P}'(t)$ and acceleration $\vec{P}''(t)$ vector of a curve, as well as its curvature $\vec{\kappa}(t)$, does not depend on the particular coordinate system considered. The radius of curvature has a magnitude defined as

$$R_{curv}(t) = \frac{1}{|\vec{\kappa}(t)|} \tag{5.20}$$

- **Porcupine curvature analysis**. This kind of analysis is helpful to the designer for visually assessing the quality of the curvature, and plotting on the graph, at each point of the profile, a vector having the same direction of the normal vector and the modulus provided by the curvature analysis in that point.

- **File-export function**. Export the curve into an `*.*igs` file. The Initial Graphics Exchange Specification (IGES), pronounced eye-jess, defines[18] a data format for exchanging digital information among computer-aided design

[18] See ref. [21].

systems. This is a kind of neutral format which is compatible with most of the commercial CAGD software, included CATIA®v5.

The details of the code are not reported in this thesis, but some features of the application created in Matlab® are described in the next paragraph.

5.3.1. Description of the Matlab® application

A script called `commandscript` is used to launch the application. It is necessary to declare a matrix of inputs, of the form:

$$\{E\} = \{[E_0], [E_1], ..., [E_n]\} \tag{5.21}$$

Each element $[E_i]$ of $\{E\}$ corresponds to the geometrical characteristics of each construction point. Every element is a matrix: the first row contains the 3D Cartesian coordinates of its position, the second row its velocity components; the third row, to be inserted only for the first and the last construction point, includes the acceleration components.

After this declaration, the script runs the function `ZESpline`, created to evaluate the points forming the curve, the Frenet-Serret unit vectors, the curvature, the radius of curvature and the torsion of the interpolating curve at each computed point (which are more than or equal to the construction points). The number of computed points forming the curve depends on the accuracy parameter $h \in \mathbb{R}$, which is given as an input by the user (if not, $h = 2$ by default) together with the structure $\{E\}$: the higher the accuracy parameter, the greater is the number of points forming the curve. In order to generate this information the set of matrices $\overset{6\times6}{[M]}$, $\overset{6\times6}{[N_U]}$, $\overset{6\times6}{[N_L]}$, and $\overset{6\times6}{[N]}$ is used within the code. Depending on the number of points that the designer wishes to interpolate, these matrices are opportunely assembled to compose the matrix $\overset{6n\times6n}{[A]}$ in general form.

The function `ZESpline` is divided into different sessions. After the first ses-

sion (described above), set for the creation of the new spline, whose characteristic elements are stored in the local workspace, the function opens a set of figures[19] automatically: they show respectively the curve alone, the curve and the construction points with their cinematic characteristics, the curve and the unit vectors of the Frenet-Serret frame, the curve with its porcupine curvature analysis, and the curve with the curvature analysis scaled on the x-axis.

The final session of the function `ZESpline` calls the function `ZEStoiges`, created to export the 'ZE-Spline curve' (or simply the ZE-Spline) into `*.*igs` files. Since the IGES format is a standard commonly used for CAD file interchange, this export feature is an essential task for using the generated curve into commercial software such as CATIA®v5 and others. Unfortunately there is no possibility to create or export directly the new kind of quintic curve as an `*.*igs` file, because it is a brand new type of interpolation technique which obviously is not included in the IGES standard settings. Hence another way of exporting data has to be found.

In order to tackle this problem, the solution herein proposed is to consider a given amount of points belonging to the quintic curve and

1. to export this set of points into an `*.*igs` file, then recreate a spline passing through these points within the commercial software used

2. to create an algorithm for generating a NURBS passing through these points, and export it as an IGES curve directly from Matlab®.

Both option 1 and 2, which are implemented in the code, can be used alternatively to reproduce the original $C3$ curve. In the first case, the points computed by the `ZESpline` function are automatically exported into an `*.*igs` file (satisfying option 1) running the function `ZEStoiges`. This file is then imported into CATIA®v5, where the points can be interpolated with the spline generator of the software. Clearly it is desirable to set an accuracy h high enough[20] to generate an amount

[19] Examples of these figures are provided in chapter 6.

[20] Several tests showed that $h = 2$ is a good value when importing the curve in CATIA®v5, being this the reason why this value is selected by default if the user is not specifying any accuracy.

of points sufficient for maintaining the shape of the profile originally created with the $C3$ interpolation method.

As regards the second case, the vector of computed points is used within the function `globalcurveinterp`, which is arranged to generate the vectors of control points and knots of a B-spline curve. This B-spline is set to interpolate the computed points forming the original quintic line. These control points and knots vectors are then used in the function `ZEStructoexp` to generate a Matlab® object, whose structure is exportable as a unique curve into an `*.*igs` file (satisfying option 2), again using the function `ZEStoiges`.

It is opportune to notice that both options, even if accurate, offer a mean of approximation only: none of them can recreate the curve designed with the $C3$ interpolation method without introducing an error. However, since this error can be very small, the resulting curve is still a faithful representation of the original. Moreover, the designer should expect the curve generated with the commercial software in use (option 1) to be slightly different from the curve exported from Matlab® directly (option 2). This happens because in all probability the algorithm of function `globalcurveinterp` is different from that of the spline generator available in CATIA®v5.

The practical meaning of these considerations is highlighted in paragraph 6.1.1. In fact, chapter 6 presents a possible application of the $C3$ interpolation technique for shaping new kinds of pusher open-rotor nacelles.

6. PRACTICAL DEVELOPMENT OF A NEW NACELLE

The various design methodologies investigated so far are not a mere study of academic nature, but they can be applied in practice to a real design case. The theoretical approach presented in chapter 5 and the computational approach described in chapter 4 are merged herein into a single design methodology, with the purpose of shaping a new pusher open-rotor nacelle concept. More in details, in order to define a new forebody from scratch, the design strategy is refined using the new $C3$ interpolation technique of section 5.3 to shape the profile of the nacelle and applying the computational approach of section 4.2 to verify the aerodynamic characteristics of the new models. These new nacelles are conceived to improve the aerodynamic performance of the engine simulated with the reference model.

6.1. The diffusive nacelle concept

The REMO nacelle is based on the shape originally designed for the GE-36 propfan. The analysis of section 4.3 showed how the axial component of the velocity of air does not decrease ahead of the rotors, despite the nacelle configuration. Section 2.2 reports the statement made in the UDF documentation [11], which specifies how the UDF forebody "[..] is shaped such that its maximum diameter is larger than

the blade hub diameter and is located approximately one blade-length upstream of the first rotor"; soon after, comments are made on the quality of the air flowing before and in-between the rotors: it is said that "[...] this flowpath shape allows the flow to diffuse just upstream of the UDF blade rows, thereby lowering the blade inlet Mach numbers", and it "[...] provides a gentle concavity to the streamlines through the blades, thus eliminating unnecessary accelerating curvatures and high Mach number regions inside the blade rows". This statement is an observation of what is occurring to the airflow when it moves towards the rotors as a consequence of the presence of a nacelle section with maximum diameter higher than the rotor-hub diameter, and placed approximately one blade-length ahead of the first rotor. However, no comments are made on the nacelle shape, which was designed with an all-convex flowpath[1]. When the term concavity is used, it is clearly mentioned not to describe the cowl shape, but the spatial behaviour of the streamlines formed by the air approaching the blades. From the simulation results presented in paragraphs 4.3.1 and 4.3.2, the effects on the airflow diffusion connected to the maximum-diameter larger than the hub diameter are clearly attenuated by the influence of the rotors: the pressure coefficient distribution over the forebody in Fig. 4.20 shows an increase towards positive values (thus a diffusion) only when operating without rotors, whilst by taking into account the effects of the rotating blades the Cp values have a minimum just ahead of the rotors already when cruising at Mach 0.7, meaning that despite its shape the forebody is not diffusing the flow enough: air is still accelerating, increasing its speed until it finally enters the rotor zone.

The UDF engine, reported in Fig. 1.10, shows a bulbous front, which is convex ahead of the rotor. Other pusher open-rotors configurations have been presented in literature with an all-convex forebody, such as the P&W & Allison engine shown[2]

[1] This term is the equivalent for 'external profile of the nacelle'.

[2] The same image was already presented in Fig. 3.1, but it is here reported again for ease of understanding and clarity of reading.

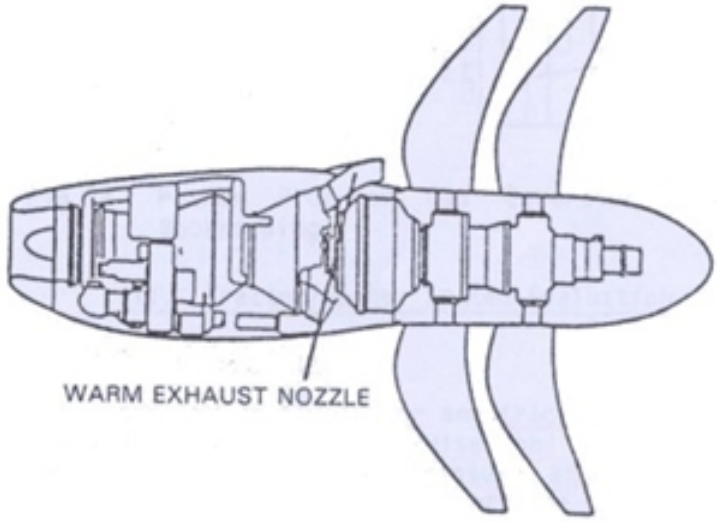

Fig. 6.1. Lateral view of the P&W-Allison propfan.

in Fig. 6.1. The exhaust system is placed upstream of the blades. This shows a bulbous front as well, which appears to be essentially convex ahead of the rotors. Given the convex shape of the nacelle, the behaviour of the airflow all over the forebody is reasonably expected to be similar to that of the UDF case, with the additional problems introduced in this second case: the exhausts impinging into the rotor adds complication to the aerodynamics of the design and so leads to losses within the rotor as well as periodic cyclic stresses whenever each blade passes through each exhaust stream.

Consequently the main concern related to the existing nacelles is that the use of a maximum diameter larger than the hub diameter is not a sufficient condition to properly diffuse the air entering the blades. The possibility to further decrease the speed of airflow before entering the rotors has to be achieved by different means. The basic intuition on how to solve this problem is here represented by the introduction of a concavity in the aft-cowl, just before the rotor zone. Thus the nacelle profile is no longer all convex, but convex-concave instead. The purpose of this shape is to favour an airflow diffusion in front of the blades, especially upstream the root region, regardless the influence played by the suction effects introduced by the rotating blades. For this reason the methodology of sections 5.3

and 4.2 can be used to design what is here called a *diffusive nacelle*.

The purpose of the innovative shape is to lower the velocity of the air entering the rotors by enhancing the diffusion, hence reducing the aerodynamic losses of the blades. In addition, the convex/concave geometry should include at least $G3$ continuity or $C3$ continuity (without presenting local oscillations of curvature) to give a smooth pressure distribution. This equates to a smooth pressure coefficient distribution, which removes localised zones of high speed flow and shock waves when flying at high speeds. This contributes to further decrease the aerodynamic losses. As a consequence, the diffusive nacelle concept is expected to favour a reduction of fuel consumption or, alternatively, the achievement of higher flight velocities.

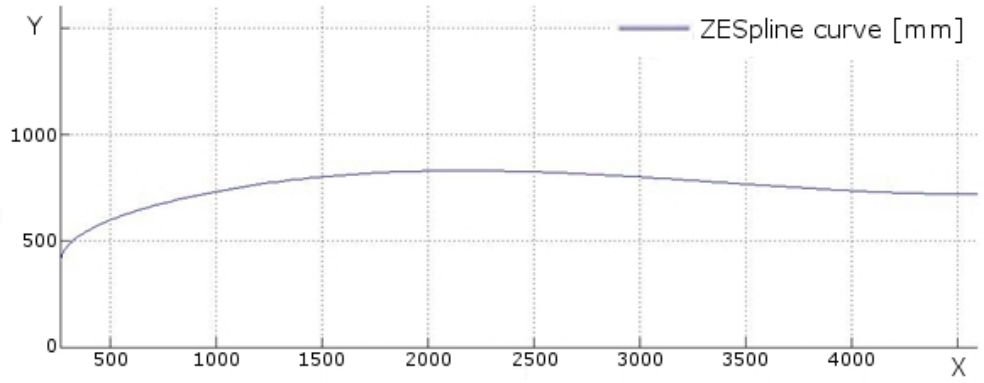

Fig. 6.2. Example of $C3$ profile outline in Matlab® (xy plane, x and y in mm).

An example of this kind of nacelle is depicted in Fig. 6.2, which is a snapshot of an external forebody of a diffusive nacelle obtained from the Matlab® code mentioned in section 5.3 for interpolating points holding $C3$ continuity. In accordance with paragraph 5.3.1, the profile is a ZE-Spline created through a command line of the type

```
[X1,Y1,Z1;Vx1,Vy1,Vz1;Ax1,Ay1,Az1],
[X2,Y2,Z2;Vx2,Vy2,Vz2],
[X3,Y3,Z3;Vx3,Vy3,Vz3;Ax3,Ay3,Az3];
```

where the terms of the type `X`,`Y`, and `Z` indicate the positional coordinates of the

three interpolated points, while `V` and `A` refer respectively to the velocity and acceleration components of the ZE-Spline on these points. The graphical results, achieved when running this code, are described in the next paragraph.

6.1.1. Design procedure for a diffusive nacelle

The 'diffusive nacelle concept' is an innovative solution proposed to improve the existing pusher open-rotor nacelle technology. A diffusion of the flow in front of the rotor can be achieved not only as a consequence of the presence of a nacelle section ahead of the rotor with maximum diameter higher than the hub diameter (as for the UDF case), but also changing the forebody diameter along its aft-cowl in such a way that the external profile of the nacelle results in a convex-concave shape. In the present work, the adjective 'diffusive' is intentionally referred to and used as a synonym of 'convex-concave' nacelle shape.

This kind of profile, an example of which is depicted in Fig. 6.2, is obtained imposing $G3$ continuity constraints using the $C3$ interpolation technique implemented in Matlab® and presented in chapter 5. The main changes with respect to a traditional pusher open-rotor nacelle pertain to the external profile of the forebody, which comprises three construction points: highlight, maximum diameter, and hub point. The maximum-diameter point could coincide for instance with the crest, the Maximum Half Breadth (MHB) or the keel point of the forebody.

To generate the new diffusive shape, these points are interpolated imposing opportune velocity and acceleration vectors to the $C3$ curve (or ZE-Spline), as shown in Fig. 6.3 (where said vectors are displayed as scaled proportionally to their magnitude). The highlight point is interpolated imposing a velocity pointing upwards and a positive acceleration parallel to the horizontal axis, pointing downstream; the tangency at the maximum diameter is set parallel to the axis with a positive direction, while the end point (which might coincide with the hub point) presents an horizontal velocity that might be slightly skewed downwards, with an acceleration

parallel to the vertical axis.

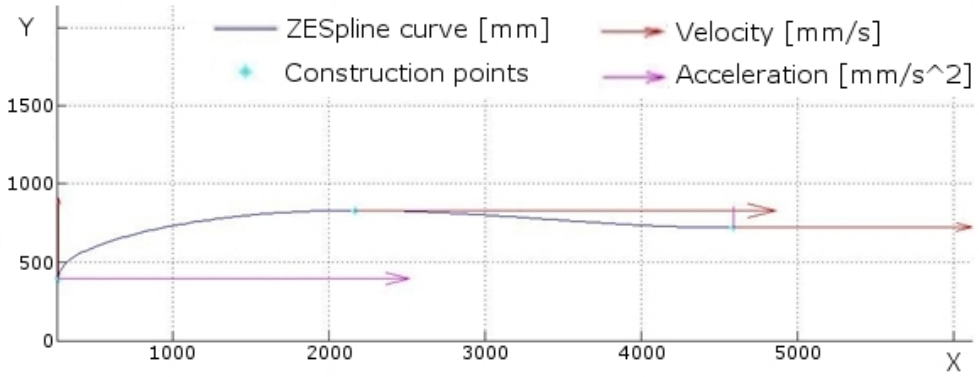

Fig. 6.3. Example of $C3$ profile with construction vectors (xy plane, x and y in mm).

The vectors normal to the profile are depicted in Fig. 6.4 and can be used to generate the porcupine curvature analysis of Fig. 6.5. It is evident how the change from convexity to concavity does occur where the vectors modify their direction on the aft-cowl, pointing downwards and not upwards when moving downstream towards the forebody (from left to right in the picture).

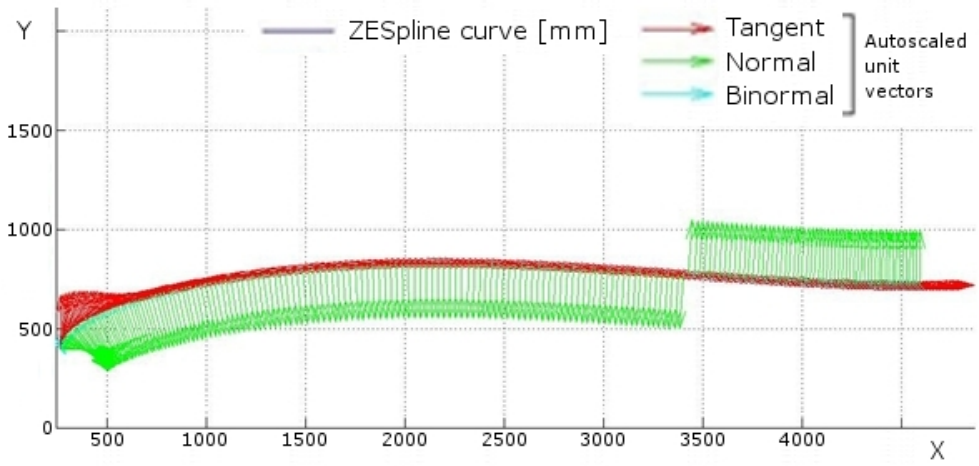

Fig. 6.4. Example of $C3$ nacelle profile in the Frenet-Serret frame created in Matlab®.

The porcupine curvature analysis is useful to graphically assess the quality of the shape. Before exporting the profile into the CFD domain, the designer can evaluate whether the curvature is oscillating, changing too steeply or globally corresponding to his/her requirements.

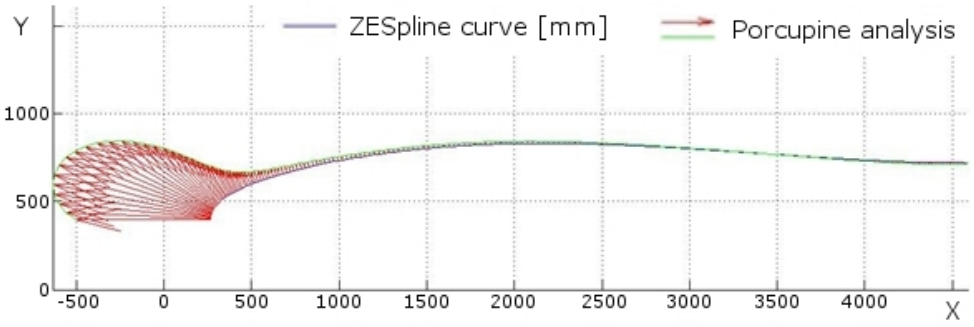

Fig. 6.5. Porcupine curvature analysis of a $C3$ profile elaborated in Matlab®.

With the purpose of illustrating the three-dimensional characteristics of the output data of the Matlab® code, Fig. 6.6 reports an example of the sample $C3$ nacelle profile analysed in the Frenet-Serret frame, so that tangential, normal and bi-normal unit vectors are depicted in space.

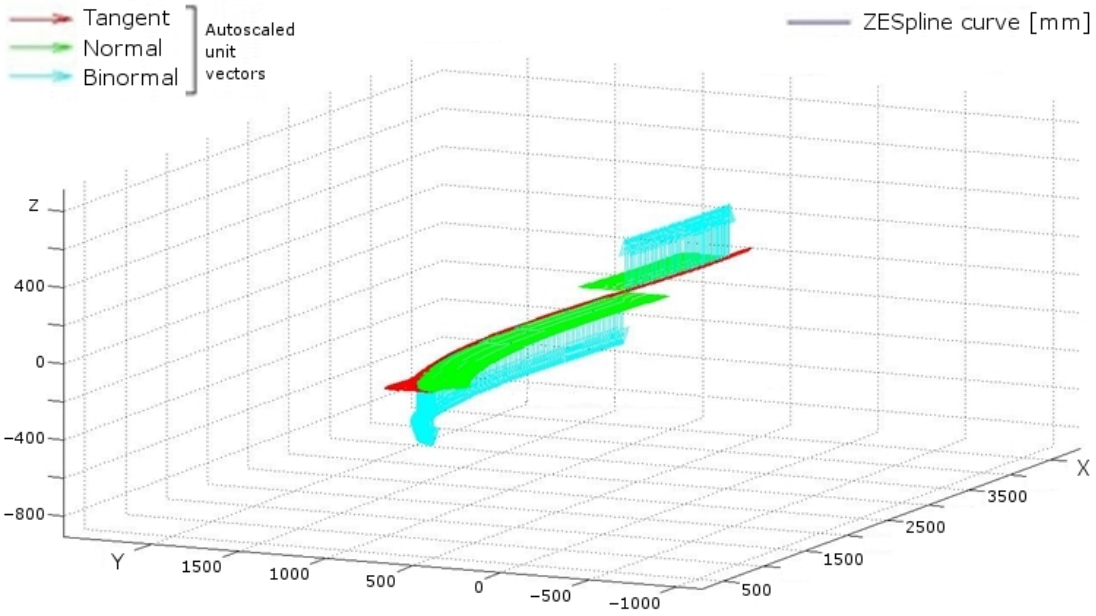

Fig. 6.6. Three dimensional view of a $C3$ nacelle profile in the Frenet-Serret frame.

Although the porcupine representation of the curvature offers an immediate visual perception of the quality of the profile, its curvature can be further analysed by plotting the magnitude of the curvature itself as a function of the horizontal axis which lies in the same plane of the profile. The characteristics of curvature variation and eventual oscillation are better individuated with this kind of analysis,

as reported in Fig. 6.7.

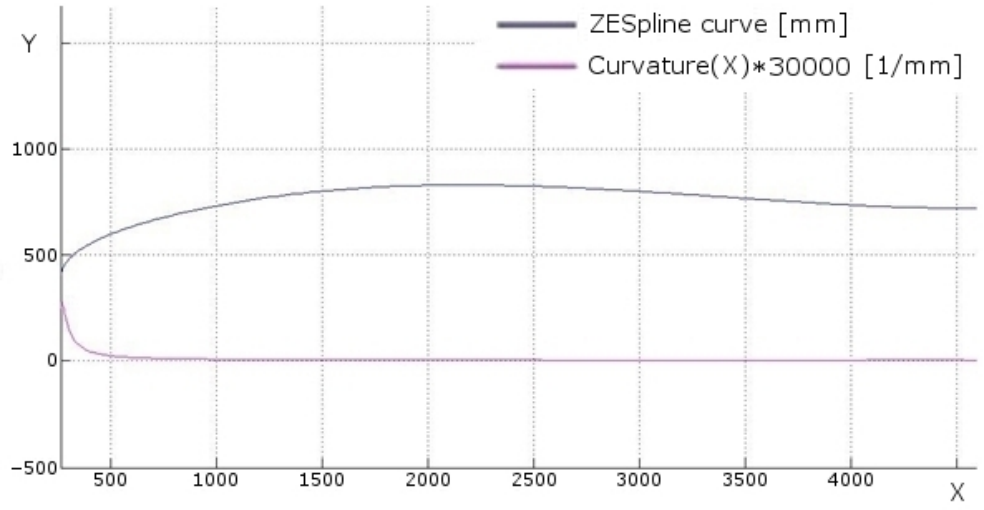

Fig. 6.7. Curvature analysis of a $C3$ profile elaborated in Matlab® as a function of x.

When the designer is satisfied with the output, the profile can be exported and utilised into CATIA®v5, where it is incorporated into the whole engine model and simulation domain. The approach of paragraph 5.3.1 presents two options for importing into CATIA®v5 the profile generated with the $C3$ interpolation technique implemented in Matlab®.

The first approach is to generate the nacelle models making use of the internal spline generator of CATIA®v5, which automatically recreates a $G3$ continuous line passing through the set of points belonging to the profile, like those illustrated in Fig. 6.8. As already mentioned in paragraph 5.3, the resulting profile might slightly differ not only from the original $C3$ curve computed in Matlab®, but also from that obtained with the second approach, which is the B-Spline interpolation built in the Matlab® code, and illustrated in Fig. 6.9.

The strategy for choosing among the two options relies on the assessment of the various output. The diversity between the two profiles and the original $C3$ curve is minimal, as highlighted in Fig. 6.10, which illustrates their curvature[3] as a function

[3]Whilst the curvature of the B-Spline is known directly from the computation of Matlab®, the curvature of the profile generated in CATIA®v5 is calculated and exported using a VBA script (`CurvRadGen.catscript`) as already mentioned in paragraph 4.2.3.

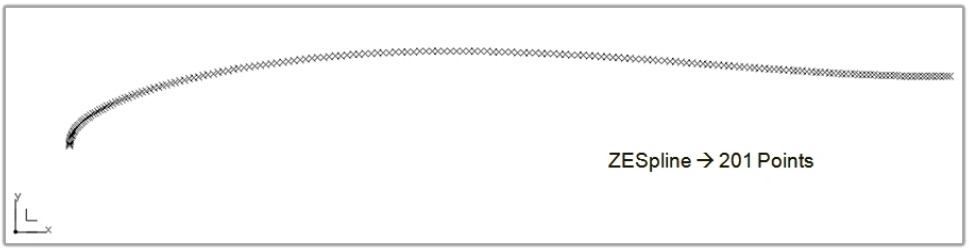

Fig. 6.8. Example of $C3$ profile exported as a set of points from Matlab® and imported into CATIA®v5.

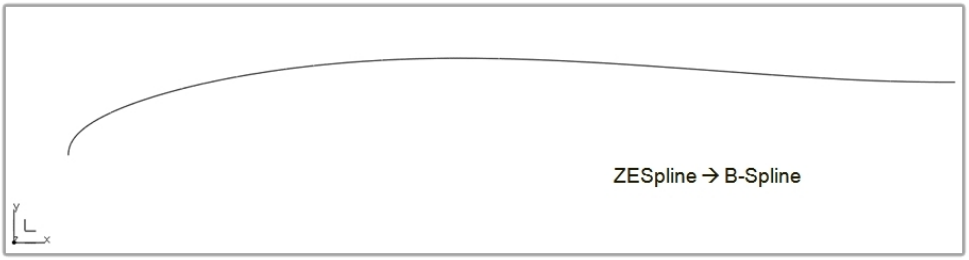

Fig. 6.9. Example of $C3$ profile exported as a B-Spline from Matlab® and imported into CATIA®v5.

of the horizonal axis. Focusing on the three lines depicting the curvature of the original $C3$ curve, of the CATIA®v5-generated curve, and of the B-Spline curve exported from Matlab®, the difference is so small that can not be distinguished, unless an analysis of the absolute error among them is done, as shown in Fig. 6.11.

The absolute error can be defined as

$$\epsilon = |\kappa(t) - \tilde{\kappa}(t)| \tag{6.1}$$

where $\kappa(t)$ is the magnitude of the curvature of the reference $C3$ curve, while $\tilde{\kappa}(t)$ indicates the magnitude of the curvature of the approximated curve. Both magnitudes are computed at the location on the curve determined by the value of parameter t.

The comparison shows that the line generated by CATIA®v5 along the set of points imported from Matlab® presents a higher error only close to the highlight, and a smaller error at the end point of the profile. The B-Spline imported into CATIA®v5 from the Matlab® code presents a smaller error at the highlight, but

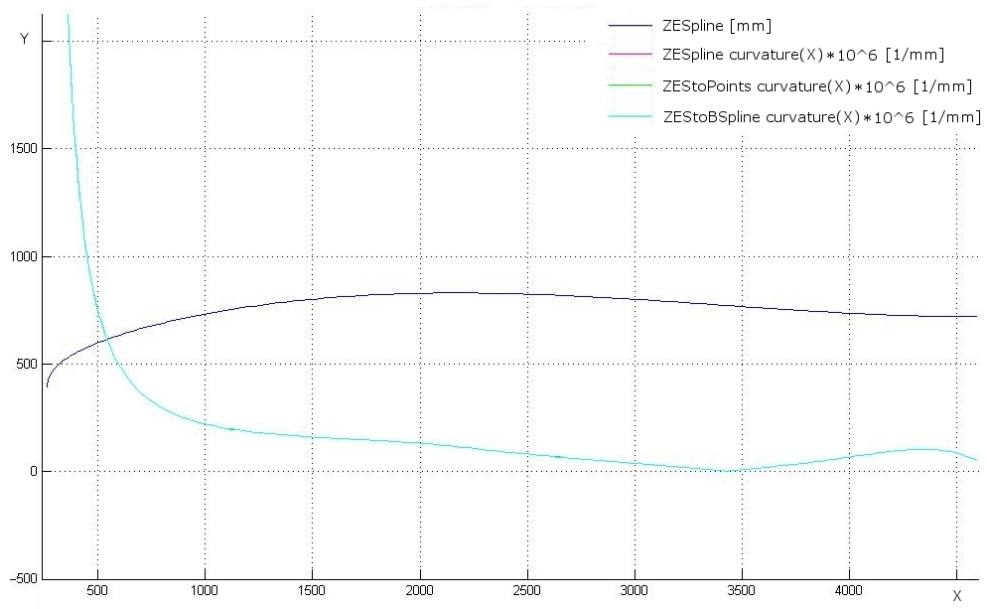

Fig. 6.10. Curvature analysis of curves obtained from different exporting systems.

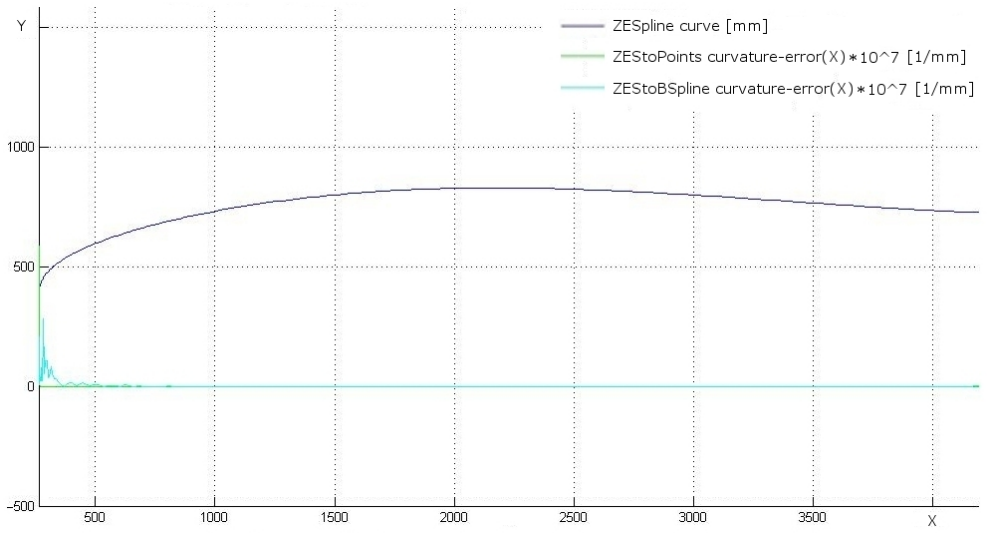

Fig. 6.11. Absolute error of curvature for curves given by different exporting systems.

keeps a higher error distributed on the initial part of the fore-cowl.

Although the error at the highlight is higher with the first approach, the influence of the different shape on the airflow due to this error is less important, because the stagnation point is expected to occur in proximity to the highlight: the airflow is stagnating in this zone when cruising at zero incidence. For these reasons, in this work the first option is preferred to the second and the models described in paragraph 6.1.2 are obtained accordingly.

Despite their presence, the absolute errors have maximum values which do not exceed $7 \cdot 10^{-5}\ 1/mm$, meaning that the original $C3$ curve is well approximated in any case. In fact, from picture 6.11 the maximum ϵ has a magnitude peak of about 700 on the y axis; however the magnitude is scaled by a 10^7 factor in order to allow a better representation on the plot: therefore the real maximum error is $700/10^7 = 0.00007 = 7 \cdot 10^{-5}\ 1/mm$, which is small enough for avoiding sensible shape discrepancy from the original $C3$ curve.

6.1.2. Description of the new models

The REMO engine is used as a baseline for all the new models, whose nacelles are created according to the diffusive concept. The afterbody, comprising the rotor zone and the exhaust nozzle, is always kept the same. For this reason, the classification of these models includes the prefix DOR (Diffusive Open-rotor from REMO). The forebody is modified according to the procedure of paragraph 6.1.1, although the end-point of the forebody coincides with the point of intersection with the first actuator disk, after the hub point. The hub point does not correspond to the end point because all the new models must have a concavity region along the aft-cowl, which sensibly changes its shape just before the rotors, thus altering the diameter of the forebody at the hub point.

Initially the innovative shapes are designed transforming mainly the REMO aft-

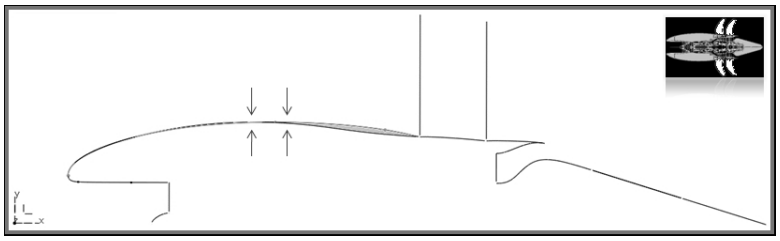

Fig. 6.12. Profile of DOR-1 nacelle.

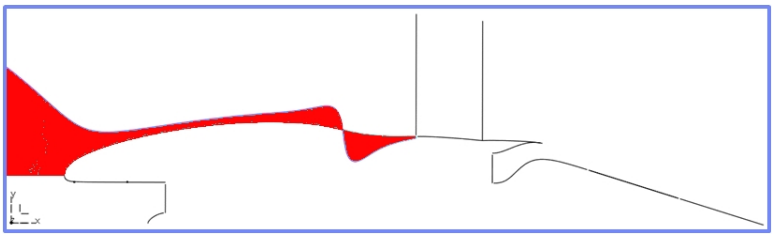

Fig. 6.13. Curvature of DOR-1 external forebody.

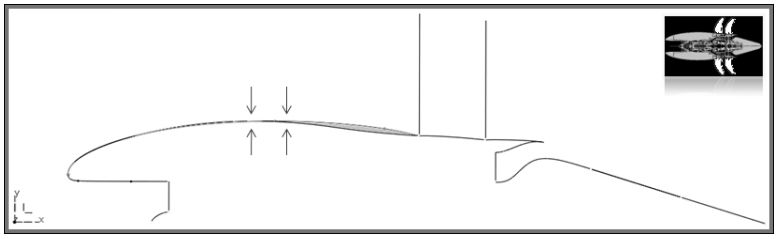

Fig. 6.14. Profile of DOR-2 nacelle.

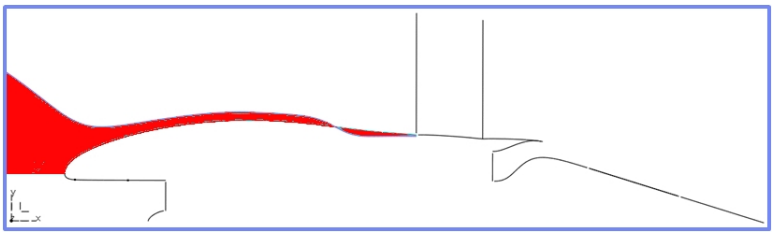

Fig. 6.15. Curvature of DOR-2 external forebody.

cowl[4], by introducing a concavity after the maximum diameter of the nacelle and before the rotor stages. Three examples of nacelles are provided by the models DOR-1, DOR-2, DOR-3 depicted in Fig. 6.12, 6.14 and 6.16, whose curvature analysis is reported in Fig. 6.13, 6.15 and 6.17 respectively.

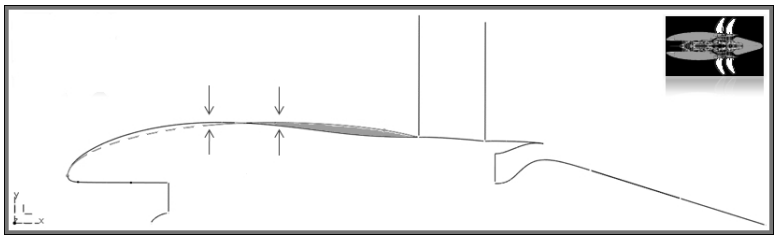

Fig. 6.16. Profile of DOR-3 nacelle.

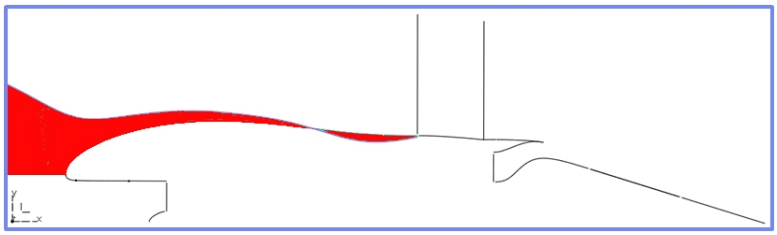

Fig. 6.17. Curvature of DOR-3 external forebody.

The DOR-1 model has the shape that most preserve the original flowpath of the REMO engine. The maximum-diameter point is located in the same position, the fore-cowl is slightly modified while holding $G3$ continuity, while the concavity region introduced before the rotors imparts to the aft-cowl a different contour. The change between convex and concave region occurs in concomitance of the point where the curvature is null, which corresponds to the point where the radius of curvature becomes infinite.

The DOR-2 model presents a fore-cowl wich broadly matches that of the REMO nacelle, although it differs towards the maximum diameter, which is kept the same but located slightly upstream with respect to the original. This allows for a more moderate passage from convexity through concavity on the aft-cowl, as highlighted by the different curvatures of Fig. 6.13 and 6.15. In order to verify the effects of

[4]For the definition of the nacelle parts, see Fig. 3.3, or alternatively Fig. 6.36 in this chapter.

moving further upstream the location of the maximum diameter, the DOR-3 model is designed with a forebody completely different from the original nacelle. Since the high-light point is kept fixed, the fore-cowl is more blunt and short, while the aft-cowl is longer, introducing a gentle variation of curvature when the concavity region appears, as illustrated in Fig. 6.17.

By removing the constraint of a fixed highlight point, thus modifying the whole forebody, the shape of the fore-cowl can be stretched reducing its bluntness, whilst the intake must be modified for allowing this elongation. The area of the compressor face is kept the same of the original, although its configuration varies. A larger ellipsoidal centrebody replaces the old one, and the internal profile of the intake is no longer quasi-horizontal. This profile is designed as a spline interpolating the highlight, the throat and the compressor face points holding $G3$ continuity. The internal profile is connected to the external profile at the highlight through a vertical tangency constraint ($G1$ is granted). Models DOR-4 and DOR-5, depicted in Fig. 6.18 and 6.20, are designed according to this kind of modification. Their porcupine curvature analysis is depicted in Fig. 6.19 and 6.21.

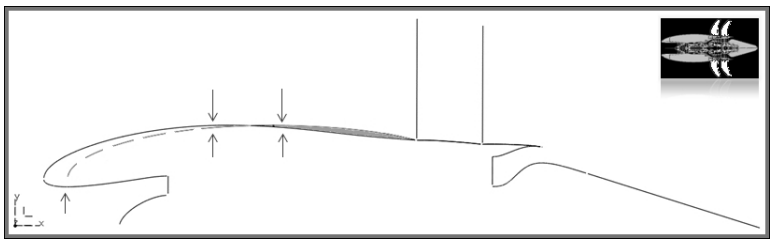

Fig. 6.18. Profile of DOR-4 nacelle.

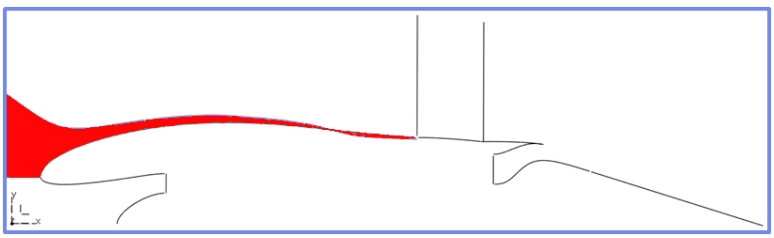

Fig. 6.19. Curvature of DOR-4 external forebody.

The throat point is relocated upstream, following the fore-cowl change, while

its diameter is kept slightly inferior for enhancing the diffusion inside the inlet. However, the area A_c of the compressor face is intentionally unvaried, so that the mass flow is imposed the same in the simulations for all models, comprised the REMO.

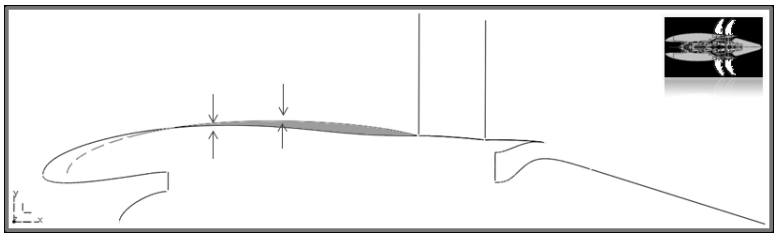

Fig. 6.20. Profile of DOR-5 nacelle.

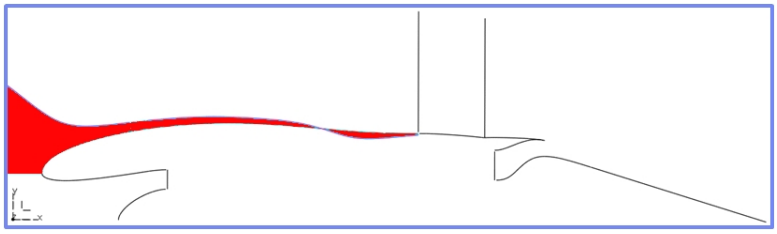

Fig. 6.21. Curvature of DOR-5 external forebody.

The different shape modifications represent various attempts for improving the aerodynamic behaviour of the existing REMO nacelle. This enhancement is inevitably connected to the geometric characteristics of the forebody, which are monitored assessing the changes of curvature occurring when the cowl of the nacelle varies. The aerodynamic features of the DOR-nacelles are elucidated in the next section.

6.2. Simulations and results

The simulations of this section are principally conducted at the fan design-point conditions of the REMO engine ($M_0 = 0.72$, $z = 35\ kft$, F7A7 blades, $\eta_{rot} = 0.81$). The results can be compared with those of paragraph 4.3.1. For this reason, most of the Cp and V_{ax} distributions plots include also the data from the REMO case.

6.2.1. Flow-field analysis

The information necessary to make an analysis of the airflow investing the innovative nacelles consists of the pressure coefficient profiles on the forebody and the axial velocity distributions before the rotors. In analogy with the investigations of paragraph 4.3.1, the axial velocity distributions are taken at a measurement station located on the aft-cowl, with an horizontal coordinate close to that of the hub point.

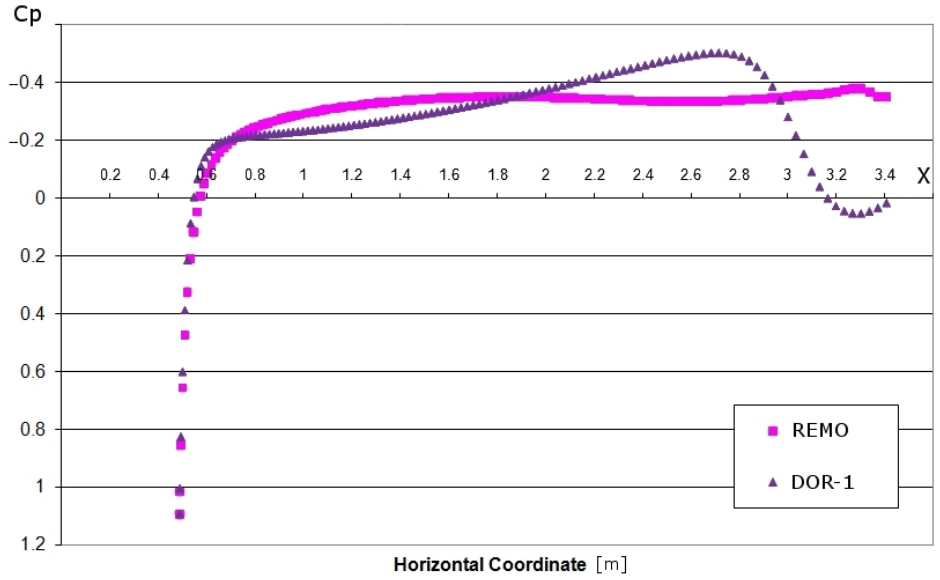

Fig. 6.22. Pressure coefficient distribution of DOR-1 nacelle ($M_0 = 0.72$, $z = 35kft$).

The first illustrations refer to the DOR-1 model: Fig. 6.22 clearly shows how the change from convexity to concavity introduces a wide single oscillation of the Cp profile. While the Cp moves towards the positive values just ahead of the rotors, the minimum Cp appears on the aft-cowl and results too close to the blades. The non-dimensional axial velocity reported in Fig. 6.23 presents a reduction at the blade root of about 13% with respect to the distribution of the REMO case, maintaining itself below the original distribution all along the spanwise direction of the blade. It might be useful to remind the reader that for this kind of figure, the blade is considered to lie horizontally, the air flowing from the top towards the bottom of the figure itself.

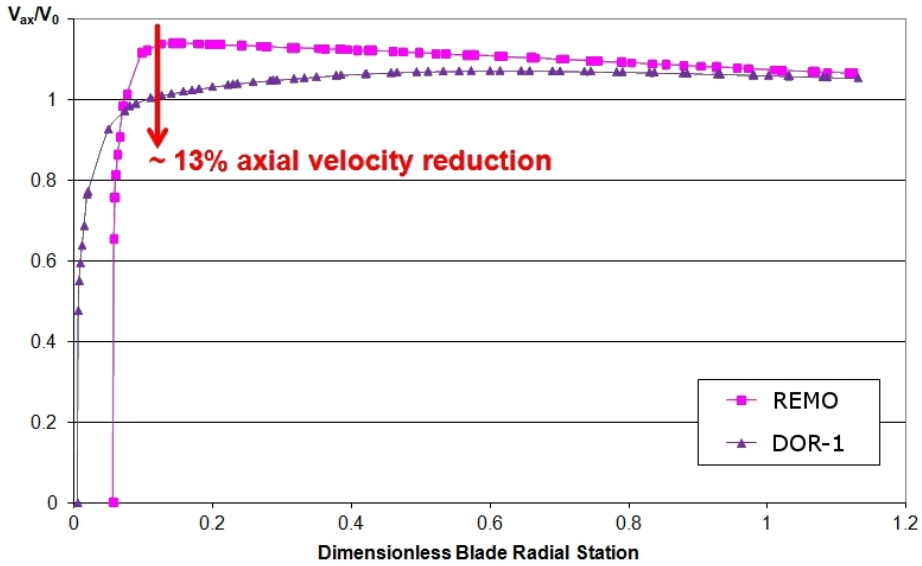

Fig. 6.23. Axial velocity distribution before rotors for DOR-1 nacelle ($M_0 = 0.72$, $z = 35kft$).

The axial velocity distribution of the DOR-1 model depicted in Fig. 6.23, together with the distribution of the other models reported in Fig. 6.25, begins closer to the hub wall, because at the measurement station the aft-cowl is different: its diameter is inferior to the original, accordingly to the shapes depicted in Fig. 6.12, 6.14, 6.16, 6.18 and 6.20, where the grey colour represents the area removed from the REMO nacelle in order to create a concave region before the rotor zone.

The results of the first three models DOR-1, DOR-2, and DOR-3, which have the same intake of the REMO engine, are grouped in Fig. 6.24 and 6.25. It is evident how the horizontal displacement of the maximum diameter in the upstream direction does affect the pressure coefficient distributions. On one hand, this change allows for achieving a better diffusion, with the Cp not oscillating and moving towards positive values after its minimum value, which is moved upstream as well. On the other hand, these shape modifications reduce the difference between the new and the original axial airspeed profile, from approximately 13% to 7% at the blades root, as shown in Fig. 6.25.

Although the diffusion achieved is a benefit for the engine performance, the pressure coefficient decreases too much and reach a minimum value too low: -0.49

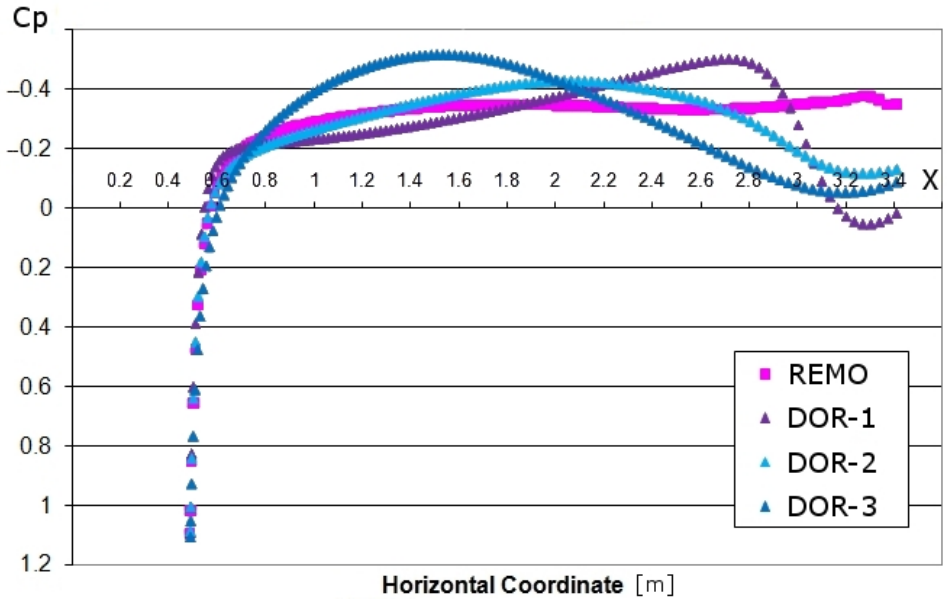

Fig. 6.24. Pressure coefficient distributions for DOR-1, DOR-2 and DOR-3 nacelles.

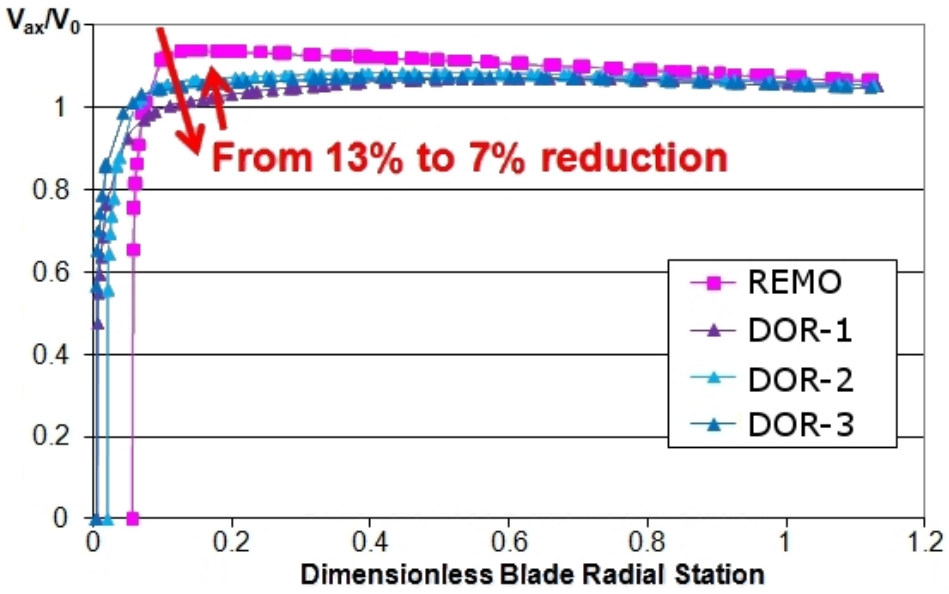

Fig. 6.25. Axial velocity distribution before rotors for DOR-1, DOR-2 and DOR-3 nacelles.

for DOR-1, −0.43 for DOR-2 and −0.52 for DOR-3. The critical Cp is computed according to equation 4.35, which gives $Cp_{cr} = -0.776$ when cruising at Mach 0.72. Supposing that in future the engine might achieve higher flight speeds due to a potential improvement of the core components and blading technology, these cowls would then introduce aerodynamic losses connected to drag rise, since their minimum Cp values are too close or even exceed the critical limit $Cp_{cr} = -0.435$ occurring at $M_0 = 0.8$ (see Fig. 4.14).

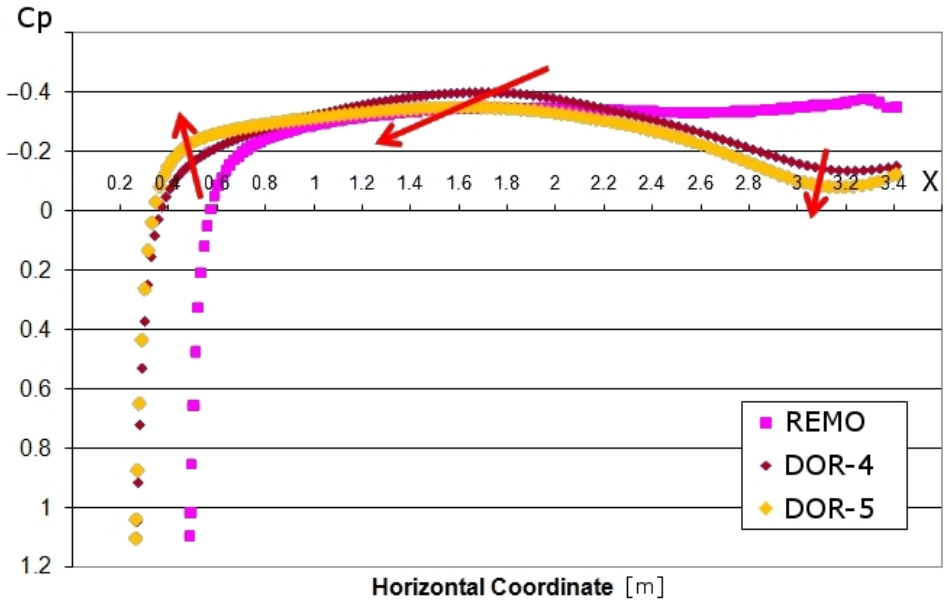

Fig. 6.26. Pressure coefficient distributions for DOR-4 and DOR-5 nacelles.

The Cp profile generated by model DOR-2, shown in Fig. 6.24, differs from the others because the DOR-2 shape has a maximum diameter that is far enough from both the highlight and hub points, so that the curvature varies gently enough all along the forebody, thus discouraging the velocity to increase too rapidly when the airflow approaches the maximum-diameter zone. This suggests that a possible solution for keeping the diffusion effects while forcing the pressure coefficient distribution towards positive values is to allow the fore-cowl and in general the forebody length of model DOR-3 to grow upstream, hence allowing its shape to become more slender.

This corresponds to the modifications introduced with the DOR-4 and DOR-5

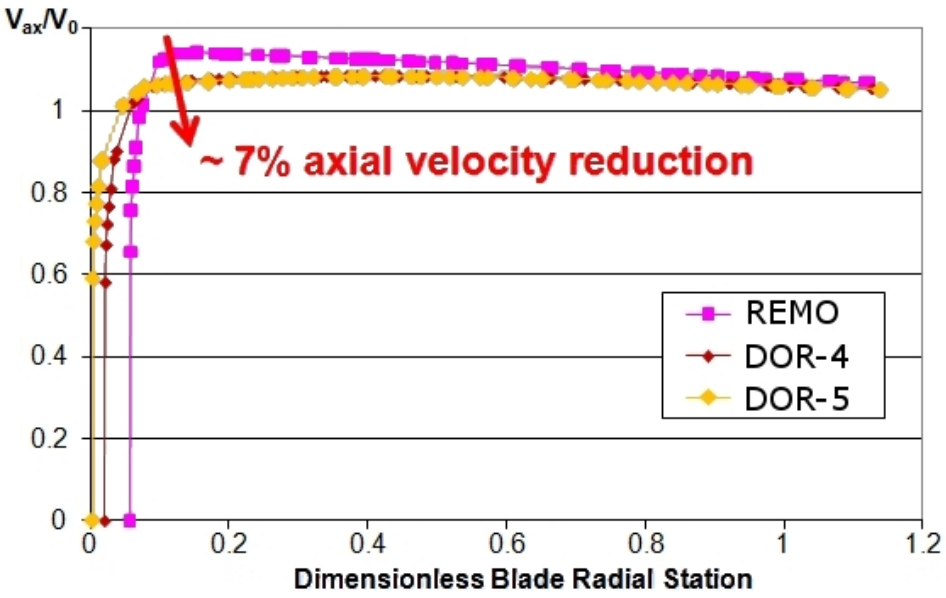

Fig. 6.27. Axial velocity distribution before rotors for DOR-4 and DOR-5 nacelles.

models, and the results reported in Fig. 6.26 and 6.27 confirm that it is possible to reduce the axial velocity distribution before the blade-root zone of about 7% while avoiding the pressure coefficient distribution to drop excessively. In fact, the Cp profile is almost constant and contained among the values -0.3 and -0.4 (far from $Cp_{cr}(0.72) = -0.776$ and $Cp_{cr}(0,8) = -0.435$), before the Cp starts to rise because of the diffusive effects provoked by the concave region on the aft-cowl. The diffusion occurring in front of the rotors is also visible, for instance, in Fig. 6.28, which depicts the contours of axial velocity for the DOR-5 case.

Due to the increased length of the fore-cowl, the intake of these models was modified, as already mentioned in paragraph 6.1.2. Since the lip is sharper than before, an indication of peak lip velocity is useful for assessing the flow acceleration on this part of the nacelle. It is desirable that the airflow never become supersonic when rapidly accelerating away from the stagnation point. The maximum velocity and Mach number of the airflow at the lip never exceed critical values when cruising at Mach 0.72, as shown for example in Fig. 6.29 and Fig. 6.30 respectively[5].

The diffusion effects obtained in front of the rotor-root region are not the only

[5]For the sake of brevity only the DOR-5 case is reported.

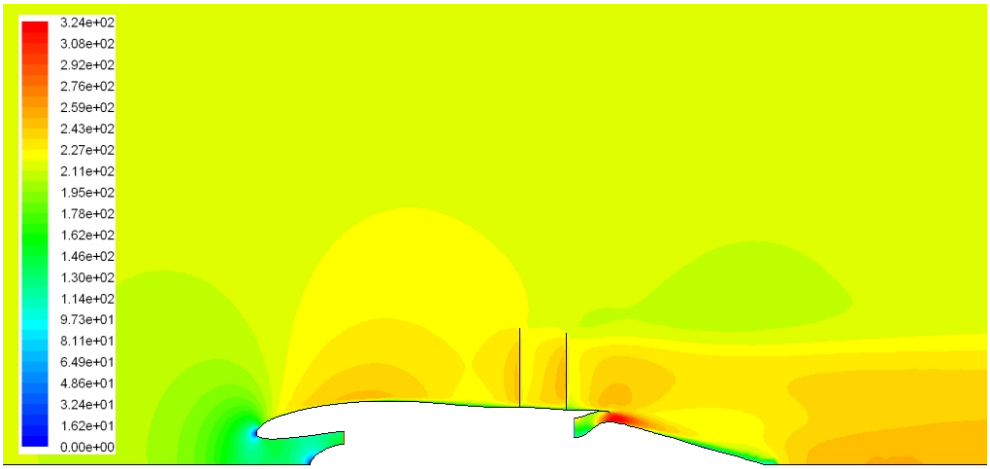

Fig. 6.28. Contours of axial velocity $[m/s]$ for DOR-5 nacelle with operative rotors ($M_0 = 0.72$, $z = \ 35kft$).

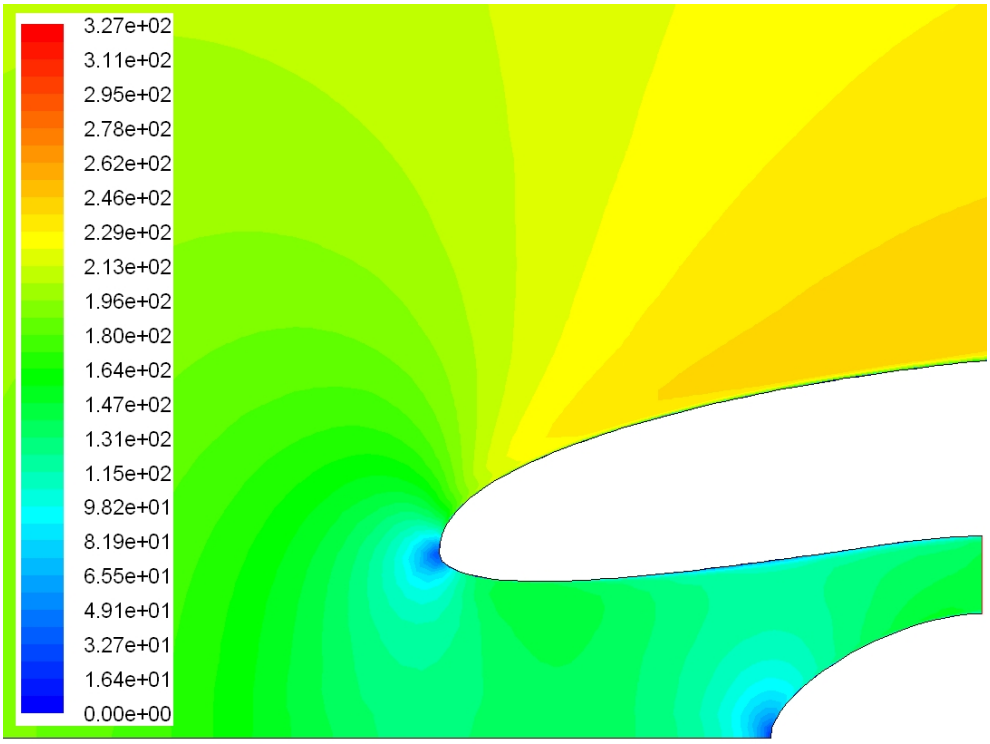

Fig. 6.29. Velocity contours $[m/s]$ at DOR-5 lip ($M_0 = 0.72$, $z = \ 35kft$).

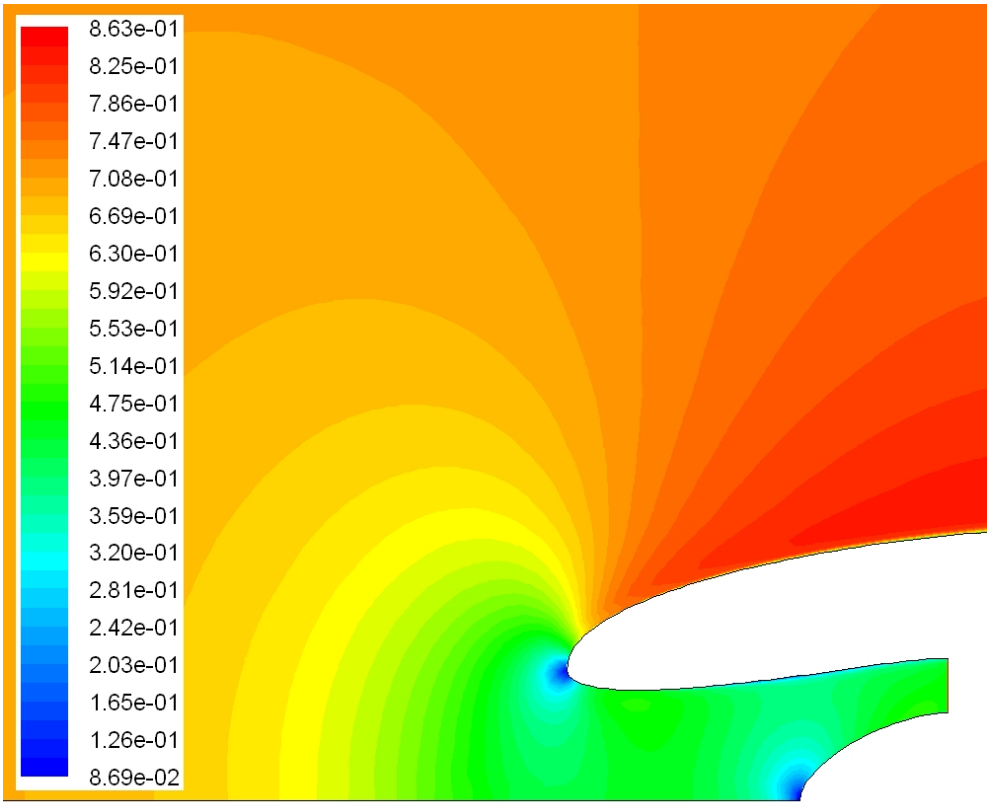

Fig. 6.30. Mach contours at DOR-5 lip ($M_0 = 0.72$, $z = \ 35kft$).

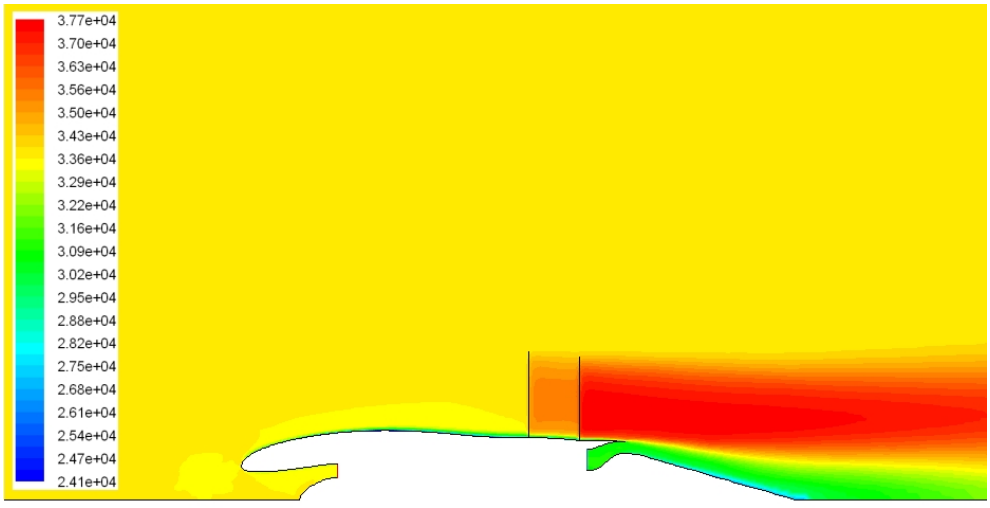

Fig. 6.31. Contours of total pressure $[Pa]$ for DOR-5 nacelle with operative rotors ($M_0 = 0.72$, $z = \ 35kft$).

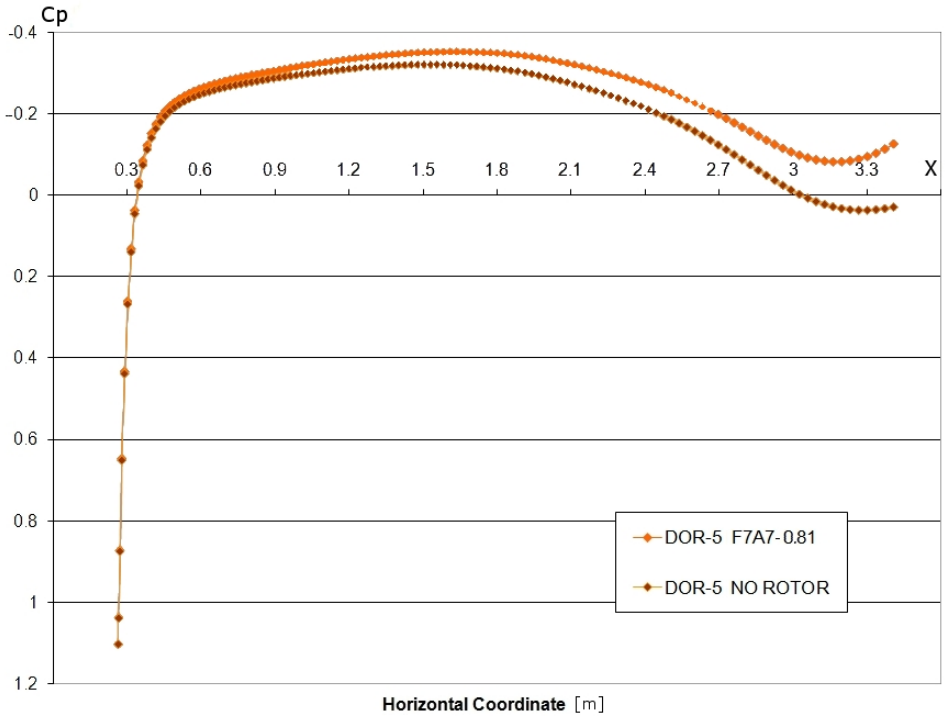

Fig. 6.32. Pressure coefficients of DOR-5 nacelle with rotors on-off ($M_0 = 0.72$, $z = 35kft$).

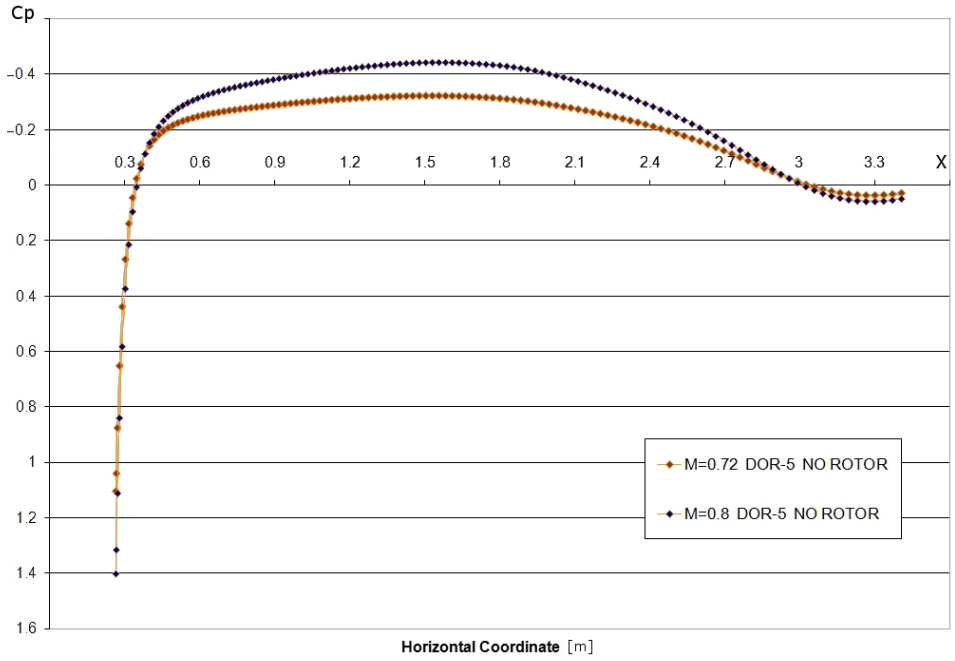

Fig. 6.33. Pressure coefficients of DOR-5 nacelle at different speeds with rotors off ($z = 35kft$).

kind of results which is possible to highlight from the CFD simulations: Fig. 6.32 shows that comparing the airflow on the same DOR-5 nacelle with and without rotors, the presence of the rotors (illustrated as operative in Fig. 6.31) is affecting the flow field up to 80% of the forebody length (starting from the hub). Hence, as for the REMO case, the external rotors are not influencing the airflow close to the highlight. Consequently, the internal profile of a pitot-intake nacelle can be designed without considering the presence of the open rotors.

It is worth to notice that in every plot presenting the pressure coefficient distributions, the effects of air compressibility are evident on the fore-cowl, in particular on the section near the highlight, where $Cp > 1$. These effects grow when the cruise speed increases to $M_0 = 0.8$, as shown by the comparative illustration of Fig. 6.33. The contours of Mach number for the DOR-5 model with rotors off are depicted in Fig. 6.34.

The difference between the pressure coefficient distribution of the nacelle operating without rotors is more accentuated for the DOR-5 than the REMO case (see Fig. 4.23). Given the different shapes and results, an assessment of the pre-entry drag associated to the two different kind of installations could provide further information for understanding the aerodynamic characteristics of the new DOR-5 model when compared to the reference one.

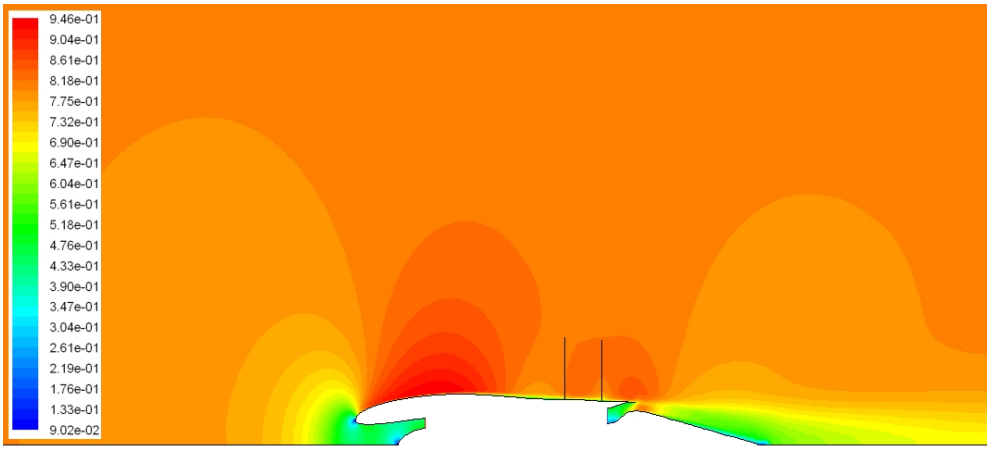

Fig. 6.34. Mach contours of DOR-5 nacelle with rotors off ($M_0 = 0.8$, $z = 35kft$).

6.2.2. Drag estimation

The approach undertaken for this study is based on the notions given in ref. [67] regarding the intake-drag prediction. The models herein compared are the DOR-5 and REMO, whose shapes are illustrated in Fig. 6.35.

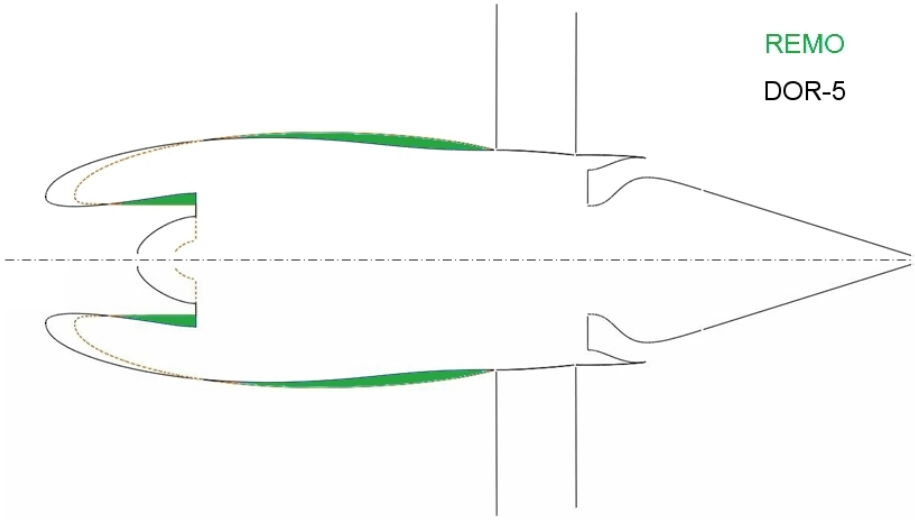

Fig. 6.35. DOR-5 and REMO nacelle profiles.

The complete designation of the various parts of the nacelle profile[6] is fully reported in Fig. 6.36. The forebody consists of two parts, fore-cowl and aft-cowl, and the intake as well can be divided into two parts: the first comprised between the highlight and the throat point (called lip zone[7]) and the second going from the throat to the compressor inlet point (called inlet zone[8]).

Table 6.1 indicates the wetted area computed in Fluent® for every part of the nacelle profiles; for this computation Fluent® considers a 3D nacelle generated as an axisymmetric body of revolution of the 2D profile examined. It is evident that changing the position of the hub point[9] and modifying the aft-cowl has an influence

[6] The designation is presented with less details also in Fig. 3.3.

[7] This part of the intake has not to be confused with the lip point. In the DOR-5 model the lip and throat points are coincident. The lip point for the REMO model ($x = 582\ mm$, $y = 353\ mm$) is not coincident with its throat point (which is at $x = 1070\ mm$, $y = 350\ mm$); the y coordinate is almost the same because the inlet is almost straight.

[8] This designation is adopted in Table 6.3 when considering the different force components acting on the walls of the forebody.

[9] The hub point differs between the two models: it has an inferior diameter in the DOR-5 model.

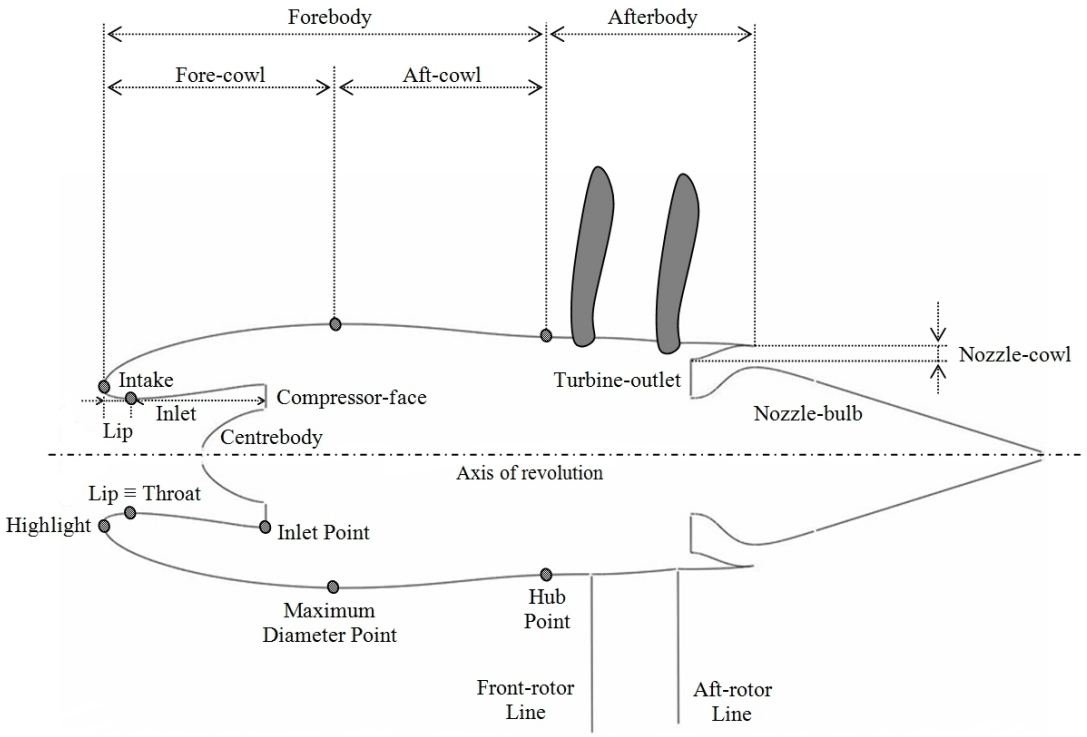

Fig. 6.36. Complete designation of the various parts of a pusher ope-rotor nacelle profile.

Table 6.1. Wetted area $[m^2]$ computed in Fluent® for every part of the nacelle profile.

Nacelle part	REMO	DOR-5
Forebody	14.984641	15.401685
Intake	2.1215165	2.7597644
Centrebody	0.07113722	0.59488815
Afterbody	6.8757777	6.7889433

on the wetted surface of the afterbody, which slightly differs between the REMO and DOR-5 models.

The calculation of the wetted area is necessary for the computation of the pre-entry drag, which can be referred to the whole forebody or to the fore-cowl alone. The theory for defining the pre-entry drag relies on the conservation of momentum for the airflow investing the nacelle. The momentum equation for fluids bound within a control volume B with external surface S is:

$$\sum \vec{F} = \frac{\partial}{\partial t} \int_B \left(\rho \cdot \vec{V}\right) dB + \int_A \left(\vec{V} \cdot \rho \cdot \vec{V} \bullet \hat{n}\right) dA \tag{6.2}$$

For a completely axisymmetric nacelle at cruise conditions, ideally flying at steady flow and zero incidence (as it was assumed in the simulations), the relevant non-zero components are those in the horizontal direction x, hence relation 6.2 becomes

$$\sum F_x = \pm \int_A \left(\rho \cdot V_x^2\right) dA \tag{6.3}$$

where the sign of the integral depends on the directions of V_x and $\hat{n}$ (+ if the vectors are pointing towards the same direction, − on the contrary). The control

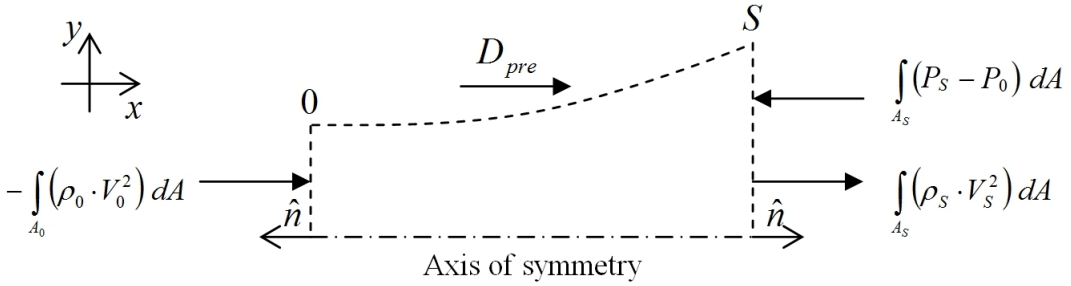

Fig. 6.37. Pre-entry drag and control volume ahead of the intake.

volume binding the streamtube ahead of the intake, from infinity (station 0) to the stagnation point (station S), is presented in the half 2D view of Fig 6.37. The pre-entry drag is here called D_{pre}. Considering all the terms involved, the linear momentum equation (only values in the x-direction will be considered from now

onwards) gives

$$D_{pre} - \int_{A_S} (P_S - P_0)dA = -\int_{A_0} (\rho_0 \cdot V_0^2)dA + \int_{A_S} (\rho_S \cdot V_S^2)dA \tag{6.4}$$

In order to avoid the determination of the stagnation point (station S), it is possible to consider a control volume bound within the intake, from the stagnation point session (station S) to the compressor face (station C), as reported in Fig. 6.38. The reaction forces acting on the fluid, due to the presence of the internal part of the nacelle and the centrebody of the compressor, are R_{in} and R_{cb} respectively.

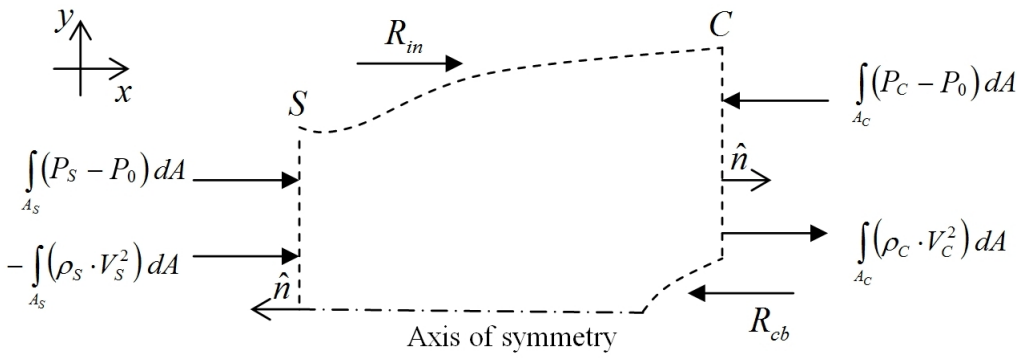

Fig. 6.38. Balance of forces at the inlet control volume.

Considering these new terms, the linear momentum equation for this control volume is:

$$\int_{A_S} (P_S - P_0)dA + R_{in} - R_{cb} - \int_{A_C} (P_C - P_0)dA = -\int_{A_S} (\rho_S \cdot V_S^2)dA + \int_{A_C} (\rho_C \cdot V_C^2)dA \tag{6.5}$$

By rearranging the terms of the momentum equations 6.4 and 6.5 of the two streamtubes in the following system

$$\begin{cases} D_{pre} = \int\limits_{A_S} [(P_S - P_0) + \rho_S \cdot V_S^2]dA - \int\limits_{A_0} (\rho_0 \cdot V_0^2)dA \\ \int\limits_{A_S} [(P_S - P_0) + \rho_S \cdot V_S^2]dA = \int\limits_{A_C} [(P_C - P_0) + \rho_C \cdot V_C^2]dA - R_{in} + R_{cb} \end{cases} \tag{6.6}$$

and by reasonably considering ρ_0 and V_0 always constant all over the entry section A_0 at infinity, it is possible to obtain:

$$D_{pre} = \int_{A_C} \left[(P_C - P_0) + \rho_C \cdot V_C^2\right] dA - R_{in} + R_{cb} - \rho_0 \cdot V_0^2 \cdot A_0 \tag{6.7}$$

The relation defining the forebody (or alternatively the fore-cowl) drag D is

$$D = D_{pre} + F_{ext} \tag{6.8}$$

where F_{ext} is the horizontal force (sum of pressure and viscous forces) acting on the external part of the nacelle starting from stagnation point. By calling F_{in} the horizontal force (sum of pressure and viscous forces) acting on the internal part of the nacelle starting from stagnation point, it is possible to write

$$F_{ext} + F_{in} = F_f + F_i \tag{6.9}$$

where F_i is the horizontal force acting on the internal part of the nacelle starting from the highlight (this boundary is called *intake* in Fluent® simulations), whilst F_f is the horizontal force acting on the external part of the nacelle starting from the highlight, which could be the forebody (then it shall be referred to as F_{fb}) or alternatively the fore-cowl (then it shall be referred to as F_{fc}). The horizontal force acting on the forebody, F_{fb}, can be written as

$$F_{fb} = F_{fc} + F_{ac} \tag{6.10}$$

where F_{fc}, as already mentioned, is the horizontal force acting on the fore-cowl, whilst F_{ac} is the horizontal force acting on the aft-cowl.

Given the balance of forces acting on each part of the engine, as reported in Fig. 6.39, it is evident that $F_{in} + R_{in} = 0$ hence $F_{in} = -R_{in}$, and $F_{cb} - R_{cb} = 0$ so $F_{cb} = R_{cb}$. The terms F_f (i.e. F_{fb} or F_{fc}), F_i and F_{cb} are available from

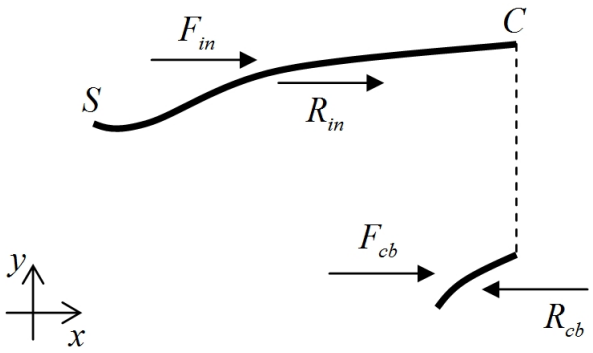

Fig. 6.39. Balance of action-reaction forces internal to the intake.

Fluent® computations; therefore, taking into account the relations between forces and reactions mentioned before, it is convenient to rewrite D as follows:

$$\begin{aligned} D &= D_{pre} + F_{ext} = \\ &= \int_{A_C} [(P_C - P_0) + \rho_C \cdot V_C^2] dA - R_{in} + R_{cb} - \rho_0 \cdot V_0^2 \cdot A_0 + F_{ext} = \\ &= \int_{A_C} [(P_C - P_0) + \rho_C \cdot V_C^2] dA - \rho_0 \cdot V_0^2 \cdot A_0 + F_{cb} + (F_{ext} + F_{in}) = \\ &= \int_{A_C} [(P_C - P_0) + \rho_C \cdot V_C^2] dA - \rho_0 \cdot V_0^2 \cdot A_0 + F_{cb} + (F_f + F_i) \end{aligned} \tag{6.11}$$

As for terms F_{ext} and F_{in}, all the forces F_{cb}, F_f, and F_i (shown in Fig. 6.40) are considered to be a sum of pressure and viscous forces.

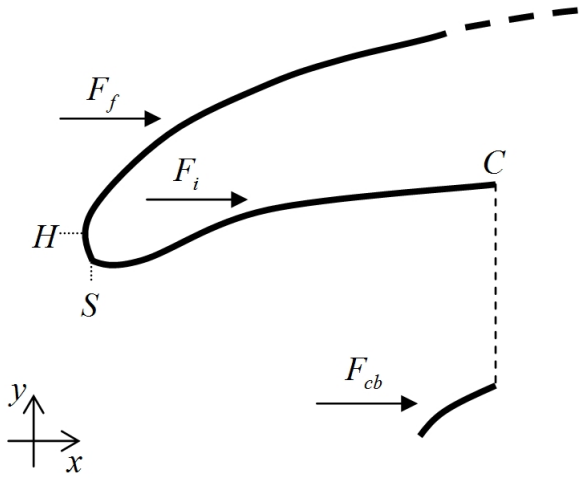

Fig. 6.40. External force and internal forces acting on the intake.

Since the mass flow rate at the compressor $\dot{m}_C$ is known, the term A_0 can be inferred from the following relation (true due to the conservation of mass, i.e. $\dot{m}_0 = \dot{m}_C$, and steady flow condition)

$$A_0 = \frac{\dot{m}_C}{\rho_0 \cdot V_0} \tag{6.12}$$

whilst it is also possible to calculate the term $\int_{A_C} [(P_C - P_0) + \rho_C \cdot V_C^2] dA$ in Fluent®, so that D can be evaluated as:

$$D = \int_{A_C} \left[(P_C - P_0) + \rho_C \cdot V_C^2\right] dA - \rho_0 \cdot V_0^2 \cdot A_0 + F_{cb} + F_f + F_i \tag{6.13}$$

More in details, taking into account $F_f = F_{fb}$, equation 6.13 provides the *nacelle forebody drag* as

$$D_{fb} = \int_{A_C} \left[(P_C - P_0) + \rho_C \cdot V_C^2\right] dA - \rho_0 \cdot V_0^2 \cdot A_0 + F_{cb} + F_{fb} + F_i \tag{6.14}$$

whilst considering $F_f = F_{fc}$ it provides the *nacelle fore-cowl drag* as:

$$D_{fc} = \int_{A_C} \left[(P_C - P_0) + \rho_C \cdot V_C^2\right] dA - \rho_0 \cdot V_0^2 \cdot A_0 + F_{cb} + F_{fc} + F_i \tag{6.15}$$

With the aid of Fluent® and MS-Excel® for the computations, the theory presented can be used to elaborate the results collected in the following tables. A comparison between the two models REMO and DOR-5 is given in Table 6.2, which presents the drag values according to equations 6.14 and 6.15, whose terms are extracted from Table 6.5.

The values of forces presented in Table 6.5 are determined considering the differ-

ent pressure and viscous force contributions calculated in Fluent® and colleted in Table 6.3 and 6.4. Figures from 6.41 to 6.43 visualise the contours of static pressure on the DOR-5 model in the three different simulation cases, and are useful for the interpretation of the sign of the pressure forces calculated in this analysis, which are gauge forces. Basically the pressure force on a wall derives from integrating $(P - P_0)$, that is absolute static pressure minus freestream pressure. The momentum equation on a closed volume gives the same information using either absolute or gauge pressure provided the same is used throughout. But the numerical values of absolute force and gauge force on a particular surface (such as the pre-entry streamtube) will be different. In Fluent® the user can set an operating pressure which might be the freestream ambient pressure or might not; force calculations use pressure defined as $(P - P_{ref})$, which is the difference between the absolute and reference pressure. In all simulations P_{ref} has been defined in the *Reference Values* menu to equal the operating pressure.

The precision of all the values in tables 6.2 to 6.5 is intentionally cut at the second decimal order; consequently the values reported as a sum of other values might not coincide with the algebraic sum of the values appearing in these tables.

Table 6.2. Results of drag computation ($\varepsilon = 0.995$, $z = 35\ kft$, F7A7-0.81).

Model	D_{fb} $[N]$	D_{fc} $[N]$	M_0	Rotors
	857.17	99.78	0.72	On
DOR-5	762.8	303.83	0.72	Off
	1040.45	459.39	0.8	Off
	1149.41	10.26	0.72	On
REMO	997.16	258.41	0.72	Off
	1389.36	409.01	0.8	Off

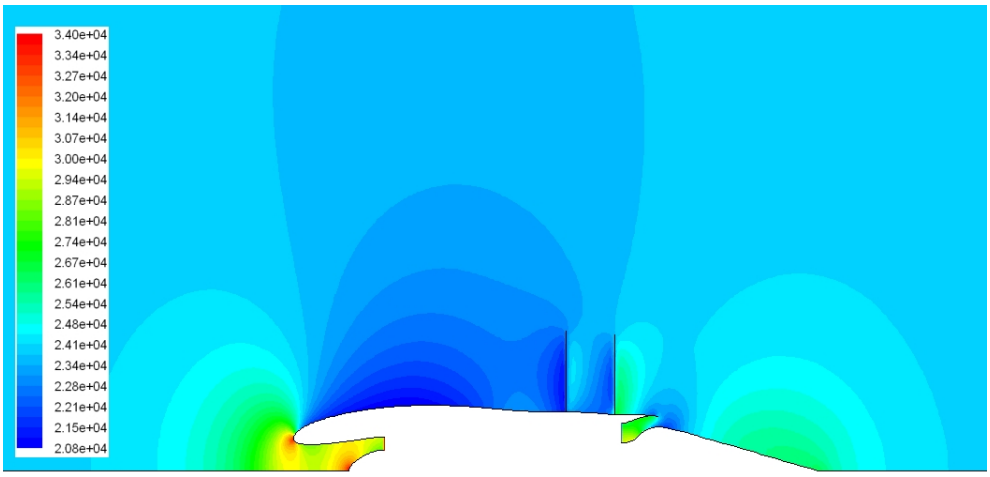

Fig. 6.41. Contours of static pressure $[Pa]$ for DOR-5 nacelle with operative rotors ($M_0 = 0.72$, $z = \ 35kft$).

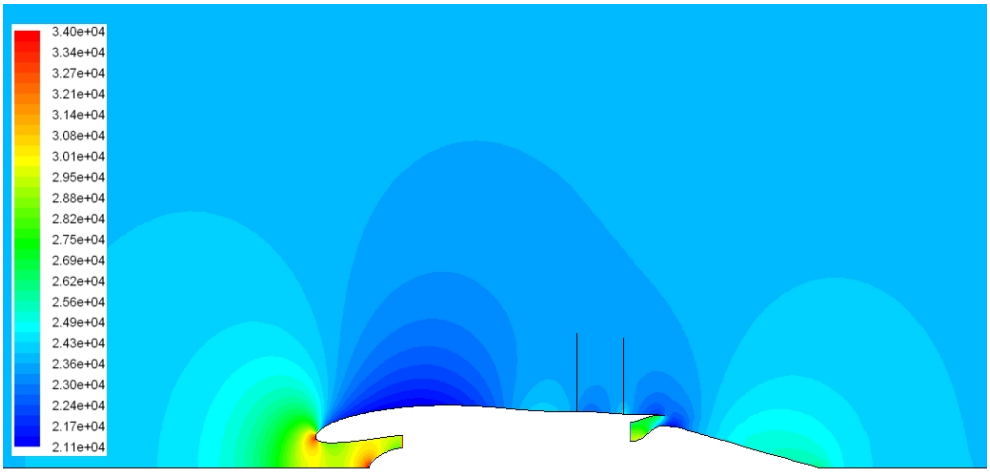

Fig. 6.42. Contours of static pressure $[Pa]$ for DOR-5 nacelle with rotors off ($M_0 = 0.72$, $z = \ 35kft$).

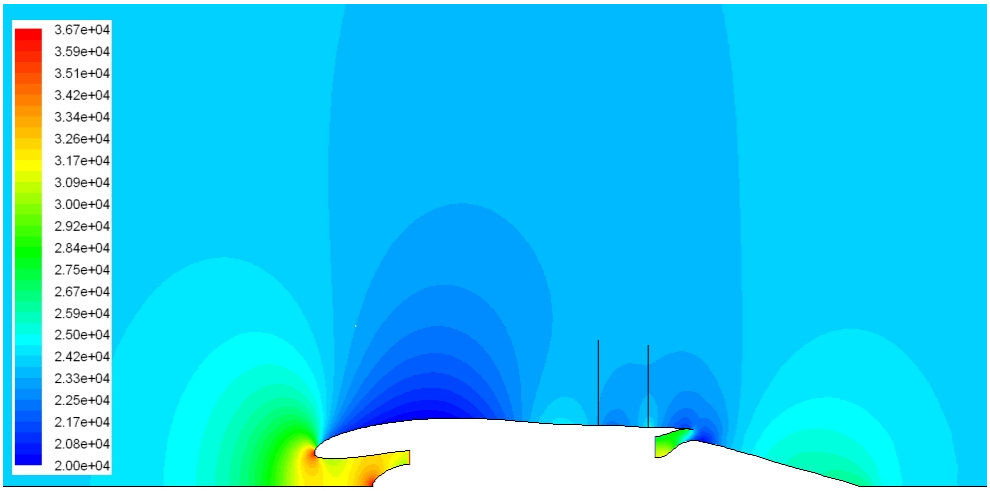

Fig. 6.43. Contours of static pressure $[Pa]$ for DOR-5 nacelle with rotors off ($M_0 = 0.8$, $z = \ 35kft$).

Table 6.3. Force components on DOR-5 model.

DOR-5 ($\varepsilon = 0.995$, $z = 35\ kft$, F7A7-0.81)									
Rotors	On			Off			Off		
M_0	0.72			0.72			0.8		
Zone	Forces* $[N]$			Forces* $[N]$			Forces* $[N]$		
	PF	VF	TF	PF	VF	TF	PF	VF	TF
Centrebody	1330.56	9.7	1340.26	1330.72	9.7	1340.43	1808.25	10.8	1819.05
Inlet	−1355.46	21.01	−1334.45	−1355.63	20.99	−1334.63	−1851.75	23.46	−1828.29
Lip	1071.92	7.88	1079.8	1071.39	7.89	1079.28	1412.43	8.7	1421.12
Fore-cowl	−1401.89	215.14	−1186.75	−1194.31	211.92	−982.38	−1561.53	255.45	−1306.08
Aft-cowl	623.43	133.96	757.39	337.07	121.89	458.96	438.09	142.96	581.06
net	268.56	387.7	656.27	189.26	372.4	561.67	245.49	441.37	686.86

* PF = Pressure Force, VF = Viscous Force, TF = Total Force.

Table 6.4. Force components on REMO model.

REMO ($\varepsilon = 0.995$, $z = 35\ kft$, F7A7-0.81)									
Rotors	On			Off			Off		
M_0	0.72			0.72			0.8		
Zone	Forces* $[N]$			Forces* $[N]$			Forces* $[N]$		
	PF	VF	TF	PF	VF	TF	PF	VF	TF
Centrebody	156.94	1.37	158.32	156.95	1.38	158.33	212.63	1.52	214.15
Inlet	33.85	18.57	52.42	33.85	18.55	52.4	46.4	20.84	67.23
Lip	1083.82	3.56	1087.38	1083.48	3.56	1087.05	1406.44	3.92	1410.35
Fore-cowl	−1776.46	249.02	−1527.43	−1523.52	244.5	−1279.02	−1974.95	294.41	−1680.54
Aft-cowl	1017.04	122.11	1139.16	629.52	109.23	738.75	849.98	130.37	980.35
net	515.21	394.64	909.84	380.29	377.21	757.51	540.49	451.06	991.55

* PF = Pressure Force, VF = Viscous Force, TF = Total Force.

Table 6.5. Elements needed for drag computation ($\varepsilon = 0.995$, $z = 35\ kft$, F7A7-0.81).

Model	DOR-5			REMO		
Rotors	On	Off	Off	On	Off	Off
M_0	0.72	0.72	0.8	0.72	0.72	0.8
$\rho_0\ [kg/m^3]$	0.379508	0.379508	0.379508	0.379508	0.379508	0.379508
$V_0\ [m/s]$	213.42	213.42	237.14	213.42	213.42	237.14
$\dot{m}\ [kg/s]$	21.48	21.48	23.37	21.48	21.48	23.37
$A_0\ [m^2]$	0.265172	0.265172	0.259678	0.265172	0.265172	0.259678
$P_0\ [N/m^2]$	23835.69	23835.69	23835.69	23835.69	23835.69	23835.69
$\rho \cdot V_0^2 \cdot A_0\ [N]$	4583.94	4583.94	5541.93	4583.94	4583.94	5541.93
$FCA^*\ [N]$	4784.84	4785.07	5895.51	4823.51	4823.59	5939.73
$F_{cb}\ [N]$	1340.26	1340.43	1819.05	158.32	158.33	214.15
$F_{inlet}\ [N]$	−1334.45	−1334.63	−1828.29	52.42	52.4	67.23
$F_{lip}\ [N]$	1079.8	1079.28	1421.12	1087.38	1087.05	1410.35
$F_i{}^\dagger\ [N]$	−254.64	−255.35	−407.16	1139.8	1139.45	1477.59
$F_{fc}\ [N]$	−1186.75	−982.38	−1306.08	−1527.43	−1279.02	−1680.54
$F_{ac}\ [N]$	757.39	458.96	581.06	1139.16	738.75	980.35
$F_{fb}\ [N]$	−429.35	−523.42	−725.02	−388.28	−540.27	−700.19
$TF_{fb}{}^\ddagger\ [N]$	656.27	561.67	686.86	909.84	757.51	991.55
$D_{fb}\ [N]$	857.17	762.8	1040.45	1149.41	997.16	1389.36
$TF_{fc}{}^\S\ [N]$	−101.12	102.7	105.8	−229.31	18.75	11.2
$D_{fc}\ [N]$	99.78	303.83	459.39	10.26	258.41	409.01

* Force at Compressor Area $FCA = \int_{A_C} [(P_C - P_0) + \rho_C \cdot V_C^2] dA\ [N]$.

† $F_i = F_{intake} = F_{lip} + F_{inlet}\ [N]$.

‡ Total force considering the forebody $TF_{fb} = F_{cb} + F_i + F_{fb}\ [N]$.

§ Total force considering the fore-cowl $TF_{fc} = F_{cb} + F_i + F_{fc}\ [N]$.

7. ADDITIONAL STUDIES

The study of innovative design methodologies for pusher open-rotor nacelles is inevitably connected to some practical aspects, such as the improvement and the final realisation of the engine. This consequently stimulates the activity of research to move towards the discovery of new areas of interest for the development of the open-rotor technology. The present chapter contains a resume of the studies[1] associated to DEMONS project and related to potential fields of further investigation for future works, which are mainly addressing practical problems.

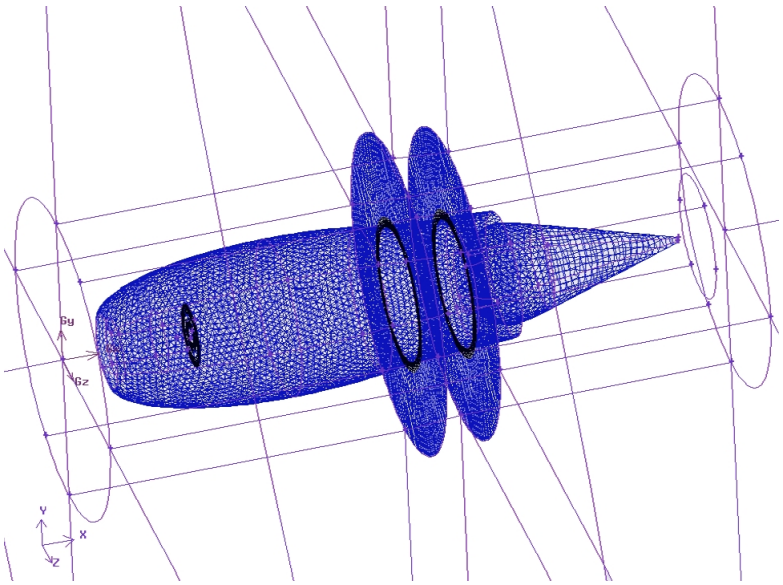

Fig. 7.1. Mesh of the isolated 3D REMO nacelle.

For instance, one of the major concerns with the introduction of the open-rotor is the integration of the engine with the aircraft. Due to their design features, the

[1]The studies were conducted by MSc students in the academic year 2008-2009.

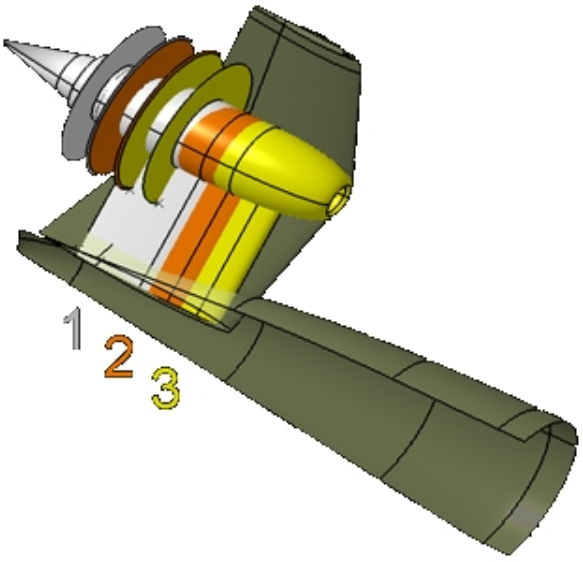

Fig. 7.2. The REMO engine installed on future U-tail aircraft at different positions along the fuselage.

open-rotors cannot be retrofitted into the existing airframe designs. As a result, new airframe architectures have to be considered to better suit the engine. Within this ambit, a possible field of investigation is represented by the assessment of the engine-airframe integration issues of an aft-top-mounted engine installed on a U-tail aeroplane[2], whose dimensions are similar to those of the current short-medium haul aircraft.

At this purpose, some CFD simulations were performed in Fluent® to analyse the behaviour of the external flow over the cowl of the REMO nacelle (Fig. 7.1) installed on the tail section of a scaled A-6 Greenliner aircraft[3]. The 3D simulations were carried out taking into account different positions of the engine (Fig. 7.2) at various pylon installation angles (Fig. 7.3). The configurations have been tested to assess the aerodynamic interaction of the airframe with the rotors operating with variable tip clearance values. Since the actuator disk model developed in paragraph 4.2.2 is valid for 2D axisymmetric domains, it could not be used in these simulations: a constant pressure jump boundary condition at the fan faces

[2]This 'future concept' has already been proposed in the recent years, for example see ref. [62].
[3]The original model is a courtesy of the Aerospace Vehicle Design MSc Group, "Environmentally Benign Airliner Design Project - 2006/2007", Cranfield University.

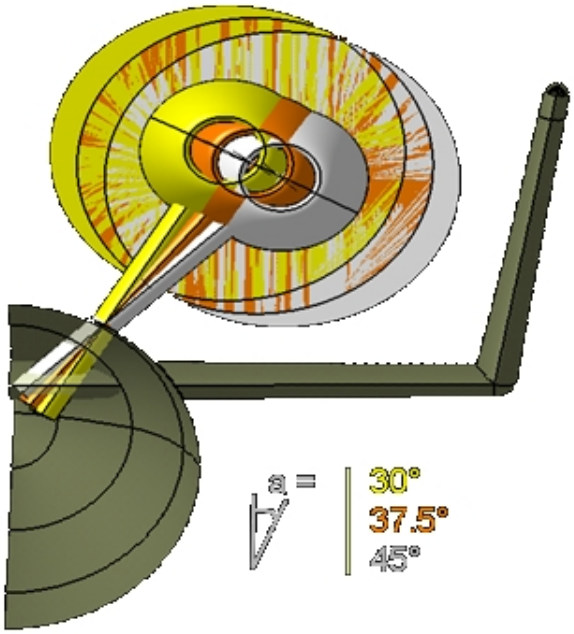

Fig. 7.3. Installation angles of the pylon.

was adopted instead.

Despite this and other simplifications made on the simulation domain[4], the analysis offered the opportunity to detect some key issues. In general the engine installation, and in particular the presence of the pylon, plays an important influence on the performance of the rotors, being a source of energy losses. More in details, the pylon wake (highlighted in Fig. 7.4 by the total pressure drop before the rotor) can create a fatigue cycle of great intensity, thus affecting the engine life and principally the propellers' life. Any phenomenon introducing effects such stress and fatigue that might increase the probability of blade failure are strongly discouraged in the design phase of an engine installation, but this is particularly true for open-rotors, which have no casing around the blades assuring the containment of a detached blade[5].

Moreover, the pylon profile has a large impact on the velocity of the flow in its surrounding region (Fig. 7.4). Hence an important design process should be

[4]See ref. [53].

[5]Turbofans need to prove, before being manufactured, that they can withstand a blade failure and that this can be contained within the engine casing.

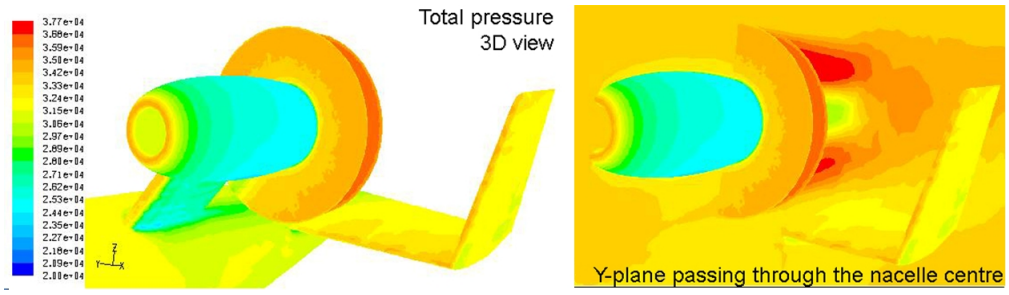

Fig. 7.4. Contours of total pressure $[Pa]$ of a rear-mounted REMO engine.

done on the pylon profile in order to minimise the wake and the supersonic flow which tends to appear around the engine. The different positions and installation angles of the pylon suggest that the flow tends to accelerate, introducing drag rise problems, when the tail and the pylon form a semi-closed passage across which the air is forced to stream while entering the rotors. This is especially true when the pylon is partially or totally placed in between the U-tail plane. In this case, when cruising at transonic speeds, the tail fins, the nacelle and the pylon act as walls forming a sort of duct that, if too narrow, accelerates the airflow up to supersonic conditions in this zone (Fig. 7.5).

While predicting the installation effects on the airflow, another important concern is thus related not only to the aerodynamic drag of the isolated engine, but also to the drag increment after its integration with the airframe. When the 3D simulations are still in an introductory phase, an advanced level of accuracy in terms of drag calculation is not achievable, due to the simplifications introduced within the CFD model. However, a preliminary estimation of drag is possible with the use of empirical and theoretical methods[6], providing basic information on the features of the open-rotor installation, which is complementary to the work done in paragraph 6.2.2.

As already mentioned, the open rotors are simplified with actuator disks in all the simulations performed. In order to overcome the absence of data regarding the blade geometries and improve the boundary condition on the actuator disk, a study

[6]See ref. [85].

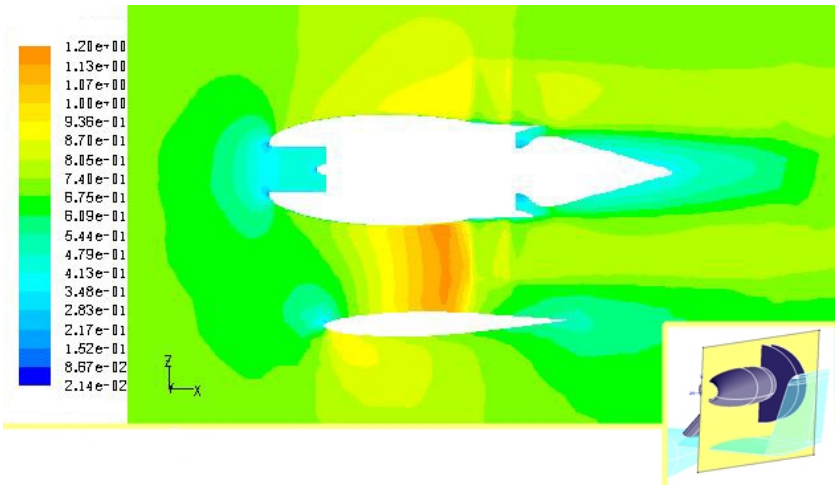

Fig. 7.5. Sectional view of Mach contours around the REMO nacelle with pylon inclined at 45 in position 3 (See Fig. 7.2).

on the effect of the propellers operating at different flight conditions and angle of attack has been carried out[7], initiating an exploration of the off-design features of the nacelle. By studying the behaviour of existing rotors and using a more detailed pressure jump distribution over each disk, which takes into account the blade performance variation in span direction, a User Defined Function in Fluent® could be created and used for better predicting the rotor aerodynamic behaviour.

The works presented so far, together with the research topics described within this dissertation, show CFD data only. Although CFD is extensively used as an aerodynamic design tool these days, results need to be assessed: in the case of DEMONS and its simulations, there is no experimental data available in public domain to properly validate the results. However, in the absence of experimental data there are some procedures to evaluate the CFD results: one possibility is to verify the quality of the solutions in terms of errors depending on the numerical method employed, concentrating on one area of verification process such as grid-independence studies. The basic idea behind it is to generate a set of successively refined grids and use them to solve the same problem, in order to obtain more accurate results, and see how these are affected by the mesh itself. A grid convergence study is used to place error bands on simulation results: the real order of accuracy

[7]See ref. [143].

of the numerical solution can be estimated, and the use of coarser mesh can be justified if the solution is in asymptotic range. The analysis[8] of the computations conducted while investigating the REMO engine demonstrated that the solutions are grid-independent[9], thus in asymptotic range. In fact, for this study the original grid was opportunely altered creating additional meshes, and the independence of the solutions from the modified grids was verified.

[8] See ref. [69].
[9] The grid dependence was checked for the domain model of chapter 4.

8. CONCLUSIONS

Civil aviation is facing one of the most critical challenges of its history. The recent rise of oil price and the actual economical crisis are stimulating the scientific community together with the aerospace industry to overcome the known limits of the existing technology, in the attempt of designing more efficient aeroplanes. The aero-engine manufacturers are called to play an important role in this technological advancement. As discussed in chapter 1, the open-rotor is one of the solutions adoptable for propelling the aircraft of the future. Conceived as a revised propfan, the open-rotor potentially offers the possibility to preserve the benefits of the work done in the 1980s, when the propfan technology was successfully pioneered, while bringing those enhancements that were required at the time to transform the propfan from a mere prototype into an operative commercial engine. The propfan demonstrated the capability of remarkably reducing the fuel consumption, although introducing additional issues such as noise production and airframe vibrations, together with a set of problematic topics, which in the past two decades were left unexplored in the open literature. Among them appears the lack of information concerning the design procedures of propfan nacelles.

Within this context, DEMONS project affords its contribution for introducing a set of design methods tailored for the new open-rotor engines. After an overview on the existing architectures and configurations of the propfan, the research was directed towards the field that appeared the less studied in literature, which is the development of methodologies for shaping the nacelle of a pusher open-rotor with

no exhaust impingement through the blades.

The definition of these methodologies is accomplished by determining the means that the designer needs for recreating an existing nacelle, or creating a new model from scratch, and for analysing the aerodynamic performance of the nacelle itself when it is installed on the engine. As described in chapter 4, the former aspect can be achieved through a graphical approach, the latter with a computational approach. Commercial software is widely used for the analysis, in particular CATIA®v5 for CAD design and Gambit-Fluent® for CFD computations.

The graphical approach starts with basic suggestions on how to recreate an existing pusher open-rotor nacelle: the GE-36 engine is taken as the baseline for a reference model, called REMO. The few data available in literature on propfans with pusher architecture do refer to this engine, and even if they are not enough for a complete validation of the computational results, at least they represent a useful source of information for comparison purposes. The profile of the nacelle initially can be studied in a two-dimensional domain. In fact, a nacelle is a body of revolution, which can be considered to be formed by a set of two-dimensional lines. These lines are intersected by a semi-infinite plane at each azimuthal station, referring to azimuth as the angle of rotation of the semi-infinite plane around the axis of rotation of the core-engine turbomachinery. Therefore the investigations focus on the quality of 2D profiles representing a generic section of the nacelle cowl. The CFD simulations are consequently based on a 2D axisymmetric domain, whose grid is meshed in Gambit® with unstructured triangular cells. The solutions are generated by the pressure based solver of Fluent® with the Spalart-Almaras one-equation turbulence model. The flight conditions simulated are those of cruise at zero AOA, which ideally represent the situation in which the nacelle will mostly work during its operative life.

The new open-rotors, in order to compete with the turbofan technology, must be conceived to cruise at transonic speeds, realistically between Mach 0.7 and 0.8.

In the transonic regime, the engine might experience the presence of sonic bubbles on its nacelle if the flow is accelerating too rapidly over the cowl. Sudden variations of the airflow velocity, even when occurring on localised regions of the nacelle only, cause unwanted drag rise. These phenomena may appear if the shape of the nacelle is not smooth enough to avoid the formation and escalation of this kind of aerodynamic losses. Geometric continuity is a mathematical way for defining smoothness of lines and surfaces in practice. The preliminary procedure for shaping the REMO nacelle, described in paragraph 4.1.3, offers an interesting opportunity for understanding how to maintain high levels of geometric continuity (hence smoothness) on a curve representing the generic outline of the nacelle: $G3$ is desirable, at least far from the stagnation zones, where air decelerates thus lower degrees of geometric continuity are tolerable. The curvature profile of the shape should also not present oscillations and steep variations localised on small regions of its surface, because this also might favour undesirable excessive accelerations of the airflow. The computational approach developed in section 4.2 completed the first part of the work, presenting the tools for obtaining and analysing the numerical results upon which the aerodynamic features of the nacelle models can be assessed. This establishes the background to the realisation of methods and solutions for improving the existing propfan technology, as suggested by the following section.

8.1. Main achievements of the research

The DEMONS project represents the beginning of a new research area with the aid of modern computational capabilities. The research aims to the definition of procedures for nacelle shaping, which can be used to intuitively design existing and new engines. This work is indispensable within a TRL 3 context, which is the preliminary evaluation phase that precedes the engine technological development, contributing to discover new methods for open-rotor nacelle shaping.

The aerodynamic characteristics of the baseline cowl with pitot intake, typical of the REMO engine, are studied using CFD software. The analysis of the pressure coefficient distributions over the forebody provides indications on the quality of the airflow streaming near the nacelle. The results demonstrate how the REMO nacelle is able to maintain the Cp distribution uniformly below critical values even at high speeds, although the effects of the rotor are influencing the change in airflow velocity upstream the rotors over 70% of the forebody. This is an important observation for identifying and quantifying the mutual aerodynamic interaction between the nacelle and the rotor stages.

Moreover, the present study shows how it is possible to use simplified rotor models to describe the nacelle-rotor aerodynamic interaction in a satisfactory and computationally efficient way. In particular, the high speed propellers can be modelled with actuator disks, obtaining for this kind of investigations a reasonable representation of the axial 'suction effects' induced by the rotors. The axial-velocity field in blade spanwise direction, measured at a station placed at the end of the forebody and before the rotors, appears in good agreement with the data existing in literature.

These simulations are very useful for initially assessing the external-cowl shape. The information loss due to the simplification of the problem around the missing 3D-blades is tolerated due the purpose of the project, which is 'nacelle design' and not 'rotor design'. It is evident from the results of section 4.3 that although the complex velocity field introduced by the rotation of the blades can not be reproduced faithfully over the rotor-hub zone, the actuator disk models are able to simulate over the forebody the aerodynamic effects introduced by the presence of the rotors in a satisfactory way, so that the mutual influence of the nacelle profile and the open rotors can be qualitatively assessed. This is in accordance with several documents available in literature, which demonstrated that actuator disks are an acceptable simplification of reality when used to simulate high-speed

propellers with the purpose of assessing the nacelle aerodynamic performance; this is true even when the nacelle is placed in the propeller wake, which is a region of high three-dimensional effects due to swirling airflow; of course this is not the case of the present study, where the nacelle is placed in front of the rotor and the three-dimensional effects are almost negligible, while the axial variation of the velocity is the only effect which is worthy to take into account due to its magnitude changes, although they are not extremely high[1].

What further emerges from this analysis and was not evident from the experimental data of reference [119], which were capturing the flow field only in a region close to the blade tip and not at its root, is that designing a nacelle with a maximum diameter larger than the hub diameter[2] is an ameliorable criterion for diffusing the air entering the rotor stages, especially towards the lower part of the blades, closer to the hub[3].

This observation, confirmed by the results of chapter 6, indirectly unveils a limitation of the graphical approach proposed: it is desirable not only that the shape of the nacelle be smooth, but also that it may be modified by the designer, regardless of the commercial software he works with. In fact, if the designer necessitates of finding more solutions, for instance running a sensitivity analysis for understanding how the change in nacelle shape may affect the airflow, or combining the CFD tool with a shape-optimiser, it is desirable to do so independently from the commercial software used for the design of the nacelle profile. Despite this limitation, the procedure of paragraph 4.1.3 highlights how the creation of the nacelle profile can be very intuitive by interpolating a set of construction points in space and imposing tangency and curvature constraints for modelling the final shape, which is obtained with connection curves modelled automatically by CATIA®v5.

[1] Information available in ref. [119].

[2] As suggested in ref. [11], see also section 2.2.

[3] For structural reasons the blade roots are thick and are not designed with thin profiles, thus they introduce losses and noise when cruising in transonic regime: the flight speed, summed to the rotational speed of the blades, is high enough to make the airflow easily become supersonic.

Although the use of commercial software allows for fast and reliable design, the need for an independent design tool, able to design a profile with an high level of geometric continuity, lead to the development of a new interpolation methodology, presented in chapter 5. With this method, called $C3$ *interpolation procedure*, the mathematical definition of the nacelle can be implemented into a custom software to interpolate a set of points in a two- or three-dimensional orthogonal space using what is believed to be a new kind of parametric interpolation curve[4], herein called *ZE-Spline*. This curve is generated by shape parameters that independently control its form, assuring it has $G3$ continuity and holds $C3$ continuity automatically, even when the shape parameters are modified by the designer. More in details, the method is based on piecewise quintic polynomials connecting the points selected for the interpolation; it can be implemented into a software program that provides a new type of interpolation curve, the ZE-Spline, which uses the components of position and velocity vectors as shape parameters that offer shaping control at each interpolated point, while the components of acceleration vectors are additional shape parameters that offer further shaping control at the two extreme (start and end) interpolated points, which may be coincident or not. The shape parameters, called *velocity* and *acceleration*, are named in this way because they refer to first and second derivatives with respect to the parameter t used to parameterise the interpolation curve, which has a cinematic analogy with the time intended in physical sense. All the shape parameters provide a completely independent control of the curve without altering its parametric continuity, which remains $C3$ (thus $G3$) always. All the parameters (positions, velocities, accelerations) can be modified by the designer at any time to adjust the form of the curve at will before saving the data. In other words, the curves generated with this methodology can be used not only to process images of smooth curves parametrically expressed on CAD systems

[4]As proved by the references cited in chapter 5, the author read many documents regarding interpolation curves, but did not find this kind of spline, although the procedure to obtain it is similar (not equal) to Hermite interpolation.

and similar applications, but also incorporated into shape optimisation schemes and implemented in design optimisers. By adopting this method, the designer can manipulate an interpolation curve keeping its $C3$ continuity automatically in an intuitive way, because the curve modifications are achieved acting on velocity and acceleration conditions, which have a precise physical meaning and are of common use in engineering. Any change made by the designer is also direct because the modification of these conditions has a straight impact on the geometry of the interpolation curve: there is no need of other algorithms to translate the variation of geometric constraints into a curve change. The use of this method is particularly indicated when designing aerodynamic profiles by interpolating a small number of points (e.g. 3 points) or when an arbitrary-high degree of freedom of the design variables is not an essential requirement in the design process (as it happens, for instance, in turbomachinery blade design). For instance it is possible to easily

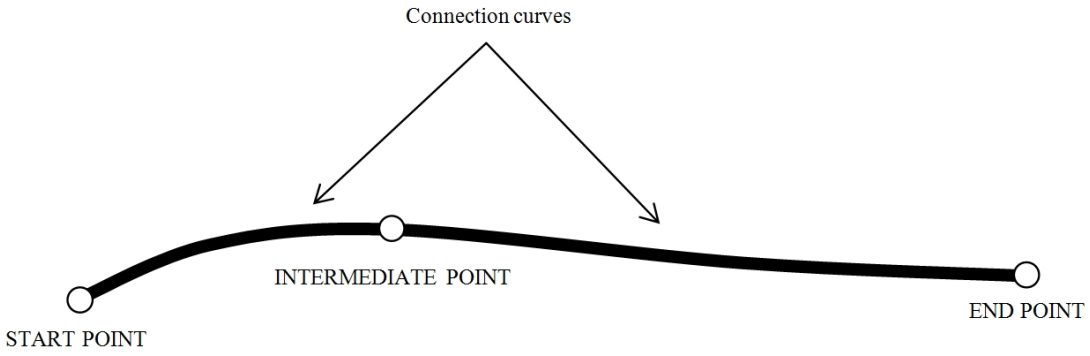

Fig. 8.1. Generic profile obtained interpolating three points in space.

design and modify external nacelle profiles, intake profiles, aerofoils, and structure profiles in general. The interpolating line may result to be a convex-concave curve, as shown in Fig. 8.1, depending on the values of the geometric constraints.

The choice of reproducing such a profile in this figure is not casual: in order to ameliorate the REMO nacelle in terms of diffusion of the airflow entering the rotor stages, a novel pusher open-rotor nacelle with convex-concave shape can be conceived. The decrease of the air speed ahead of the rotor stages is essentially improved by the introduction of a concavity in the aft-cowl of the nacelle, just

before the rotor-zone. By transforming the typical REMO nacelle, which is all convex, into a convex-concave 'bulb', the airflow diffuses in front of the rotors. The deceleration of the flow (reported in Fig. 6.25 and 6.27) occurs almost all over the blade span; this effect is predominant in the lower section of the blade, especially before entering the root region, hence reducing the tendency to generate supersonic flow on this part of the engine. The convex-concave geometry was assessed on different models, which are modifications of the REMO nacelle. All the new models, designated as DOR-1, DOR-2, DOR-3, DOR-4 and DOR-5, are designed making use of the $C3$ interpolation method defined in chapter 5. The analysis of the simulations of these models shows how their profiles, when flying at cruise conditions, not only present smooth pressure coefficient distributions, removing localised zones of shock wave formation at high flight speed, but also increase the Cp values along the forebody, downstream towards the rotors. This promotes a deceleration of the flow in spanwise direction, as computed on the vertical measurement station located in front of the first rotor stage: the axial velocity, if compared with the data of the REMO case, is lowered from about 13% to 7% (depending on the model), contributing to further decrease the aerodynamic losses. As a consequence, the diffusive nacelle concept can favour a reduction of fuel consumption or, alternatively, the achievement of higher flight velocities.

In analogy with the REMO case, also in the study of these new models the computational approach resulted very useful for individuating how the flow on the nacelle can be affected by the action of the rotors: about 80% of the forebody, upstream the blades, results influenced by 'suction effects', while no remarkable influence is shown at the beginning of the forebody, next to the intake. This suggests that intakes, or at least their internal profiles, can be designed with classical methods. However, the designer should consider that the dimensions of the intake are affecting the shape of the whole forebody, thus the way the cowl is interacting with the rotors and vice-versa[5].

[5]This sort of interaction can be critical if annular intakes are adopted instead of classic pitot

It is interesting to observe how the pressure coefficient distribution of the five new models can be progressively improved. The DOR-5 model in particular presents a Cp profile which is always below the critical value even at very high speed conditions ($M_0 = 0.8$). This enhancement is the consequence of a modified forebody, designed after reshaping the intake. The different nacelle and intake configuration of this final DOR-5 model, with respect to the reference one, encouraged the assessment of the pre-entry drag, as computed in paragraph 6.2.2. The comparison between the data achieved by the analysis (Table 6.2) shows how despite this difference the new nacelle is worsening only the fore-cowl drag D_{fc}. In fact, the presence of the rotors in combination with the convex-concave shape introduces less forebody drag D_{fb} when considering the whole forebody, upstream the rotors.

A diagram resuming all the project activities that allowed the accomplishment of these results is reported in Fig. 8.4 at the end of this chapter, just after the recommendations for future works.

8.2. Recommendations for future works

The conclusion of a project does not imply the end of the research activities involved in it: this would unacceptably limit the meaning of research itself, upon which the human comprehension of nature and its laws relies for crossing new frontiers and building a better future. In the case of DEMONS, the guidelines for subsequent works are mentioned herein as a collection of indications for the realisation of new projects, with the purpose of encouraging further studies and thus widen the knowledge necessary for the development of open-rotor nacelles.

8.2.1. Simulations

The results obtained computationally in the present research, especially those accomplished on the new diffusive nacelle, should be validated by an experimental

intakes, as will be explained in the suggestions for future works.

examination, which was not part of this doctoral research. In the absence of experimental results, it is wise to improve as much as possible the quality of the simulations.

At this purpose, an interesting field of investigation is the enhancement of the actuator-disk modelling. It is worthy to ameliorate the actual models by considering how to recreate the pressure jump distributions also when the rotors are operating at angle of attack. This could allow better 3D simulations, through which it would also be possible to evaluate the nacelle aerodynamics at any off-design conditions. The blade element theory could be applied to actuator disks for improving the rotor modelling, although this could be more desirable when analysing open-rotors with tractor architecture[6].

The information needed to fill the boundary conditions representing the actuator disks can be found in literature or can be imposed knowing experimental results. When none of these solutions is available, it is possible to run simulations adopting what is guessed to be the best representation of the rotors, trying to get close to reality as much as possible. By doing so, the outcome of the investigation is not the production of quantitative data, but the collection of qualitative results which can be useful for assessing the problem in a preliminary way. Despite the well known limitations, this can be considered satisfactory when done in a preliminary phase of 'research and development', such as the TRL 3 in which DEMONS can be collocated. The qualitative results are useful to obtain the first ideas on what is needed to be measured and assessed in future test rigs, tailoring the experiments around the real needs of the research, avoiding the risk of collecting huge amount of data that might be in large part unnecessary to understand and/or solve practical problems.

The simulations make use of the Spalart-Allmaras one-equation turbulence model.

[6]The wake could be better modelled, and this is important for a correct assessment of the intake performance, since with the puller architecture the inlet is generally invested by the wake of the rotors.

In future, new simulations should be taken into consideration for assessing the results with other turbulence models. More computational challenges are also represented by CFD drag prediction improvements, together with the integration of shape optimisation processes within the design procedure discussed in chapter 5.

8.2.2. Alternative implementations of the interpolation method

The code developed in Matlab® according to the descriptions of paragraph 5.3, and used to implement the $C3$ interpolation method described in paragraph 5.2, could be further refined. First of all, the quality of the converted/exported curve might be improved. In order to accomplish this task, the following topics have to be investigated:

- Influence of the accuracy parameter h on the geometric features of the curve.
- Influence of the B-spline parameterisation on the quality of the curve.
- Attempt to make use of local interpolation schemes or other 'conversion' methods.

Moreover, the `globalcurveinterp` function[7] included in the code written in Matlab®, which performs a global curve interpolation to point data, is already prepared not only for setting a chord-length or centripetal parameterisation, but also for building a uniform or non-uniform (with an averaging technique) vector of knots[8]. In future this function could be modified so that the end-user may select these options, for instance as function inputs. By default the function adopts the more stable and reliable settings, which are the centripetal parameterisation coupled with the generation of a non-uniform normalised knot vector. Different settings may easily

[7] This function was created to generate the vectors of control points and knots of an exportable B-spline curve, which interpolates the set of computed points forming the original quintic $C3$ line (see ref. [118]).

[8] Notions on these topics are given for example in ref. [118] and [129].

introduce unwanted curvature oscillations. Further studies on the spline generation would be crucial in advancing the export capabilities of the code. Another improvement consists in the creation of a GUI to ease the input and automatic-display of the interpolation curve. This would allow the designer to shape the nacelle in a CAD fashion.

Although Matlab® is widely utilised in the scientific community, its usage was principally useful to demonstrate the possibility of creating a new kind of interpolation method for the design of smooth aerodynamic profiles, like a generic part of a pusher open-rotor nacelle. Anyhow, the flexibility of Matlab® is still bounded to the commercial licence of this software. In order to avoid any sort of restrictions in terms of licenses, it would be necessary to build a program executable from machines working with or without Matlab®. This can be done by rewriting the code into another programming language, such as C++ or Fortran, to generate an interpolator which is completely free from commercial software limitations.

Having no restrictions, the code could be coupled with or incorporated into a shape optimiser, together with a CFD solver, for the automatic generation of nacelle shapes. This could ease, for instance, the study of the correlation between the size and power of the rotor stages (which is fixed) and the length of the nacelle (variable), discovering when the influence of the rotors might invest the entire nacelle and not just a portion of it. If it was necessary to analyse not only a generic profile belonging to the nacelle but also the entire cowl, the theory presented in paragraph 5.2 should be extended from 3D lines to 3D surfaces, allowing for the design of whole non-axisymmetric shapes in a faster way.

8.2.3. Installation studies

Another source of inspiration for future works can be found in the topics presented in chapter 7. Primarily important is the assessment of the open-rotor installation on a new airframe, considering not only the issues related to the interference be-

tween engines and fuselage, tail or wing of the aircraft, but also the possibility to analyse how the nacelle affects aerodynamically the performance of the rotor blades in case of altitude relight. For pusher open-rotors, these challenging tasks are complicated by the presence of the mounting pylon, which generates a wake entering the rotor stages.

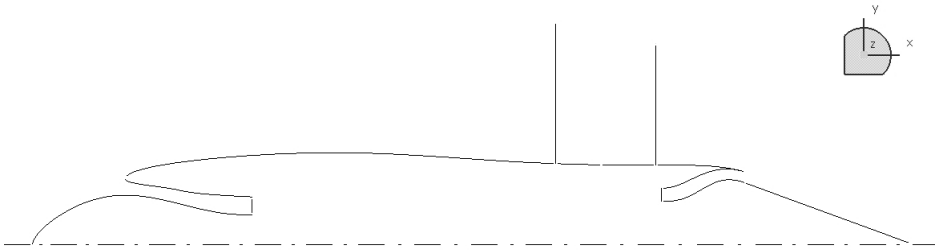

Fig. 8.2. Example of annular intake and pusher open-rotor nacelle.

The installation of the engine might be influenced also by the configuration of the intake. More in details, new studies could be addressed to the nacelle-intake-compressor design: even if the rotors are not affecting the flow at the intake like in the REMO and DOR models, a modified or innovative intake could have an impact on the highlight position, thus on the shape of the external cowl and consequently on the airflow before the rotors. This also would affect the pre-entry drag, which may be calculated with the procedure presented in paragraph 6.2.2. In fact, the pitot intake, as already mentioned in section 3.1.2, could be reassessed. For instance, the annular intakes, together with the chin or bifurcated solutions, are completely new layouts, available as a promising research matter. These kinds of intake, jointly with the integration of particle separators, are able to offer an increased protection to the engine core, augmenting the probability to avoid the undesirable phenomenon of debris/birds ingestion. Adopting an annular intake, for example like the one depicted in Fig. 8.2, the debris ingestion could be limited because the centrebody is shielding and deviating any foreign body away from the intake, so that they hardly can enter the core engine through the inlet. However this configuration requires that the forebody be redesigned, thus the interaction of

the nacelle with the rotors should be reassessed.

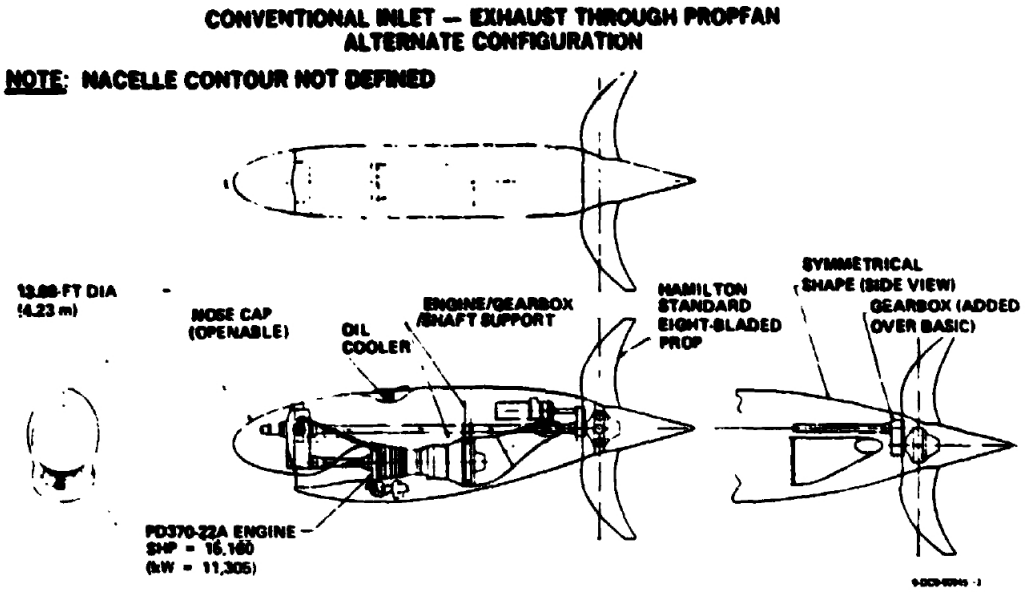

Fig. 8.3. Pusher propfan nacelle arrangement with chin inlet (source: ref. [68]).

Furthermore, these configurations introduce multiple issues, because they might add not only penalties in terms of cowl weight and aerodynamic losses (for instance flow detachment within the inlet), but also difficulties in terms of design method definition. Said configurations are an innovative solution for the pusher architecture, which has never been studied in depth before, and strongly depend on the power system. A preliminary sketch of chin intake for pusher propfan is shown[9] in Fig. 8.3: the intake design is strictly connected to the propfan configuration; it has to be noticed how in this preliminary design the exhaust system is situated before the pusher rotor, which is driven by a power shaft through a reduction gearbox.

The future works proposed are all connected to this project and were suggested as a consequential evolution of DEMONS, as indicated in Fig. 8.4.

[9]In Fig. 8.3 the intake is called "conventional inlet" because it is the typical intake of turboprops.

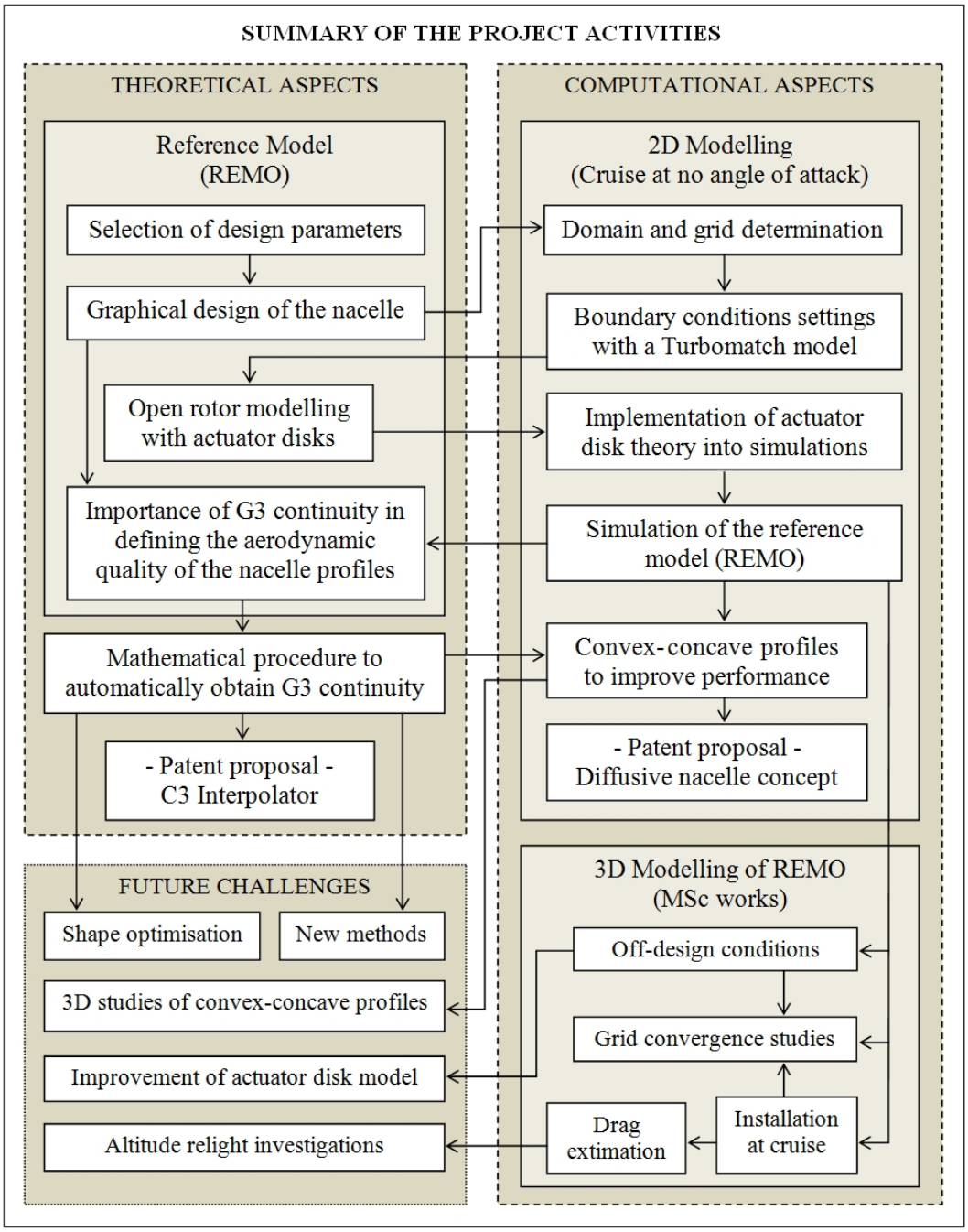

Fig. 8.4. Diagram of the project activities.

A. Turbomatch Code for the REMO Engine

The Turbomatch scheme presented in Fig. 4.9 is just a simplification of the real scheme used to reproduce the cycle of the REMO engine, which is based on the UDF engine. The complete scheme is reported in Fig. A.1. The following code is the transcription of the `*.*dat` file executable in the Turbomatch environment to run a cycle performance prediction of the REMO engine, based on the information achieved from the UDF engine documentation[1].

```
!Turbomatch program -> Engine cycle: GE-36 (UDF).
!Core engine: modified GE F404 (reduced operating cycle).
!File created on the 3rd of March, 2009.
!Author: Erminio Samuele Zanenga.
////
OD SI KE VA FP
-1
-1
INTAKE S1,2         D1-4        R100
COMPRE S2,3         D5-11       R110      V5     V6
PREMAS S3,4,18      D12-15
COMPRE S4,5         D16-22      R120      V16    V17
PREMAS S5,6,21      D23-26
PREMAS S6,7,22      D27-30
BURNER S7,8         D31-33      R130
```

[1] See ref. [11].

```
MIXEES S8,22,9
TURBIN S9,10        D34-41,120,42         V35
DUCTER S10,11       D43-46      R140
TURBIN S11,12       D47-54,110,55         V48
DUCTER S12,13       D55-59      R160
MIXEES S18,21,19
DUCTER S19,20       D60-63      R170
MIXFUL S13,20,14    D64-66
DUCTER S14,15       D67-70      R180
TURBIN S15,26       D71-80                V71    V72
DUCTER S26,27       D81-84      R181
TURBIN S27,28       D85-94                V85    V86
DUCTER S28,29       D95-98      R182
NOZCON S29,30,1     D99         R190
ARITHY              D310-316
PERFOR S1,0,0       D400,401-403,190,100,130,0
CODEND
////
!INTAKE
1 0.0              !ALTITUDE
2 0.0              !DEVIATION FROM STANDARD TEMPERATURE
3 0.0              !MACH NUMBER
4 0.995            !PRESSURE RECOVERY (0.9975 for civil engines at cruise)
!LP COMPRESSOR
5 -1.0             !SURGE MARGIN
6 0.892            !REL ROT SPEED (UDF/F404 from p.12 Design Report)
7 3.103            !PRESSURE RATIO
8 0.85             !ISENTROPIC EFFICIENCY
9 0.0              !ERROR SWITCH
10 5.0             !MAP NUMBER
11 0.0             !VARIABLE ANGLE
!BYPASS TO POWER TURBINES
12 0.746           !LAMBDA W
13 0.0             !DELTA W
```

```
14 1.0              !LAMBDA P
15 0.0              !DELTA P
!HP COMPRESSOR
16 -1.0             !SURGE MARGIN
17 0.964            !REL ROT SPEED (UDF/F404 from p.12 Design Report)
18 5.675            !PRESSURE RATIO
19 0.85             !ISENTROPIC EFFICIENCY
20 0.0              !ERROR SWITCH
21 5.0              !MAP NUMBER
22 0.0              !VARIABLE ANGLE
!PREMAS FOR BLEEDING
23 1.0              !
24 0.0              !
25 1.0              !
26 0.0              !
!PREMAS FOR AIR-COOLING BEFORE COMBUSTION CHAMBER
27 0.85             !
28 0.0              !
29 1.0              !
30 0.0              !
!COMBUSTION CHAMBER (BURNER)
31 0.05             !PRESSURE LOSS
32 0.99             !EFFICIENCY
33 -1.0             !FUEL FLOW
!AIR-MIXING FOR BURNER COOLING
!HP TURBINE
34 10000.0          !AUXILIARY WORK
35 0.8              !NON DIMENSIONAL MASS FLOW
36 0.6              !NON DIMENSIONAL SPEED
37 0.8              !ISENTROPIC EFFICIENCY
38 -1.0             !REL ROT SPEED OF POWER TURBINE (-1 COMPRESSOR)
39 2.0              !COMPRESSOR NUMBER (0 FOR POWER TURBINES)
40 2.0              !MAP NUMBER
41 1.5              !POWER LAW INDEX
```

```
42 0.0              !STATOR ANGLE (0 AT DESIGN POINT)
!DUCTER
43 0.0              !
44 0.01             !PRESSURE LOSSES
45 0.0              !
46 0.0              !
!LP TURBINE
47 0.0              !AUXILIARY WORK
48 0.8              !NON DIMENDIONAL MASS FLOW
49 0.6              !NON DIMENSIONAL SPEED
50 0.8              !ISENTROPIC EFFICIENCY
51 -1.0             !REL ROT SPEED OF POWER TURBINE (-1 COMPRESSOR)
52 1.0              !COMPRESSOR NUMBER (0 FOR POWER TURBINES)
53 1.0              !MAP NUMBER
54 1.5              !POWER LAW INDEX
55 0.0              !STATOR ANGLE (0 AT DESIGN POINT)
!DUCTER
56 0.0              !
57 0.01             !PRESSURE LOSSES
58 0.0              !
59 0.0              !
!AIR-MIXING FOR BYPASS
!DUCTER OF BYPASS
60 0.0              !
61 0.01             !
62 0.0              !
63 1000000.0        !
!MIXFUL
64 1.0              !
65 1.0              !
66 0.40             !MACH NUMBER
!DUCTER
67 0.0              !
68 0.01             !
```

```
69 0.0            !
70 1000000.0      !
!FRONT POWER TURBINE ------------------------------------------------------------
71 6447500.0      !SHAFT POWER
72 -1.0           !NON DIMENSIONAL MASS FLOW
73 0.25           !NON DIMENSIONAL SPEED
74 0.9            !ISENTROPIC EFFICIENCY
75 0.8            !REL ROT SPEED OF POWER TURBINE (-1 COMPRESSOR)
76 0.0            !COMPRESSOR NUMBER (0 FOR POWER TURBINES)
77 1.0            !MAP NUMBER
78 -1.0           !POWER LAW INDEX
79 -1.0           !COMPRESSOR WORK (-1 FOR POWER TURBINES)
80 0.0            !STATOR ANGLE (0 AT DESIGN POINT)
!DUCTER
81 0.0            !
82 0.01           !PRESSURE LOSSES
83 0.0            !
84 1000000.0      !
!REAR POWER TURBINE
85 6447500.0      !SHAFT POWER
86 -1.0           !NON DIMENSIONAL MASS FLOW
87 0.25           !NON DIMENSIONAL SPEED
88 0.9            !ISENTROPIC EFFICIENCY
89 0.8            !REL ROT SPEED OF POWER TURBINE (-1 COMPRESSOR)
90 0.0            !COMPRESSOR NUMBER (0 FOR POWER TURBINES)
91 1.0            !MAP NUMBER
92 -1.0           !POWER LAW INDEX
93 -1.0           !COMPRESSOR WORK (-1 FOR POWER TURBINES)
94 0.0            !STATOR ANGLE (0 AT DESIGN POINT)
!DUCTER
95 0.0            !
96 0.01           !PRESSURE LOSSES
97 0.0            !
98 1000000.0      !
```

```
!NOZCON
99 -1.0            !
!SUM THE SHAFT POWER OF THE 2 POWER TURBINES "DEFINING" BRICK DATA 400
310 1.0            !Sum
311 -1.0           !
312 400.0          !"DEFINITION" OF BRICK DATA 400 (store the result into it)
313 -1.0           !
314 71.0           !Brick 71 |
315 -1.0           !         |-> Sum these two brick data
316 85.0           !Brick 85 |
!PERFOR
401 0.62           !PROPELLER EFFICIENCY see AGARD-CP-421 (22-5)
402 0.0            ! -> NO-SCALE
403 0.0            ! -> NO-SCALE
-1
1 2 57.153
8 6 1628.706
2 8 0.359
28 8 0.766
-1
1 10668
3 0.70
401 0.80
-1
8 6 1420.0
-1
3 0.72
401 0.81
-1
8 6 1430.0
-1
3 0.8
401 0.77
-1
```

```
8 6 1500.0
-1
-3
```

The results obtainable by running the above code are collected in a *.*tmr file, whose main parts are presented as follows. As regards the SLS computation, considered to be the design point of the engine, the output is:

```
                The Units for this Run are as follows:-

 Temperature = K   Pressure = Atmospheres   Length = metres

 Area = sq metres  Mass Flow = kg/sec       Velocity = metres/sec

 Force = Newtons   s.f.c.(Thrust) =  mg/N sec   s.f.c.(Power) = mug/J

 Sp. Thrust =    N/kg/sec     Power =   Watts
1

      ***** DESIGN POINT ENGINE CALCULATIONS *****

 ***** AMBIENT AND INLET PARAMETERS *****
 Alt. =      0.0      I.S.A. Dev. =    0.000       Mach No. =  0.00
 Etar = 0.9950        Momentum Drag =      0.00

 ***** COMPRESSOR  1 PARAMETERS *****
 PRSF =  0.40113E+00     ETASF =  0.10494E+01     WASF =  0.13645E+01
 Z = 0.85000             PR =   3.103             ETA = 0.85000
 PCN =   0.8920          CN = 0.89200             COMWK =  0.74336E+07
 STATOR ANGLE =   0.00

 ***** COMPRESSOR  2 PARAMETERS *****
 PRSF =  0.75318E+00     ETASF =  0.10529E+01     WASF =  0.34115E+00
 Z = 0.85000             PR =   5.675             ETA = 0.85000
 PCN =   0.9640          CN = 0.96400             COMWK =  0.13411E+08
```

```
STATOR ANGLE =   0.00

***** COMBUSTION CHAMBER PARAMETERS *****
ETASF =  0.99000E+00
ETA = 0.99000           DLP = 0.8761            WFB =   1.0001

***** TURBINE  1 PARAMETERS *****
CNSF =  0.11073E+03     ETASF =  0.89588E+00     TFSF =  0.11893E+02
DHSF =  0.95184E+04
TF = 1210.214            ETA = 0.80000            CN =  2.750
AUXWK =  0.10000E+05     NGV ANGLE = 0.00

***** TURBINE  2 PARAMETERS *****
CNSF =  0.11145E+03     ETASF =  0.93171E+00     TFSF =  0.15805E+01
DHSF =  0.38081E+04
TF =  401.640            ETA = 0.80000            CN =  2.800
AUXWK =  0.00000E+00     NGV ANGLE = 0.00

***** MIXING MACH NUMBERS *****
Station 13, M= 0.401    Station 20,M = 0.262    Station 14,M = 0.379

***** TURBINE  3 PARAMETERS *****
CNSF =  0.50806E-02     ETASF =  0.10681E+01     TFSF =  0.70330E+00
DHSF =  0.48936E+04
TF =  401.640            ETA = 0.90000            CN =  1.312
AUXWK =  0.64475E+07     NGV ANGLE = 0.00

Additional Free Turbine Parameters:-
Speed =  80.0%          Power =  0.64475E+07

***** TURBINE  4 PARAMETERS *****
CNSF =  0.48196E-02     ETASF =  0.10681E+01     TFSF =  0.45677E+00
DHSF =  0.54380E+04
TF =  401.640            ETA = 0.90000            CN =  1.312
```

```
AUXWK =  0.64475E+07     NGV ANGLE = 0.00

Additional Free Turbine Parameters:-
Speed =  80.0%          Power =  0.64475E+07

***** CONVERGENT NOZZLE  1 PARAMETERS *****
NCOSF =  0.10000E+01
Area =  0.5323          Exit Velocity =  229.42  Gross Thrust =  12983.99
Nozzle Coeff. =  0.97321E+00

Scale Factor on above Mass Flows, Areas, Thrusts & Powers =     1.0000
```

Station	F.A.R.	Mass Flow	Pstatic	Ptotal	Tstatic	Ttotal	Vel	Area
1	0.00000	57.153	1.00000	1.00000	288.15	288.15	0.0	******
2	0.00000	57.153	******	0.99500	******	288.15	******	******
3	0.00000	57.153	******	3.08749	******	417.15	******	******
4	0.00000	42.636	******	3.08749	******	417.15	******	******
5	0.00000	42.636	******	17.52149	******	718.29	******	******
6	0.00000	42.636	******	17.52149	******	718.29	******	******
7	0.00000	36.241	******	17.52149	******	718.29	******	******
8	0.02760	37.241	******	16.64541	******	1628.71	******	******
9	0.02346	43.636	******	16.64541	******	1506.65	******	******
10	0.02346	43.636	******	6.15808	******	1260.57	******	******
11	0.02346	43.636	******	6.09649	******	1260.57	******	******
12	0.02346	43.636	******	3.23596	******	1121.05	******	******
13	0.02346	43.636	2.91607	3.23596	1093.63	1121.05	257.2	0.1802
14	0.01750	58.153	2.89835	3.18533	936.91	959.00	226.8	0.2347
15	0.01750	58.153	******	3.15348	******	959.00	******	******
16	0.00000	0.000	******	0.00000	******	0.00	******	******
17	0.00000	0.000	******	0.00000	******	0.00	******	******
18	0.00000	14.517	******	3.08749	******	417.15	******	******
19	0.00000	14.517	******	3.08749	******	417.15	******	******
20	0.00000	14.517	2.91607	3.05661	411.57	417.15	106.4	0.0545
21	0.00000	0.000	******	0.00000	******	0.00	******	******

```
   22   0.00000     6.395    ******  17.52149  ******  718.29  ******  ******
   23   0.00000     0.000    ******   0.00000  ******    0.00  ******  ******
   24   0.00000     0.000    ******   0.00000  ******    0.00  ******  ******
   25   0.00000     0.000    ******   0.00000  ******    0.00  ******  ******
   26   0.01750    58.153    ******   1.96247  ******  862.99  ******  ******
   27   0.01750    58.153    ******   1.94285  ******  862.99  ******  ******
   28   0.01750    58.153    ******   1.14188  ******  764.99  ******  ******
   29   0.01750    58.153    ******   1.13046  ******  764.99  ******  ******
   30   0.01750    58.153   1.00000   1.13046  741.40  764.99   229.4  0.5323

  Shaft Power =  12895000.00
   Net Thrust = 12983.99
 Equiv. Power =  13732168.00
    Fuel Flow =   1.0001
       S.F.C. =  77.5605
     E.S.F.C. =  72.8321
Sp. Sh. Power =    225622.45
Sp. Eq. Power =    240270.30
Sh. Th. Effy. =   0.2990
          Time Now 12:59:01
```

As regards the off-design conditions imposed in the `*.*dat` file reported before, the results are respectively resumed as follows:

```
     ***** OFF DESIGN ENGINE CALCULATIONS. Converged after  13 Loops *****

***** AMBIENT AND INLET PARAMETERS *****
Alt. =  10668.0      I.S.A. Dev. =    0.000       Mach No. =  0.70
Etar = 0.9950        Momentum Drag =   4383.16

***** COMPRESSOR  1 PARAMETERS *****
PRSF =  0.40113E+00     ETASF =  0.10494E+01     WASF =  0.13645E+01
Z = 0.89480             PR =   3.310             ETA = 0.84607
PCN =   0.8310          CN = 0.90991             COMWK =  0.24565E+07
STATOR ANGLE =   0.00
```

```
***** COMPRESSOR  2 PARAMETERS *****
PRSF =  0.75318E+00     ETASF =  0.10529E+01     WASF =  0.34115E+00
Z = 0.85588             PR =   5.747             ETA = 0.84813
PCN =   0.8957          CN = 0.96930             COMWK =  0.44096E+07
STATOR ANGLE =   0.00

***** COMBUSTION CHAMBER PARAMETERS *****
ETASF =  0.99000E+00
ETA = 0.99000           DLP = 0.3094             WFB =   0.3198

***** TURBINE  1 PARAMETERS *****
CNSF =  0.11073E+03     ETASF =  0.89588E+00     TFSF =  0.11893E+02
DHSF =  0.95184E+04
TF = 1211.143            ETA = 0.79969            CN =  2.738
AUXWK =  0.89568E+04     NGV ANGLE = 0.00

***** TURBINE  2 PARAMETERS *****
CNSF =  0.11145E+03     ETASF =  0.93171E+00     TFSF =  0.15805E+01
DHSF =  0.38081E+04
TF =  402.278            ETA = 0.80081            CN =  2.803
AUXWK =  0.00000E+00     NGV ANGLE = 0.00

***** MIXING MACH NUMBERS *****
Station 13, M= 0.401    Station 20,M = 0.256    Station 14,M = 0.377

***** TURBINE  3 PARAMETERS *****
CNSF =  0.50806E-02     ETASF =  0.10681E+01     TFSF =  0.70330E+00
DHSF =  0.48936E+04
TF =  401.500            ETA = 0.90685            CN =  1.414
AUXWK =  0.22031E+07     NGV ANGLE = 0.00

Additional Free Turbine Parameters:-
Speed =  80.0%          Power =  0.22031E+07
```

```
***** TURBINE  4 PARAMETERS *****
CNSF =  0.48196E-02     ETASF =  0.10681E+01     TFSF =  0.45677E+00
DHSF =  0.54380E+04
TF =  409.340            ETA = 0.86993            CN =  1.421
AUXWK =  0.28605E+07     NGV ANGLE = 0.00

Additional Free Turbine Parameters:-
Speed =  80.0%          Power =  0.28605E+07

***** CONVERGENT NOZZLE  1 PARAMETERS *****
NCOSF =  0.10000E+01
Area =  0.5323          Exit Velocity =  286.13  Gross Thrust =   6100.31
Nozzle Coeff. =  0.97526E+00

Scale Factor on above Mass Flows, Areas, Thrusts & Powers =     1.0000
```

Station	F.A.R.	Mass Flow	Pstatic	Ptotal	Tstatic	Ttotal	Vel	Area
1	0.00000	21.107	0.23524	0.32640	218.81	240.33	207.7	******
2	0.00000	21.107	0.28337	0.32476	231.12	240.33	135.8	0.3590
3	0.00000	21.107	******	1.07499	******	356.24	******	******
4	0.00000	16.180	******	1.07499	******	356.24	******	******
5	0.00000	16.180	******	6.17838	******	621.20	******	******
6	0.00000	16.180	******	6.17838	******	621.20	******	******
7	0.00000	13.753	******	6.17838	******	621.20	******	******
8	0.02325	14.073	******	5.86895	******	1420.00	******	******
9	0.01977	16.500	******	5.86895	******	1312.03	******	******
10	0.01977	16.500	******	2.16346	******	1091.66	******	******
11	0.01977	16.500	******	2.14182	******	1091.66	******	******
12	0.01977	16.500	******	1.12873	******	965.89	******	******
13	0.01977	16.500	1.01692	1.12873	941.45	965.89	240.3	0.1802
14	0.01485	21.861	1.01218	1.11218	807.14	826.73	210.3	0.2347
15	0.01485	21.861	******	1.10106	******	826.73	******	******
16	0.00000	0.000	******	0.00000	******	0.00	******	******

17	0.00000	0.000	******	0.00000	******	0.00	******	******
18	0.00000	5.361	******	1.07499	******	356.24	******	******
19	0.00000	5.361	******	1.07499	******	356.24	******	******
20	0.00000	5.361	1.01691	1.06424	351.65	356.24	96.3	0.0545
21	0.00000	0.000	******	0.00000	******	0.00	******	******
22	0.00000	2.427	******	6.17838	******	621.20	******	******
23	0.00000	0.000	******	0.00000	******	0.00	******	******
24	0.00000	0.000	******	0.00000	******	0.00	******	******
25	0.00000	0.000	******	0.00000	******	0.00	******	******
26	0.01485	21.861	******	0.66883	******	736.72	******	******
27	0.01485	21.861	******	0.66214	******	736.72	******	******
28	0.01485	21.861	0.27579	0.30147	602.41	616.91	176.5	0.7660
29	0.01485	21.861	******	0.29846	******	616.91	******	******
30	0.01485	21.861	0.23524	0.29846	578.64	616.91	286.1	0.5323

```
  Shaft Power =   5063637.00
   Net Thrust =  1717.15
 Equiv. Power =   5509380.00
    Fuel Flow =   0.3198
       S.F.C. =  63.1585
     E.S.F.C. =  58.0486
Sp. Sh. Power =    239906.53
Sp. Eq. Power =    261025.06
Sh. Th. Effy. =   0.3672
          Time Now 13:02:07
```

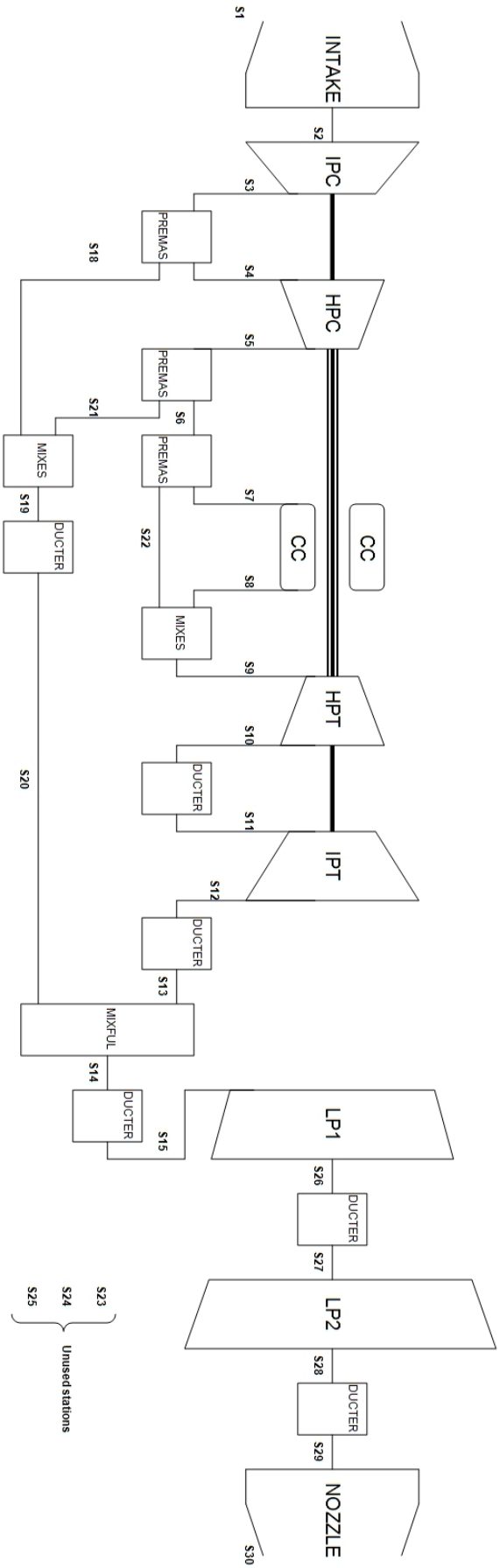

Fig. A.1. Complete REMO cycle scheme.

B. Simulation Procedure

The purpose of this appendix is to present the procedure adopted to design and simulate the basic nacelle cases. The procedure used to simulate a generic nacelle model is reported in Fig. B.1; it shows how the software/hardware tools selected to accomplish the present research are logically interconnected.

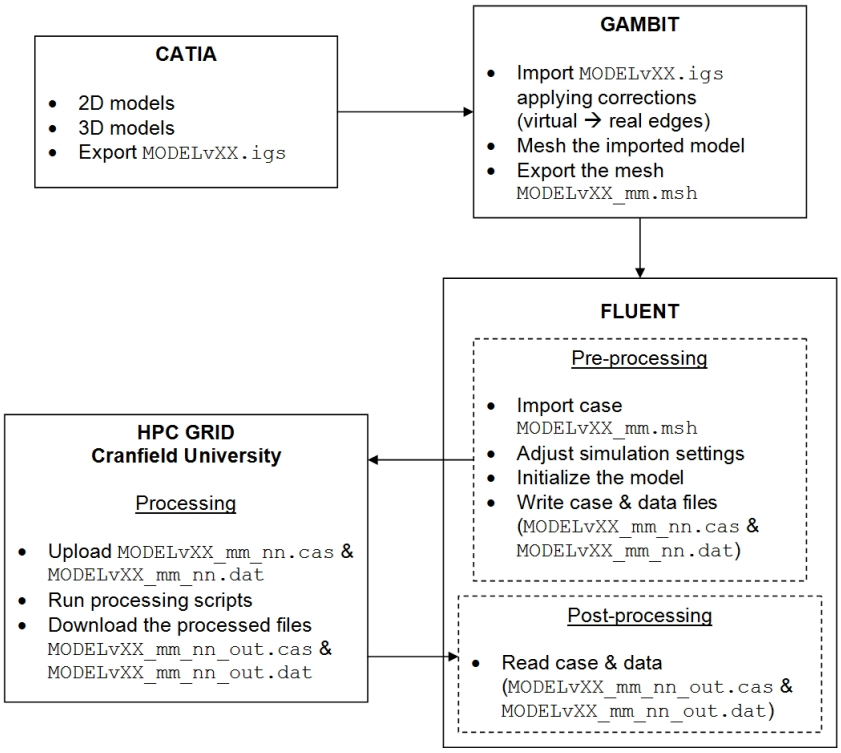

Fig. B.1. Simulation procedure.

When expecting to have more than one model and a consistent amount of simulations to analyse, by default the following file nomenclature can be adopted in order to clearly and univocally identify them:

- `MODEL`: the name of the model
- `vXX`: it stands for the version of the model (`v2D` for a two dimensional model, otherwise `v3D`)
- `_mm`: the number of the mesh version (from `00` to `99`); low numbers identify a coarse mesh, growing numbers apply to more refined versions of the grid
- `_nn`: the number of the simulation (from `00` to `99`), which may vary from the worst to the finest simulation, or to different physical conditions such as different cruise speed and altitude
- `_out`: identifies files processed by the High Performance Computing (HPC) Grid.

The methodology adopted to analyse any nacelle model is resumed by the following points:

- physical assumptions depending on flight conditions: altitude, flight speed, angle of attack (fixed at zero degrees for the 2D cases)
- definition of boundary conditions (e.g. Mach number and mass-flow demand at compressor face) from the cycle modelled in appendix A
- grid selection.

The procedure to pre-process the 2D models in Fluent is the following:

- Run Fluent (2ddp version)
- From menu
  - File
    - Read → Case... → `MODELvXX.msh`
  - Grid

    - Check
    - Info → Size
    - Scale... (models in CATIA are designed in millimetres)
- Define
    - Models
        - Solver... (set to 'axisymmetric')
        - Energy... (active)
        - Viscous... (Spalart-Allmaras with default options)
    - Materials... (Air - ideal gas)
    - Operating Conditions... (All set to zero)
    - Boundary Conditions... (for each condition the values of the physical parameters involved in the simulation have to be evaluated in advance)
- Solve
    - Monitors... (as default)
    - Initialize → Initialize
- File
    - Write → Case & Data...

The Case and Data files are then passed to the Cranfield University High Performance Computing (HPC) Grid for the processing phase, at the end of which the output files are post-processed using Fluent®.

C. DEMONS Logo

This appendix is a brief presentation of the logo associated to DEMONS and created by the doctoral candidate (figure C.1).

Fig. C.1. Graphic logo of the project.

Since DEMONS is the singular acronym of the project title, the choice of the graphic subject was made by doing a selection among mythological demons. Influenced by his personal passion for both horse-riding and human flight, the author designed the logo by representing one of the Plutonian demon-steeds: Alastor, Abatos, Aeton and Nonios. These hell-horses are known to be the bat-winged

steeds of Pluto (Hades). In the mythology, they draw his black chariot when Pluto abducted Persephone (Proserpina/Cora) the Goddess of Spring and daughter of Zeus and Demeter (Ceres). Alastor means 'avenger', Abatos means 'inaccessible', Aeton means 'swift as an eagle' and Nonios means 'measure'.

The white horse pictured in the logo represents these flying demons, as they are seen in the imagination of the author. The magnificent steed is painted in the act of jumping, ready for take off, in the sky, all over the world. the Latin motto 'semper in aere' means 'always in the air'. The message resumed by the logo consists in the purpose to avenge with open-rotors the ambiguous past of propfans, improving their performance to levels before believed inaccessible, through the measure of engineering techniques. In the name of a 'cleaner' aviation, the hope is that one day short/medium-haul aircraft, with their new engines, will always be able to fly swift as eagles.

References

[1] Geometrical characteristics of typical bodies. Technical Report 77028, ESDU, 1977.

[2] Profile drag of axisymmetric bodies at zero incidence for subcritical Mach numbers. Technical Report 78019, ESDU, 1978.

[3] Drag of axisymmetric cowls at zero incidence for subsonic Mach numbers. Technical Report 81024, ESDU, 1981.

[4] Mass flow and momentum functions for one-dimensional flow of gas in ducts. Technical Report 81004, ESDU, 1981.

[5] Representation of drag in aircraft performance calculations. Technical Report 81026, ESDU, 1981.

[6] Estimation of spillage drag for a wide range of axisymmetric intakes at $M < 1$. Technical Report 84004, ESDU, 1984.

[7] Aerodynamics and acoustics of propellers. Technical Report CP-366, AGARD, 1985.

[8] Introduction to installation effects on thrust and drag for propeller-driven aircraft. Technical Report 85015, ESDU, 1985.

[9] Thrust and drag accounting for propeller/airframe interaction. Technical Report 85017, ESDU, 1985.

[10] Propeller/body interaction for thrust and drag. Technical Report 86017, ESDU, 1986.

[11] Full scale technology demonstration of a modern counterrotating unducted fan engine concept - Design report. Technical Report CR-180867, NASA, 1987.

[12] *Advanced propellers and their installation on aircraft: proceedings [of an] International Conference, Royal Aeronautical Society, 26-27 September, 1988*. Royal Aeronautical Society, London, 1988. International Conference on Advanced Propellers and their Installation on Aircraft (1988, London).

[13] Air intakes for high speed vehicles. Technical Report AR-270, Advisory Group for Aerospace Research and Development (AGARD), 1991.

[14] *Propeller/Propfan In-Flight Thrust Determination*. SAE, Warrendale, 1993. Society of Automotive Engineers.

[15] NACA-1 series geometry representation for computational fluid dynamics. Technical Report 94013, ESDU, 1994.

[16] Surface pressure coefficient distributions for axisymmetric forecowls at zero incidence ($M < 1.5$). Technical Report 94015, ESDU, 1994.

[17] Wave drag coefficient for axisymmetric forecowls at zero incidence ($M < 1.5$). Technical Report 94014, ESDU, 1994.

[18] *Aircraft propulsion system performance station designation and nomenclature*. SAE, Warrendale, 1997. Society of Automotive Engineers.

[19] Estimation of airframe drag by summation of components: principles and examples. Technical Report 97016, ESDU, 1997.

[20] Design considerations for enclosed turboprop engine test cells. Technical Report SAE AIR 5295, Society of Automotive Engineers, 1998.

[21] Digital Representation for Communication of Product Definition Data. Technical Report NBSIR 80-1978, U.S. National Bureau of Standards, January 1980.

[22] A. I. A. Galvez and F. Gutierrez. Applying MATLAB to Computer Graphics and CAGD. Application to a Visualization Problem in the Automotive Industry. Technical Report Moscow, The 9-th International Conference on Computer Graphics and Vision, 1999.

[23] A. S. Aljabri, V. Lyman, and R. J. Parker. Evaluation of Propeller/Nacelle Interactions in the PTA Program. Technical Report 1552, AIAA, 1986.

[24] B. H. Anderson, D. R. Reddy, and K. A. Kapoor. Comparative Study of Full Navier-Stokes and Rreduced Navier-Stokes Analyses for Separating Flows within a Diffusing Inlet S-Duct. Technical Report 2154, AIAA, 1993.

[25] J. Anderson. *Introduction to Flight.* McGraw-Hill, New York and London, 1989.

[26] J. D. Anderson. *Modern Compressible Flow With Historical Perspective.* McGraw-Hill, New York and London, 2004.

[27] N. E. Anderson and D. A. Wagner. Development testing of the 578 propfan gear system. Technical Report 2817, AIAA, 1989.

[28] R. D. Anderson, J. C. Gill, and A. S. Novick. Advanced propfan engine characteristics and technology needs. Technical Report 1155, AIAA, 1983.

[29] J. P. Angus and D. A. Perry. Hollow aerofoil blade, 1987.

[30] H. J. Banach and C. N. Reynolds. Turboprop engine propulsion for the 1990's. *Journal of Aircraft*, 21(4):238–243, 1984.

[31] B. A. Barsky and D. T. DeRose. Geometric Continuity of Parametric Curves. Technical Report UCB/CSD 84/205, Berkeley Computer Graphics Laboratory, 1984.

[32] B. A. Barsky and D. T. DeRose. Three Characterizations of Geometric Continuity for Parametric Curves. Technical Report ACM/SIGGRAPH'88 Course 25, Berkeley Computer Graphics Laboratory, 1988.

[33] A. B. Barta, W. A. Bennett, B. R. Vittal, and M. R. Krishnan. Design and Development of a Compact Bifurcated Turboprop Inlet. Technical Report 2017, AIAA, 1991.

[34] R. H. Bartels, J. C. Beatty, and B. A. Barsky. *An Introduction to Splines for Use in Computer Graphics and Geometric Modeling.* Morgan Kaufmann Publishers inc., California, 1987.

[35] J. A. Baum, P. J. Dumais, M. G. Mayo, F. B. Metzger, A. M. Shenkman, and G. G. Walker. Prop-fan data support study - technical report. Technical Report CR-152141, NASA, 1978.

[36] H. W. Bennett and C. W. Robey. Propfan aircraft propulsion engine, 1984.

[37] D. Biermann and W. H. Gray. Wind-tunnel tests of single- and dual-rotating pusher propellers having from three to eight blades. Technical Report L-359, NACA Wartime Report, 1942.

[38] C. W. Boppe and B. S. Rosen. Computation of Prop-Fan Engine Installation Aerodynamics. *Journal of Aircraft*, 23(4):299, 1986.

[39] C. W. Boppe and B. S. Rosen. Computation of Prop-Fan Engine Installation Aerodynamics. *Journal of Aircraft*, 23(4):299–305, 1986.

[40] J. M. Bousquet and P. Gardarein. Recent Improvements in Propeller Aerodynamic Computations. Technical Report 4124, AIAA, 2000.

[41] F. J. Boyle et al. Comparison of PIV Measurements with CFD Predictions for a High Speed Propeller. Technical Report 2387, AIAA, 1999.

[42] F. J. Boyle et al. Three-Dimensional Euler Solutions for Axisymmetric and Non-Axisymmetric Advanced Propeller Flows. Technical Report 2386, AIAA, 1999.

[43] A. P. Brown. An investigation into the identification of net installed propulsive efficiency on a turboprop transport aeroplane. Technical Report 4940, AIAA, 2004.

[44] M. L. Celestina, R. A. Mulac, and J. J. Adamczyk. A numerical simulation of the inviscid flow through a counterrotating propeller. *Journal of Turbomachinery*, 108:187–193, 1986.

[45] B. Chandrasekaran. *Method for the prediction of the installation aerodynamics of a propfan at subsonic speeds.* NASA, Washington, D.C., 1985.

[46] D. C. Chapman, R. E. Fleury, and D. E. Smith. Testing of the 578-dx propfan propulsion system. Technical report, AIAA, 1989.

[47] J. T. Conway. Analytical Solutions for the Actuator Disk with Variable Radial Distribution of Load. *Journal of Fluid Mechanics*, 297(1):327–355, 1995.

[48] R. Coppinger. European research to focus on open-rotor aircraft engines. Technical report, Flight International, 8 August 2007.

[49] T. Q. Dang. Simulations of Propeller/Airframe Interference Effects Using an Euler Correction Method. *Journal of Aircraft*, 26(11):994–1001, 1989.

[50] J. B. Delano and J. L. Crigler. Compressible-Flow Solutions for the Actuator Disk. Technical Report RM-L53A07, National Advisory Committee for Aeronautics, 1953.

[51] J. E. Donelson, W. T. Lewerenz, and R. T. Durbin. UHB technology validation - the final step. Technical Report 2807, AIAA, 1988.

[52] J. E. Donelson, W. T. Lewerenz, and R. T. Durbin. UHB demonstrator flight test program - phase 2. Technical Report 2582, AIAA, 1989.

[53] M. Dubosc. 3D Simulation and Analysis of a Pusher Open-rotor Nacelle Installation. Technical Report MSc Thesis, Cranfield Univerity, September 2009.

[54] A. Dziubinski and W. Stalewski. Vortex Ring State Simulation Using Actuator Disc. Technical Report 1, Proceedings 21st European Conference on Modelling and Simulation, 2007.

[55] T. A. Egolf, O. L. Anderson, and D. E. Edwards. *An analysis for high speed propeller-nacelle aerodynamic performance prediction.* NASA, Washington, D.C, 1988. Contents: Vol. 1: Theory and application; Vol. 2: User's manual.; Affiliation: United Technologies Research Center.

[56] E. Envia. Prediction of noise field of a propfan at angle of attack. Technical report, U.S. Government Printing Office, 1991.

[57] G. Farin. A History of Curves and Surfaces in CAGD. Technical Report AZ 85257-5406, Arizona State University, 2002.

[58] J. P. Fielding. *Introduction to aircraft design.* Cambridge University Press, Cambridge, 1999.

[59] D. L. Finn. Quintic Hermite Interpolation. Technical Report December, Geometric Modelling Course Notes, 2004.

[60] B. Fowler and R. Bartels. Constrained-Based Curve Manipulation. Technical Report September, IEEE Computer Graphics and Applications, 1993.

[61] F. N. Fritsch and R. E. Carlson. Monotone Piecewise Cubic Interpolation. Technical Report 17 (2), SIAM Journal on Numerical Analysis, 1980.

[62] P. E. Gall and C. Cros. Aircraft Having Reduced Environmental Impact. Technical Report 20090020643, US Patent, 22 January 2009.

[63] D. Garber and W. Willshire. En route noise levels from propfan test assessment airplane. Technical report, U.S. Government Printing Office, 1994.

[64] G. L. Gentry, D. M. Dunham, and M. A. Takallu. *Effect of solidity and inclination on propeller-nacelle force coefficients.* NASA, Washington, D.C, 1991. Affiliation: Langley Research Center; Lockheed Engineering & Sciences Company.

[65] J. Godston and C. N. Reynolds. Propulsion system integration configurations for future prop-fan powered aircraft. *Journal of Aircraft*, 22(12):1027, 1985.

[66] D. P. Golden, T. J. Barber, and W. C. Chin. An axisymmetric nacelle and turboprop inlet analysis including power simulation. *Journal of Aircraft*, 20(6):536–542, 1983.

[67] E. L. Goldsmith and J. Seddon. *Intake aerodynamics.* Blackwell Science, 1999.

[68] I. M. Goldsmith. A study to define the research and technology requirements for advanced turbo/propfan transport aircraft. Technical Report CR-166138, NASA, 1981.

[69] V. Gorantla. Quality Evaluation of CFD Simulation on the Aerodynamics of Pusher Open-rotor Nacelle. Technical Report MSc Thesis, Cranfield Univerity, September 2009.

[70] J. F. Groeneweg and L. J. Bober. NASA advanced propeller research. Technical Report TM-101361, National Aeronautics and Space Administration, 1988.

[71] R. D. Hager and D. Vrabel. Advanced turboprop project. Technical Report SP-495, NASA, 1988.

[72] J. P. Hancock. PTA test bed aircraft engine inlet model test report. Technical Report CR-174845, NASA, 1985.

[73] J. P. Hancock, V. Lyman, and A. P. Pennock. Analysis of results from wind tunnel tests of inlets for an advanced turboprop nacelle installation. Technical Report CR-174937, NASA, 1986.

[74] R. W. Harris and R. D. Cuthbertson. *UDF-727 flight test program.* AIAA, New York, 1987. Paper presented at: AIAA/SAE/ASME/ASEE 23rd joint propulsion conference; Affiliation: General Electric Company, Boeing Commercial Aircraft Company.

[75] G. S. Hodges and J. H. R. Sadler. Turboprop and open rotor propulsion for the future. Technical Report 1472, AIAA, 1986.

[76] S. F. Hoerner. *Fluid-Dynamic Drag.* Published by the author, 1958.

[77] J. H. Horlock. *Actuator Disk Theory.* McGraw-Hill Education, 1978.

[78] C. E. Hughes. Low-speed wind tunnel performance of high-speed counterrotation propellers at angle-of-attack. Technical Report 2583, AIAA, 1989.

[79] C. E. Hughes and J. A. Gazzaniga. Summary of low-speed wind tunnel results of several high-speed counterrotation propeller configurations. Technical Report 3149, AIAA, 1988.

[80] D. H. Hunter. A-85 powerplant installation, 1986.

[81] D. T. Jensen and J. M. Leonard. The forgotten allison engines. Technical Report 3566, AIAA, 2002.

[82] R. J. Jeracki, D. C. Mikkelson, and B. J. Blaha. Wind tunnel performance of four energy efficient propellers designed for mach 0.8 cruise. Technical Report TM-79124, NASA, 1979.

[83] R. J. Jeracki and G. E. Rose. Effect of reduced aft diameter and increased blade number on high-speed counterrotation propeller performance. Technical Report TM-102077, NASA, 1989.

[84] G. E. Juola, H. R. Welge, and D. N. Smyth. Analytical and experimental study of a complex 3-D inlet for turboprop applications. Technical Report 2203, AIAA, 1984.

[85] A. Kaul. Drag Estimation Techniques for Open-rotor Engines with Pusher Architecture. Technical Report MSc Thesis, Cranfield Univerity, September 2009.

[86] K. Kaza, M. Williams, M. Mehmed, and G. Narayanan. Aeroelastic response of metallic and composite propfan models in yawed flow. Technical report, U.S. Government Printing Office, 1988.

[87] D. Kuchemann and J. Weber. *Aerodynamics of propulsion.* McGraw-Hill, New York, 1953.

[88] H. Kunta, R. Gatineau, R. Prydz, and F. Balena. Development and testing of cabin sidewall acoustic resonators for the reduction of cabin tone levels in propfan powered aircraft. Technical report, U.S. Government Printing Office, 1991.

[89] N. D. Kuznetsov. Propfan engines. Technical Report 1981, AIAA, 1993.

[90] K. M. Lee and S. C. M. Yu. Computational Studies of Flows in the RAE 2129 S-Shaped Diffusing Duct. Technical Report 0658, AIAA, 1994.

[91] B. H. Little and B. L. Hinson. *Inlet design for high-speed propfans.* Society of Automotive Engineers, Warrendale, 1982. Paper presented at: Aerospace Congress & Exposition Anaheim, California October 25-28, 1982; Affiliation:Lockheed-Georgia Co; SAE Aerospace Congress & Exposition.

[92] B. H. Little and B. L. Hinson. *Revised guidelines for propfan inlet design based on recent analytical and test experience.* AIAA, New York, 1987. Paper presented at: AIAA 25th aerospace sciences meeting. Affiliation: Lockheed-Georgia Company; AIAA Aerospace Sciences Meeting.

[93] B. H. Little and W. S. Trimboli. *An experimental investigation of S-duct diffusers for high-speed propfans.* AIAA, ASME, SAE, New York, 1982.

[94] B. H. Little Jr. Propulsion System Installation Design for High-Speed Prop-Fans. *Journal of Aircraft*, 20(5):411–417, 1983.

[95] B. H. Little Jr and B. L. Hinson. Revised guidelines for propfan inlet design based on recent analytical and test experience. Technical Report 0163, AIAA, 1987.

[96] B. H. Little Jr and W. S. Trimboli. An experimental investigation of S-duct diffusers for high-speed propfans. Technical Report 1123, AIAA, 1982.

[97] A. Lopez-Diez, L. Ruiz-Calavera, J. Castillo-Calvo, and R. F. Prieto-Ibanez. Front End Optimization of High Speed Turboprop Engines. Technical Report 4204, AIAA, 2005.

[98] P. Lotstedt. Accuracy of Propeller Model in Inviscid Flow. *Journal of Aircraft*, 32(6):1312–1321, 1995.

[99] V. Lyman and J. P. Hancock. Comparison of Theory and Experiment for Propfan Inlets. *Journal of Propulsion*, 3(6):534–541, 1987.

[100] J. C. Mankins. *Technology Readiness Levels: A White Paper*. NASA, Office of Space Access and Technology, Advanced Concepts Office, 6 April 1995.

[101] Y. Matsuo and C. Arakawa. Navier-Stokes Computations for Flowfield of an Advanced Turboprop. Technical Report 3094, AIAA, 1988.

[102] Y. Matsuo and C. Arakawa. Navier-Stokes Simulations Around a Propfan Using Higher-Order Upwind Schemes. Technical Report 2699, AIAA, 1989.

[103] P. McDill. S-duct inlet/diffusers for turboprop offset gearbox applications. Technical Report 1462, AIAA, 1986.

[104] P. L. McDill. An experimental evaluation of S-duct diffuser configurations for turboprop offset gearbox applications. Technical Report CR-197454, NASA, 1986.

[105] P. L. McDill and L. I. Tolle. Analytical design and experimental verification of S-duct diffusers for turboprop installations with an offset gearbox. Technical Report 1211, AIAA, 1983.

[106] O. Mehmed and A. P. Kurkov. Experimental investigation of counter-rotatingpropfan flutter at cruise conditions. *Journal of Propulsion and Power*, 10(3):343–347, 1994.

[107] O. Mehmed and D. Murthy. Experimental investigation of propfan aeroelastic response in off-axis flow with mistuning. Technical report, U.S. Government Printing Office, 1988.

[108] R. D. D. Menzies, K. J. Badcock, G. N. Barakos, and B. E. Richards. Validation of the Simulation of Flow in an S-Duct. Technical Report 2808, AIAA, 2002.

[109] D. C. Mikkelson, B. J. Blaha, G. A. Mitchell, and J. E. Wikete. Design and performance of energy efficient propellers for mach 0.8 cruise. Technical Report TM X-73612, NASA, 1977.

[110] C. J. Miller and G. G. Podboy. Euler analysis comparison with LDV data for an advanced counter-rotation propfan at cruise. Technical Report TM-103249, NASA, 1990.

[111] F. Moens and P. Gardarein. Numerical Simulation of the Propeller/Wing Interactions for Transport Aircraft. Technical Report 2404, AIAA, 2001.

[112] D. F. Myring. The Profile Drag of Bodies of Revolution in Subsonic Axisymmetric Flow. Technical Report TR-72234, Royal Aircraft Establishment, 1973.

[113] D. A. Naik. 3-D Euler calculations for aft-propfan integration. Technical Report 2147, AIAA, 1990.

[114] M. Nallasamy, E. Envia, B. Clark, and J. Groeneweg. Near-field noise of a single-rotation propfan at an angle of attack. Technical report, U.S. Government Printing Office, 1990.

[115] NASA. *Historical data book*, volume 6, chapter 3. National Aeronautics and Space Administration.

[116] R. H. Nichols. Calculation of the Flow in a Circular S-Duct Inlet. Technical Report 0174, AIAA, 1991.

[117] A. B. Parry and D. G. Crighton. Open rotor blading, 1990.

[118] L. Piegl and W. Tiller. *The NURBS Book - Second Edition*. Springer, 1997.

[119] G. G. Podboy and M. J. Krupar. Laser velocimeter measurements of the flow field generated by an advanced counterrotating propeller. Technical Report TM-101437, NASA, 1989.

[120] D. T. Poland, H. W. Bartel, and P. C. Brown. PTA flight test overview. Technical Report 2803, AIAA, 1988.

[121] A. Pressley. *Elementary Differential Geometry*. Springer-Verlag, 2001.

[122] A. Raichle et al. A New Actuator Disk Model for the TAU Code and Application to a Sailplane with a Folding Engine. *New Results in Numerical and Experimental Fluid Mechanics*, 6(1):52–61, 2007.

[123] T. Reddy and K. Kaza. Analysis of unswept propfan blade with a semi empirical dynamic stall model. Technical report, U.S. Government Printing Office, 1989.

[124] C. Reid. Overview of Flight Testing of GE Aircraft Engines' UDF® Engine. Technical Report 3082, AIAA, 1988.

[125] C. N. Reynolds. Advanced Prop-fan Engine Technology (APET) single- and counter-rotation gearbox/pitch change mechanism. Technical Report CR-168114, Vol. II, NASA, 1985.

[126] C. N. Reynolds. Advanced prop-fan engine technology (APET) single- and counter-rotation gearbox/pitch change mechanism. Technical Report CR-168114, Vol. I, NASA, 1985.

[127] M. P. Robichaud, W. D. Bartolomeo, K. Heikurinen, and W. G. Habashi. Turboprop Air Intake Design Using 3-D Viscous Analysis. Technical Report 171, AIAA, 1997.

[128] T. Robinson. Prize fight. *Aerospace International*, July:34–37, 2008.

[129] D. F. Rogers and J. A. Adams. *Mathematical Elements for Computer Graphics - Second Edition*. McGraw-Hill, New York and London, 1989.

[130] J. Roskam. *Airplane Aerodynamics and Performance*. DARcorporation, 1997.

[131] S. Saito and H. Kobayashi. Predicted Flow Field Around the Advanced Propeller at Take-Off. Technical Report 3151, AIAA, 1988.

[132] D. Salomon. *Curves and Surfaces for Computer Graphics*. Springer, 2006.

[133] S. S. Samant and N. J. Yu. Flow prediction for propfan engine installation effects on transport aircraft at transonic speeds. Technical Report CR-3954, NASA, 1986.

[134] S. S. Samant et al. Flow Prediction for Propfan Engine Installation Effects on Transport Aircraft at Transonic Speeds. Technical Report CR-3954, National Aeronautics and Space Administration, 1986.

[135] J. Sanchez-Reyes. A Simple Technique for NURBS Shape Modification. Technical Report January-February, IEEE New Image-Generation Techniques, 1997.

[136] T. Schwarcz. Hermite-curves with given curvature. Technical Report August, 13 Conference on Geometry and Graphics, Dresden, Germany, 2008.

[137] J. S. Serafini. Laser-Velocimeter Flow-Field Measurements of an Advanced Turboprop. Technical Report 1568, AIAA, 1981.

[138] Shattuck, Colmanyoung, and Jon. Modern propeller systems for advanced turboprop aircraft. Technical Report 1846, AIAA, 1993.

[139] J. Simonich et al. Flow Visualization of a Prop-Fan Leading-Edge Vortex at Takeoff. Technical Report 0386, AIAA, 1992.

[140] L. H. Smith. Unducted fan aerodynamic design. *Journal of Turbomachinery*, 109:313–324, 1987.

[141] A. Sobester and A. J. Keane. Airfoil Design via Cubic splines - Ferguson's Curves Revisited. Technical Report 2881, AIAA, 2007.

[142] J. S. Sokhey. Three-dimensional transonic flow analysis of turboprop inlet and nacelle configurations. Technical Report 0193, AIAA, 1984.

[143] P. M. G. Solera. Off-Design Characteristics of a Pusher Open-rotor Nacelle. Technical Report MSc Thesis, Cranfield Univerity, September 2009.

[144] A. R. Stuart. The unducted fan engine. Technical Report 1190, AIAA, 1985.

[145] A. Stuermer. Unsteady CFD Simulations of Contra-Rotating Propeller Propulsion Systems. Technical Report 5218, AIAA, 2008.

[146] A. Stuermer and J. Yin. Low-Speed Aerodynamics and Aeroacustics of CROR Propulsion Systems. Technical Report 3134, AIAA, 2009.

[147] T. J. Sullivan. Aerodynamic performance of a scale-model, counterrotating unducted fan. *ASME Journal of Turbomachinery*, 112:579–586, 1990.

[148] T. Tenerowicz. Flow Behind Single- and Dual-Rotation Propellers at Angle of Attack. Technical Report 1750, AIAA, 1987.

[149] H. Theisel. *Computer Aided Geometric Design*. Geometric conditions for G3 continuity of surfaces, 1997.

[150] T. Theodordsen. *Theory of propellers*. McGraw-Hill Book Co., New York, 1948.

[151] T. G. Tillman et al. Hot Wire Measurements Downstream of a Prop-Fan. Technical Report 2698, AIAA, 1989.

[152] R. Tognaccini. *Aerodinamica dell'Ala Rotante*. University of Naples - Federico II, 2004.

[153] Various Authors. Equations, Tables, and Charts for Compressible Flow. Technical Report R-1135, National Advisory Committee for Aeronautics, 1953.

[154] L. L. M. Veldhuis and G. W. Luursema. Comparison of an Actuator Disk and a Blade Modeling Approach in Navier-Stokes Calculations on the SR-3 Propfan. Technical Report 4528, AIAA, 2000.

[155] A. W. Vogeley. Axial-Momentum Theory for Propellers in Compressible Flow. Technical Report TN-2164, National Advisory Committee for Aeronautics, 1951.

[156] Q. R. Wald. The aerodynamics of propellers. *Progress in Aerospace Sciences*, 42:85–128, 2006.

[157] P. P. Walsh and P. Fletcher. *Gas Turbine Performance*. Blackwell Publishing, 2004.

[158] F. E. Weick. *Aircraft propeller design*. McGraw-Hill book company, inc., New York and London, 1930.

[159] D. L. Whitfield. Euler Equations Simulation of Propeller-Wing Interaction in Transonic Flow. *Journal of Aircraft*, 21(11):835–839, 1984.

[160] D. L. Whitfield et al. Three-Dimensional Unsteady Euler Solutions for Propfans and Counter-Rotating Propfans in Transonic Flow. Technical Report 1197, AIAA, 1987.

[161] J. B. Whitlow Jr and G. K. Sievers. Nasa advanced turboprop research and concept validation program. Technical Report TM-100891, NASA, 1988.

[162] R. P. Woodward. Measured noise of a scale model high speed propeller at simulated takeoff/approach conditions. Technical Report TM-88920, NASA, 1987.

[163] S. J. Yoon and J. A. Schetz. Numerical Navier-Stokes Solutions of High-Speed Propeller Flows. *Journal of Propulsion*, 4(4):291–292, 1988.

[164] N. J. Yu, K. Kusunose, H. C. Chen, and D. M. Sommerfield. Flow Simulations for a Complex Airplane Configuration Using Euler Equations. Technical Report 0454, AIAA, 1987.

[165] N. J. Yu et al. Flow Prediction for Propfan Configurations Using Euler Equations. Technical Report 1645, AIAA, 1984.

[166] A. Zachariadis and C. A. Hall. Application of a Navier-Stokes Solver to the Study of Open Rotor Aerodynamics. Technical Report 59332, ASME Turbo Expo, 2009.